UNIVERSIDADE FEDERAL DE SANTA CATARINA
CENTRO TECNOLÓGICO
PROGRAMA DE PÓS-GRADUAÇÃO EM ENGENHARIA QUÍMICA

THIAGO MACHADO NEUBAUER

Crystallization of calcium carbonate: Modelling thermodynamic equilibrium, pathway, nucleation, growth, agglomeration, and dissolution kinetics for the calcium carbonate polymorphs formation.

Florianópolis
2022

Thiago Machado Neubauer

Crystallization of calcium carbonate: Modelling thermodynamic equilibrium, pathway, nucleation, growth, agglomeration, and dissolution kinetics for the calcium carbonate polymorphs formation

Tese submetida ao Programa de Pós de Graduação em Engenharia Química da Universidade Federal de Santa Catarina para a obtenção do título de Doutor em Engenharia Química
Orientadora: Profª. Drª. Cristiane da Costa
Coorientadores: Prof. Dr. Pedro Henrique Hermes de Araújo e Profª. Drª. Claudia Sayer

Florianópolis
2022

Ficha de identificação da obra elaborada pelo autor,
através do Programa de Geração Automática da Biblioteca Universitária da UFSC.

Machado Neubauer, Thiago
Crystallization of calcium carbonate: Modelling thermodynamic equilibrium, pathway, nucleation, growth, agglomeration, and dissolution kinetics for the calcium carbonate polymorphs formation / Thiago Machado Neubauer ; orientador, Cristiane Da Costa, coorientador, Pedro Henrique Hermes de Araújo, coorientador, Claudia Sayer, 2022.
190 p.

Tese (doutorado) - Universidade Federal de Santa Catarina, Centro Tecnológico, Programa de Pós-Graduação em Engenharia Química, Florianópolis, 2022.

Inclui referências.

1. Engenharia Química. 2. Populational Balance. 3. Calcium carbonate polymorphism. 4. Mathematical modelling of Crystallization. I. Da Costa, Cristiane. II. Hermes de Araújo, Pedro Henrique. III. Sayer, Claudia IV. Universidade Federal de Santa Catarina. Programa de Pós Graduação em Engenharia Química. V. Título.

Thiago Machado Neubauer

Crystallization of calcium carbonate: Modelling thermodynamic equilibrium, pathway, nucleation, growth, agglomeration, and dissolution kinetics for the calcium carbonate polymorphs formation

O presente trabalho em nível de doutorado foi avaliado e aprovado por banca examinadora composta pelos seguintes membros:

Prof. Bruno Francisco Oechsler, Dr.

Universidade Federal de Santa Catarina

Prof. Elton Franceschi, Dr

Universidade Tiradentes

Prof. Wagner Aldeia, Dr.

Instituto de Pesquisas Tecnológicas do Estado de São Paulo

Certificamos que esta é a **versão original e final** do trabalho de conclusão que foi julgado adequado para obtenção do título de Doutor em Engenharia Química.

Documento assinado digitalmente
Debora de Oliveira
Data: 28/07/2022 14:33:22-0300
CPF: 728.453.929-15
Verifique as assinaturas em https://v.ufsc.br

Profª. Drª. Débora de Oliveira

Coordenadora do Programa de Pós-Graduação em Engenharia Química

Documento assinado digitalmente
Cristiane da Costa
Data: 27/07/2022 13:35:33-0300
CPF: 041.369.219-18
Verifique as assinaturas em https://v.ufsc.br

Profª. Drª. Cristiane da Costa

Orientadora

Florianópolis, 2022

AGRADECIMENTOS

Primeiramente, quero agradecer a minha família por todo apoio ao longo dessa jornada. E esse agradecimento também inclui você, mãe, por continuar sendo o meu norte.

Também agradeço aos meus colegas que me ajudaram ao longo do doutorado, tanto tecnicamente quanto pessoalmente, esse trabalho não teria acontecido sem a ajuda de todos vocês. Em um aspecto mais pessoal, seria injusto da minha parte não agradecer nominalmente a minha namorada Mariana Campagnoni por todo apoio, compreensão e carinho ao longo de todo esse doutorado. Fique sabendo que nenhuma calcita, vaterita ou aragonita teria sido calculada sem você ao meu lado.

Devo agradecer alguns amigos muito especiais ao longo desse trabalho, nominalmente André Eliezer Polloni, Arthur Cordeiro, Thomas Medrado e Fabiane Serpa. Todos vocês contribuiram para esse trabalho. Espero um dia ser capaz de retribuir a vocês tudo isso.

Agradeço aos professores Claudio Dariva, Gustavo Borges e Elton Franceschi por terem me dado a oportunidade de participar desse projeto e aberto a porta do laboratório de vocês, Instituto de Tecnologia e Pesquisa, para que eu pudesse aprender e crescer com a equipe muito competente que vocês organizam. Agradeço também meus coorientadores Claudia Sayer e Pedro Henrique Hermes de Araújo, por terem me indicado a participar desse projeto e por terem compartilhado seus conhecimentos e experiências comigo. Outro participante desse projeto que desejo agradecer é o Bruno Barbosa Castro, por toda ajuda ao longo desse trabalho, com certeza sua contribuição acrescentou muito a esse trabalho. Agradeço também ao Wagner Aldeia, pelos dados experimentais, fundamentais a essa tese, e por compartilhar da sua experiência e conhecimento comigo. Fechando a equipe, agradeço minha orientadora Cristiane da Costa, que me orienta há 6 anos, por toda a paciência, apoio e orientação tanto nos aspectos técnicos quanto nos pessoais ao longo desse trabalho.

Por fim, agradeço a Universidade Federal de Santa Catarina pela oportunidade de fazer meu doutorado em um curso de excelência e a Coordenação de Aperfeiçoamento Pessoal de Nível Superior-CAPES pelo apoio financeiro.

“Just keep swimming.”

(Dory, 2007)

RESUMO

A cristalização de carbonato de cálcio é uma operação unitária extensamente estudada tanto na academia quanto na indústria; sua incrustação em equipamentos industriais custa bilhões de doláres ao setor industrial todo ano. Mas o fenônemo da formação do $CaCO_3$ é complexo, devido aos diversos fatores termodinâmicos e cinéticos envolvidos no processo de formação das partículas. Esta tese apresenta o desenvolvimento e aplicação de um modelo matemático para descrever os aspectos termodinâmicos e cinéticos do $CaCO_3$ em sua formação. O algoritmo do modelo inclui equilíbrio termodinâmico e perfis de energia, balanços de massa e populacionais, nucleação, crescimento, aglomeração e rearranjo polimórfico. A estrutura da modelagem foi usada com diferentes conjuntos experimentais. O primeiro conjunto de dados apresentou cristalizações em batelada com concentrações iniciais de cálcio e bicarbonato de 50 a 20 $mmol.L^{-1}$ a 25ºC. O modelo foi ajustado para distribuição do tamanho dos cristais, massa cristalina total e proporção polimórfica para este conjunto, apresentando um erro médio quadrático de 4% por variável. Foi possível descrever que a elevação na supersaturação causou a elevação tanto na massa total quanto no tamanho dos cristais obtidos e que o maior teor de calcita foi obtido no experimento de 40 $mmol.L^{-1}$. O segundo conjunto de dados utilizado apresentou resultados de cristalização de experimentos com uma faixa de concentração de íons divalentes, Mg (30 a 144 ppm), Ba (28 a 280 ppm) e Sr (33 a 1500 ppm) com 1 e 0,297 $mol.L^{-1}$ de cálcio e bicarbonato a 25ºC. Para este segundo conjunto, o modelo também foi ajustado para distribuição de tamanho dos cristais, massa cristalina total e proporção polimórfica, obtendo uma boa concordância geral com um erro médio quadrático de 12%. O modelo também capturou o maior diâmetro volumétrico médio, conteúdo de calcita e menor massa cristalina total observado para os experimentos com Mg, Ba e Sr em comparação com o experimento base, embora com mecanismos diferentes para cada íon. Para o terceiro conjunto de dados, foi realizado um estudo de caso com informações experimentais da Petrobras para avaliar a influência da presença de uma válvula *choke* na formação de carbonato de cálcio. Foi possível observar que as diferentes condições observadas nos poços produziram impactos diferentes na presença da válvula, com o poço mais problemático, em termos de formação de preciptados, apresentando maior proporção de bicarbonato/cálcio e temperaturas. Por sua vez, também apresentou maiores tempos de residência. Consequentemente, o poço mais problemático apresentou uma diferença de 340% entre o potencial termodinâmico e cinético de produção salina. Ao final das simulações, os potenciais termodinâmicos e cinéticos dos poços foram comparados proporcionalmente ao seu teor de água, sendo possível observar que campos menos desenvolvidos podem apresentar potenciais de formação proporcionalmente maiores. Com as simulações, pode-se observar que um balanço populacional completo pode fornecer uma ferramenta valiosa para avaliar os mecanismos termodinâmicos e cinéticos da formação de carbonato de cálcio. Embora o modelo tenha sido ajustado apenas para uma faixa específica de concentrações, pode ser útil no processo de cristalização de carbonato de cálcio como uma ferramenta de estudo prático para avaliar os efeitos da supersaturação, íons divalentes e variações de temperatura, pressão e tempo de residência na formação de $CaCO_3$ para aplicações acadêmicas e industriais.

Palavras-chave: Balanço populacional. carbonato de cálcio. Polimorfismo. Modelagem matemática. Cristalização.

RESUMO EXPANDIDO

Introdução

A cristalização é uma operação unitária extensamente estudada tanto na academia quanto na indústria; os estudos da cristalização podem ser aplicados para investigar como ocorrem a formação de sólidos cristalinos e sua incrustação em equipamentos industriais. Sua ocorrência é um problema universal significativo que custa bilhões de dólares às indústrias todos os anos. Esta formação pode conter uma mistura de materiais inorgânicos, orgânicos e biológicos em diferentes fases e pode ocorrer em várias regiões dentro da estrutura industrial. O carbonato de cálcio é um dos componentes mais comuns nessas formações e sendo mais difundido em instalações de produção de petróleo e gás.

Além do interesse industrial, o carbonato de cálcio também é um modelo adequado para estudar a formação e o crescimento de fases metaestáveis e sua transformação na(s) forma(s) estável(s). A investigação dos mecanismos cinéticos e termodinâmicos envolvidos na precipitação do carbonato de cálcio ajuda a elucidar a natureza e o comportamento das fases metaestáveis em geral e a compreender como combater e previnir a sua formação. No entanto, deve-se notar que tais mecanismos estão correlacionados com as condições do sistema, como sua supersaturação, concentração iônica, temperatura e pressão parcial de dióxido de carbono. Assim, é necessário estudar o sistema por completo para a captura completa do efeito. A modelagem matemática tem sido reconhecida como uma ferramenta valiosa para simulação, otimização e controle baseado em modelos de processos de cristalização, oferecendo a possibilidade de investigar os mecanismos de muitas taxas simultaneamente.

Estimar a distribuição de tamanhos de partículas, taxas de precipitação e proporções polimórficas a partir desses modelos é um problema de grande importância para pesquisadores envolvidos em estudos de cristalização e precipitação. Apesar do grande esforço feito por alguns autores para explicar os mecanismos envolvidos na cristalização aquosa do carbonato de cálcio, ainda há desafios a serem superados na modelagem e validação experimental dos fenômenos que podem ocorrer na precipitação do carbonato de cálcio.

Objetivos

O objetivo geral desta tese foi desenvolver um modelo matemático para a cristalização do carbonato de cálcio, que descreva tanto os aspectos cinéticos quanto os termodinâmicos da sua formação.

Os objetivos específicos foram desenvolver um modelo capaz de simular a distribuição do tamanho dos sólidos, a massa total produzida e a distribuição polimórfica dos cristais obtidos, utilizando como variáveis de entrada as condições de temperatura, pressão, salinidade e composição das fases do sistema de interesse; ajustar e validar o modelo para simular o efeito da supersaturação da solução em relação aos sólidos do carbonato de cálcio nas taxas de cristalização do $CaCO_3$ previstas pelos modelos cinéticos e de equílibrio termodinâmico, sendo capaz de avaliar a influência dessa variável nas características dos sólidos produzidos; ajustar e validar o modelo para representar o efeito da presença de íons divalentes Mg, Sr e Ba nas taxas de cristalização do carbonato de cálcio previstas pelos modelos cinético e de equilíbrio termodinâmico, sendo capaz de avaliar a influência desses íons nas características dos sólidos produzidos; e por fim, elaborar uma ferramenta computacional capaz de simular a formação do carbonato de cálcio para uma faixa de condições, tanto laboratorais quanto industriais, e para operações tanto em modo batelada e contínuo.

Metodologia

Inicialmente, o modelo termodinâmico responsável pelo cálculo da atividade e da fugacidade dos componentes na mistura foi proposto baseado nos cálculos de Pitzer e uma equação não-interativa como função da temperatura e pressão. Após isso, propuseram-se as ferramentas de cálculo de supersaturação, tanto para sistemas abertos quanto fechados, baseadas nas constantes de equílbrio presentes no sistema do carbonato de cálcio para as respectivas equações para o tipo de operação. Assim, pode-se propor o cálculo do *step rule* responsável por definir a ordem de aparecimento dos sólidos de acordo com suas energias de superfície e estabilidades termodinâmicas.

Com o aspecto termodinâmico desenhado, o modelo cinético baseado em balanço populacional resolvido pelo método das classes foi desenvolvido, no qual foram designadas as equações responsáveis pelo cálculo das taxas de nucleação, crescimento, dissolução, aglomeração, transformação e influência dos íons externos. Para a simulação do modelo foi proposta uma ferramenta de integração numérica baseada nas *Backward differentiation*

formulas de ordens 1 a 5 juntamente com um otimizador híbrido do tipo *Particle Swarm* e Nelder-Mead *Simplex*, responsável por minimizar a função objetivo proposta pelo método da Máxima Verossimilhança. O algoritmo do modelo foi utilizado com 3 conjuntos de dados: o primeiro obtido do NUESC/ITP o qual representa cristalizações do carbonato de cálcio variando a concentração de cálcio e bicarbonato entre 20 e 50 $mmol.L^{-1}$ a 25ºC, realizando medidas de distribuição do tamanho dos sólidos, via *Focused Beam Reflectante Measuraments* (FBRM), da massa cristalina total e da distribuição polimórfica, via *Scanning Electron Microscopy* (SEM) e *X-ray diffraction* (XRD). Tais dados foram utilizados para ajuste e validação do modelo para a captura do efeito que o aumento da concentração dos íons causou na distribuição do tamanho, na massa e na distribuição dos polimorfos. Já o segundo conjunto de dados foi obtido do LPP/IPT, representando cristalizações do carbonato de cálcio variando a concentração dos íons divalentes Mg^{2+}, Ba^{2+} e Sr^{2+} entre 30 e 144, 28 e 280, 33 e 1500 ppm, respectivamente; realizando medidas de distribuição do tamanho dos sólidos, via *Dynamic Light Scattering* (DLS), da massa cristalina total e distribuição polimórfica, por *Scanning Electron Microscopy* (FEG-SEM) e *X-ray diffraction* (XRD).

Esses dados foram utilizados para o ajuste e validação do modelo para a captura do efeito que os íons divalentes Mg^{2+}, Ba^{2+} e Sr^{2+} causaram na distribuição do tamanho, na massa e na distribuição dos polimorfos. O último conjunto de dados, obtidos da PETROBRAS, representam as condições em torno de uma válvula *choke* presente na plataforma, operando com concentrações de cálcio e bicarbonato em torno de 25 a 56 $mmol.L^{-1}$, temperaturas de 25 ºC a 50 ºC, pressões de 20 a 40 atm e vazões volumétricas de 35 m^3/dia. Os dados desse conjunto foram utilizados como variáveis de entrada para a ferramenta termodinâmica e cinética avaliar o impacto apresentado pela válvula nos potencias cinéticos e termodinâmicos para um total de 7 plataformas diferentes.

Resultados e Discussão

O modelo foi ajustado para distribuição de tamanho de cristal, massa cristalina total e de proporção polimórfica para a faixa de condições de cristalização dos dados NUESC/ITP, apresentando um erro médio quadrático de 4% por variável que passou com sucesso no teste de qui-quadrado, atestando a qualidade do processo de estimação de parâmetros. O modelo foi capaz de descrever o aumento que a elevação da supersaturação causou tanto na massa total quanto na distribuição de tamanho dos cristais obtidos, com erros de -8% ± 6% e 3% ± 5%, respectivamente; sendo capaz de avaliar o efeito da supersaturação sobre as taxas cinéticas que

produziram os efeitos observados. Observando a condição com maior teor de sólido e massa da fase cristalina, a concentração de 50 mmol.L^{-1} de $CaCO_3$ obteve proporção entre os fenômenos que produzem aumento, crescimento, aglomeração, diminuição, nucleação e dissolução na distribuição do tamanho dos cristais, 120% maior que a condição com o menor teor de sólido e massa da fase cristalina, 20 mmol.L^{-1}. Os cálculos também representaram corretamente a distribuição polimórfica final, correspondendo ao maior teor de calcita que a condição de 40 mmol.L^{-1}, 5,35% em massa, possuía sobre as outras condições testadas. Sendo novamente capaz de avaliar que a condição que mais produziu calcita obteve proporção entre os fenômenos que produzem calcita, crescimento e transformação, e produzem vaterita, nucleação e crescimento da vaterita, 650% maior que a condição que, essencialmente, não apresentou calcita, a 20 mmol.L^{-1}.

O modelo ajustado para os dados LPP/IPT sobre a distribuição de tamanho de cristal, massa cristalina total e predição de proporção polimórfica para condições de cristalização de estudadas, obteve uma boa concordância geral com um erro médio quadrático de 12% por variável. Para as condições com Magnésio, o modelo impôs uma redução de 62,3% e 57,9% na taxa de nucleação de vaterita e uma aceleração de 2342% e 1210% da taxa de transformação polimórfica, vaterita-calcita, nas condições de Mg-30 e Mg-144 para ser capaz de representar o aumento médio de 21% e 13% no diâmetro volumétrico, 12% e 8% de diminuição da massa cristalina e 40% e 23% maior teor de calcita que os experimentos de Mg obtiveram em relação ao experimento base. Quanto às condições de Bário e Estrôncio, o modelo impôs um aumento de 9%, 28%, 8% e 52% na taxa de crescimento de calcita e 9,420%, 9,660%, 5,170% e 5,430% de aumento na taxa de transformação vaterita-calcita, para poder para modelar o aumento de 56%, 34%, 24% e 23% no diâmetro médio volumétrico, 18%, 16%, 11% e 13% de redução média, ao longo do tempo, na produção de massa cristalina e 62%, 80%, 50% e 69% maior teor de calcita que os experimentos de Ba e Sr obtiveram em comparação com o experimento sem esses íons.

No estudo de caso utilizando os dados da PETROBRAS na ferramenta proposta, foi possível observar o maior potencial precipitante que o poço Well-1 apresentou frente ao Well-2 e como as variáveis temperatura, pressão e salinidade foram responsáveis por isso. Além disso, notou-se como a presença da válvula influenciou as maiores taxas cinéticas do poço Well-1 de maneira 340% maior que no poço Well-2.

Adicionalmente, o polimorfo calcita, embora apresentasse maior estabilidade termodinâmica, não foi o sólido mais presente devido aos baixos tempos de residência para a ocorrência do fenômeno de transição. Ao final das simulações, compararam-se os potenciais

termodinâmicos e cinéticos dos poços com relação ao teor de água, pois observou-se que esse teve forte influência nos valores obtidos. A partir dessa comparação foi possível observar que campos menos desenvolvidos e, portanto, com menores frações de água, apresentaram maiores potenciais de formação, destacando a problemática que tais poços podem apresentar na continuidade de sua operação.

Considerações Finais

O modelo matemático desenvolvido nesta tese buscou representar os aspectos termodinâmicos e cinéticos da precipitação de carbonato de cálcio, com base nas observações teóricas e experimentais disponíveis na literatura atual. O modelo foi testado para 3 diferentes conjuntos de dados e apresentou resposta satisfatória para as diferentes condições apresentadas. Para o conjunto de dados que variou a supersaturação do sistema, obtido do ITP/NUESC, o modelo foi ajustado para distribuição de tamanho de cristal, massa cristalina total e previsão de proporção polimórfica para a faixa de condições de cristalização, obtendo um erro médio de 4% por variável. O modelo foi capaz de representar o aumento causado pela elevação na supersaturação tanto na massa total quanto na distribuição de tamanho e também representou corretamente o fato que a condição de 40 $mmol.L^{-1}$ produziu mais calcita. Para o segundo conjunto de dados que analisou a presença dos íons divalentes Mg^{2+}, Ba^{2+}e Sr^{2+}, o modelo também foi ajustado para distribuição de tamanho de cristal, massa cristalina total e proporção polimórfica, obtendo uma boa concordância geral com um erro quadrático médio de 12%.

Por fim foi realizado um estudo de caso com informações experimentais da PETROBRAS, sendo possível observar que as diferentes condições de temperatura, pressão, salinidade e vazões observadas nos poços produziram impactos diferentes na presença da válvula, com o poço Well-1 apresentando uma diferença de 340% entre o potencial termodinâmico e cinético de produção salina. Também foi possível observar que campos menos desenvolvidos podem apresentar potenciais de formação proporcionalmente maiores. Embora o modelo tenha sido ajustado apenas para uma faixa específica de concentrações, pode ser útil no processo de cristalização de carbonato de cálcio como uma ferramenta de estudo prático para avaliar os efeitos da supersaturação, íons divalentes e variações de temperatura, pressão e residência de tempo na formação de $CaCO_3$ para aplicações acadêmicas e industriais.

ABSTRACT

Calcium carbonate crystallization is an essential but complex unit operation due to the different thermodynamic and kinetic factors during particle formation. This thesis presents a modeling approach to understand the thermodynamic and kinetic aspects of $CaCO_3$ in its formation. A model algorithm that includes thermodynamic equilibrium and energy profiles, mass, and populational balances, including nucleation, growth, agglomeration, and polymorphic rearrangement was developed. The modeling framework was used with different experimental sets. The first data set showed batch crystallizations with initial calcium and bicarbonate concentrations from 50 to 20 $mmol.L^{-1}$ at 25ºC. The model was adjusted for crystal size distribution, total crystal mass, and polymorphic proportion for this set, obtaining a mean squared error of 4% per variable. The model also captured that increasing supersaturation increased the total mass and the crystals size and that the highest calcite content was obtained in the experiment of 40 mmol.L-1. The second data set used presented crystallization results from experiments with a range of divalent ions concentration, Mg (30 to 144 ppm), Ba (28 to 280 ppm), and Sr (33 to 1500 ppm) with 1 and 0.297 $mol.L^{-1}$ of calcium and bicarbonate at 25°C. For this second set, the model was also adjusted for crystal size distribution, total crystal mass, and polymorphic ratio, presenting a good general agreement with a mean square error of 12%. It also captured the highest average volumetric diameter, calcite content, and lowest total crystal mass that the Mg, Ba, and Sr experiments produced compared to the base experiment, albeit with different mechanisms for each ion. For the third set of data, a case study was carried out with experimental information from Petrobras to evaluate the influence of the presence of a choke valve on the formation of calcium carbonate. It was possible to observe that the different conditions observed in the wells produced different impacts of the presence of the valve, with the well with the higher precipitation potential presenting a higher proportion of bicarbonate/calcium and temperatures. In turn, residence times were also longer. Consequently, the most problematic well, in terms of precipitate formation, presented a difference of 340% between the thermodynamic and kinetic potential of saline production. At the end of the simulations, the thermodynamic and kinetic potentials of the wells were compared proportionally to their water content, and it was possible to observe that less developed fields may have proportionally higher formation potentials. With the simulations, it can be seen that a complete population balance can provide a valuable tool to assess the thermodynamic and kinetic mechanisms of calcium carbonate formation. Although the model was only adjusted for a specific range of concentrations, it may be helpful in the calcium carbonate crystallization process as a practical study tool; being able to assess the effects of supersaturation, external ions, and variations in temperature, pressure, and time residence in $CaCO_3$ formation for academic and industrial applications.

Keywords: Populational Balance. Calcium carbonate precipitation. Polymorphism. Mathematical modelling. Inorganic crystallization.

LIST OF FIGURES

LIST OF TABLES

LIST OF ABBREVIATIONS AND ACRONYMS

ACC Amorphous Calcium Carbonate

ICP-AES Inductively coupled plasma – atomic emission spectrometry

NUESC Center for Studies on Colloidal Systems

LPP Process and Bionano Particle Technology

pH Hydrogenic potential

PETROBRAS Petróleo Brasileiro S/A

SEM Scanning Electron Microscopy

TGA Thermogravimetric analysis

XRD X-ray Powder Diffraction

SS Supersaturation

LIST OF SYMBOLS

$A_{B,n}$ Crystal agglomeration birth rate in class n [$1.s^{-1}$]

$A_{D,n}$ Crystal agglomeration death rate in class n [$1.s^{-1}$]

$a_{ion,rate}$ Linear coefficient of external ion effect in the rate [-]

a_{ion} ion activity [$mol.kg^{-1}$]

$b_{ion,rate}$ Angular coefficient of external ion effect in the rate [-]

B_{ca} Pitzer second virial coefficient for opposite charges [-]

C_{ca} Pitzer parameter for oposite charges [-]

$c^*(L)$ solubility of particle with size L [$mol.kg^{-1}$]

c_∞ bulk solubility of particle [$mol.kg^{-1}$]

D Crystal dissolution rate [$m.s^{-1}$]

D_{ff} Diffusion coefficient of the ions [$m^2.s^{-1}$]

$D_{ion,p}$ Distribution coefficient of the ion in the polymorph p [-]

f Number density function [$1.m^{-1}$]

F Faraday constant [$Coulomb.mol^{-1}$]

F_{obj} Objective function for kinetic parameter determination [-]

G Net generation of particles [$1.m^{-1}\ s^{-1}$]

G_{av} Net generation of particles averaged in the physical space [$1.m^{-1}\ s^{-}$]

$\overline{G_i}$ Net generation of particles in the class C_i [$1.s^{-1}$]

g Crystal growth order [-]

k transformation rate constant [$1.s^{-1}$]

k_b Boltzmann constant [$m^2\ kg.s^{-2}\ K^{-1}$]

k_A Crystal agglomeration rate constant [$s.m^{-7}$]

k_a Crystal area factor [-]

k_D Crystal dissolution rate constant [$m.s^{-1}$]

$k_{d,i}$ Solid-liquid mass transfer coefficient for class i [$m.s^{-1}$]

k_G Crystal growth rate constant [$m.s^{-1}$]

k_N Nucleation rate constant [$1.m^{-3}\ kg^{-1}\ s^{-1}$]

K_{sp} Solubility product of the solute [-]

K_W Dissociation constant of water [-]

K_1 Dissociation constant of carbonic acid [-]

K_2 Dissociation constant of bicarbonate ion [-]

k_v Crystal volume factor [–]

L Crystal size [m]

L_c Critical crystal size [m]

m_a molality of the ion [$mol.kg^{-1}$]

m_0 Mass of initially dissolved solute [kg]

m_{cr} Total mass of crystals [kg]

m_r Total mass of crystallization mixture [kg]

m_{sol} Mass of solvent [kg]

N_a Avogadro Number [$1.mol^{-1}$]

NE Number of experiments [-]

NY Number of dependent variables [-]

N_i Number of crystals in class i [-]

n Nucleation order [-]

n_1 Heterogeneous nucleation order [-]

P Dissipated power per unit mass [$W.kg^{-1}$]

R Gas constant [$J.mol^{-1}\ K^{-1}$]

$Re_{p,i}$ Reynolds number of crystals in class i [-]

$R_{A,i}$ Crystal agglomeration rate in the class C_i [$1.s^{-1}$]

r_A Crystal agglomeration rate [$1.m^{-1}\ s^{-1}$]

r_o transformation reaction order [-]

R_N Nucleation rate [$1.s^{-1}$]

r_N Nucleation rate [$1.m^{-1}\ s^{-1}$]

$R_{Trans,i}$: Rate of appearance by transformation in the class C_i [$1.m^{-1}\ s^{-1}$]

r_{Trans}: Rate of appearance of crystal by transformation [$1.m^{-1}\ s^{-1}$]

S_i Average size of crystals in class i [m]

Sc Schmidt number [-]

SS Supersaturation of solute in continuous phase [-]

T Temperature [K]

V_{sol} Solution volume [m^3]

V_m Solid molar volume [$m^3.mol^{-1}$]

w_i Size class width [m]

y_{exp} Normalized experimental crystal number in class i for solid product [-]

y_m Normalized simulated crystal number in class i at time t [-]

z_i charge of ion I [-]

GREEK LETTERS

α capillary length [m]

$\beta_{j,k}$ Agglomeration kernel [$1.m^{-3}.s^{-1}$]

γ solid-solution interfacial tension [$N.m^{-1}$]

ΔG_{ex} Change in Gibbs free energy produced per solid [J/mol]

$\delta_{i,j}$ Kronecker delta [-]

η_i Crystal growth effectiveness factor for crystals in class i [-]

μ_r Dynamic viscosity of the crystallization mixture [$Pa.s^{-1}$]

$\nu_{(i)}$ Linear crystal growth rate for the particle in the class C_i [$m.s^{-1}$]

ν_r Kinematic viscosity of the crystallization mixture [$m^2.s^{-1}$]

τ Residence time [s]

ρ_{cr} Density of the crystals [$kg.m^{-3}$]

ρ_r Density of the crystallization mixture [$kg.m^{-3}$]

Ψ Population density [$1.m^{-1}$]

SUPERSCRIPT

aq Aqueous phase

l Liquid phase

g Gas phase

oil Oil phase

s Solid phase

v Vapor phase

SUMMARY

1 INTRODUCTION

The inorganic salts formation and its deposition on the surfaces of industrial equipment represents a financial and technological challenge for the industries, especially the oil industry, due to its production and transport of multiphase fluids (water, oil, and gas) with high temperature, pressure and salinity (SERPA, 2015). The deposition of such precipitates is a significant universal problem that costs industries billions of dollars every year (CRABTREE, M., ESLINGER, D., FLETCHER, P., MILLER, M., JOHNSON, A., KING, 1999; KAMAL et al., 2018). Consequently, it is desired to avoid operating conditions favorable to the formation and deposition of precipitates at different stages of the process; thus, the monitoring and control of the phenomena involved in the nucleation and growth of crystals from the fluid phase are the fundamental importance.

One of the most common precipitating/fouling agents is calcium carbonate, the most widespread in oil and gas production facilities and marine formations (GOWER, 2008; LAKSHMI et al., 2013; KAMAL et al., 2018). Calcium carbonate is also a suitable model for studying metastable phases formation and growth as well as their transformation into the stable form(s); appearing in several solid forms, three hydrated forms, amorphous, mono and hexahydrate calcium carbonate, and three anhydrous polymorphs, calcite, vaterite and aragonite (BREČEVIĆ; KRALJ, 2008; GOWER, 2008; BLUE et al., 2017; DU; AMSTAD, 2019). The comprehension of the kinetic and thermodynamic aspects involved in the phase equilibrium of these solids can be achieved by investigating the mechanisms in the precipitation of these calcium carbonate forms, being one of the most critical and studied aspects of the calcium carbonate research and applications (RODRIGUEZ-BLANCO; SHAW; BENNING, 2011; GEBAUER et al., 2014; DU; AMSTAD, 2019).

The supersaturation of the calcium carbonate solutions influences both the thermodynamic and kinetics aspects of the process, influencing the size, mass of the produced crystals, and the crystalline phases that can appear (COSMO, 2013; OLAJIRE, 2015; BLUE et al., 2017). Likewise, the investigation of the influence of external ions on the kinetics and mechanisms of the precipitation processes, as well as on the mode and sites of their possible incorporation into the calcium carbonate crystal lattice, contributes to the elucidation of the mechanisms of polymorphic formation (KITANO, 1962; ASTILLEROS et al., 2000; ASTILLEROS; FERNÁNDEZ-DÍAZ; PUTNIS, 2010; RODRIGUEZ-BLANCO et al., 2011). The Mg/Ca ratio in the aqueous phase may be the driving force for the polymorphic changes in

the calcium carbonate formation, favoring aragonite or calcite formation as function of the system conditions (HARDIE, 1996; MORSE; WANG; TSIO, 1997; LOWENSTEIN et al., 2003; BLUE et al., 2017; DU; AMSTAD, 2019). Barium and Strontium can become a natural substitute for calcium due to their similarities in properties (NAKA; CHUJO, 2001; AL-ANEZI; JOHNSON; HILAL, 2008); although the capacity to accommodate these larger ions can variate among the polymorphs (KITANO; KANAMORI; OOMORI, 1971; ASTILLEROS et al., 2000; MAYORGA; ASTILLEROS; FERNÁNDEZ-DÍAZ, 2019). It has been reported that Strontium can increase the abundance of aragonite and influence the performance of scale inhibitors, whereas the Barium ions can promote vaterite formation (SANJIV RAJ; DEVI; SUBRAMANIAN, 2020).

Mathematical modeling is widely accepted as a valuable tool for simulation, optimization, and model-based control of crystallization processes (CHAKRABORTY; BHATIA, 1996a; ABBAS; ROMAGNOLI, 2007; VETTER et al., 2013a). Developing a detailed mechanistic model can minimize time and material requirements necessary to ensure a better theoretical understanding of complex processes behind crystallization and generate relevant information (SCHMIDT et al., 2004; NAGY; FUJIWARA; BRAATZ, 2008). Thus, the mathematical prediction and analysis of particle size distribution, precipitation rates, and polymorphic proportions from the experimental data available in the literature is a problem of great importance for researchers engaged in studies about crystallization and precipitation (CHAKRABORTY; BHATIA, 1996a; COSTA; MACIEL; FILHO, 2007; BESENHARD et al., 2015; LASSIN et al., 2018). A complete simulation of the particles, characterizing both the kinetic and thermodynamic aspects of the $CaCO_3$ produced within the fluids produced in the oil and gas industry could be used as a virtual sensor for potential control and monitoring of incrustation problems, offering a more complete tool than the pure thermodynamic simulations that are usually used as prediction tool by the oil and gas industry (COSMO, 2013, OLAJIRE, 2015, KAMAL et al. 2018). One major advantage of a combined kinetic and thermodynamic model is the fact that a populational kinetic model is able to simulate the size distribution of the solids formed along the process, with this information being fundamental to determine possible flow's obstruction caused by the incrustation, as different solid's size can deposit with different rates and mechanisms (ROSA, 2011, LASSIN et al. 2018).

Chakraborty and Bhatia (1996a, 1996b) proposed a populational balance model to simulate calcium carbonate formation with specific nucleation, growth, and agglomeration rates for each polymorph within two different precipitation regimes. It was noted that the agitation,

supersaturation, and crystallite size, can cause expressive differences in the obtained kinetic rates and that polymorph-specific rate offers a robust modeling strategy for polymorphic crystallization study, as vaterite presented lower agglomeration tendencies and higher nucleation rate in comparison with its counterpart calcite. Brečević and Kralj (2008) conducted a series of experiments to evaluate the growth rate of both vaterite and calcite; the authors found a quadratic relation within the supersaturation and a surface-controlled mechanism of ions controlled the growth rate for both polymorphs. It was also determined that the calcite growth controlled the vaterite-calcite transformation. Rodriguez-Blanco et al. (2011) carried out calcium carbonate precipitation experiments to analyze the polymorphism rearrangement and study the kinetics of the crystallization process. The author observed that the amorphous calcium carbonate, ACC, particles rapidly transformed to vaterite; secondly, the vaterite transformed to calcite via dissolution and reprecipitation mechanism, with the latter stage being approximately ten times slower than the former. In a subsequent work, the authors observed that the magnesium addition increased ACC's stability and favored calcite formation over vaterite (RODRIGUEZ-BLANCO et al., 2011). Sanjiv et al. (2020) realized studies on the crystallization of calcium carbonate ions within different concentrations of Sr^{2+} and $Ba2^{+}$; it was observed that the Ba^{2+} promoted vaterite formation and that the Sr^{2+} presence increased aragonite production. As can be seen, the great effort made by some authors to explain the mechanisms involved in the crystallization of calcium carbonate can offer a robust base to continue investigating the calcium carbonate polymorphic crystallization phenomenon with its complexity and interrelation among its variables. Thus, the goal of the present work is to develop a thermodynamic-kinetic model that can predict the particle size distribution, the mass crystalline profiles, and the polymorphic proportions from different solution conditions with the presence, or not, of Mg^{2+}, Ba^{2+}, Sr^{2+} in relation with the calcium and carbonate equilibrium.

1.1 OBJECTIVES

To develop a mathematical model for the calcium carbonate crystallization including both thermodynamic and kinetic aspects of its formation. The following items are specific objectives of this work:

- Develop a model able to represent the carbonate precipitation process, producing the solids size distribution, its total mass, and polymorphic distribution as output to system conditions;
- To adjust and validate the model to describe the supersaturation influence with the crystallization;
- To adjust and validate the model to describe the influence of divalent external ions in the crystallization;
- To produce a computational tool to simulate the calcium carbonate formation with a range of laboratory or industry conditions at batch or continuous crystallizations.

2 LITERATURE REVIEW

2.1 INORGANIC PRECIPITATION OF CALCIUM CARBONATE

The formation of calcium carbonate solids is a major problem in the oil and natural gas industry, with $CaCO_3$ being the most common and important source of mineral scales in petroleum industries (LIU et al., 2015; NATSI; ROKIDI; KOUTSOUKOS, 2016; COSMO et al., 2019). Petroleum industries invest millions of dollars every year to develop potent inhibitors and new methodologies to prevent the adherence and growth of scales on metal surfaces (AZIMI *et al.*, 2014; KUMAR; NAIYA; KUMAR, 2018). Thus, the inorganic precipitation of calcium carbonate from supersaturated solutions is of particular interest, being extensively studied by many authors (KITANO, 1962; PLUMMER; BUSENBERG, 1982; BREČEVIĆ; KRALJ, 2008; COSMO, 2013; VENÂNCIO; DO ROSÁRIO; CAJAIBA, 2017; SANJIV RAJ; DEVI; SUBRAMANIAN, 2020).

Mineral precipitation occurs when the inorganic salt concentration is greater than its solubility in the medium, thus forming an insoluble ionic solid from the ions (PEIPER; PITZER, 1982; ANDERSON; CRERAR, 1994; SHI *et al.*, 2013). The presence of precipitates, mainly minerals, can be widespread systems with high salinity, pressure, and temperature, specially in the calcium carbonate solids with their endothermic crystallization (CRABTREE, M., ESLINGER, D., FLETCHER, P., MILLER, M., JOHNSON, A., KING, 1999; COSMO *et al.*, 2019). Calcium carbonate formation in the surface of the equipment for oil and gas production has been recognized to be highly associated with the extreme conditions that these equipments can operate (OLAJIRE, 2015; KAMAL *et al.*, 2018).

Investigating the mechanisms involved in calcium carbonate precipitation can helps to elucidate the nature and behavior of those phases in general and comprehend the whole process (BREČEVIĆ; KRALJ, 2008). For example, the investigation of the influence of external ions in these inorganic precipitations, as well the effect of the system conditions, as temperature, pressure and salinity, are considered an important step for the comprehension of the precipitation mechanism (GOWER, 2008; MYASNIKOV; CHIPRYAKOVA; KULOV, 2013; LASSIN *et al.*, 2018).

To connect all the variables that can influence calcium carbonate precipitates, it is important to know where the ions responsible for the precipitates formation are or come from (DUAN; SUN, 2003). An example of this analysis can be made for a reservoir of gas and oil,

where those products co-exist in a system that can present a significant potential for scale formation (COSMO, 2013; KAMAL *et al.*, 2018).

An oil and gas reservoir can be of a calcium carbonate formation; the oil is held in the pores of a reservoir rock composed mainly of calcium carbonate. There are three necessary components in generating and accumulating oil: source rock, reservoir rock, and cap rock. Source rock has a high concentration of organic material that can be transformed into oil under high temperatures. An example of the source rock is limestone composed of $CaCO_3$, the main building element in seashells. Cap rock is the overlying rock with lower permeability than the reservoir; these rocks prevent the oil from seeping into the surface of the Earth. The presence of these elements, a source rock, and reservoir rock in conjunction with a correct maturation level, are the principal conditions for an exploration well to be worthwhile for drilling (THOMAS, 2001; ROSA; CARVALHO; XAVIER, 2011).

Carbonate precipitation can originate from carbonate and arenitic rock formations. In both, the brine occupies the porous space present in the rock, together with the hydrocarbons, which is responsible for keeping the calcium and carbonate ions dissolved in the medium (DUAN; LI, 2008; COSMO, 2013). In the carbonate reservoirs, the rocky environment itself and the composition of sea water contribute to the supply of these ions (MAZZULLO; CHILINGARIAN, 1992; MORAIS, 2013).

The calcium carbonate formation depends not only on the supply of the ionic solution but also on the dissolved carbon dioxide content, pH, temperature, pressure, morphology of the formed solid, and the kinetics of these solids formation; being one of the more sensitive incrustations to variations in the system conditions (OLAJIRE, 2015; KAMAL *et al.*, 2018). Thus, it is fundamental to understand the behavior of these ions in solution and the formation of carbonate solids in a multidisciplinary view.

This multidisciplinary view can be separated as: the equilibrium of the carbonate solutions, with the solids thermodynamics and its formation kinetic (NANCOLLAS; REDDY, 1974; LASSIN *et al.*, 2018; REIS *et al.*, 2018), which relates to the rate of formation of carbonate solids, the precipitation process and carbonate crystallization under well conditions. With these three different views, it is possible to understand the whole incrustation pathway, as represented schematically in Figure 2.1.

Figure 2.1 - Main phenomena involved in calcium carbonate scaling.

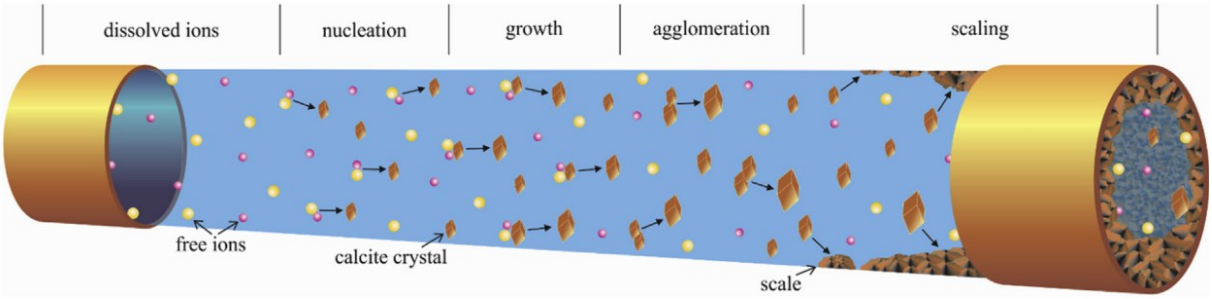

Source: Cosmo *et al.* (2019)

2.2 PHASE EQUILIBRIA AND EQUILIBRIUM CONSTANTS

The balance between the water, oil (if present), gas phases, and the ions present in the solution under the temperature and pressure conditions have to be considered to represent the behavior of phases that can be present in a $CaCO_3$ precipitating system (DUAN; LI, 2008; COSMO, 2013). Besides that, a study of the carbonate system could be made in real application involves extreme conditions, as of an oil basin, pressures up to 700 atm, temperatures up to 200ºC and high ionic concentration, up to 10 M, that can represent a challenge for the thermodynamical models to handle these non-idealities (OLAJIRE, 2015). Based on the complexities that can occur in the necessary calculations to fully evaluate a precipitation system, Duan and Li (2008) propose that for the calculation of the system equilibria present in a mineral formation, one could follow four steps:

1. Identify all species, phases, and chemical reactions in the system.

2. Obtain relationships between standard chemical potential and species concentrations in identified reactions and how they vary with temperature and pressure.

3. Equate the non-idealities of the system, obtaining the activity and fugacity coefficients as a function of temperature, pressure, and composition of the system.

4. Find an algorithm capable of calculating the systems equilibrium for given conditions of temperature, pressure, and composition.

Essentially, there are two types of water in the oil systems: the formation trapped water within the reservoir rocks and the seawater, injected into the system to enhance oil recovery by

preventing the pressure decline as the fluids are being produced (OLAJIRE, 2015). Seawaters are typically rich in magnesium and sulfate ions, besides sodium and chloride, while formation waters contain sodium, calcium, and chloride ions (Table 2.1). The mixing of these waters produces a new fluid with combined concentrations that can be above solubility limits for these inorganic minerals, thus producing a scale (HAARBERG; SELM, 1990; CRABTREE, M., ESLINGER, D., FLETCHER, P., MILLER, M., JOHNSON, A., KING, 1999; BIN MERDHAH; YASSIN, 2007).

Table 2.1- Example of compositions found in Seawater and Formation water.

Ion	Seawater [ppm]	Formation water [ppm]
Na^{1+}	12,075	474,89
Mg^{2+}	1,849	1,345
Ca^{2+}	432	157,04
K^{1+}	470	2,293
Ba^{2+}	<1	44
Sr^{2+}	6.85	663
pH	7.73	6.77
Cl^{1-}	223,90	786,76
SO_4^{2-}	3,184	908
HCO_3^{1-}	151	314

Source: Adapted from Crabtree et al.(1999) and Olajire (2015).

The oil is composed of a mixture of hydrocarbons. The main components of natural hydrocarbons belong to three groups: paraffin, n-alkanes for n = 5 to 15, naphthenes, and saturated rings. The aliphatic chain can contain 5 to 7 carbons and aromatics, hydrocarbons containing at least one benzene ring. It is essential to know the oil composition because the presence of other phase can influence the stability of the inorganic scale and can also influence the CO_2 partition between the aqueous and oil phase (NATSI; ROKIDI; KOUTSOUKOS, 2016). There can be mainly four species in the vapour phase: water, carbon dioxide, methane, and sulfide acid. Finally, the solid phase is composed of precipitated solids, which can be amorphous or crystalline, being formed by a combination of the ions present in the solution; thus, it can be seen that a significant number of different solids can appear in the thermodynamic calculations (HAARBERG; SELM; *et al.*, 1992; DUAN; LI, 2008).

Potentially two mass changing phenomena are possible in this multicomponent system: phase changes and chemical species reactions within the phases. Phase changes alter the mass distribution between vapour, liquid, and solid (the calcium carbonate polymorphs and other ionic solids present supersaturation). In contrast, chemical changes cause the formation

or dissociation of ions in the liquid phase. It is important to note that both phenomena are intrinsically related and affect each other (GARCÍA; THOMSEN; STENBY, 2006; DUAN; LI, 2008).

These changes can be englobed as the component's temperature, pressure, and molality functions. Given enough time, the various changes will approach macroscopic equilibrium states in a given condition. However, the components microscopically still move from one phase to another, and the species still dissociate or associate to form different species. Geochemically, many systems have been static for thousands of years, and therefore it is plausible to treat them as equilibrium systems in many cases. Correspondingly, there are two types of equilibrium for understanding system chemical changes under various conditions: phase equilibrium and chemical species within the phases equilibrium (COSMO, 2013; OLAJIRE, 2015).

In phase equilibrium, the chemical potentials of any component are equal across all phases. For example, in the equilibrium between the liquid and vapor phases, the chemical potential of CO_2 in the liquid is equal to its chemical potential in the vapor phase. For the computation of the solubility of calcium carbonate (calcite, for example) in a liquid phase, the chemical potential must be equal in the liquid and solid phases, as shown in Equation 2.1.

$$\mu_{CaCO3(s)} = \mu_{Ca^{2+}_{(aq)}} + \mu_{CO3^{-2}_{(aq)}} \tag{2.1}$$

Where μ_j represents the chemical potential of species j present in the liquid phase and can be obtained as follows (Equation 2.2).

$$\mu_j^l = \mu_j^0 + RTlnm_j + RTln\gamma_j \tag{2.2}$$

Where μ_j^0 representing the standard chemical potential of the species in the reference state, which is defined as an ideal gas in the vapor phase at 1 atm or as an ideal solution with a concentration of 1 mol.L^{-1} in the liquid phase, m_j represents the molality in the aqueous phase of species j and γ_j represents the activity coefficient of the species in the liquid phase, R represents the universal gas constant, and T the temperature. The chemical potential for the species in the vapor is similar. However, the partial pressure of the component in the gas phase replaces the molality, and the fugacity coefficient replaces the activity coefficient, respectively (KESZEI, 2012).

In order to relate the chemical potentials of the species of interest in the system, it is possible to start from the fundamental relation of Gibbs free energy (G), considering three phases, liquid, vapor, and solid coexisting in equilibrium (Equation 2.3, 2.4, 2.5).

$$d(\mathrm{G})^{L} = (\mathrm{V})^{L}\mathrm{dP} - (\mathrm{S})^{L}\mathrm{dT} + \sum_i \mu_i^{L}\mathrm{dn}_i^{L} \tag{2.3}$$

$$d(\mathrm{G})^{V} = (\mathrm{V})^{V}\mathrm{dP} - (\mathrm{S})^{V}\mathrm{dT} + \sum_i \mu_i^{V}\mathrm{dn}_i^{V} \tag{2.4}$$

$$d(\mathrm{G})^{S} = (\mathrm{V})^{S}\mathrm{dP} - (\mathrm{S})^{S}\mathrm{dT} + \sum_i \mu_i^{S}\mathrm{dn}_i^{S} \tag{2.5}$$

Where P, S^k, $n_{i,}$ and V^k represent the pressure, entropy, the number of moles of species i, and the volume corresponding to each phase k under analysis, respectively. As the interest lies in the chemical species equilibrium between the phases, it was assumed thermal and mechanical equilibrium between phases, dP=0 and dT=0.

Since the variation of the Gibbs free energy of the system is equal to the sum of the Gibbs free energy of the phases involved in the reaction, it is possible to obtain the equilibrium constant for each possible reaction. This calculation is possible by relating the chemical potentials of all species that interact with each other in the specific reaction (Equation 2.6).

$$\ln K_i = -\frac{\Delta G_f^0}{RT} = -\frac{\sum \nu_j \mu_j^0}{RT} \tag{2.6}$$

Where K_i represents the equilibrium constant of the ith reaction, $-\Delta G_f^0$ the change in the standard Gibbs free energy of the reaction and ν_j the stoichiometric coefficient of the species j.

Considering that high pressure and high temperature reservoirs can considerably influence the equilibrium constant, the impacts on the equilibrium constant due to change in this state variables cannot be neglected (OLAJIRE, 2015).

One can start by considering a system in equilibrium in a reference state P_{ref} = 1 atm Tk_{ref} = 298,15 K and $K_{eq,ref}$, when it is submitted at pressure P and temperature T, the equilibrium constant varies with these variables. Returning to the fundamental relation of Gibbs energy (Equations 2.3 to 2.5), analyzing only variations in T and P, the van't Hoff equations can be obtained (Equation 2.7 and 2.8). These equations make the calculating of how the equilibrium constants change with temperature and pressure variations possible. However, it is

necessary to integrate those differential forms to obtain the actual values of the constants with the conditions.

$$\left(\frac{\delta lnK_{eq}}{\delta P}\right)_{T_k} = \frac{\Delta V_r^0}{RT_k} \tag{2.7}$$

$$\left(\frac{\delta lnK_{eq}}{\delta T}\right)_{P} = \frac{\Delta H_r^0}{RT_k^2} \tag{2.8}$$

Where ΔV_r^0 represents the change in the standard molar volume of the reaction and ΔH_r^0 the change in the standard enthalpy of the reaction. Following the steps proposed by Duan and Li (2008), it is now necessary to obtain equations that can calculate the non-idealities of the phases, i.e., the activity and fugacity coefficient of all the species present in the system.

Activities are used to describe the deviation of a solution concentration from ideal solution behavior; this ideal solution can be described as homogeneous, where the interaction between molecules of components is the same as the interactions between the molecules of each component itself (PITZER, 1991). The activities can be described as follows: the activity coefficient, γ_i, and the concentration, c_i, of the ion in question, i (Equation 2.9).

$$a_i = \gamma_i \, c_i \tag{2.9}$$

In an ideal solution, the activity coefficient can be assumed to be unity, and the activity is equal to molality (PITZER; MAYORGA, 1973). It is difficult to measure the activity of a specific ion in a solution experimentally. Generally, only the mean activity coefficient of the solution can be measured as it is not possible to measure each individual ions (PITZER, 1991). Various empirical and semi-empirical models exist to calculate the activity of an ion in a solution (CHRISTOV; MOLLER, 2004; KAN; TOMSON, 2012; SUNDERMANN, 2016). These are limited in their range of applications, with the validity generally depending on the solution's ionic strength. The ionic strength of a solution describes the concentration of ionic charge, as shown in Equation 2.10. It is used to reflect the effect of charges and interionic interactions when calculating electrolyte activities, with z_i representing the charge of each ionic species i (SOLOMON, 2001).

$$I = \frac{1}{2}\sum_I c_i \, z_i^2 \tag{2.10}$$

The original theory on calculating activity coefficients is the Debye-Hückel theory introduced in 1923. This theory is also the foundation for the work done on developing subsequent models for calculating activity coefficients (PITZER, 1991; SUNDERMANN, 2016). The original model assumes ions to be point charges in a continuous dielectric system and only takes long-range interactions into account, making it only valid for systems with very low ionic strengths (LALLEMAN *et al.*, 2012). Extensions to the original Debye-Hückel model were made to make it applicable at higher ionic strengths. An overview of the equations of the original Debye-Hückel and various extensions of this and their validity ranges are shown in Table 2.2 (JR *et al.*, 1986; COSMO, 2013; SUNDERMANN, 2016).

Table 2.2 - Debye-Hückel models and validity ranges.

Model	**Equation**	**Validity [mol.L^{-1}]**
Debye-Hückel	$log\gamma_{\pm} = -A\lvert z_+ z_i\rvert\sqrt{I}$	I<0.001
Extended Debye-Hückel	$log\gamma_{\pm} = -\frac{A\lvert z_+ z_i\rvert\sqrt{I}}{1 + B\ a\ \sqrt{I}}$	I<0.1
Davies	$log\gamma_{\pm} = -A\lvert z_+ z_i\rvert(\frac{\sqrt{I}}{1+\sqrt{I}} - 0.3I)$	I<0.5
Truesdell-Jones	$log\gamma_{\pm} = -\frac{A\lvert z_+ z_i\rvert\sqrt{I}}{1 + B\ a\ \sqrt{I}} + b\ I$	I<2

Source: Adapted from Sundermann (2016)

In Table 2.2, A, B, a, and b are Debye-Hückel constants and specific parameters for each ionic pair. Due to the high ionic strength that can appear in the calcium carbonate formation in industrial formations, these simple equations are not applicable. However, they are still shown here as the more robust subsequent models can be built up from this theory. Debye-Hückel theory has been used by different literature sources in calculating the activity coefficients in $CaCO_3$ precipitation. The Davies equation was used by Rigopoulos and Jones (2003) in the gas-liquid precipitation of $CaCO_3$ in a bubble column reactor, by Collier; Hounslow (1999) in calcite precipitation from seeded batch experiments and by Beck *et al.* (2013) as the Truesdell-Jones equations were used in the thermodynamic calculations of Cosmo *et al.*, (2019). For systems that present higher ionic strengths and need a more robust activity calculation, Pitzer theory has widely been used for $CaCO_3$ precipitation systems (PITZER,

1991; CHRISTOV; MOLLER, 2004; DEYHIMI; GHALAMI-CHOOBAR, 2005; DUAN; LI, 2008; SUN *et al.*, 2011; SUNDERMANN, 2016).

Chemical engineers and geochemists widely use the Pitzer model to calculate the activity coefficients in electrolyte solutions with high ionic strengths (PITZER, 1991; MARSHALL; MAY; HEFTER, 1995; LI; DUAN, 2011). The model uses semi-empiric equation systems to describe the non-ideal behavior (PITZER; MAYORGA, 1973; SUNDERMANN, 2016). The Pitzer equations are complexes, with variations in how they are expressed and the notations used, depending on the source material (PITZER; MAYORGA, 1973; HARVIE; MØLLER; WEARE, 1984; SUNDERMANN, 2016; LASSIN; ANDRÉ; LACH, 2017).

In thermodynamics, the fugacity of a real gas is an effective partial pressure that replaces the mechanical partial pressure in an accurate computation of the chemical equilibrium constant (KESZEI, 2012; MATSOUKAS, 2012).

Fugacities are determined experimentally or estimated from various models, such as a Van der Waals state equation which describes the real gas behavior closer than ideal gas state equation. The real gas pressure and fugacity are related through the dimensionless fugacity coefficient φ (Equation 2.11)

$$\varphi_i = \frac{f_i}{P_i} \tag{2.11}$$

For an ideal gas, fugacity and partial pressure are equal, so $\varphi_i = 1$. Taken at the same temperature and pressure, the difference between the Gibbs molar free energies of a real gas and the corresponding ideal gas is equal to RT ln φ (KESZEI, 2012).

Accurate chemical equilibrium calculations for real gases should use fugacity rather than pressure. Suppose the chemical potential of each gas is expressed as a function of fugacity. In that case, the equilibrium condition may be transformed into the familiar reaction quotient form except that the pressures are replaced by fugacities (DUAN *et al.*, 2006; MATSOUKAS, 2012).

Thus, fugacity can be used to determine gas solubility in solution, from the balance between its chemical potential in the liquid phase μ_j^l and that in the gas phase, μ_j^v. The potential can be written as a function of fugacity and activity (Equation 2.12, 2.13).

$$\mu_j^v = \mu_j^{v(0)} + RTln\, f_j \quad (2.12)$$

$$\mu_j^l = \mu_j^{l(0)} + RTln\, a_j \quad (2.13)$$

At equilibrium, it is possible to equate these two equations to obtain a relation between the partial pressure of the j component in the gas phase with its molality j in the aqueous phase (Equation 2.14).

$$ln\frac{y_j P}{m_j} = \frac{\mu_j^{l(0)} - \mu_j^{v(0)}}{RT} - ln\varphi_j + ln\gamma_j \quad (2.14)$$

With the relation obtained in Equation 2.14, it is possible to calculate the gas solubility based on the activities and fugacities calculations.

The equilibrium constants and standard chemical potentials are functions of temperature and pressure, and fugacity and activity are functions of temperature, pressure, and composition. Thus, a interactive algorithm is needed to solve the multicomponent system composed by a coupled phase and aqueous species equilibrium. After the minimum in the Gibbs free energy of the system is obtained, it can be determined whether precipitation or dissolution was required to achieve equilibrium. This determination can be made by comparing the species concentrations before and after the precipitation/dissolution, evaluating if precipitation by consumption of the specific species occurred or dissolution by producing the species happened (HAARBERG; SELM; ET AL., 1992; DUAN; LI, 2008).

2.2.1 CALCIUM CARBONATE POLYMORPHIC FORMS

The calcium carbonate has multiple crystalline forms; according to the Gibbs rules of phase equilibria, these unique forms are dependent on intensive variables such as temperature, pressure, ionic strength, and pH (DONNET; BOWEN; LEMAÎTRE, 2009; MYASNIKOV; CHIPRYAKOVA; KULOV, 2013). $CaCO_3$ can be organized in three forms: hydrated phases, amorphous calcium carbonate, monohydrate, and hexahydrate, and in three polymorphic crystalline forms: vaterite, calcite and aragonite (COSMO, 2013). These crystalline forms can co-exist in intermediate temperatures (PLUMMER; BUSENBERG, 1982; MAYORGA; ASTILLEROS; FERNÁNDEZ-DÍAZ, 2019).

Amorphous calcium carbonate (ACC), which can appear as a precursor in spontaneous precipitation at relatively high supersaturations, is a somewhat unstable solid phase that undergoes a rapid transformation to more stable anhydrous forms. Although an amorphous hydrated calcium carbonate was described in 1938, physical characterizations of this polymorph only appeared later (BREČEVIĆ; NIELSEN, 1989). In Figure 2.2 is presented a Time-resolved SEM obtained by Walker *et al.* (2017), showing the presence of ACC in a spherical habit after 1 minute of reaction.

Figure 2.2 - Time-resolved SEM micrographs for ACC particles.

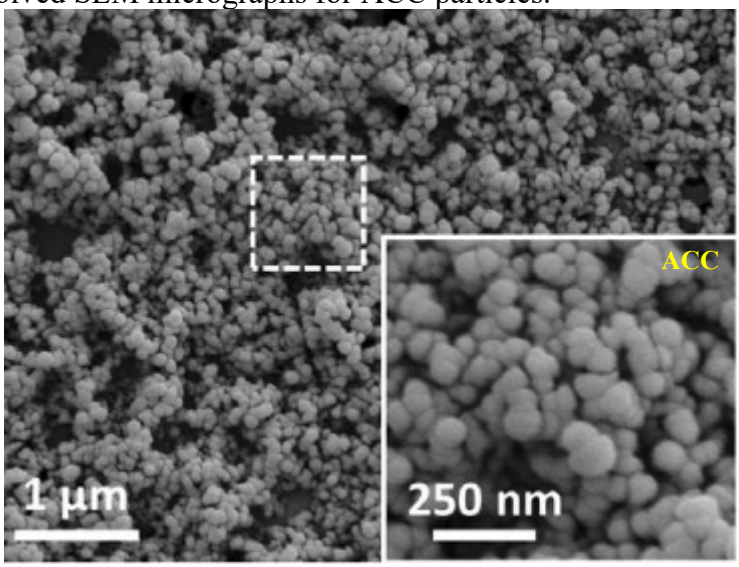

Source: Adapted from Walker *et al.*(2017)

The thermodynamic equilibrium constant in aqueous solutions of the amorphous calcium carbonate, $K_{sp\ (amorph)}$, was determined by Brecevic and Kralj (2008) in the temperature ranges from 10 to 50°C and was found to be higher than the solubilities of all other calcium carbonate modifications.

Two hydrated forms of calcium carbonate, the hexahydrate and monohydrate are more stable than the amorphous phase (BREČEVIĆ; KRALJ, 2008; DU; AMSTAD, 2019). These modifications can be kept unchanged for a few days at temperatures below 0°C before transforming calcite (BLUE *et al.*, 2017). Generally, these hydrated forms often precipitate from supersaturated solutions before the more stable anhydrous forms, with the polymorphic properties of these crystals influencing the observed pathway (GOWER, 2008). Although it appeared in biological and mineral systems studies from the nineteenth century, both hydrated forms crystallographic properties were not characterized until the twentieth century (HUME;

TOPLEY, 1926; DICKENS; BROWN, 1970; HULL; TURNBULL, 1973; EFFENBERGER, 1981). The solubility of both forms was higher than calcite, aragonite, and vaterite and lower than amorphous calcium carbonate, with the monohydrate being more soluble than the hexahydrate. (BREČEVIĆ; KRALJ, 2008). In Figure 2.3, a high-resolution TEM micrograph is presented of monohydrate calcium carbonate solids obtained in the work of Rodriguez-Blanco *et al.* (2014).

Figure 2.3 - HR-TEM microphotographs of monohydrate calcium carbonate solids.

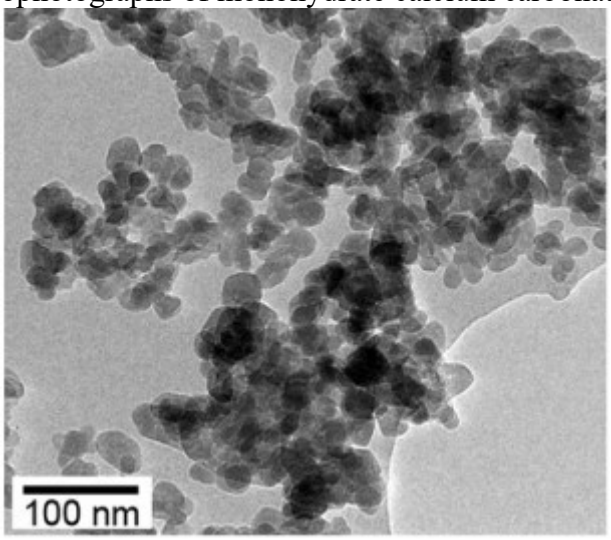

Source: Adapted from Rodriguez-Blanco *et al.* (2014)

Vaterite is the least stable calcium carbonate anhydrous polymorph under standard conditions and can be transformed into the thermodynamically more stable forms (aragonite, calcite) (DU; AMSTAD, 2019).

Besides, there are reports on vaterite being the first solid phase in many spontaneously formed calcium carbonate precipitates (BREČEVIĆ; KRALJ, 2008; BOTS *et al.*, 2012) and scale formation (DALAS; KOUTSOUKOS, 1989; KAMAL *et al.*, 2018). In support to this presumption are the experimental observations that unstable phases of calcium carbonate precipitate first from medium and high supersaturated solutions (GOWER, 2008; RODRIGUEZ-BLANCO; SHAW; BENNING, 2011; GEBAUER *et al.*, 2014; BLUE *et al.*, 2017; DU; AMSTAD, 2019).

Vaterite has a hexagonal crystalline structure with characteristic (101) and (102) crystallographic planes, where the carbonates are parallel to the c axis, and the calcium atoms are in eightfold coordination with oxygen atoms (KAMHI, 1963; WANG; BECKER, 2009). Although the vaterite crystalline unit has a hexagonal structure, its crystalline habit can have a

spherical aspect (Figure 2.4). This polymorph is also the more soluble of the anhydrous forms at standard conditions (PLUMMER; BUSENBERG, 1982; BECK; ANDREASSEN, 2010).

Figure 2.4 - SEM image of the vaterite morphology.

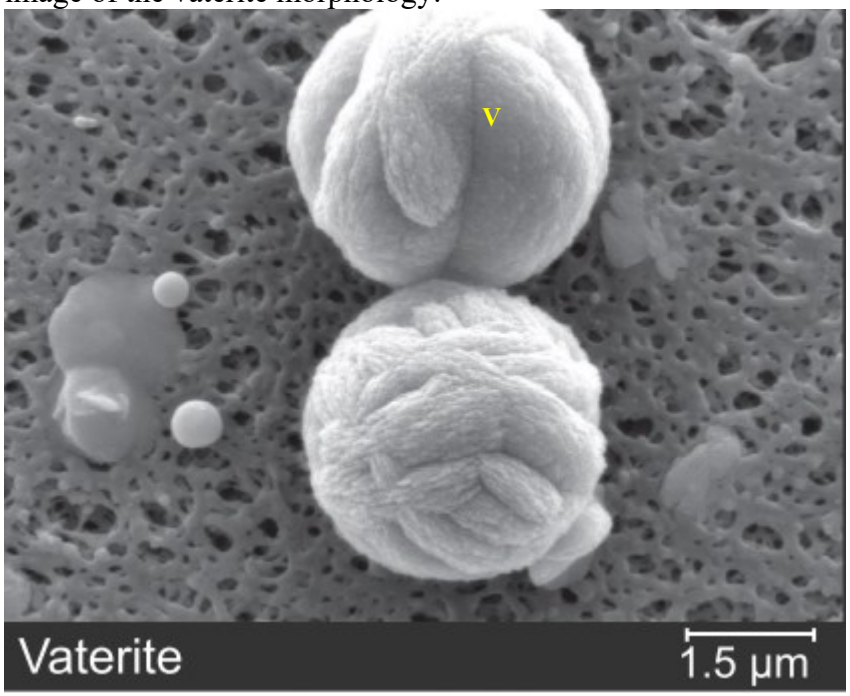

Source: Blue *et al.* (2017)

At ordinary temperature and pressure, calcite is a thermodynamically stable modification of calcium carbonate to which all metastable forms tend to transform (BREČEVIĆ; KRALJ, 2008). Because of its importance, primarily in sedimentary carbonate petrology but also in biology, environmental and industrial processes, this polymorph has been the subject of investigations by many authors (PLUMMER *et al.*, 1988; WEINER; ADDADI, 1997; RAMISCH *et al.*, 1999; GARCÍA; THOMSEN; STENBY, 2006; JIANG; WORDEN; YANG, 2018; LASSIN *et al.*, 2018; ZHAO *et al.*, 2018). One of the most studied subjects is the observation that calcite is usually the final form of all unstable phase transitions and its properties under different conditions (BREČEVIĆ; KRALJ, 2008; GEBAUER; VÖLKEL; CÖLFEN, 2008).

Calcium carbonate in the form of calcite scale is frequently encountered in oil field operations since this is the more stable form in oil field conditions (MOGHADASI *et al.*, 2007). Besides that, it also represents the majority of the carbonate minerals in deep-sea rocks (PENG *et al.*, 2015). That happens because this arrangement can have the lower superficial energy in the standard and basin conditions, i.e., high temperature, pressure, and salinity, compared with

the aragonite and vaterite forms (DONNET; BOWEN; LEMAÎTRE, 2009; KAMAL *et al.*, 2018).

Calcite has a rhombohedral crystalline structure with characteristic (211) and (011) crystallographic planes, where the carbonates are perpendicular to the c axis, and the calcium atoms have sixfold coordination with oxygen atoms (KAMHI, 1963; VILLIERS, 1971; MARKGRAFR; REEDER, 1985). Different from vaterite, the crystalline habit of the calcite reflects its rhombohedral structure, as shown in Figure 2.5.

Figure 2.5 - SEM micrographs of pure calcite particles.

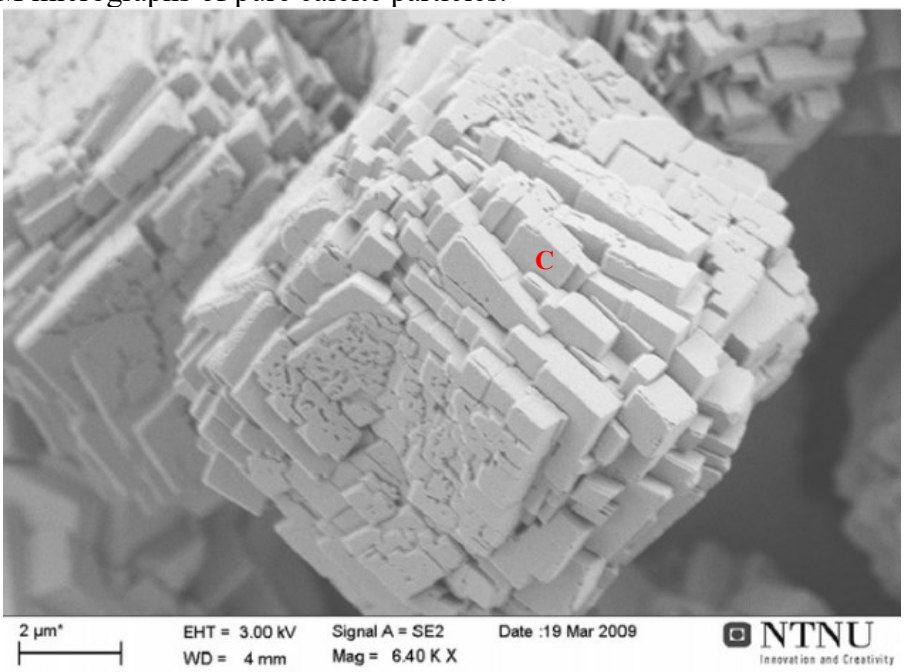

Source: Beck and Andreassen (2010)

Aragonite, another polymorphic form of the calcium carbonate, can be stable under certain temperature conditions or in the presence of other ions (PLUMMER; BUSENBERG, 1982; OGINO; SUZUKI; SAWADA, 1990). However, it is less common and less stable than calcite, although both forms can be found together (MAYORGA; ASTILLEROS; FERNÁNDEZ-DÍAZ, 2019). The solubility of this crystal is lower than the solubility of amorphous calcium carbonate and vaterite but higher than the solubility of calcite (at 25ºC and 1 bar). Then, that aragonite is more stable than the metastable forms of calcium carbonate and can be produced by the rearrangement of vaterite and amorphous calcium carbonate (KITANO, 1962; TOBLER *et al.*, 2016; BLUE *et al.*, 2017; LASSIN *et al.*, 2018). In addition, Jimoh *et al.* (2018)

demonstrated that high Mg^{2+} concentration, up to 0.5 $mol.L^{-1}$, influences the stability of the aragonite particles at acid pH and high temperatures.

Aragonite has an orthorhombic crystalline structure with characteristic (001), (011), (010), (110) crystallographic planes, where the carbonates are perpendicular to the c axis, and the calcium atoms have ninefold coordination with oxygen atoms (KAMHI, 1963; VILLIERS, 1971; MARKGRAFR; REEDER, 1985). This crystalline form can present various crystalline habits, although aragonite particles are often found as needles, as presented in Figure 2.6.

Figure 2.6 - Time-resolved SEM micrographs of aragonite crystals.

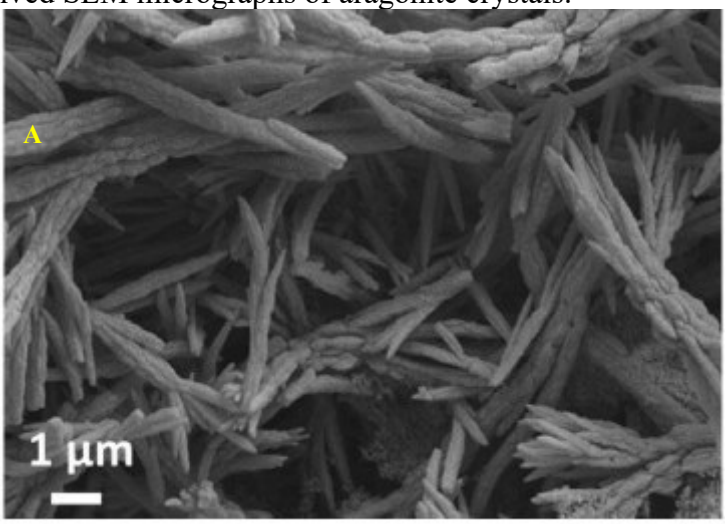

Source: Walker; Marzec; Nudelman (2017)

In many cases regarding the calcium carbonate formation, the nucleated phase can have a different structure from the crystallization process final product (GEBAUER *et al.*, 2014; CHANG *et al.*, 2017a). Thus, in studying this mineral formation, one should carefully evaluate the polymorphic pathway that can occur along with the crystallization with the order of appearance of these solids (GOWER, 2008; DONNET; BOWEN; LEMAÎTRE, 2009).

Regarding the nucleating phases, Mann (1983) stated, “Since amorphous phases are more soluble than crystalline phases at equilibrium, it seems possible that the formation of amorphous precursors could be widespread in biomineralization”. This statement was based on his discussion of $CaCO_3$ crystallization via a stepwise precursor pathway, illustrated with a reaction coordinate diagram, as shown in Figure 2.7 (MANN, 1983; GOWER, 2008).

The reaction coordinate diagram represents different pathways to lowering the Gibbs free energy. Pathway A represents the conventional crystallization pathway, which occurs for mineral precipitation from solution without passing through any intermediate phase(s). Pathway

B demonstrates the formation of a crystalline mineral from the metastable phase(s) of different crystal structures or even the amorphous phase. The energy barriers for the pathways differ, where the first step requires a $\Delta G_{Nucleation} + \Delta G_{Growth}$, while the subsequent steps only require a ΔG_{Phase} transformation. Various pathways are possible, depending on the relative values of the energy barriers, such as the formation of ACC and transformation directly to calcite (DONNET; BOWEN; LEMAÎTRE, 2009). Gower (2008) also proposed a new step in the ACC pathway, consisting of a polymer-induced liquid-precursor (PILP) phase, a potential intermediate to the solid ACC phase.

Empirical observations of such reaction pathways have long been observed. They are often attributed to the Ostwald-Lussac rule of stages, which specifies that if a solution is super-saturated concerning more than one phase, the more soluble (least stable) phase is often the first phase to form (MANN, 1983; SANTEN, 1984; DU; AMSTAD, 2019). Given sufficient time and energy, the products should ultimately transform into the lower energy, more thermodynamically stable state. As illustrated in Figure 2.7, the pathway followed for the multistep reaction will depend on the relative heights of the energy barriers between the metastable states. For example, while calcite is the most thermodynamically stable phase, it can be preceded by the less stable phase(s) due to their lower energy barriers, which could be metastable vaterite or aragonite, or even the unstable amorphous calcium carbonate (ACC) under conditions of high supersaturation (OGINO; SUZUKI; SAWADA, 1987; RODRIGUEZ-BLANCO; SHAW; BENNING, 2011; CHANG *et al.*, 2017a).

Figure 2.7 - Reaction coordinate diagram representing different pathways to lowering the Gibbs free energy: A refers to the conventional pathway; B demonstrates the formation of metastable forms prior to equilibrium.

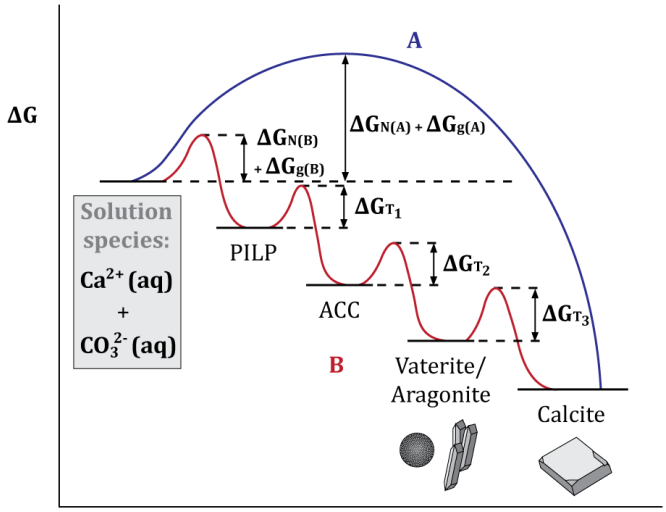

Source: Adapted from Gower (2008)

The change in the Gibbs free energy associated with each polymorphic state in Figure 2.7 can be determined based on the assumption that the nanoscopic nuclei behave like the macroscopic phase (crystal), i.e., have the same bulk structure and exhibit corresponding interfacial energy (DONNET; BOWEN; LEMAÎTRE, 2009; VETTER *et al.*, 2013a; GEBAUER *et al.*, 2014). The result of this assumption is shown in Equation 2.15, which represents the change in Gibbs free energy caused by the formation of crystals of size L from a supersaturated solution (IGGLAND; MAZZOTTI, 2012).

$$\Delta G_{ex}(L, SS) = -\frac{3}{2}\frac{k_v R T}{N_a}\ln(SS)\ L^2 + \frac{2\,\gamma\, k_a V_m}{N_a}\ L \tag{2.15}$$

Where V_m constitutes the molar volume, R the universal gas constant, T the temperature, k_v and k_a the volume and area shape factors, N_a the Avogadro's number, and γ represents the interfacial tension between the solid and the solution.

The Gibbs free energy calculations associated with this pathway can be used to predict polymorphic reaction order according to the conditions with the precipitation system (DONNET; BOWEN; LEMAÎTRE, 2009; KAWANO *et al.*, 2009).

2.2.2 Thermodynamic studies associated with $CaCO_3$ precipitation

In this section, some works from the literature are presented, which discussed or demonstrated the thermodynamic equilibrium, between phase or species, either theoretically or experimentally.

Haarberg and Selm (1992) proposed a quasi-theoretical solubility model to predict the solubility of the scale-forming minerals, such as$CaCO_3$, $CaSO_4$, $SrSO_4$, and $BaSO_4$, for various temperatures up to 150°C and pressures up to 30 atm. The authors utilized experimental data collected from the literature to fit the scales solubility constants as functions of temperature, pressure, and ionic concentrations. The solubility model was then used to predict sulfate and carbonate salts formation. The equilibrium reactions are presented in Equations 2.16 to 2.24. The initial brine composition consists of Ca^{2+}, Sr^{2+}, Ba^{2+}, CO_3^{2-}, SO_4^{2-}, and CO_2, where the aqueous phase is in equilibrium with the oil and gas phases. Furthermore, to solve the species

mass balance, the electroneutrality of the brine was assumed in this model, i.e., the sum of all ionic charges is zero.

$$CaCO_{3(\text{calcite})} \leftrightharpoons Ca^{2+}_{(\text{aq})} + CO_3^{2-}{}_{(\text{aq})} \quad (2.16)$$

$$CaSO_{4(s)} \leftrightharpoons Ca^{2+}_{(\text{aq})} + SO^{2-}{}_{4(aq)} \quad (2.17)$$

$$SrSO_{4(s)} \leftrightharpoons Ca^{2+}{}_{(aq)} + SO_4^{2-}{}_{(aq)} \quad (2.18)$$

$$BaSO_{4(s)} \leftrightharpoons Ba^{2+}{}_{(aq)} + SO_4^{2-}{}_{(aq)} \quad (2.19)$$

$$CO_{2(aq)} \leftrightharpoons CO_{2(\text{g})} \quad (2.20)$$

$$CO_{2(oil)} \leftrightharpoons CO_{2(\text{g})} \quad (2.21)$$

$$H_2O_{(l)} + CO_{2(aq)} \leftrightharpoons HCO_3^{1-}{}_{(aq)} + H^+{}_{(aq)} \quad (2.22)$$

$$HCO_3^{1-}{}_{(aq)} \leftrightharpoons H^+{}_{(aq)} + CO_3^{2-}{}_{(aq)} \quad (2.23)$$

$$H_2O_{(l)} \leftrightharpoons OH^-{}_{(aq)} + H^+{}_{(aq)} \quad (2.24)$$

The authors first calculated the equilibrium state before the precipitation/dissolution to solve the model. After the minimum in the Gibbs free energy of the system was obtained, the supersaturation was calculated. Then, it was determined if the precipitation was likely to occur or not. After that, the authors used the solubility-equilibrium model to estimate the precipitation potential caused by mixing different types of water.

García *et al.* (2006) developed an accurate thermodynamic model to calculate the solubility of the salts under hydrothermal conditions, i.e., up to 300°C and 1000 bar. The central concept of that model was based on vapor-liquid-solid equilibria for carbonate salts such as $CaCO_3$ and solid-liquid equilibria for sulfate salts such as $CaSO_4$. The extended UNIQUAC model presented by Thomsen and Rasmussen (1999) was used to calculate aqueous phase activity coefficients, while the Soave–Redlich–Kwong state equation was used to compute the fugacities in the gas phase. The model was improved by adding two parameters to account for the pressure dependency of solubility. The extended UNIQUAC model was chosen over other alternatives due to its accuracy and simplicity. It only requires two parameters per species, plus two per species pair, while the model equations accounted for temperature dependency.

Duan and Li (2008) developed a model for calculating coupled phase and aqueous species equilibrium in the H_2O–CO_2–NaCl–$CaCO_3$ system from 0 to 250°C, 1 to 1000 bar with NaCl concentrations up to saturation of halite. This model proposed that Equations 2.25 to 2.34 can represent the equilibrium in the aqueous phase, considering that the concentration of other

ions, such as Mg^{2+}, K^{1+}, Ba^{2+}, SO_4^{2-} affects only the ionic strength and, consequently, the concentration, the thermodynamic activity, and fugacity of the species of interest.

$$H_2O_{(l)} + CO_{2(aq)} \leftrightharpoons HCO_3^{1-}{}_{(aq)} + H^+_{(aq)} \quad (2.25)$$

$$HCO^{1-}{}_{3(aq)} \leftrightharpoons H^+_{(aq)} + CO_3^{2-}{}_{(aq)} \quad (2.26)$$

$$H_2O_{(l)} \leftrightharpoons OH^-_{(aq)} + H^+_{(aq)} \quad (2.27)$$

$$CaHCO_3^{1+}{}_{(aq)} \leftrightharpoons Ca^{2+}_{(aq)} + HCO_3^{1-}{}_{(aq)} \quad (2.28)$$

$$CaCO_3^0{}_{(aq)} \leftrightharpoons Ca^{2+}_{(aq)} + CO_3^{2-}{}_{(aq)} \quad (2.29)$$

$$Ca(OH)^{1+}{}_{(aq)} \leftrightharpoons Ca^{2+}_{(aq)} + OH^{1-}{}_{(aq)} \quad (2.30)$$

$$CO_{2(aq)} \leftrightharpoons CO_{2(g)} \quad (2.31)$$

$$H_{2(aq)} \leftrightharpoons H_2O_{(g)} \quad (2.32)$$

$$CaCO_{3(calcite)} \leftrightharpoons Ca^{2+}_{(aq)} + CO_3^{2-}{}_{(aq)} \quad (2.33)$$

$$NaCl_{(halite)} \leftrightharpoons Na^{1+}_{(aq)} + Cl^{1-}{}_{(aq)} \quad (2.34)$$

To determine the equilibrium constants, Duan and Li (2008) used the standard chemical potential of the species from the literature or adjusted from the literature data for the extreme temperature and pressure conditions up to 250ºC, 1000 bar, and NaCl concentration of 20 M. To calculate the distribution of the species between the liquid and vapor phases, the authors used the activity coefficient of the species in the liquid phase from Pitzer equations (PEIPER; PITZER, 1982) and adjusted the Poynting correction factor to correlate fugacity with water and CO_2 activity in the liquid phase.

In order to obtain a methodology that needs fewer parameters to be solved and is more readily applicable to the oil systems, Cosmo (2013) used Equation 2.35, in which the equilibria involving calcium carbonate were rearranged and combined in a single equation representing the global chemical equilibrium. It can be noted that this equation suggests that the $CaCO_3$ is formed by a reaction of calcium with bicarbonate ion instead of carbonate ion. This combination is because only a small percentage of the bicarbonate ions dissociates in carbonate at the pH values presented in Table 2.1 (WALY, 2011).

$$Ca^{2+}_{(aq)} + 2HCO_3^{1-}{}_{(aq)} \leftrightharpoons CaCO_{3(s)} + H_2O_{(l)} + CO_{2(aq)} \quad (2.35)$$

For this reaction, the equilibrium constant equation was obtained as a function temperature (up to 100 ° C), pressure (up to 100 atm), and activity coefficients (calculated using the Debye-Hückel correlations) of the compounds of interest in NaCl concentrations of up to 300,000 ppm. This methodology reveals an advantage of using a global equation to represent the calcium carbonate equilibrium instead of solving all the possible equilibriums. The author only had to expand one equilibrium constant to include the temperature and pressure effects instead of expanding all associated constants as made by Haarberg *et al.* (1992). However, it should be noted that the author's simulations did not include any additional ions besides those directly involved in the calcium carbonate formation.

The methodology used represented the displacement generated by the thermodynamic changes caused by the flow. The results obtained were compared with the commercial software Multiscale®, used by the oil industry to predict saline precipitation, and the errors obtained for the studied conditions were lower than 10%. With these parameters, the author obtained a process model to predict the mass of calcite that must precipitate from the solution with changes in pressure and temperature.

Understanding the carbonate chemical equilibrium makes it possible to notice why the CO_2 reinjection is a viable technology for scale control (PENG *et al.*, 2015; CRUZ; CISTERNAS; KRASLAWSKI, 2018). In Equation 2.35, it is seen that with the increase of $CO_{2(aq)}$, the equilibrium is shifted to the calcium carbonate dissolution. Besides that, the carbon dioxide reinjection favors reservoir pressure maintenance, favoring the flux of gas and oil (CHANG *et al.*, 2017a).

Many works presented in the literature consider calcium carbonate precipitation only in the calcite form, because this is the most stable form in the majority of the systems that present calcium carbonate formation (LIU *et al.*, 2015; OLAJIRE, 2015; KAMAL *et al.*, 2018). As already discussed, there are other hydrated or anhydrous forms in which calcium carbonate can precipitate, depending on the pH and temperature conditions (GEBAUER; VÖLKEL; CÖLFEN, 2008; KELLERMEIER *et al.*, 2016; ORAL; ERCAN, 2018). Thus, for a robust understanding of the system under study, it is necessary to include the other forms for carbonate solids, since the problem of the incrustation of the calcium carbonate also depends on the morphology of the precipitated crystal phase. (DONNET; BOWEN; LEMAÎTRE, 2009; YANG *et al.*, 2010; KAMAL *et al.*, 2018; DU; AMSTAD, 2019).

Plummer and Busenberg (1982) evaluated the differences in the solubility of calcite, vaterite, and aragonite to an aqueous system with $CaCO_3$ and CO_2. The authors used the Debye-

Hückel equations to calculate the dissolved ions activity coefficients and obtain the constants as a function of temperature, ranging from 10ºC to 90ºC, and potentiometric measurements. The authors observed that the equilibrium pH changes according to the polymorph form, thus obtaining different solubility constants for the calcite, aragonite, and vaterite. The first form, calcite, was less soluble for the majority of the temperatures evaluated. Although, at temperatures close to 90ºC, aragonite became the more insoluble polymorph.

Kawano *et al.* (2009) proposed and constructed a new "precipitation diagram" with two variables: the driving force for nucleation/growth and temperature. As a result, a calcite–vaterite co-precipitation zone, a vaterite precipitation zone, vaterite–aragonite co-precipitation zone, and an aragonite precipitation zone were defined as presented in Figure 2.8.

The curves in Figure 2.8 for the reaction of formation of calcium carbonate polymorphs and amorphous calcium carbonate were calculated from an equation similar to Equation 2.6. They were obtained by calculating the points where the activity product, AP, were equal to the solubility constant for each polymorph, i.e, when $\Delta\mu$ (or ΔG)= 0. In Figure 2.8A, it can be seen that the calcite presented the lowest solubility and the amorphous the highest, for temperatures smaller than 40ºC, with all polymorphs, except the $CaCO3{\cdot}6H_2O$(ikaite), diminishing its solubility with the temperature increase. It also can be seen that the calcite polymorph presented the highest thermodynamic stability, assuming an infinitely large particle as the Kelvin's law consideration was not yet made for the particle solubility with Equation 2.6, for all range of temperature studied, with aragonite approaching calcite as the temperature increased.

Figure 2.8 - Diagrams with (A) the equilibrium curves for the formation of polymorphs during precipitation and (B) experimental data of precipitated polymorphs.

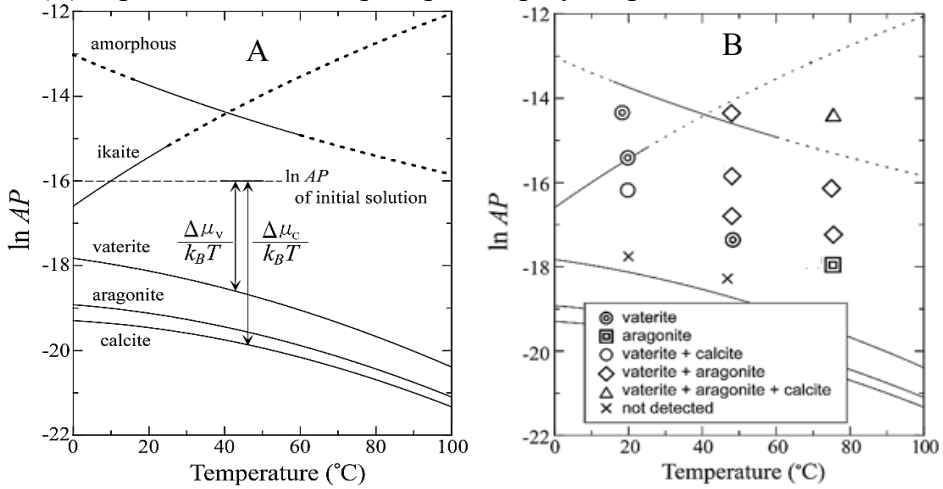

Source: Adapted from Kawano *et al.* (2009)

Where AP represents the activity product between calcium and carbonate ions, $\Delta\mu_{i\ is}$ the chemical potential for the reaction, $k_{b\ is}$ the Boltzmann's constant, and T is the absolute temperature. With the comparison between the experiments made by the authors and the equilibrium calculations, the authors could observe the appearance of the polymorphs defined five distinct zones(Figure 2.8 B):

1. Calcite-vaterite co-precipitation zone, at 20ºC and ln AP =-16.20;
2. Vaterite precipitation zone, for ln AP above -16, at 20ºC;
3. Vaterite-aragonite co-precipitation zone, with for higher ln AP, above -17, and conditions at 50 and 80ºC;
4. Aragonite precipitation zone, for ln AP = -17.96, at 80ºC;
5. In addition to the four zones described above, another zone can be defined, where the ln AP value is higher than the equilibrium curve for ACC.

The study made by the authors revealed the prime importance of surface free energies in the nucleation of polymorphs, as the nucleation barrier can be used to evaluate the polymorphic order of appearance, as already discussed in Figure 2.7. Using the surface free energies, the authors theoretically calculated the nucleation barriers and then were able, together with the solubility calculations, to successfully predicted, the polymorphs that appeared in the experiments presented in Figure 2.7B. The concepts obtained in this study also had important implications for investigating the impurity effect on calcium carbonate precipitation. The results implied an effect on the surface entropy of aragonite (or other polymorphs) can be due to impurity absorption on the crystal surface. Such an effect can be expected in both biological and industrial systems, as these can present a whole set of impurities that can affect the whole energetic profile of the calcium carbonate diagram (KAWANO et al., 2009).

Donnet *et al.* (2009) extend solubility calculations to help elucidate possible precipitation reaction pathways during the entire reaction. The authors considered precipitation reactions as a succession of small quasi-equilibrium states to achieve this. Thus, possible equilibrium precipitation pathways could be evaluated by calculating the surface charge, particle size, and interfacial energy evolution during the ongoing reaction. The calculated values showed a good agreement with the experimental polymorphic pathway, correctly predicting the direct precipitation of calcite from system conditions of 4 $mmol.L^{-1}$ of calcium nitrate and sodium carbonate. These approaches were also applied to calculate surface charge changes or

interfacial energy evolution during precipitation reactions for ionic crystals. The authors concluded that the inclusion of the Kelvin's Law, to express the influence of particle size on the solubility constant of precipitates and the Nernst's law to calculate surface potentials from solubility calculations offered a robust tool to future works predict the possible calcium carbonate polymorphic pathways.

Chen and Xiang (2009) investigated the temperature effect on the calcium carbonate by injection of $CaCl_2$ and NH_4-HCO_3 solutions with temperatures ranging from 30 to 80°C. They found that the vaterite content at 30, 60, 70, and 80°C was 98.6, 74.6, 19.6, and 0%, respectively, whereas the molar content of calcite was lower than 4.4% in this temperature range. The aragonite was favorably formed at 50°C, and the content increased with an increase in temperature.

Chang *et al.* (2017b) examined the effects of temperature on $CaCO_3$ polymorphs under controlled pH and carbonate/calcium rates using $CaCl_2$ and K_2CO_3 with concentration ranging from 20 to 40 mmol.L^{-1} solutions via ATR FT-IR and PXRD spectroscopies at temperatures ranging to 25 up to 80ºC. They observed that vaterite was a major component with calcite at 25ºC and with alkaline pH, higher than 8, vaterite became the most present species. At the highest temperature, 80ºC, aragonite represented most polymorphic distribution. Gebauer *et al.* (2008) also identified that for alkaline pH higher than 9.5, the vaterite could be the most abundant polymorph, although the acidification of the system induces calcite formation at lowers temperatures or aragonite formation at high temperature.

Graham *et al.* (2003) showed that the presence of other ions, such as magnesium, affects the stability of the formed crystals, within petroleum fields with a high concentration of this ion, up to 10 M, presenting a higher formation of aragonite than calcites in both acidic and basic pH.

The effect of the Magnesium ion on the calcium carbonate transformation was also investigated by Zhang *et al.* (2012). It was observed that the presence of Mg^{2+} in low ratios, up to 1/2, promotes the transformation of the amorphous phase into aragonite. In contrast, monohydrated calcium carbonate was formed at higher ratios, up to 4/1. They suggested that the presence of Mg^{2+} decreased the thermodynamic stability of calcite through inclusion in its lattice owing to the Mg^{2+} higher hydration, resulting in aragonite formation.

Magnesium, Barium, and Strontium, being divalent elements and belongs to the calcium group due to their similarities in properties, can become a natural substitute for calcium and influence the polymorphic distribution of the calcium carbonate solids (KITANO;

KANAMORI; OOMORI, 1971; SANJIV RAJ; DEVI; SUBRAMANIAN, 2020). Thus, it is essential to determine how these ions will distribute among the solid and aqueous phases to investigate how they influence carbonate formation (ASTILLEROS *et al.*, 2000).

Kitano *et al.* (1971) measured Sr and Ba distributions with low, 8 mg/L, and high Mg, 1.3 g/L, within calcite or aragonite precipitation from calcium bicarbonate solutions containing strontium or barium, $MgCl_2$, $NaCl_2$, and citrate salts. To investigate Sr and Ba partition, the authors prepared bicarbonate solutions, with a concentration of Ca^{2+} and HCO_3^{-1} of 400 mg/L, which were mixed with solutions of $SrCl_2$, 0 to 50 mg/L, and $^{85}Sr^{2+}$, as a tracer, or with solutions of $BaCl_2$, 0.1 mg/L, and ^{140}Ba as a tracer. In both laminar and turbulent regimes, the solutions were stirred from one week to one month. During the precipitation process, portions of the supernatant solution were taken up to determine the decrease in Ca, Sr, and Ba contents with the time. The distribution coefficient was calculated with Doerner-Hoskin's Equation. The average distribution coefficient for Sr and Ba, at 20ºC, were 0.08(calcite), 1.1(aragonite), 0.1(calcite) and 1.5(aragonite), respectively. However, higher values were observed at the early stages of carbonate precipitation within calcite formation, 0.45 and 4.8, with the Ba distribution being heavily influenced by the agitation. The obtained values for both Sr and Ba were considered abnormally high, indicating a higher, up to 733%, capacity of the calcite lattice to accommodate Ba^{2+} and Sr^{2+} under far-from-equilibrium conditions, supersaturations higher than 10, especially at the early stages of carbonate precipitation.

Sawada *et al.* (1990) studied the distribution coefficients of Mg^{2+} between the calcium carbonate polymorphs, amorphous, vaterite, and calcite, with two different periods of the precipitation, adding Mg^{2+} after or before the amorphous appearance. The $CaCO_3$ was precipitated by mixing 67 $mmol.L^{-1}$ of $CaCl_2$ and 130 $mMol.L^{-1}$ of Na_2CO_3 with $MgCl_2$ solutions to achieve Mg^{2+}/Ca^{2+} ratios of 1 to 0 at 25ºC. The values of the distribution coefficient of vaterite, calcite, and amorphous increased with the decrease of Mg concentration, producing average values of 0.0615, 0.0484, and 0.062, with the obtained values agreeing with those previously obtained in the literature (MUCCI; MORSE, 1983). Besides that, the author also observed that the Mg^{2+} slowed each step of the calcium carbonate formation, attributing this to the slow dehydration rate that the magnesium ion presented.

2.3 KINETICS OF THE CALCIUM CARBONATE PRECIPITATION

2.3.1 Nucleation

Supersaturated solutions are solutions that are not in chemical equilibrium with its components, and precipitation occurs in order to move to an equilibrium state (MYASNIKOV; CHIPRYAKOVA; KULOV, 2013). The supersaturation is consumed by a combination of nucleation and crystal growth. Nucleation refers to the "birth" of crystals; this process significantly determines the number and size of crystals formed in a precipitation process (SUNDERMANN, 2016; ZHAO *et al.*, 2018). Although, the appearance of the crystals cannot occur immediately after the solutions achieve the supersaturation. The time difference from supersaturation to the formation of the first detectable crystals in the system is known as the induction period. This period, as a function of the supersaturation of the solution, its temperature and pressure and even the measuring equipment used to monitor the crystals, can be used to determine the mechanisms involved in the kinetics of crystallization (SPANOS; KOUTSOUKOS, 1998; MYASNIKOV; CHIPRYAKOVA; KULOV, 2013). After the induction period, nucleation can be divided into primary, both homogeneous or heterogeneous, and secondary nucleation, as shown in Figure 2.9

Figure 2.9 - Illustration of the nucleation mechanisms.

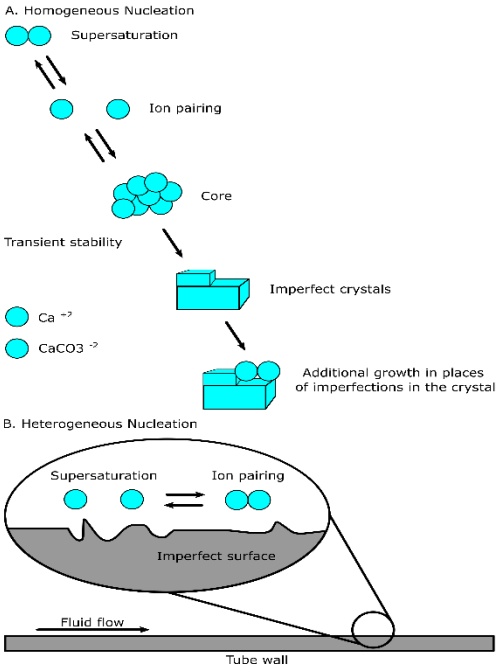

Source: Adapted of Crabtree *et al.*, (1999)

The classical nucleation theory, CNT, dictates that the formation of nuclei in a supersaturated solution is governed by the balance between the bulk and surface energy (GEBAUER *et al.*, 2014). The formation of nuclei is a consequence of microscopic density fluctuations, due to random collisions of dissolved constituents (KOUTSOUKOS; KONTOYANNIS, 1984; GEBAUER *et al.*, 2014; ZHAO *et al.*, 2018). As the interfacial and bulk energy of a nuclei scale with the square and the cube of the radius r, in a spherical nucleus, the destabilizing interfacial contribution dominates at small sizes, and the favorable bulk energy dominates at larger sizes, as shown in Figure 2.10 (GEBAUER; VÖLKEL; CÖLFEN, 2008; MYASNIKOV; CHIPRYAKOVA; KULOV, 2013).

Figure 2.10 - Illustration of the Gibbs free energies as function of nucleus's size.

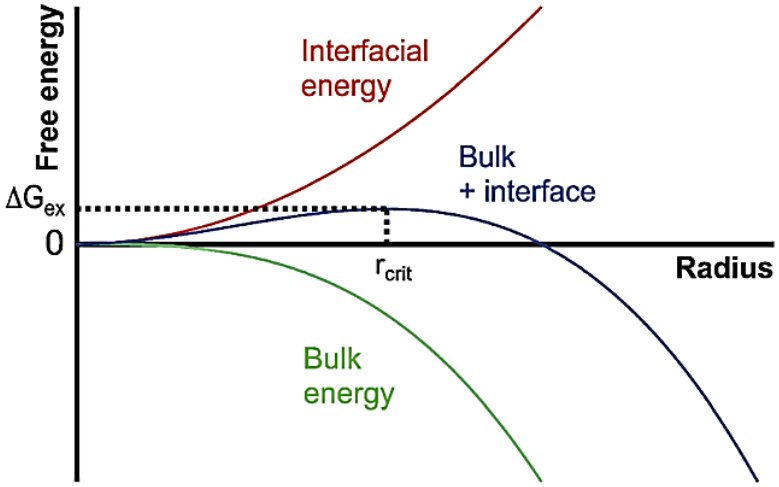

Source: Adapted from Gebauer *et al.* (2014)

There is a nucleus size when the bulk contribution compensates for the energetic costs arising from the interfacial surface, and this moment is called the critical size, r_{crit}. By analogy with the notion of an activated complex in kinetics studies, ΔG_{ex} can be the basis of the thermodynamic barrier for nucleation (MYASNIKOV; CHIPRYAKOVA; KULOV, 2013; GEBAUER *et al.*, 2014). Additional kinetic barriers could be taken into account too, that can originate with rearrangements with the nucleus. Thus, the nucleation rate can be expressed as Equation 2.35.

$$J = A\, exp^{\frac{-E_a}{k_b T}} exp^{\frac{-\Delta G_{ex}}{k_b T}} \tag{2.35}$$

With E_a representing the overall activation energy, ΔG_{ex} the excess free energy of the nucleus on its surface, k_b the Boltzmann's constant, and T the absolute temperature. The first exponent represents the kinetic barrier to the nucleation, while the second estimate the thermodynamic barrier. The parameter A depends on the properties of the investigated material with the solution.

The classical nucleation theory is a model that assumes that both γ and supersaturation are constant against the nucleus radius r. However, there are nucleation pathways that do not follow the classical theory, processes that present an alternative pathway, with lower energy barriers than those of the homogeneous nucleation defined above (GEBAUER *et al.*, 2018).

As already discussed, the formation of clusters or nuclei with a stepwise phase transition occurs in two mechanisms that have been identified for the $CaCO_3$ precipitation (GEBAUER; VÖLKEL; CÖLFEN, 2008; ZHAO *et al.*, 2018). Thus, the crystallization of calcium carbonate can be considered non-classical when the conditions favoring the formation of initial metastable phases. Many stepwise phase transitions could be involved. Figure 2.11 represents a schematic illustration of the crystal transitions paths in classical and non-classical approaches accompanied by the Gibbs free energy profiles associated with the stepwise transition.

Figure 2.11 - Illustration of the homogeneous paths for calcium carbonate. (A) Classical, top route, and non-classical, bottom route, nucleation paths. (B) Changes of free energy profiles through stepwise phase transition.

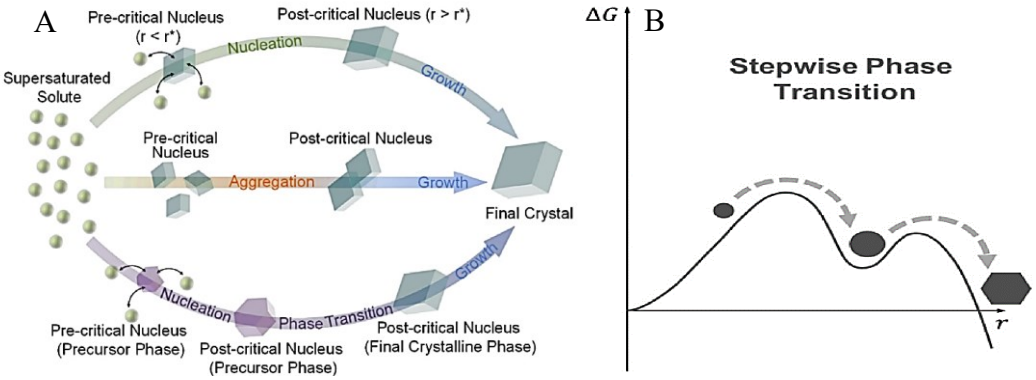

Source: Adapted from Zhao *et al.* (2018)

It is possible to associate Figure 2.11 and Figure 2.7 to summarize the possible transition paths for $CaCO_3$ from polymer-induced liquid-precursor to an amorphous phase, then to an anhydrous crystalline phase. Both figures are a representation of the empirical Ostwald's rule of stages applied for the calcium carbonate formation by polymorphic changes (NAVROTSKY,

2004; BREČEVIĆ; KRALJ, 2008; GOWER, 2008; RODRIGUEZ-BLANCO; SHAW; BENNING, 2011; BLUE *et al.*, 2017; ZHAO *et al.*, 2018; DU; AMSTAD, 2019).

Many theoretical frameworks have been proposed and evaluated recently to these non-classical behaviors: spinodal decomposition, liquid-liquid phase separation, and pre-nucleation clusters (GEBAUER *et al.*, 2014). Karthika *et al.* (2016) summarize the recent and classical theories that can have applicability with the calcium carbonate formation. The author concluded that a significant theoretical and experimental foundation is needed to understand the governing kinetics of the formation of crystals from clusters and extract more information on the polymorphic mechanisms. Moreover, despite significant literature advances, there is still work to be developed, especially with the cluster actuation in the polymorphism and that no single mechanism alone can be able to explain the nucleation pathway of the calcium carbonate formation. Du *et al.* (2019) emphasized that water is a critical component in the non-classical pathways with the calcium carbonate formation. The authors observed that water in the amorphous phases was associated with the final form produced, showing the necessity to study its structure and properties, an aspect that researchers often overlook (BLUE *et al.*, 2017).

The heterogenous nucleation can be a dominant process for precipitates, or scale, formation in metal surfaces that can be present in industrial equipment and tubbing (CRABTREE, M., ESLINGER, D., FLETCHER, P., MILLER, M., JOHNSON, A., KING, 1999; CHEN; NEVILLE; YUAN, 2005; SANTOS *et al.*, 2017; KAMAL *et al.*, 2018; DE SOUZA; ROSÁRIO; CAJAIBA, 2019). As shown in Figure 2.9, heterogeneous nucleation refers to nucleation in the presence of foreign substances, these act by reducing the interfacial energy, significantly reducing the energy barrier for forming nuclei on this surface (SUNDERMANN, 2016). The change in the Gibbs free energy during heterogeneous nucleation can be given by Equation 2.36.

$$\Delta G_{Het} = V_s \Delta G_V + A_{LS}\gamma_{LS} - A_{SM}(\gamma_{LM} - \gamma_{SM}) \tag{2.36}$$

Where ΔG_V is the excess free energy per volume of the bulk particle, V_s is the volume of particle, A_{LS} and A_{SM} are the surface areas of the interfaces between the liquid and the solid, and the solid and the material of the surface; γ_{LS}, γ_{LM} and γ_{SM} represents the interfacial energy between liquid and solid, liquid and the material, and solid and the material, respectively. As can be seen in Equation 2.36, multiple factors can affect heterogeneous nucleation, the surface chemistry, roughness of the material, hydrophilicity, and surface changes of the substrate as

well the lattices accommodation between the crystals and the substrate (WINKLER *et al.*, 2008; YAMANAKA *et al.*, 2009; LI *et al.*, 2014). Besides that, Zhao *et al.* (2018) concluded that measuring heterogeneous nucleation is a non-trivial task. The deposit of particles and formation of new particles on those surfaces have to be in-situ characterized to evaluate the problem thoroughly. Furthermore, the agglomeration of particles on these particles can also influence the phenomena.

2.3.2 Growth

After a nucleus of critical size is formed, it will start to grow into a larger crystal. The growth of crystals can be complex, and there are many theories to describe the mechanisms and growth rate of crystals (SUNDERMANN, 2016; GEBAUER *et al.*, 2018)

At the microscopic level, solute molecules, moving with the solution, adsorb onto the solid surface of the crystal and are incorporated into the crystal lattice. Thus, crystalline growth can be considered a two-step process, which involves: the transfer of mass, either by diffusion or convection, from within the solution to the surface of the crystal and the surface reaction, by which the units of growth are integrated into the crystal lattice. Either step can control the growth process as a whole (ASTILLEROS; FERNÁNDEZ-DÍAZ; PUTNIS, 2010; TRAMPUŽ; TESLIĆ; LIKOZAR, 2019). It was shown by Brečević and Kralj (2008) that the rate-determining mechanism in the growth process of the anhydrous forms of the calcium carbonate was at the moment when they integrate into the growth sites, with the integration rate for the calcite being much slower than the other polymorphs. However, the size of the crystal and its solubility had an effect on which two crystallization steps were dominant. Thus, both steps must be evaluated when calculating the growth rate in a crystalline distribution (MERSMANN, 2001; TRAMPUŽ; TESLIĆ; LIKOZAR, 2019).

The surface reaction step can involve several individual processes that can be diverse and complex. Crystal topology must be considered to theoretically describe crystal growth since a rough surface can lead to continuous growth, which is not the case for a smooth crystal surface (MERSMANN, 2001). The surface reaction step is generally divided into the following mechanisms: spiral growth, polynuclear growth (both considered smooth growths), and rough growth.

Spiral growth is also known as BCF (Burton-Cabrera-Frank) growth. This type of growth can be predominant in low supersaturations, presenting a rate with a quadradic relation

with the supersaturation (COSTA, 2003). In this model, displacement spirals are responsible for growth, with these defects being developed in crystals during their growth. Around the defect line, the step curves and forms a spiral step. After a layer completes, displacement is still present (MULLIN, 2001). Figure 2.12 illustrates spiral growth.

Figure 2.12 - Illustration of the spiral growth mechanism.

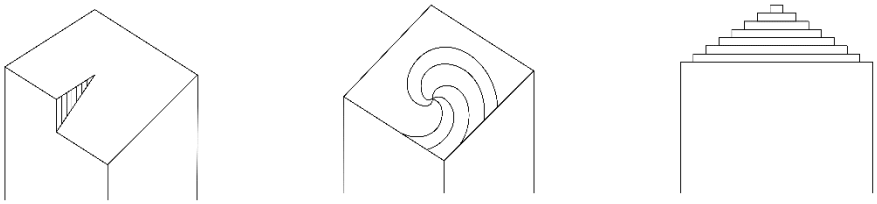

Source: Adapted from Costa (2003)

Polynuclear growth, also known as the B+S (birth and spread) model, occurs as a nucleus growth over a nucleus in a two-dimensional manner. The formation of nuclei occurs on the crystal surface, which grows like islands, spreading laterally across the surface of the crystal. This island may grow and cover the entire surface before a new island is formed on top of it, or several islands may nucleate across the entire surface, including new, incomplete layers formed by the laterally spreading islands (MERSMANN, 2001; BREČEVIĆ; KRALJ, 2008). In Figure 2.13, an illustration of polynuclear growth is presented. In this B+S model, growth is related to supersaturation through a complex power relation and is also dependent on the 2D nucleation rate of the formed islands (MULLIN, 2001; COSTA, 2003).

Figure 2.13 - Illustration of the polynuclear growth.

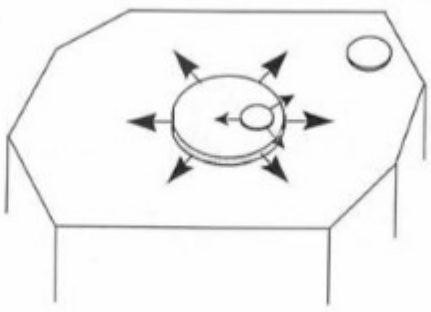

Source: Adapted from Costa (2003)

Rough growth occurs on surfaces that present roughness, with no preferred sites for growth. The growth rates of these faces are dependent on the difference in the flows of the

growth units in two directions: going towards the growth position and leaving the surface. This type of growth has a linear relationship with supersaturation (MERSMANN, 2001; COSTA, 2003).

Along with the nature of the crystallized substance, the growth mechanism is strongly affected by the supersaturation of a solution, as the value of SS increases, the mononucleation mechanism can be replaced by simultaneous spiral and polynucleation mechanisms, then by diffusion-controlled growth (TENG *et al.*, 2000; MYASNIKOV; CHIPRYAKOVA; KULOV, 2013).

As the dependence of growth with supersaturation is different for each model, in principle, it would be possible to experimentally determine which type of mechanism is present in the growth of calcium carbonate polymorphs. However, such determination can be complex due to the influence of one polymorphic growth on another, which may lead to correlations between the adjusted growth constants and several other errors inherent to growth measurements (CHAKRABORTY; BHATIA, 1996a; MULLIN, 2001).

The mass transfer driving force from the bulk solution to the crystal surface is the chemical potential difference in these regions. Thus, the difference in concentrations, the width of the boundary layer, and the species diffusion coefficient are essential parameters for calculating this transfer. For solutions with high supersaturation, the convective mass transport can be related to the crystal growth by Equation 2.37 (NANCOLLAS; REDDY, 1974; COSTA, 2003).

$$\frac{dm}{dt} = \frac{k_{di}}{(1-\mathrm{W})} A(c_b - c^*) \tag{2.37}$$

With k_d representing the diffusivity of the species i, A being the crystal surface, c_b the concentration with the solution and c* the concentration at equilibrium, and w the molar fraction of the solute species. *D* is proportional to the squared velocity of the diffusing particles, which depends on the temperature, viscosity of the fluid, the size and charge of the diffusing species according to the Nernst-Einstein Equation. In dilute aqueous solutions, the diffusion coefficients from calcium, bicarbonate, and carbonate ions can have values in the range of 0.6–20×10^{-10} $m^2.s^{-1}$ for temperatures up to 50ºC and different salinity contents (BREČEVIĆ; KRALJ, 2008; REIS *et al.*, 2016).

The convective mass transfer coefficient, k_{di}, can be calculated from the Sherwood number, representing the ratio of the convective mass transfer to the rate of diffusive mass transport (PERRY *et al.*, 2007). There are many correlations for calculating Sh, such as the Froessling Equation (Equation 2.38), with L_{car} representing the solid characteristic length, Re_p the particle Reynolds number, and Sc the Schmidt number.

$$Sh = \frac{k_d\, L_{car}}{D} = 2 + 0.552\, Re^{1/2} Sc^{1/3} \tag{2.38}$$

Regarding the convective term, theoretical considerations suggest a 1/2 dependence on the Reynolds number and a 1/3 dependence on the Schmidt number can be used for the majority of the proposed equations for Sh. But the discrimination of the relevant particle Reynolds number and an appropriated mass diffusivity is one of the significant factors in this parameter calculation (SCALA, 2013).

2.3.3 Agglomeration

In many crystallization processes, including the calcium carbonate, the final structure of the crystals can be heavily influenced by multiple agglomeration levels (CHAKRABORTY; BHATIA, 1996b; LASSIN et al., 2018). Agglomeration itself results from two steps: a binary collision of mother particles and sticking by the growth of crystalline bridges between the particles (DAVID; MARCHAL; MARCANT, 1995). In Figure 2.14, is illustrated a conceptual model for the steps present in the binary agglomeration of two distinct particles.

Figure 2.14 - Illustration of the steps in the binary agglomeration.

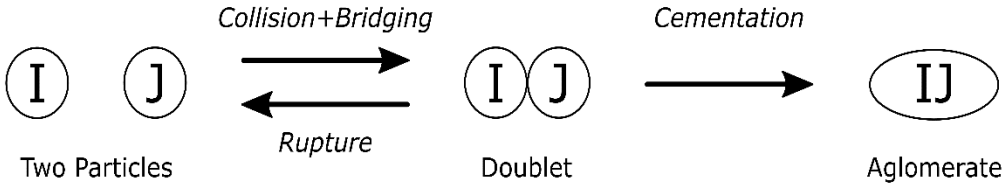

Source: Livk; Ilievski (2007)

The multiplicity and efficiency of collision mechanisms for each agglomeration step are a function of the size domain of mother particles and agglomerate, and by the hydrodynamic conditions (DAVID; MARCHAL; MARCANT, 1995; HOUNSLOW *et al.*, 2001;

MERSMANN, 2001). These collision mechanisms can be distinguished between Brownian, laminar, and turbulent. Similarly, the efficiency factor depends on the influence of these conditions on the particles size (MERSMANN, 1995; LIVK; ILIEVSKI, 2007). The information on the agglomeration mechanisms can be loaded in the agglomeration kernel, representing the mechanisms of collisions and the overall efficiency of the steps shown in Figure 2.14 (LIVK; ILIEVSKI, 2007). These kernels, represented as β, can be calculated by its collision mechanism, shown in Equations (2.39-2.41), with the transition of one agglomeration kernel to another being related to the microscales ranging from the Batchelor to the Taylor (DAVID; MARCHAL; MARCANT, 1995; MERSMANN, 1995; HOUNSLOW *et al.*, 2001; DAVID *et al.*, 2003). In these equations k_a, represents the agglomeration rate constant, G the crystal growth rate, S the average solid size, f the Marchal's relative size function, N the stirring speed, D the particle diffusivity, P the dissipated power per unit of mass and v the kinematic viscosity.

1. Brownian collision for crystals smaller than the Batchelor scale, l_b, i.e., $S_{agg} < (\frac{v\,D^2}{P})^{1/4}$:

$$\beta_{j,i} = k_A\, G\, \frac{(S_j+S_i)^2}{S_j S_i} \tag{2.39}$$

2. Laminar collision for crystals between Batchelor Scale and Kolmorogov, scale, i.e., $l_b < S_{agg} < (\frac{v^3}{P})^{1/4}$:

$$\beta_{j,i} = k_A\, G\, (S_j + S_i)^3 (\frac{P}{v})^{1/2} \tag{2.40}$$

3. Turbulent collision for crystals larger than the Kolmorogov scale, i.e., $l_k < S_{agg}$:

$$\beta_{j,i} = k_A\, G\, \frac{(S_j+S_i)^2}{S_j} f\left(\frac{S_i}{S_j}\right) N\, D\, (1 - \frac{(S_j+S_i)^2}{\lambda_c^2}) \tag{2.41}$$

The agglomeration kernels can describe the resulting agglomeration rates and the summation of all colliding particles that produce or consume a particle by this mechanism.

In the calcium carbonate formation, where the product can comprise two or more polymorphs, there can be differences in the growth rates and agglomeration tendencies.

Chakraborty *et al.* (1994) noted that the calcite agglomerated more strongly than its anhydrous counterparts, observing that the models must be extended to allow different rates for each polymorph for the correct size particle prediction. Thus, multiple agglomeration collisions and rate types have to be considered. These different kernels can appear simultaneously for the whole polymorphic size distribution (CHAKRABORTY; BHATIA, 1996a; DAVID et al., 2003; LIVK; ILIEVSKI, 2007).

2.3.4 Ageing (Ostwald ripening)

The crystallization process is usually described as a combination of several mechanisms: nucleation, both homogeneous and heterogenous, growth, and agglomeration. The combination of these effects can determine the evolution of the particle size distribution until the supersaturation of the solution is depleted (BOTS *et al.*, 2012; LASSIN *et al.*, 2018). After the depletion of the supersaturation, a mechanism known as Ostwald ripening take over and further influences the evolution of the particle size. At the same time, agglomeration can continue to act on crystallization (VETTER *et al.*, 2013). The calcium carbonate polymorphic phases, both hydrated and anhydrous, have various thermodynamic stability that manifests as the different solubilities at given conditions. Thus, the Ostwald ripening can have a significant role in the process that controls the polymorphs size distribution, even contributing to the crossover on that thermodynamic stability that leaves on a polymorphic rearrangement among the forms (BREČEVIĆ; KRALJ, 2008; GEBAUER *et al.*, 2014).

The thermodynamic basis of the ripening is the size-dependence of solubility based on the influence of the Laplace pressure on the curvatures of a surface (DONNET; BOWEN; LEMAÎTRE, 2009). Kelvin's law can express this effect for a single component liquid-vapor system (Equation 2.42).

$$\ln\left(\frac{P_c}{P_0}\right) = \frac{\gamma V_m C}{R\,T} \tag{2.42}$$

Where P_C represents the partial gas pressure at curvature C, P_0 is the partial gas pressure at zero curvature, V_m is the molar liquid volume and γ is the liquid-vapor interfacial energy. C is the interface curvature related to spherical particles with radius r presented in Equation 2.43.

$$C = \frac{8\,\pi\,r^2}{4\,\pi\,r^3}\frac{dr}{dr} = \frac{2}{r} \tag{2.43}$$

As for crystallization processes, Kelvin's equation can be derived in Equation 2.44 for the solid-solution equilibrium, which can capture the phenomena for the solids distributed along with the solution media.

$$\ln\left(\frac{M_{X,C}}{M_{X,0}}\right) = \frac{\gamma V_m}{R\,T}\,\frac{2}{r} \tag{2.44}$$

With $M_{X,C}$ representing the molar solubility of solid X in the form of particles with curvature C, and $M_{X,0}$ is the molar solubility of solids with zero curvature, i.e., infinitely large particles. Equation 2.44 represents the Gibbs-Thomson-Kelvin equation that represents the solubility of a solid substance concerning its particle size (IGGLAND; MAZZOTTI, 2012).

Equation 2.44 is strictly valid for spherical particles of non-dissociating species with a homogeneous and flat surface whose sizes are larger than the size of individual molecules (FARKAS, 1927; DONNET; BOWEN; LEMAÎTRE, 2009). Furthermore, the interfacial tension should be independent of the solute concentration (GREENWOOD, 1956; IGGLAND; MAZZOTTI, 2012). These conditions are not fulfilled for the calcium carbonate species that often presents non-spherical and faceted crystals. Wagner (1961) proposed an equation with stoichiometric factors to account for dissociating species. This equation can also be modified to include nonspherical crystals, including area and volume factors, k_a and k_v. These modifications can be used to obtain Equation 2.45, which defines the critical size of a crystal. Beyond that size, the nuclei are stable and grown, and smaller crystals will dissolve by ripening. (VETTER *et al.*, 2013a)

$$\frac{c^*(L)}{c_\infty} = \mathrm{e}^{\frac{2\,\gamma\,k_a\,V_m}{3\,k_v\,R\,T\,L}} \tag{2.45}$$

In the Equation 2.45, c*(L) represents the solubility of a particle of size L, c_∞ the solubility of an infinitely large particle and γ is the weighted average of the surface tension along with all faces. It is usually assumed that a single surface tension can describe the crystal for the sake of simplicity (IGGLAND; MAZZOTTI, 2012; VETTER *et al.*, 2013).

This mechanism can be responsible for increased polymorph size, either diffusion or surface-controlled. Including these calculations is recommended for any model that wants to achieve the size and polymorphic distribution in the calcium carbonate precipitation, as the dissolution of small particles for the simultaneous growth of large particles is a well-known fact in this inorganic precipitation (BREČEVIĆ; KRALJ, 2008).

2.3.5 Calcium carbonate polymorphic transformation

Another major kinetic factor in calcium carbonate precipitation is how the intermediate phase(s) appears and transforms to the final crystalline product. The growth of crystals from precursor phases of a different crystallographic structure requires reorganization of the ions to new lattice coordinates (MANN, 1983; GOWER, 2008). Phase transformations can occur via surface dissolution of the precursor followed by reprecipitation of a second phase, often upon particles of the initially formed solid, analogous to secondary nucleation (BREČEVIĆ; KRALJ, 2008; RODRIGUEZ-BLANCO *et al.*, 2011; BOTS *et al.*, 2012; BLUE *et al.*, 2017). Alternatively, the second phase can be formed via an in situ solid-state transformations, mainly when there is a close structural match and low interfacial energies between the two phases (IHLI *et al.*, 2014; KONRAD *et al.*, 2016; WALKER; MARZEC; NUDELMAN, 2017; DU *et al.*, 2018). It should be noted that the rate of appearance of a polymorph is not the only function of its transformation rate; the growth rate and the ripening can also be the determining steps on the appearance of a more stable polymorph (CHAKRABORTY; BHATIA, 1996b; BREČEVIĆ; KRALJ, 2008; DU; AMSTAD, 2019). The controlling factors for each polymorph consumption/appearance rate and its mechanisms are heavily influenced by the studied conditions. Therefore, there are no overall mechanisms that rule at all conditions. Although it can be generally noted that the dissolution-reprecipitation mechanism can offer lower kinetic barriers than the solid-state transformation if the solids are sufficiently diluted in water(BOTS *et al.*, 2012; DU; AMSTAD, 2019). Thus, when evaluating the polymorphic transformation process among the calcium carbonate solids, its specific conditions should also be evaluated. There are many conditions when calcite, the usually more stable polymorph, can transform itself via dissolution-reprecipitation into another polymorph by a crossover in the kinetic and thermodynamic stability (BREČEVIĆ; KRALJ, 2008; NATSI; ROKIDI; KOUTSOUKOS, 2016; SUNDERMANN, 2016; BLUE *et al.*, 2017; WALKER; MARZEC; NUDELMAN, 2017; DU; AMSTAD, 2019).

2.3.6 Kinetic studies for crystalline formation

In this section, some works reported in the literature are presented, which discussed or demonstrated the kinetic rates discussed above, either theoretically or experimentally.

Spanos and Koutsoukos (1998) evaluated the influence of pH on the induction time. The authors fixed the temperature, 25ºC, and the supersaturation, from 1.88 to 3.39, estimating the induction time and the form of the first solids. They observed that the induction time for the formation of vaterite particles is lower than for calcite, maybe due to the differences in the thermodynamic stability of the calcite and vaterite centers. In addition, the authors observed that the induction time was more influenced by the presence of heterogeneous centers than by an increase in supersaturation.

Ramstad *et al.* (2005) calculated the time required to form the first carbonate solids at temperatures ranging from 85°C to 130°C, pressures from 23 to 55 bar, and supersaturation of 1.41 to 10.75, using the Multiscale® software. The authors observed that at 33ºC, 85ºC, and supersaturation below 2.5, the induction time was higher than the residence time in the cell used. However, with the increase in temperature, to 130ºC, the induction period became less dependent on the supersaturation , and lower induction times were obtained (about 4 times lower than that at 85 °C). The results also presented that an earlier, almost half, shorter induction time appeared in the system having oil presence. Thus, the authors concluded that wells operating at high temperatures and high oil fractions can present a higher risk of presenting calcium carbonate formation.

Chien *et al.* (2007) studied the mathematical relationship between the induction time and the heterogeneous nucleation rate for a calcium carbonate solution. The studied supersaturation ranged from 4 up to 7 at 25ºC, with external particles, presented as diatomaceous Earth, were added up to 15 mg. The authors observed that the presence of particles dispersed in the medium greatly influences the induction time for solutions with low supersaturation, up to 5.85, observing – through conductivity measurements - a significant increase in the heterogeneous nucleation rates. However, for solutions with high supersaturations, starting at 6.41, the addition of particles had an insignificant effect on nucleation rates, so the induction time was not changed. The authors concluded that the formation of nuclei by adsorption of ions on particles surfaces, i.e., heterogeneous nucleation, is only more significant than homogeneous nucleation when the medium has a low supersaturation. With these conclusions, the authors proposed

Equation 2.46, which models the nucleation rate based on the Michaelis-Menten mechanism for nuclei formation under the influence of foreign particles, FP.

$$J_h = \frac{1}{-105.25\,SS+762} + \frac{(0.00782\,SS-0.02895)[FP]}{1.505x10^{-3}+[FP]} \quad (2.46)$$

In order to determine the presence of ionic cluster in calcium carbonate nucleation, the use of selective impedance electrodes to calcium and carbonate have been demonstrated by Gebauer *et al.* (2008). The studied conditions were based on alkaline pH, from 9 to 10, the temperature of 25ºC, and supersaturations up to 5. The formation of more stable crystals, such as calcite and aragonite, has been identified through the transformation of the ionic clusters of greater solubility, as the amorphous calcium carbonate. The precursor particles have lower surface energy than the final solid, thus being more stable in the aqueous medium in sizes at the nanometers range. However, with the subsequent growth of these species, the bulk energy starts to have more influence on the total surface energy, decreasing the stability of this precursor in front of the anhydrous forms. These results emphasized the importance of knowing the calcium carbonate arrangements to obtain kinetic parameters compatible with the formed solids, as the observed nucleation rate of a polymorph could encompasses the nucleation rate of cluster of greater solubility and its growth until the appearance of the observed polymorph.

Reis *et al.* (2016) performed a series of volumetric experiments, with concentrations of $CaCl_2$ and Na_2CO_3 up to 3.42 mol.L^{-1} at room temperature with the pH variation from 6 to 8.5. In these experiments, $CaCO_3$ precipitates were formed faster in supersaturated solutions with higher concentrations of sodium chloride. The authors then suggested that the intermolecular forces among the ionic species significantly influenced the diffusive processes related to the nucleation processes. In that direction, they also concluded that the ions diffusion controls the calcium carbonate nucleation to the growing site by exploiting the Muller-Liu formulation for the second law of thermodynamics.

Gebauer *et al.* (2014) summarized the role of pre-nucleation clusters, PNC, which can be a solute precursor on the calcium carbonate nucleation, even appearing before the solution achieves its supersaturation. Their presence is mainly discussed from biogenic conditions, at standard conditions, at 25ºC, 1 atm, and ionic concentrations up to 1 mol.L^{-1}. However, it can also be possible up to higher temperatures, pressures, and concentrations. These PNC are composed of the constituent atoms presented in the solution that forms by association like a

polycondensation reaction, are small in size, smaller than nm, but are thermodynamically stable and do not form a boundary with the surrounding solution. These molecular precursors to the nucleating phase have structural relation with the corresponding calcium carbonate crystalline phase suggesting that the nucleation can proceed through PNC formation like the polymer induced liquid precursor, PILP. The authors proposed that the crystallization of calcium carbonate along the PNC pathway can be understood chemically and structurally as a progressive, stepwise loss of hydration water, according to the sequence $Ca^{2+}_{(aq)}$/ $CO_3^{2-}{}_{(aq)}$ - PNC - dense liquid nanodroplets - liquid ACC - solid ACC - anhydrous crystalline polymorphs.

Nielsen *et al.* (2014) in situ TEM observations demonstrated that multiple nucleation pathways exist for the crystalline phases of $CaCO_3$, including direct formation from solution and direct transformation from more disordered phases. The experiments varied the $CaCl_2$ and $NaHCO_3$ concentrations, in millimolar and molar flow, in microliters per minute, at room temperatures, and neutral pH. The solution conditions varied from 30:100 to 50:50 proportion between the saline concentration and 9:1 to 10:0.2 of the proportion of the feeding salt rate. Their findings show that these multiple pathways and phases are simultaneously available to the system at moderate to high supersaturations, up to 10, as fully expected from classical considerations. Although the authors observed the transformation of the amorphous nucleus to a crystalline phase could be possible and indeed occur, it was never directly observed the direct transformation of amorphous calcium carbonate to calcite. Figure 2.15 shows TEM micrographs of the concurrent formation of multiple phase nucleation clusters of calcium carbonate. Based on the author interpretations, from A to D can be noted the simultaneous nucleation and growth of calcite crystals and either ACC or vaterite, from E to H can be observed the direct nucleation of vaterite and aragonite and its subsequent growth. At the last line, calcite formation occurs on aragonite particles followed by the calcite growth, and concomitant dissolution of aragonite can be noted from I to L.

Figure 2.15 - TEM micrographs of multiple phases nucleation clusters formation. The scale bars represent 500 nm.

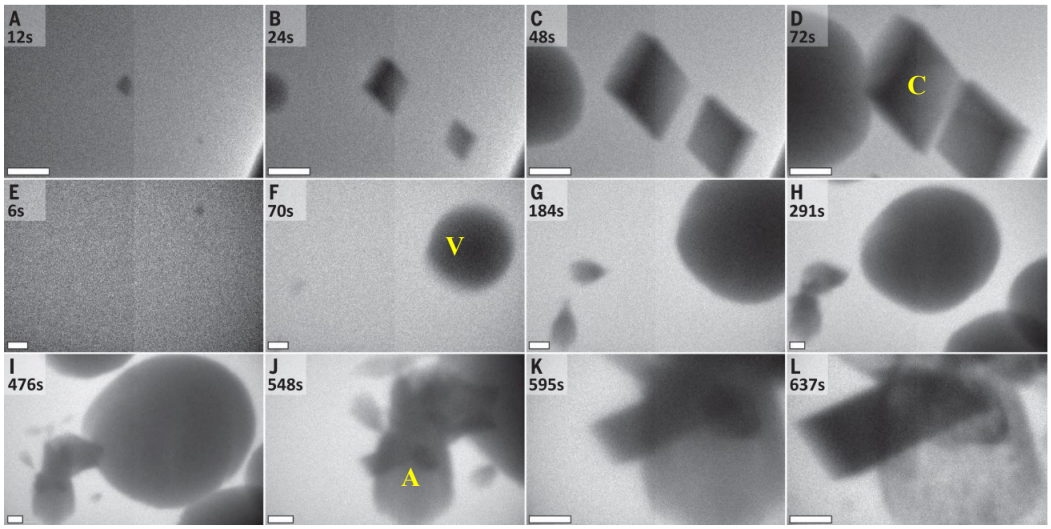

Source: Adapted from Nielsen *et al.* (2014)

Pin *et al.* (2018) provided a coupled theoretical and experimental study on the pathways that precede the initial stages of $CaCO_3$ nucleation. The experiments were done at pH ranging from 9 to 10, with $CaCl_2$ concentrations from 0.001 to 0.1 $mol.L^{-1}$, with temperatures ranging from 15 to 25ºC. The authors correctly predicted bulk thermodynamic quantities and experimental data from molecular simulations, including equilibrium constants, titration curves, and x-ray absorption spectra taken from the supersaturated $CaCO_3$ solutions. The authors' conclusions agreed with classical views of ions and ion pairs dominating the clusters populations, with the concomitant free energy landscapes for all nucleation steps following classical nucleation energy landscapes theory presented in Figure 2.7.

The pioneering work of Nancollas and Reddy (1971) showed that the rate of the crystalline growth of $CaCO_3$ is a function of the concentrations of calcium and carbonate, the solubility of the crystalline phase formed, and the surface area of the crystals. The crystallization experiments were done in a seeded batch mode with temperatures of 10, 25 and 45ºC, with the concentration of the calcium and hydrogen concentrations being monitored by atomic absorption, the ionic concentration ranged from 1 to 4.5 $mol.L^{-1}$ and the seed mass from 34 to 167 mg per 100 microliters of solution.

The global equation obtained by Nancollas and Reddy (1971) included both the second-order relation and the dissolution of the ions responsible for representing the growth of the carbonate crystals. In Equation 2.47, where k is the rate constant of growth, a_s the surface area

of crystals, K_{sp} is the calcium carbonate solubility product, and f_2 is the divalent activity coefficient.

$$\frac{dCa^{2+}}{dt} = -k\ a_s\ (\ [Ca^{2+}][CO_3^{2-}]) - \frac{K_{sp}}{f_2^2} \tag{2.47}$$

Shiraki and Brantley (1995) proposed three affinity rate models based upon the described growth mechanism in section 2.2.1, at 100ºC, 100 atm, and acid pH with the system NaOH-$CaCl_2$ – CO_2 – H_2O presenting concentrations up to 10 mmol.L^{-1}. The study showed that the calcite growth rate is a function of the activity product and hydrodynamics, represented by different agitation speeds, with the reactor. At higher stirring speeds, faster than 1200 rpm, and carbonic acid activity smaller than 2.33 x 10^{-3}, the growth rate showed a parabolic dependence upon supersaturation for saturations smaller than 1.72. For higher supersaturations, the rate increased exponentially and followed a rate based upon the surface limiting reaction. When the carbonic acid activity was higher than 5.07 x 10^{-3}, the rate showed a linear dependence with the supersaturation, suggesting a surface adsorption mechanism. With those three different mechanisms of the calcite growth rate, the authors were able to propose Equations 2.48-2.50 to represent the rates for each governing mechanism.

$$R_{spiral\ growth} = 10^{-9}\ (e^{\frac{\Delta G}{RT}} - 1)^{1.93} \tag{2.48}$$

$$R_{adsorption} = 10^{-8.64}\ (e^{\frac{\Delta G}{RT}} - 1)^{1.09} \tag{2.49}$$

$$R_{surface\ nucleation} = 10^{-7.28}\ e^{-\frac{RT\ 2.36}{\Delta G}} \tag{2.50}$$

Plummer and Busenberg (1999) studied the calcite growth rate from Ca and HCO_3 solutions at 34ºC, varying the calcite supersaturation from 0.2 to 1.9 and the dioxide carbon partial pressure from 0.0012 atm to 0.101 atm. At constant CO_2 pressure, the authors observed linear relation between the ionic activity product of the species and growth/dissolution rate. However, the growth rate was nearly independent of the dioxide carbon concentration at constant supersaturation.

Brečević and Kralj (2008) conducted a series of experiments to evaluate the growth rate of both vaterite and calcite. The vaterite experiments were made at pH = 9.3-9.9, at Ca^{2+} and CO_3^{-2} concentrations of 2.5 x 10^{-3} mol.L^{-1}, ranging temperature from 10 to 45ºC and ionic

strength from 15 to 315 mmol.L^{-1}. These experiments observed a parabolic relation with the supersaturation, with the growth rate constant varying from 0.180 to 1.860 nm/s at 11.4 and 42.5ºC, respectively. Besides that, a rather weak dependence of the vaterite growth rate on the ionic strength was found; only an 8% increase in the growth rate was found at 20 times higher ionic strength. After that, the authors obtained the energy of activation of the growth rate of 57.1 kJ.mol^{-1}, supporting a surface-controlled mechanism in which the integration of ions controls the reaction rate.

For calcite polymorph, experiments were performed under temperatures of 25 and 45ºC and ionic strengths between 15 and 415 mmol.L^{-1} with the addition of initial seed of calcite particles with an average diameter of 3 μm. The experiments indicated a square root relation between the growth rate of the calcite and the supersaturation, indicating that the integration of ions into the spiral step mechanism. The values of the rate constant of calcite growth rate varied from 0.006 nm.s^{-1} to 0.122 nm.s^{-1} from 10.2 to 54.5ºC and presented energy of activation of 55 kJ.mol^{-1}, also indicating a surface-controlled crystallization. The activation energy was in agreement with Myasnikov *et al.* (2013), who made a review discussing the theory pertinent with the energy of activation adjustment of crystalline kinetics and experimental methods related to these phenomena.

Rosa *et al.* (2011) studied the $CaCO_3$ growth kinetics by mass crystallization, recording pH as a function of time. The phase crystallizing was vaterite at 25ºC, calcite at 30ºC, and aragonite at 37ºC. Growth kinetics at the initial stage followed that of the polynuclear surface nucleation mechanism. A simplified kinetic equation derived by Christoffersen *et al.* (1998), was possible to estimate the free energy related to the step formation on these crystal surfaces. The values were: calcite 35.4 pJ/m at 30ºC, aragonite 32.3 pJ/m at 37ºC, and vaterite 24.2 pJ/m at 25ºC. These values agreed reasonably well with literature values determined by other methods. They were able to test the validity of the relation between step distance of a growth spiral and size of a critical surface nucleus as assumed in the Burton–Cabrera–Frank, BCF, theory (DICKENS; BOWEN, 1971; EFFENBERGER; ZEMANN; MEREITER, 1981; WANG; BECKER, 2009). The lower value for vaterite than the two polymorphs is not surprising because of its less dense structure and higher solubility. Calcite and aragonite were expected to have similar values as they have more similar properties than vaterite.

To accurately describe the Ostwald ripening phenomena is necessary to describe the behavior of subcritical crystals, which dissolve, and supercritical crystals, which grow. Thus, it is also necessary to study the kinetics of dissolution of the calcium carbonate polymorphs, as

the ripening can occur with all polymorphs at the moment of crystallization (VETTER *et al.*, 2013a; GEBAUER *et al.*, 2018).

Plummer *et al.* (1978) studied the kinetics of the calcite dissolution in the H_2O-CO_2 system from 5 to 60ºC and 0 to 1 of partial pressure of dioxide carbon. The authors utilized two different methods to evaluate the dissolution behavior: one method to study the dependencies far from equilibrium and the other to evaluate as the reaction approaches the equilibrium. These methods cover pH from 2 to 7.7.

The dissolution rate was independent of partial pressure of dioxide carbon and directly proportional to the bulk-fluid hydrogen ion activity in pH < 3.5. Dissolution rate depended on both pH and P_{CO2} in 3.5 < pH < 5.5, and the precipitation became important in pH > 5.5. The dissolution rate was not pH-dependent above pH 5.5. With these results, the authors proposed that three mechanisms of reactions regulate the dissolution kinetics of this calcium carbonate polymorph (Equations 2.51-2.53).

$$CaCO_3 + H^+ \leftrightharpoons Ca^{2+} + HCO_3^{1-} \quad (2.51)$$

$$CaCO_3 + H_2CO_3 \leftrightharpoons Ca^{2+} + 2HCO_3^{1-} \quad (2.52)$$

$$CaCO_3 + H_2O \leftrightharpoons Ca^{2+} + HCO_3^{1-} + OH^{1-} \quad (2.53)$$

Based on these equations, the authors propose that Equation 2.54 represents the overall reaction rate, representing dissolution and precipitation mechanisms at fixed temperature and carbon dioxide concentration.

$$R = k_1 a_{H+} + k_2 a_{H2CO3} + k_3 a_{H20} - k_4 a_{Ca2+} a_{HCO3-} \quad (2.54)$$

With the three first constants being presented and adjusted in the author's work being a function of the temperature, the last constant was obtained as a function of the three first constants.

Shiraki and Brantley (1995) also studied that the mechanism based upon individual elementary reactions proposed by Plummer *et al.* (1978) accurately predicts dissolution and precipitation calcite kinetics under temperatures up to 100ºC. The growth presented a quadratic relation with the supersaturation, in contrast to 3 affinity-based models already presented in Equations 2.18-2.19 that could not predict dissolution in these conditions. The authors concluded that this complicated behavior of the dissolution/precipitation kinetics demonstrates

that for the correct prediction of the overall rate, one should understand the regime's growths together with the dissolution regimes, with both being related, although in different ways, with the hydrodynamics of the reactor used.

Brečević and Kralj (2008) also performed dissolution experiments for the monohydrate calcium carbonate and vaterite polymorphs. They tested a theoretical model to adjust the kinetic parameters and the dissolution rate step. The monohydrate experiments were performed at 15, 25, 35, and 45ºC with a population of this polymorph ranging between 15-30 μm. Among the models tested, a second-order model, in relation with the undersaturation, was found to best describe the experimental data. With the dissolution rate constants obtained at different temperatures, the activation energy for the dissolution was also obtained, 73.3 $kJ.mol^{-1}$. This high value was associated with a surface-controlled mechanism, probably the detachment of ions with the crystalline structure. The vaterite dissolution kinetics was performed in two sets of experiments, in which either the temperature (15 to 45ºC) or the ionic strength (50 to 200 $mmol.L^{-1}$) were studied. The vaterite crystals presented diameters with 2.7 to 4.6 μm. In both sets of experiments, a straight line was observed when -r(dr/dt) was plotted against the undersaturation, indicating that the diffusion of hydrated ions away from the solution controls the dissolution rate. The authors also concluded that the influence on the dissolution was negligible as the particles were smaller than 5 μm. It was also possible to estimate the activation energy for this vaterite step, 24 $kJ.mol^{-1}$, being a value typical of the diffusion of ions in aqueous solutions (MYASNIKOV; CHIPRYAKOVA; KULOV, 2013).

Peng *et al.* (2015) performed calcite dissolution experiments in water saturated with carbon dioxide for four temperatures, from 323 to 373 K at pressures ranging from 6.0 to 13.8 MPa. The undersaturation ranged from -4 to -10. The results were similar for a polished calcite surface and a surface presenting rough defects, presenting dissolution rates of 0.0015 $mol.m^{-2}.s^{-1}$ at 353 K and 13.8 MPa. It can be seen in Figure 2.16 that the calcite dissolution rate increases with the temperature and pressure. These results differed from those of Pokrovsky *et al.* (2009). However, the authors pointed out that their dissolution rates were gathered in a mass-transfer controlled regime instead of the surface reaction-controlled regime presented by Peng *et al.* (2015). Pokrovsky reported a dissolution rate at T = 373 K and p = 5.0 MPa of 6×10^{-4} $mol \cdot m^{-2} \cdot s^{-1}$ while, in this study, the dissolution rate at the same temperature and p = 6 MPa was 8.2×10^{-4} $mol \cdot m^{-2} \cdot s^{-1}$. The authors discussed that the higher dissolution rates obtained in this work might be consistent with eliminating mass-transfer resistance. From the slope of the linear regression lines, the apparent activation energy for calcite dissolution in both systems

was found to be 16 kJ.mol^{-1}. The authors conclude that their measurements were made at higher Reynolds numbers, which may explain why they found a reaction-controlled regime. This factor aside, the differences between the apparent activation energies reported in the literature and the present study may be associated with the different regimes of pH and salinity studied.

Figure 2.16 - Calcite dissolution rates in the acid-free system as a function of temperature with ◆, P= 6MPa; ■, P =10MPa; ▲, P= 13.8MPa.

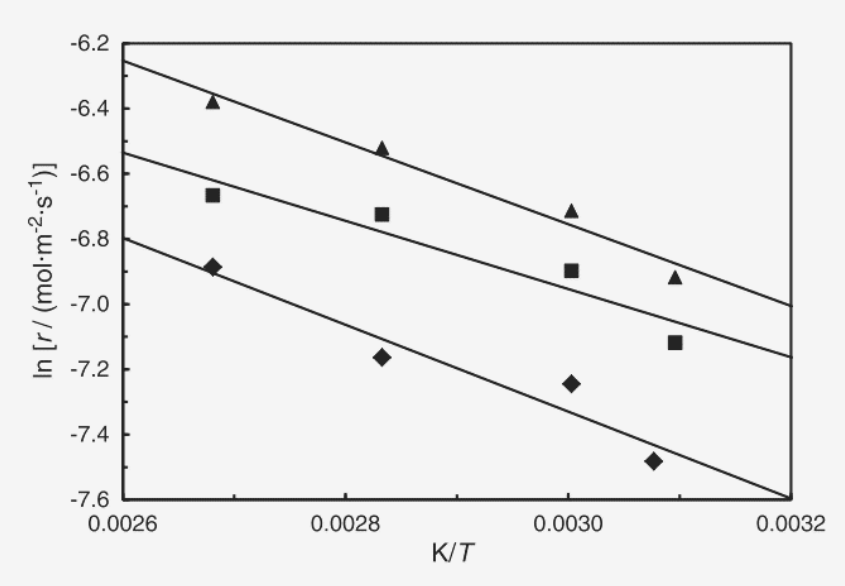

Source: Adapted from Peng *et al.* (2015)

With the growth and dissolution rates, one must also evaluate the transformation rates with the possible calcium carbonate solids. These rates can influence each other; besides, each solid can have different growth and dissolution rates (CHAKRABORTY; BHATIA, 1996a; DU; AMSTAD, 2019).

Ogino *et al.* (1990) studied the transformation of vaterite and aragonite to calcite under temperatures of 25 to 80ºC and calcium and carbonate activities ranging from $10^{-2.5}$ M to $10^{-4.1}$ and $10^{-4.1}$ M to $10^{-5.7}$, respectively. It was observed that these transformations proceed by the dissolution of the less stable phase and the subsequent growth of calcite, with the latter being the rate-determining step for both transformations. The apparent energy of activation obtained from the experiments, 70 kJ mol^{-1}, also suggested that the surface reaction of calcite growth controlled the transformation. These results agreed with Davey *et al.* (1986), who also concluded that the calcite growth rate is the rate-determining step, obtaining this from a kinetic model of solvent-mediated phase transformation based on similar experiments of Ogino (1990).

Rodriguez-Blanco *et al.* (2011) studied the kinetics of the crystallization process by carrying out calcium carbonate precipitation experiments with 1 M of Na_2CO_3 and $CaCl_2$ in an 80 mL stirred cell at a range of temperatures of 7.5, 10, 20 and 25ºC. The crystal characterization was made using synchrotron-based in situ time-resolved Energy Dispersive X-ray Diffraction (ED-XRD) in conjunction with high-resolution electron microscopy, ex situ X-ray diffraction, and infrared spectroscopy. The authors observed that the crystallization occurred in two stages: firstly, the amorphous CC particles rapidly dehydrate and aggregate to form particles of vaterite; secondly, the vaterite transforms to calcite via dissolution and reprecipitation mechanism (Figure 2.17). The authors used X-ray diffraction, infrared spectroscopy, and electron scanning microscopy to experimentally identify the transitions between the carbonate phases and conclude that the transition of the vaterite to calcite is controlled by the surface area of the carbonate solid. Besides that, they observed that the second stage of the reaction is approximately ten times slower than the first, associating that the first stage is controlled by amorphous dissolution and the second by calcite growth. The authors also obtained activation energies of calcite nucleation and growth of 73 and 66 kJ mol^{-1}.

Figure 2.17 - SEM micrographs of the solid carbonate evolution from amorphous calcium carbonate to calcite.

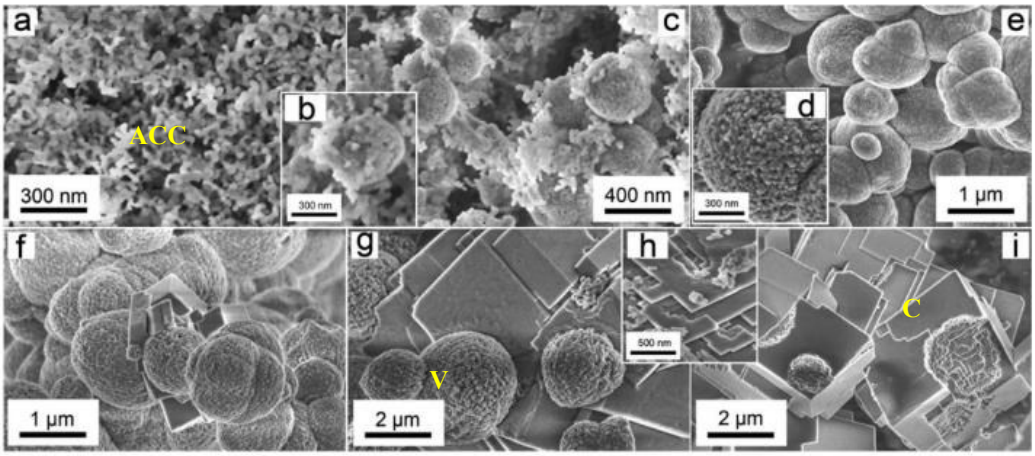

Source: Adapted from Rodriguez-Blanco *et al.* (2011)

Bots *et al.* (2012) studied the mechanism associated with the amorphous calcium carbonate, ACC, crystallization by rapidly mixing solutions of $CaCl_2$ and Na_2CO_3 solutions of 1 M. The crystallization characterization was made by in situ small- and wide-angle X-ray scattering (SAXS/WAXS) together with FER-SEM and pH samplings. The authors observed that the ACC crystallizes to vaterite via a three-stage process. Firstly, hydrated and disordered

ACC forms rapidly transform to more ordered and dehydrated ACC. In conjunction with this, vaterite forms via a spherulitic growth mechanism. Secondly, when the supersaturation of the solution concerning vaterite decreases sufficiently, the mechanism changes to ACC dissolution and vaterite crystal growth. The third stage is controlled by the Ostwald ripening of the vaterite particles, and because ripening is a dissolution mechanism the further ripening is easily displaced by a dissolution-reprecipitation transformation leading to the final calcite. Combining the obtained results with information of vaterite-calcite transformation, as Rodriguez-Blanco *et al.* (2011), the authors proposed a mechanistic understating of the whole calcium carbonate crystallization process. Figure 2.18 presents a schematic representation of the proposed multistage crystallization proposed by the authors.

Figure 2.18 - Schematic representation of the proposed multistage ACC → vaterite → calcite crystallization pathway with the combined reaction progress - the green triangles and full black squares represent the ACC and vaterite from Bots *et al.* (2012), and the open squares and red triangles represent the vaterite and calcite from Rodriguez- Blanco *et al.* (2011).

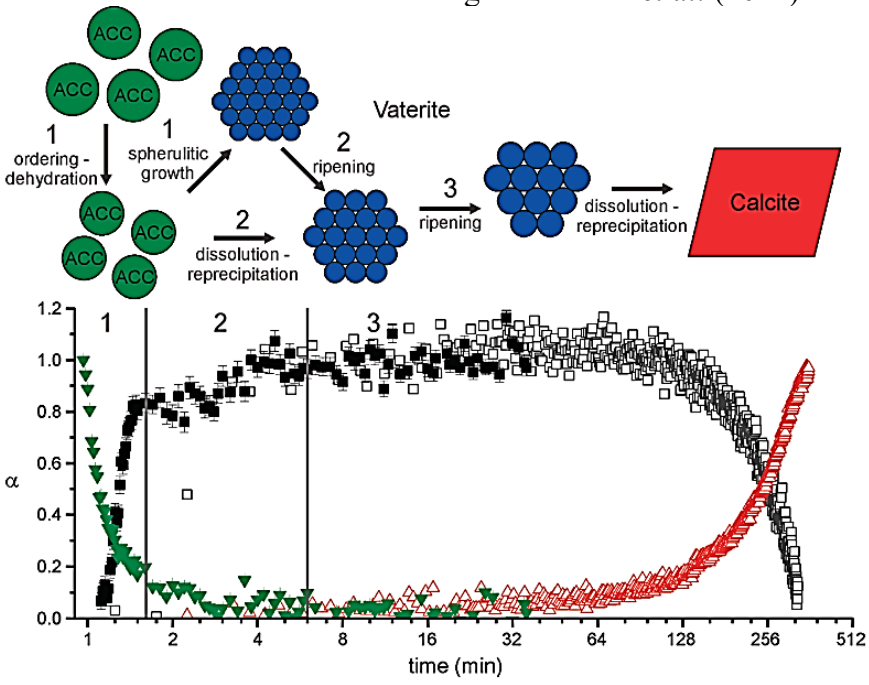

Source: Adapted from Bots *et al.* (2012)

Natsi *et al.* (2016) experimented in seeded and unseeded solutions at constant supersaturations ranging from 6 to 7, at 25ºC and pH = 8.5 containing mono ethylene glycol and n-dodecane to evaluate the influence of organic solvents with the calcium carbonate formation. The author found out that the organic phase stabilized the vaterite polymorph with the final solution containing co-existing calcite, indicating the transformation of vaterite to

calcite is still occurring (Figure 2.19). Besides that, they observed that the induction time was shorter as a higher amount of n-dodecane was used, showing an effect that is known in the crystallization field by the poor solvent effect, when the increase of supersaturation occurs, which is inversely proportional to induction time, by adding a non-soluble phase in the system (COSTA, 2003).

Figure 2.19 - SEM micrographs of the precipitated calcium carbonate in the presence of an organic phase with 60% v/v of dodecane.

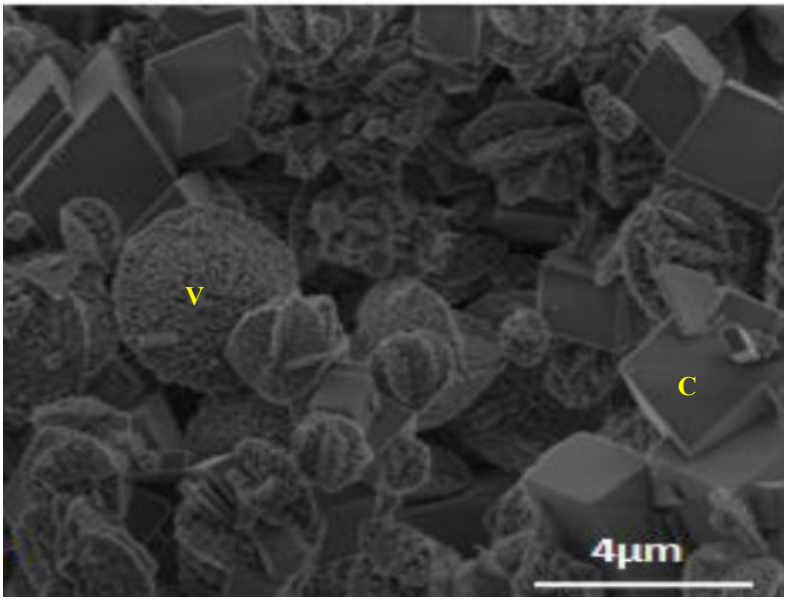

Source: Natsi; Rokidi; Koutsoukos (2016)

Walker *et al.* (2017) identified that the formation mechanism of aragonite is not as studied as that of calcite in the literature and studied the mechanism of the aragonite formation produced by amorphous calcium carbonate. To obtain a system in which aragonite is the most stable form, the authors used a mixture of $CaCl_2$ and Na_2CO_3, both with 25 mmol.L^{-1} and ethanol, 50 vol%, which has been identified as inducing the formation of aragonite against calcite (COSTA; MACIEL; FILHO, 2007). The crystallization characterization was made by Cryo-TEM imaging together with SEM, and the polymorph characterization was obtained by powder X-ray diffraction (XDR) and Raman spectroscopy. Initially, small ACC particles form, up to 20 nm, then agglomerate into larger particles. These aggregated particles combine to become a larger linear structure. Nanoscale crystals form with this amorphous framework, which grows to form the final needle structure, as observed in the time-resolved micrographs of this crystallization shown in Figure 2.20.

Figure 2.20 - SEM micrographs of the solid carbonate evolution from amorphous calcium carbonate to aragonite.

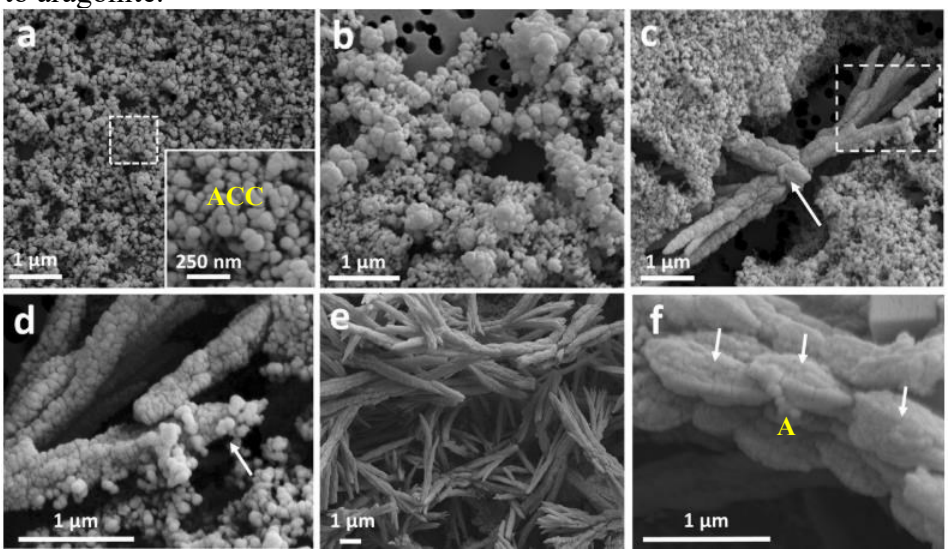

Source: Walker; Marzec; Nudelman (2017)

Du *et al.* (2019) summarized the current understanding of the solute concentration, pH, temperature, solvent, and additives during the $CaCO_3$ formation. The author discussed that different synthesis methods could form different calcium carbonate solids through different pathways, proposing a scheme shown in Figure 2.21 that summarizes eight different steps that the calcium carbonate precipitation can present. In I and II, the crystalline $CaCO_3$ nuclei can form and grow into larger crystals through ion-by-ion attachment following the classical nucleation theory if the solution is supersaturated concerning any crystalline $CaCO_3$ form, undersaturated concerning amorphous calcium carbonate. In III, ions associate with each other such that they form highly hydrated chain-like ion clusters, so-called prenucleation clusters (PNCs). PNCs subsequently aggregate, forming liquid phases or small ACC particles, and can appear even if the solution is not supersaturated, especially at low temperatures, T<10ºC. In IV, an aqueous solution containing Ca^{2+} and CO_3^{2-} ions undergoes a spinodal or binodal liquid-liquid phase separation to form a solute-rich liquid phase where ACC particles form through dehydration of the liquid phase or nucleation from the liquid phase. This step is usually present in solutions close to the equilibrium, at SS<3. In V, the ACC nuclei directly forms in the aqueous solution, usually the case for far from equilibrium conditions, SS_{ACC}>10. In VI, the formed small ACC particles grow until they transform into crystals, this transformation can occur through a VII, dissolution-recrystallization mechanism if ACC is in contact with bulk water or, VIII, solid-state transformation if ACC is not in contact with bulk water, based on the observations that the water reduces the kinetic barrier of the transformation.

Figure 2.21 - Schematic illustration of proposed mechanisms of the $CaCO_3$ formation.

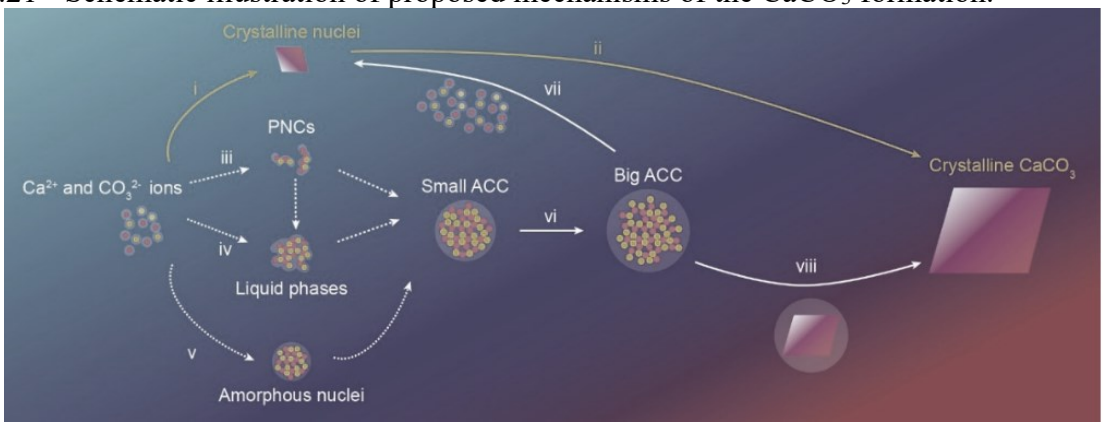

Source: Adapted from Du *et al.* (2019)

Chakraborty and Bhatia (1996b, 1996a) proposed a populational balance to predict the size distribution of the calcium carbonate particles, with the polymorphs having different growth rates and agglomeration tendencies. The Hounslow method was used to discretize the population balance equation, modified for improved stability and accuracy, and then used to solve the obtained model equations for polymorph precipitation in a continuous system. There were two different scenarios evaluated when there was the simultaneous nucleation of both calcite and vaterite polymorphs, and a second when the nucleation of vaterite was followed by its transformation to calcite. With the proposed models, the second article realized a range of experiments with a continuous reactor with the inlet supersaturation varying from 15.8 to 56.56, 1 to 12 minutes of residence time, and 100 to 1250 rpm of stirring speeds, and then fitted the experimental size distribution to obtain the kinetic rates, growth, nucleation, agglomeration and transformation for each condition based on the model's calculations. Then, the authors adjusted the appropriate kinetic parameters evaluating the kinetic rates variations within the studied variables, obtaining experimental correlations for variations for each precipitation regime.

At high $[Ca^{2+}]/[CO_3^{2-}]$ ratio values, close to 10, vaterite was precipitated. In contrast, at low values, SS up to 25, vaterite was homogeneously nucleated, gradually transforming to the more aggregating calcite with the reactor. In a specific supersaturation and ionic ratio range, close to 36 and 5, both calcite and vaterite were simultaneously nucleated heterogeneously. The particle size distributions in each regime are determined and fitted by the models of the companion paper (Chakraborty and Bhatia, 1996). In the regime of vaterite nucleation and transformation, the kinetic parameters for nucleation, growth, transformation, and agglomeration are well correlated by power-law models, as presented in Table 2.3. With two

different precipitation regimes, the first denominated LSS were those with mean particle size low about 1 μm, and high number density about 10^7 mL^{-1}, the second one denominated USS, the mean particle size was about 4-5 μm, relatively low number density of $5x10^4$ mL^{-1} at moderated supersaturations close to 20. With Table 2.3, the authors could observe that vaterite presented faster growth rates than vaterite in both regimes that calcite agglomerated much more strongly than vaterite, with the vaterite agglomerated kernel not presented statistical relevance with the parameter estimation. Besides that, it was concluded that different precipitation regimes could cause significant differences among the adjusted rates, affirming the importance of the experimental conditions determinations when discussing the kinetic rates.

Table 2.3 - Power Law Correlations for Growth, Nucleation, and Agglomeration rates.

LSS	**USS**
Nucleation rates [mL^{-1} min^{-1}]	**Nucleation rates [mL^{-1} min^{-1}]**
Calcite: $B_N = 1.52x10^{-2}\ SS^{7.77}$	Only vaterite was observed to nucleate
Vaterite: $B_N = 9.36\ SS^{6.55}$	Vaterite: $B_N = 7{,}960\ SS^{0.671}$
Growth rates [μm.min^{-1}]	**Growth rates [μm.min^{-1}]**
Calcite: $G_{calc} = 6.27x10^{-7}\ SS^{5.66}$	Calcite: $G_{calc} = 0.217\ SS^{0.474}$
Vaterite: $G_{vat} = 5.64x10^{-4}\ SS^{2.52}$	Vaterite: $G_{vat} = 0.106\ SS^{1.62}$
Agglomeration kernel [mL.min^{-1}]	**Transformation rate [min^{-1}]**
$\beta_{calc} = 6.52x10^{-8}\ SS^{0.43}$	$R_{vat\text{-}calc} = 4x10^{-8}\ SS^{7.38}$

Source: Adapted from Chakraborty and Bhatia (1996a)

Lassin *et al.* (2018) developed a kinetic model based on a transition-state-theory (TST)/surface-complexation-model (SCM) coupling. It aimed to describe the successive precipitation of amorphous calcium carbonate (ACC) and calcite, taking account of their mutual influence: ACC precipitates according to the standard transition state theory and creates surface complexation sites from which calcite can form and create new surface complexation sites. This model was first compared to the experiments of Gebauer *et al.* (2008), and then applied with a reactive transport calculation code to a dynamic experiment on a microfluidic device composed of a single straight channel based on Beuvier *et al.* (2015) experiments. Gebauer *et al.* (2008) experimental data and the model results for the same conditions, 10 $mmol.L^{-1}$ Na_2CO_3 aqueous solution, Cl^{1-} content being twice the total of Ca^{2+}, are compared in Figure 2.22. The results are given in moles of $Ca^{2+}_{(aq)}$ as a function of time during continuous addition of feed $CaCl_2$ solution. It was possible to see that the results are in a qualitative agreement with the

experimental data, with the shape of the concentration drop was correctly predicted by the kinetic model, being able to capture the sequence of Ca^{2+} transition and surface complexation mechanisms that Gebauer *et al.* (2008) observed in their experiments:

1. The growth of ACC;
2. The simultaneous creation of ACC surface complexation sites from which calcite starts to precipitate;
3. The calcite growth from ACC;
4. The creation of calcite surface complexation sites from which it can further precipitate (i.e., grow).

Figure 2.22 - Evolution of Ca^{2+} aqueous species content with time, at various pH values, for the experimental conditions investigated. The solid lines represent the experimental measurements, the short-dashed lines are the simulation results obtained in the study made by Lassin *et al.* (2018)

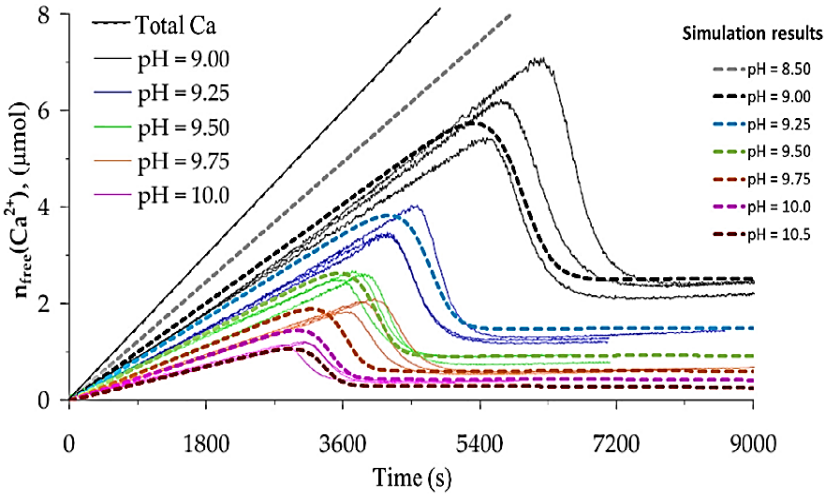

Source: Adapted from Gebauer *et al.* (2008)

The study also highlighted that simple geometrical configuration could provide information on the dynamics of chemical processes relevant to identifying critical steps in the successive transformations of $CaCO_{3(s)}$ polymorphs, especially in the continuous precipitation of calcium carbonate interacts with the pore walls.

Kitano (1962) studied the effects of various inorganic ions on the polymorphic crystallization of $CaCO_3$ from bicarbonate solutions. The authors observed that magnesium ions highly favored aragonite formation, with $MgCl_2$ being more favorable to aragonite production than $Mg(HCO_3)_2$ or $MgSO_4$ with calcium and bicarbonate concentrations of 353 ppm and the Magnesium salts ranging from 0 to 1313 ppm. It was noted that increasing in Sr^{2+}concentration

produced aragonite up to a maximum, at 2 ppm of strontium. However, when this cation was added as $SrCl_2$ ions, aragonite was inhibited, and calcite was favored. In these experiments, bicarbonate and calcium concentrations were close to 187 ppm, and Strontium salts concentration varied from 0 up to 250 ppm. The effect of Barium ions was also a function of its concentration with the presence of a small number of Ba^{2+} up to 48 ppm, favoring calcite formation. Whether higher concentrations favored vaterite, in these experiments, the bicarbonate and calcium concentration were close to 187 ppm, and the Barium salts concentration varied from 0 up to 250 ppm. Both $Sr^{2+}$and $Ba^{2+}$was always entrained in the calcium carbonate precipitates, regardless of their concentrations.

Chen and Neville (2004) studied the influence of Mg^{2+} on the kinetics and crystal morphology of calcium carbonate formation on both metal surfaces and bulk solutions. Scanning electron microscopy (SEM), Energy dispersive X-ray analysis (EDX), and Focused beam reflectance measurement (FBRM) were used to analyze the scale crystals. The effect of the Mg ion was evaluated in Mg/Ca ratios ranging from 0.1 to 0.5. It was observed that the Mg ion accelerates the crystal transformation from vaterite to calcite. With the increase in the Mg ratio, the amount of calcite increased to the point that with 600 ppm of Mg, calcite was the main polymorph that composed the crystal mass. It was also observed that the vaterite crystals formed in solutions with Mg presence increased the roughness of the vaterite particles. From 0 to 200 ppm, the chord length of the vaterite particles was about 10 μm, and the crystal surfaces were smooth; as for the 600 ppm, the length of vaterite particles was only 6 microns with a highly roughed surface. Two kinds of calcite crystals were formed on the metal surface. The first type is the perfect calcite crystal, and the second type is the distorted crystal. The perfect calcite is rhombohedral. For the distorted calcite crystals, the edge and the surface of the rhombohedral are distorted. All calcite crystals were perfect in 0 ppm Mg scale formation solution. With the increase of Mg concentration in the solution the percentage of the distorted calcite increases. All the calcite crystals are distorted in 600 ppm Mg scale formation solution, and no perfect calcite is observed. Also, the experiments showed that the ratio of Mg incorporated into the scale was proportional to the ratio of Mg and Ca in the bulk solution.

Rodriguez-Blanco *et al.* (2011) studied the effects of pH and Mg on the crystallization of amorphous calcium carbonate (ACC) to vaterite and calcite using a combination of in situ time-resolved synchrotron-based techniques and electron microscopy. ACC crystallization experiments were carried out at 10–25ºC by rapidly mixing, under constant and vigorous stirring, equal volumes of Na_2CO_3 1 M (pH = ∼11.2) and $CaCl_2/MgCl_2$ (pH = ∼6.7) solutions.

The experiments showed that Mg increased the stability of ACC and favored the formation of calcite over vaterite. A neutral (~7) starting pH during mixing promoted the transformation of ACC into calcite via a dissolution/reprecipitation mechanism. Conversely, when ACC formed in a solution that started with a high initial pH (~11.5), the transformation to calcite occurred via metastable vaterite, which formed via a spherulitic growth mechanism. In a second stage, this vaterite transformed to calcite via a surface-controlled dissolution and recrystallization mechanism.

Sanjiv *et al.* (2020) realized studies on the crystallization of calcium carbonate ions from $CaCl_2$ and Na_2CO_3 in Sr^{2+} and Ba^{2+} ions in concentrations at least 20 times higher than the more concentrated of Kitano (1962). It was observed that the Ba^{2+} promoted vaterite formation and that the Sr^{2+} presence increased aragonite production. It should be noted that Sanjiv *et al.* (2020) continued to observe aragonite favoring with the increase of Sr^{+2} by kinetic reasons linked with the concentration gradient of the Sr ions with the media. Although for the Ba^{2+}, the authors also observed that the vaterite production was favored with the increase in this ion concentration, as all concentrations evaluated were higher than 48 ppm. The authors proposed that as the reaction proceeds, the localized abundance of strontium and barium ions can create a possibility of forming respective carbonates, causing a delay in the calcium carbonate production and favoring the production of metastable phases.

2.4 FINAL CONSIDERATIONS REGARDING THE LITERATURE REVIEW

This topic aimed to provide a detailed review of the theoretical concepts that are involved in the formation of calcium carbonate solids from solutions that present variations in the pressure, temperature, and salinity conditions. Also to discuss some works from the literature that used these concepts to evaluate, thermodynamically or kinetically, the calcium carbonate formation in a range of experimental or theoretical conditions, such as the work of García *et al.* (2006) with high temperature and pressure, or the work of Gebauer *et al.* (2008) with standard temperature and pressure (more focused on mechanistic steps with calcium carbonate formation).

The thermodynamic aspect of the calcium carbonate formation presented two main focuses in the studies: the supersaturation calculation of the possible forms with the aqueous solutions conditions, as reported by Plummer *et al.* (1982), or even with a multiphase system,

as reported by Haarberg *et al.* (1992); and the energy profile of these forms to predict or observe an order of stability and possibly appearance, as stated by the step rule of Ostwald (1897), with the calcium carbonate solids in a range of conditions, as the works of Donnet *et al.* (2009) and Chang *et al.* (2017b).

The kinetic element of the calcium carbonate formation, as can be seen, is widely studied with many focuses: the evaluation of the individual rates with different conditions and polymorphs, as those of nucleation in Chien *et al.* (2007), growth and dissolution in Brečević and Kralj (2008). The rate-limiting steps of these kinetic rates as studied by Reis *et al.* (2016) and Shiraki and Brantley (1995), the polymorphic transformation among the calcium carbonate solids, its velocity and mechanisms as described by Rodriguez-Blanco *et al*. (2011) and Bots *et al.* (2012), or how it behaved among different phases and external ions, as reported by Kitano (1962), Natsi *et al.* (2016) and, Walker *et al.* (2017).

Thus, it was possible to observe that many factors act on a system to produce a calcium carbonate polymorph, such as the magnitude of supersaturation, temperature, pH, calcium and bicarbonate/carbonate ratio, CO_2 pressure, presence of external ions. Besides that, there is the influence of metastable forms that can act as intermediates in the formation of a more stable form, and their formation also depend in that factors, especially the water content, as studied by Du and Amstad (2019). Such complexity in the calcium carbonate formation underlying mechanisms is still not completely understood, despite the significant progress that these authors produced (LASSIN *et al.*, 2018; SANJIV RAJ; DEVI; SUBRAMANIAN, 2020).

This conclusion is also proper for calcium carbonate systems that operate at high temperatures, pressures, and salinity. Proportionally to the thermodynamic aspect, there are not many kinetic studies for this precipitation for industrial conditions; the supersaturation calculations tool is widely studied and validated for these conditions, although for the calcium carbonate pathway not so much. However, it should be noted that the difficulty in obtaining data extracted from high temperature, pressure, and salinity systems is a significant limitation on the quality of the thermodynamic and kinetic parameters (COSMO et al., 2019). Nevertheless, besides all these difficulties, it can be seen that there is a great interest and effort on the part of the researchers in the continuous elaboration of tools capable of adding a different approach or conclusion to this theme widely studied by engineers, chemists, and geologists (OLAJIRE, 2015; KAMAL et al., 2018).

Through the analysis of the current topic, summarized in some of the works presented in Table 2.4, it can be observed that there is scope for research in the present theme. The

development of a mathematical model that combines the understanding of solution equilibrium and the calcium carbonate polymorphism in a continuous or batch system can add to the present knowledge and appear like a valuable tool to study these phenomena in an interconnected way.

Table 2.4 - Summary of calcium carbonate studies discussed in the literature review. (Continues on next page)

Reference	Topic	Tool	Conditions
(HAARBERG; SELM; *et al.*, 1992)	Ionic solution equilibrium solution for $CaCO_3$, $CaSO_4$, $SrSO_4$ and $BaSO_4$	Solubility Model with P, T e Ionic Strength dependence obtained by fitting experimental data	Temperatures from 20 to 150ºC, pressures up to 400 atm and ionic strength up to 1,4 mol/kg
(COSMO, 2013)	Quantification of the content of calcite likely to precipitate in an aqueous solution of Ca^{2+}, HCO_3^{1-} and CO_2	Thermodynamical model obtained by an explicit equation, function of temperature and pressure, of the global equilibrium constant	Temperatures up to 100ºC, pressures up 100 bar and ionic strength up to 1 mol/kg
(KAWANO *et al.*, 2009)	Precipitation diagram of possible calcium carbonate solids formation based on solubility and surface energy calculations.	Equilibrium curves for the formation reaction of polymorphs of calcium carbonate (calcite, aragonite, vaterite, and amorphous calcium carbonate together with experiments)	Temperatures up to 80ºC, pressures up 1atm, 1-5 $mmol.L^{-1}$ of $CaCl_2$ and Na_2CO_3 concentrations and ionic strength up to 0.1 mol/kg
(GEBAUER; VÖLKEL; CÖLFEN, 2008)	Precipitation mechanism of calcium carbonate and specified complex crystal structures on nucleation considering the formation of metastable ion clusters.	Selective impedance electrodes to calcium and WAXS (wide angle x-ray scattering) measurements of experimental data to evaluate the superficial energy of calcium carbonate structures	Temperature of 25ºC, pH from 9 to 10, and supersaturations up to 5
(BLUE *et al.*, 2017)	Control the transformation of the ACC into crystalline polymorphs by manipulating the solution composition and evaluating the polymorphic response.	Mixed flow reactor crystallization batches with SEM, XRD, TGA and ICP-AES measurements	Ambient temperature, atmospheric pressure, and ionic strengths up to 1 mol/L with Mg^{2+} additions
(RAMSTAD *et al.*, 2005)	Determination of induction times and growth rates of calcium carbonate scaling with and without the presence of oil	Precipitation experiments in a scale cell that supports high pressures and temperatures and is connected to an optic system	Temperatures up to 200ºC, pressures up 700 bar and ionic strengths up to 1,5 mol/L

Reference	Topic	Tool	Conditions
(BREČEVIĆ; KRALJ, 2008)	Investigations of the conditions for formation, crystal growth, and dissolution of the $CaCO_3$ polymorphs	Precipitation experiments with seeded and unseeded batch crystallization of calcite and vaterite together with parameter rate adjustment fed by SEM, XDR, and FTIR measurements	Temperatures from 10ºC to 45ºC, calcium and carbonate concentrations of 2.5 x 10^{-3} $mol.L^{-1}$ and ionic strengths of 15 to 315 $mmol.L^{-1}$
(RODRIGUEZ-BLANCO; SHAW; BENNING, 2011)	Study of the kinetics and mechanism of calcium carbonate crystallization to calcite, via vaterite	Crystallizations were monitored using online and offline XRD and infrared spectroscopy. An empirical model to calculate the degree of calcite formation has also been proposed.	Temperatures up to 25ºC, atmospheric pressures and ionic strengths up to 2 mol/L
(NATSI; ROKIDI; KOUTSOUKOS, 2016)	Calcium carbonate formation in aqueous phase with or without an organic phase	Seeded or unseed batch experiments of nucleation and crystal growth with pH, atomic absorption spectroscopy, XRD, and SEM measurements	Temperatures up to 25ºC, ambient pressure and alkaline medium
(CHAKRABORTY; BHATIA, 1996b, 1996a)	Calcium carbonate precipitation populational modeling and kinetic rates evaluation	Population balance for $CaCO_3$ polymorphs discretized by the Hounslow method for aqueous precipitation of calcium carbonate together with continuous crystallization experiments measured by optical microscopy, XRD, and SEM.	Temperatures of 25ºC, inlet supersaturation varying from 15.8 to 56.56, 1 to 12 minutes of residence time, and 100 to 1250 rpm of stirring speeds
(KITANO, 1962)	The effects of inorganic ions on the polymorphic crystallization of calcium carbonate	Batch experiments from bicarbonate solutions varying or adding Magnesium, Barium, and Strontium ions measured by XRD, pH, and gravimetry.	Temperatures of 25ºC, calcium and bicarbonate concentrations up to 353 ppm and Magnesium, Barium, and Strontium salts concentrations up to 1313 and 250 ppm.

Source: Own authorship

3 PROPOSED MODEL

The model discussed in this thesis has two main sections. The first is a thermodynamic calculation determining the driving forces of the process, the supersaturation, and Gibbs free energy associated with formation of the solids. The second step combines the kinetic calculations, which seek to determine the rate at which nucleation, growth, agglomeration, and polymorphic transformation occur. Thus, with the association of both sections, it becomes possible to simulate the process, obtaining both the spontaneity and kinetic rates of reactions involved in the crystallization process.

3.1 THERMODYNAMIC MODEL

3.1.1 Activity and Fugacity calculation

Amongst the existing activity models able to describe highly concentrated aqueous systems and solid-liquid or gas-liquid equilibria, up to elevated temperatures and pressures, the semi-empirical Pitzer model has been shown to be robust and precise (HARVIE; MØLLER; WEARE, 1984; PITZER, 1991; LASSIN; ANDRÉ; LACH, 2017)

The activity calculations presented in Equations 3.1, 3.2 and 3.3, represent the solvent activity (water), the cation's coefficient activity ($ln\gamma_m$) and the anion's coefficient activity ($ln\gamma_x$) (HARVIE; MØLLER; WEARE, 1984). The cations and anions can be all ionic species present in the aqueous media, for example, the ions presented in Table 2.1 which compose the seawater.

$$ln\, a_{H2O} = -\frac{W}{1000}(\sum_i m_i)\,\phi \tag{3.1}$$

$$ln\gamma_m = z_m^2 F + \sum_a m_a(2\mathrm{B}_{ma} + Z\,C_{ma}) + \sum_c m_c(2\Phi_{mc} + \sum_a m_a \Psi_{Mca}) + \sum_a \sum_{a'} m_a m_{a'} \Psi_{aa'M} + |z_m| \sum_c \sum_a m_c m_a C_{ca} + \sum_n m_n\,(2\lambda_{nm}) \tag{3.2}$$

$$ln\gamma_x = z_x^2 F + \sum_a m_a(2\mathrm{B}_{cx} + Z\,C_{cx}) + \sum_a m_a(2\Phi_{xa} + \sum_c m_c \Psi_{xac}) + \sum_a \sum_{c'} m_c m_{c'} \Psi_{cc'X} + |z_x| \sum_c \sum_a m_c m_a C_{ca} + \sum_n m_n\,(2\lambda_{nx}) \tag{3.3}$$

In Equation 3.1, W is the molecular weight of water and the sum represents the summation among all solutes in solution. There is also the osmotic coefficient, ϕ, which can be calculated with Equation 3.4.

$$\sum_i m_i(\phi - 1) = 2\left(\frac{-A^{\Phi} I^{\frac{3}{2}}}{1+1.2\, I^{\frac{1}{2}}}\right) + \sum_c \sum_a m_c m_a \left(B_{ca}^{\phi} + Z\, C_{ca}\right) + \sum_m \sum_c m_c m_m (\Phi_{mc}^{\phi} + \sum_a m_a \Psi_{mca}) + \sum_x \sum_a m_a m_x (\Phi_{xa}^{\phi} + \sum_c m_c \Psi_{xac}) + \sum_n \sum_a m_n m_a \lambda_{na} + \sum_n \sum_c m_n m_c \lambda_{nc} \quad (3.4)$$

In the equations above, m_c and z_c are the molality and charge of cation c. The summations with index c represent the total number of cations. Similar definitions apply for anions, a, and neutral species, n. The subscripts m, x, and n also refer to cations, anions, and neutrals.

The neutral species terms include new parameters, λ, which account for the interactions between neutral species and ionic species in the solution (PITZER, 1991). In the carbonate system, the inclusion of neutral species (e.g., $CO_{2\,(aq)}$) is required to describe observed solution behavior. Equation 3.5 presents the natural logarithm calculation of the activity coefficient for neutral species.

$$ln\gamma_n = \sum_c m_c\, (2\lambda_{nc}) + \sum_a m_a\, (2\lambda_{na}) \quad (3.5)$$

With the equations for the activity calculations presented for all species, what remains is to define the remaining parameters A^{ϕ}, F, Z, C, B, Φ, and Ψ.

Pitzer defines A^{ϕ} to be equal to the Debye-Hückel's constant, but with the first term replaced by 1/3, as presented in Equation 3.6.

$$A^{\Phi} = \frac{1}{3}\frac{e}{\sqrt{D\, k_b\, T}}^{3} \sqrt{\frac{2\,\pi\, N_0\, \rho_W}{1000}} \quad (3.6)$$

Where *e* is the absolute electronic charge, D the static dielectric constant of pure water, T the temperature in Kelvin, N_0 the Avogadro's number, ρ_w the specific mass of water, and k_b the Boltzmann's constant.

As for F, C_{mx}, and Z calculation, Equations 3.7-3.9 are presented.

$$F = -A^{\Phi}\left(\frac{I^{\frac{1}{2}}}{1+1.2\, I^{\frac{1}{2}}} + \frac{2}{1.2}\ln\left(1 + 1.2\, I^{\frac{1}{2}}\right)\right) + \sum_c \sum_a m_c m_a B'_{ca} + \sum_c \sum_m m_c m_m \Phi'_{mc} + \sum_a \sum_x m_a m_x \Phi'_{ax} \quad (3.7)$$

$$C_{mx} = \frac{C_{mx}^{\phi}}{2} |z_m z_x|^{1/2} \quad (3.8)$$

$$Z = \sum_i |z_i| m_i \tag{3.9}$$

The second virial coefficient for opposite charges, B, that appear in Equations 3.2-3.4 can be calculated by the following ionic strength dependences (Equations 3.6-3.10).

$$B_{ca}^{\phi} = \beta_{ca}^{(0)} + \beta_{ca}^{(1)} e^{-\alpha_{ca}\sqrt{I}} + \beta_{ca}^{(2)} e^{-12\sqrt{I}} \tag{3.6}$$

$$B_{ca} = \beta_{ca}^{(0)} + \beta_{ca}^{(1)} g(\alpha_{ca}\sqrt{I}) + \beta_{ca}^{(2)} g(12\sqrt{I}) \tag{3.7}$$

$$B'_{ca} = \beta_{ca}^{(1)} \frac{g'(\alpha_{ca}\sqrt{I})}{I} + \beta_{ca}^{(2)} \frac{g'(12\sqrt{I})}{I} \tag{3.8}$$

The functions, g and g', are defined in Equations 3.9-3.10.

$$g(x) = \frac{2(1-(1+x)e^{-x})}{x^2} \tag{3.9}$$

$$g'(x) = \frac{-2(1-(1+x+\frac{x^2}{2})e^{-x})}{x^2} \tag{3.10}$$

With x = $\alpha_{ca}\sqrt{I}$ or $12\sqrt{I}$. When either cation C or anion A present a univalent charge $\alpha_{ca} = 2$. For higher valence pairs $\alpha_{ca} = 1.4$.

The parameters Φ and ψ are for aqueous mixtures of ionic salts, with Φ accounting for cation-cation and anion-anion interactions and ψ accounting for cation-cation-anion and anion-anion-cation interactions. These two parameters were neglected from calculations as the relevant parameters for the ions in our system could not be found. The complete set of parameters necessary for the calculation of the non-ideal behavior of the solution are: $\beta_{ca}^{(0)}$, $\beta_{ca}^{(1)}$, $\beta_{ca}^{(2)}$ and $C_{ca}^{(\phi)}$ for each cation-anion pair; and λ_{nc} for each ion-neutral pair interaction. For the activity calculation of the the species discussed in Table 2.1, the necessary Pitzer parameters are presented in APPENDIX A – Table A1.

With the relation obtained in Equation 2.14, it is possible to calculate the gas solubility based on the activities and fugacities calculations by using the methodology of Duan and Sun (2003, 2006). For simplicity, it is assumed that only CO_2 and H_2O can be present in the vapor phase. As can be seen in Equation 2.14, only the difference between the standard chemical potential in the liquid and vapor phase need to be calculated. Thus, for simplicity, the $\mu_{CO_2}^{v(0)}$ was set to zero by Duan and Sun (2003). The authors also assumed that the water vapor pressure,

P_{H_2O}, in the mixture CO_2-H_2O is the same as pure water saturation pressure. Thus, allowing the calculation of CO_2 molar fraction in the vapor with Equation 3.11.

$$y_{CO_2} = \frac{(P - P_{H_2O})}{P} \tag{3.11}$$

The water pressure is taken from the steam tables of Haar *et al.* (1984). The CO_2 coefficient activity was obtained from a Pizter semi-empirical equation, substituting the neutral Pitzer equation in Equation 2.14, one can obtain Equation 3.12.

$$\ln \frac{y_{CO_2} P}{m_{CO_2}} = \frac{\mu_{CO_2}^{l(0)}}{RT} - ln\varphi_{CO2} + \sum_c m_c \, (2\lambda_{CO2-c}) + \sum_a m_a \, (2\lambda_{CO2-a}) + \sum_c \sum_a \xi_{CO2-a-c} m_c m_a \tag{3.12}$$

In this equation, Duan e Sun (2003) observed that λ, ξ and $\mu_{CO_2}^{l(0)}$ are dependent on the temperature and total pressure and proposed that those parameters can be represented by an empirical equation adjusted from experimental data collected in the literature.

For the CO_2 fugacity coefficient calculation, Duan *et al.* (2006) proposed that this parameter could also be calculated as a function of temperature and pressure, as an alternative to the time-consuming calculation of the fifth-order virial equation. The resulting equations to calculate the dioxide carbon solubility for a temperature-pressure-ionic range of 273 to 533 K, 0 to 2000 bar, and 0 up to 4.5 mol.L^{-1} is shown in Equation 3.13-3.15.

$$\ln m_{CO2} = ln y_{CO2} \varphi_{CO2} P - \frac{\mu_{CO_2}^{l(0)}}{RT} - 2\lambda_{CO2-Na} \sum_c z_c m_c - \sum_a m_a \, (2\lambda_{CO2-a}) - \xi_{CO2-Na-Cl} m_{Cl} \sum_c m_c + 0.07 m_{SO_4} \tag{3.13}$$

$$\frac{\mu_{CO_2}^{l(0)}}{RT}, \lambda_{CO2-Na} \; or \; \xi_{CO2-Na-Cl} = c_1 + c_2 T + \frac{c_3}{T} + c_4 T^2 + \frac{c_5}{630-T} + c_6 P + c_7 P \, lnT + \frac{c_8 P}{T} + \frac{c_9 P}{630-T} + \frac{c_{10} P^2}{(630-T)^2} + c_{11} T lnP \tag{3.14}$$

$$\varphi_{CO2} = c_1 + \left(c_2 + c_3 T + \frac{c_4}{T} + \frac{c_5}{T-150}\right) P + \left(c_6 + c_7 T + \frac{c_8}{T}\right) P^2 + (c_9 + c_{10} T + \frac{c_{11}}{T}) lnP + \frac{(c_{12} + c_{13} T)}{P} + \frac{c_{14}}{T} + c_{15} T^2) \tag{3.15}$$

With T in Kelvin and P in bar. The parameters c1, c2… c11 for Equation 3.14 and the parameters for Equation 3.15 are presented in APPENDIX A – Table A2 and A3.

3.1.2 Supersaturation calculation

3.1.2.1 Open systems

The supersaturation (SS), which represents how far the system is from the chemical equilibrium, was calculated using Equation 3.16.

$$SS = \frac{a_{Ca^{2+}} \quad a_{CO_3^{2-}}}{K_{sp}} \tag{3.16}$$

The solubility constants for calcium carbonate (K_{sp}) were obtained from Plummer and Busenberg (1982) for the three possible crystalline polymorphs, calcite, aragonite, and vaterite (Equations 3.17-3.19).

$$logK_{spc} = -171.9065 - 0.077993\,T + \frac{2839.319}{T} + 71.595\log T \tag{3.17}$$

$$logK_{spa} = -171.9773 - 0.077993\,T + \frac{2903.293}{T} + 71.595\log T \tag{3.18}$$

$$logK_{spv} = -172.1295 - 0.077993\,T + \frac{3074.688}{T} + 71.595\log T \tag{3.19}$$

In cases where only the ions responsible for the calcium carbonate formation were present in the solution, the ionic concentrations were calculated with three additional equilibrium reactions: bicarbonate formation (K_1), bicarbonate dissociation (K_2), and water dissociation (K_W) (Equations 3.20-3.22). It should be noted that the CO_2 dissolved, calculated with equations 3.13-3.15, in water is also included in the calculations, as it influences the bicarbonate formation. The bicarbonate equations were also obtained from Plummer, and Busenberg (1982), valid to a range of 0-100ºC and 1 atm, and water dissociation constant was calculated by a correlation of Marshall and Franck (1981), valid from 0-1,000ºC and 1-10,000 bar.

$$logK_1 = -359.3094 - 0.06092\,T + \frac{21{,}834.37}{T} + 126.8839\log T - \frac{1{,}684{,}915}{T^2} \tag{3.20}$$

$$logK_2 = -107.8871 - 0.032528\,T + \frac{5{,}151.79}{T} + 38.92561\log T - \frac{563{,}713.9}{T^2} \tag{3.21}$$

$$K_w = -4.098 - \frac{3{,}245.2}{T} + \frac{223{,}620}{T^2} - \frac{39{,}840}{T^3} + (13{,}957 - \frac{1{,}262.3}{T} + \frac{856{,}41}{T^2})\rho_w \quad (3.22)$$

As can be seen, it is necessary to know the specific mass of the solvent, water, to calculate its dissociation constant. Thus, the equations proposed by Chen *et al*. (1977), valid up to 100ºC and 1,000 atm, were used to determine the specific mass of water at 1 atm and any temperature with the range (Equation 3.24) and to consider the pressure effect with this parameter (Equation 3.23-3.28). With T_c and P_a being the temperature in Celsius and the absolute pressure in atm.

$$\rho_{H_2o}(T_c) = 0.99983952 + 6.78826\ x\ 10^{-5}T_c - 9.08659\ x\ 10^{-6}T_c^2 + -1.02213\ x\ 10^{-7}T_c^3 - 1.35439\ x\ 10^{-9}T_c^4 + 1.47115\ x\ 10^{-11}T_c^5 - 1.11663\ x\ 10^{-13}T_c^6 + 5.04407\ x\ 10^{-16}T_c^7 - 1.00659\ x\ 10^{-18}T_c^8 \quad (3.23)$$

$$\rho_{H_2o}(P_a, T_c) = \frac{\rho_{H_2o}(T_c)}{1 - \frac{1.01325(P_a - 1)}{k_w}} \quad (3.24)$$

$$k_w = k'_w + 1.01325A'(P_a - 1) + 1.01325^2B'(P_a - 1)^2 \quad (3.25)$$

$$k'_w = 19{,}652.17 + 148.183T_c - 2.3T_c^2 + 0.01281\ T_c^3 - 4.91564\ x\ 10^{-5}T_c^4 + 1.0355310\ x\ 10^{-7}T_c^5 \quad (3.26)$$

$$A' = 3.26138 + 5.223\ x\ 10^{-4}T_c + 1.324\ x\ 10^{-4}\ T_c^2 - 7.655x\ 10^{-7}\ T_c^3 + 8.584\ x\ 10^{-10}T_c^4 \quad (3.27)$$

$$B' = 7.2061\ x\ 10^{-5} - 5.8948\ x\ 10^{-6}T_c + 8.699\ x\ 10^{-8}\ T_c^2 - 1.01x\ 10^{-9}\ T_c^3 + 4.322\ x\ 10^{-12}T_c^4 \quad (3.28)$$

When the specific mass of the solvent is defined, it is possible to do all model calculations with a molality base instead of molarity. This allows a more precise calculation as the changes with the volume of reaction along the variations of temperature and pressure are captured by the specific mass modeling.

As more ions are added, the solubility constants for each possible solid and its dissociation reaction were added to the calculations. To determine whether precipitation or dissolution is required to decrease the system's Gibbs energy, the supersaturation of each possible solid is calculated. If the supersaturation of the specific solid is higher than one, the water is supersaturated, and precipitation of the solid is likely to occur. If SS< 1, dissolution will occur if the mineral is present in its solid state (HAARBERG; SELM; *et al.*, 1992, MYASNIKOV; CHIPRYAKOVA; KULOV, 2013).

As these calculations were made for open systems at 1 atm, there was no need to use the van't Hoff equations to calculate the pressure influence on the equilibrium constants.

3.1.2.2 CLOSED SYSTEMS

In closed carbonate systems, the presence of CO_2 can highly influence reactions in which it is involved because high pressures solubilize dioxide carbon in both water and oil phases (COSMO *et al.*, 2019). The flow of these fluids often occurs during industrial applications. The possible depressurization can promote CO_2 release from the solution, unbalancing the system and favoring the formation of carbonate salts, as discussed in section 2.1.1. Thus, regarding those closed systems, the methodology by Cosmo (2013) was used to calculate the global equilibrium constant, K_{eq}, representing the whole formation of this salt by combining the equilibrium steps associated with its formation. For clarity, the equation of this reaction (Equation 2.35) is show below.

$$Ca^{2+}{}_{(aq)} + 2HCO^{1-}{}_{3(aq)} \leftrightharpoons CaCO_{3(s)} + H_2O_{(l)} + CO_{2(aq)} \tag{2.35}$$

The computation of solution supersaturation associated with K_{eq} is shown in Equation 3.29.

$$SS = \frac{a_{Ca^{2+}}\, a_{HCO_3^{2-}}{}^2}{K_{eq}\, a_{CO_2}\, a_{H_2O}} \tag{3.29}$$

It can be noted that Equation 3.29 also considers that the evaporation of water that can occur with the changes of the fluid temperature and pressures conditions causes an increase in supersaturation and will favor calcium carbonate formation. With this methodology is not necessary to solve the whole species equilibrium, as in the open system, only is necessary to

evaluate the calcium, bicarbonate and dioxide carbon concentrations, calculated with mass of salt formed and with equations 3.13-3.15, based on the informed initial values.

Equation 3.30 was used to calculate the global equilibrium constant with the standard conditions of 25ºC and 1 atm. With $-\Delta G_r^0$ representing the standard change in Gibbs free energy associated with the calcium carbonate formation by this global equilibrium.

$$\ln K_{eq} = \frac{-\Delta G_r^0}{RT} \tag{3.30}$$

To calculate the influence of the pressure and temperature with the global equilibrium constant, the extended forms of van't Hoff equations (Equations 3.31 and 3.32) were used for each possible polymorph.

Equation 3.31 is the integrated form of Equation 2.7; which considers that heat capacity and enthalpy variations are constants with the temperature changes (COSMO, 2013). Equation 3.32 is an equation developed by Aggarwal *et al.* (1990) that considers the effects of the pressure on the molar volume of the species by calculating the compressibility of the water for each studied pressure, representing the integrated form of Equation 2.8. This equation relies on more easily calculated parameters, as the molar compressibility of all the ionic species present in the aqueous system would be difficult to obtain (COSMO, 2013).

$$logK_{eq,T} = logK_{eqref} + \frac{\Delta H_r^0}{R\ ln10}\left[\frac{1}{T_{ref}} - \frac{1}{\mathrm{T}}\right] + \frac{\Delta Cp_r^0}{R}\left[\frac{1}{ln10}\left(\frac{T_{ref}}{\mathrm{T}} - 1\right) - log\frac{T_{ref}}{\mathrm{T}}\right] \tag{3.31}$$

$$ln\left(\frac{K_{eq_P}}{Keq_{ref}}\right) = -\left(\frac{\Delta V_r^0}{RT_K k_{H2O,ref}^T}\right) ln\frac{\rho_{H2O(P)}}{\rho_{H2O(ref)}} \tag{3.32}$$

With Keq_{ref} representing the equilibrium constant at the 25ºC and 1 atm, ΔH_r^0 being the standard enthalpy of the calcium carbonate formation, ΔCp_r^0 is the standard heat capacity of the calcium carbonate formation, R is the universal gas constant, T_{ref} and T represent the reference temperature and temperature. As for Equation 3.30, Keq_{ref} represents the equilibrium constant at 1 atm and a fixed temperature between 0 and 100ºC, ΔV_r^0 the standard molar volume of calcium carbonate formation, $k_{H2O,ref}^T$ the isothermal compressibility of water and ρ_{H2O} the specific mass of water at determined pressure and temperature.

The isothermal compressibility of water calculation was made with Equation 3.33, also proposed by Chen *et al.* (1977). The parameters k_w, k'_w, A' and B' were obtained from Equations 3.25-3.28.

$$k_{H2O}^{T}(P_a, T_c) = \frac{k'_w - 1.01325B'(P_a-1)^2}{k_w(k_w - 1.01325(P_a-1)} \quad (3.33)$$

3.2 KINETIC MODEL

3.2.1 Populacional balance

The basis of a population balance model is that the number of entities with some property in a system is a balanceable quantity. This framework considers space as the physical one and any essential system property, which changes due to the system intrinsic mechanisms and external influences. The state vector coordinates refer to spatial coordinates denoted as external coordinates concerning the physical space. The coordinates corresponding to the entities properties, internal coordinates, are associated with size, mass, age, or any other relevant characteristic of the particulate (COLLIER; HOUNSLOW, 1999; COSTA; MACIEL; FILHO, 2007; RAMKRISHNA; SINGH, 2014; RASMUSSON *et al.*, 2014). These characteristics established the populational balance mathematic framework as robust approach to deal with the complex crystallization kinetics, as those of calcium carbonate kinetics with its particulate system (CHAKRABORTY; BHATIA, 1996a; COSTA; MACIEL; FILHO, 2007; IGGLAND; MAZZOTTI, 2012; RAMKRISHNA; SINGH, 2014; RASMUSSON et al., 2014).

To obtain a representative populational balance, let be defined a population of crystals flowing in a tubular region (Figure 3.1). The crystals are characterized, at time t, at position x, and their length l. They supposedly can grow, disappear, clump together with another particle and appear from the nucleation or agglomeration of smaller particles.

Figure 3.1 - Flow of crystals in a tubular region.

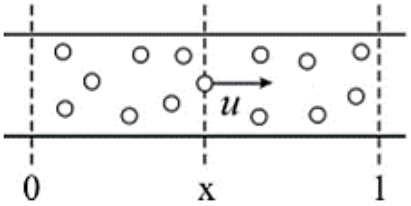

Source: Adapted from Rasmusson *et al.* (2014)

Considering a control surface Δx Δl (Figure 3.2), it can be defined:

- f (x, l, t) ΔxΔl representing the number of crystals with the range l, l+Δl, and x, x+Δx;
- G(x ,l, t) = G^+- G^- be the net generation of crystals, where G^+ represents birth and G^- represents death;
- ν (=dl/dt) be the growth rate of an individual crystal in a uniform medium of constant composition;
- u (=dx/dt) represents an individual crystal axial velocity in a uniform medium.

Figure 3.2 - Base control surface for population balance.

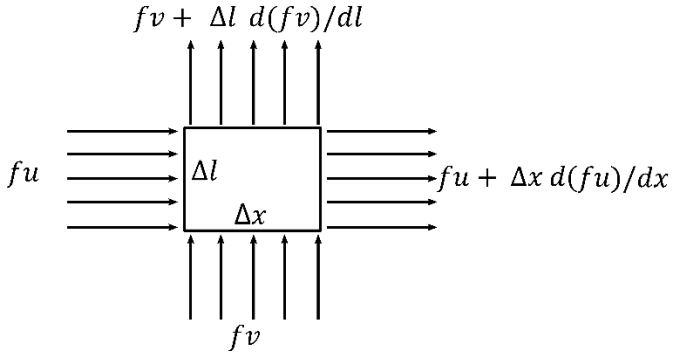

Source: Adapted from *Rasmusson et al.* (2014)

Thus, the mass balance for the crystals in space x, length l, and time t is represented by Equation 3.34:

Accumulation = net "growth" + net "inflow" + net "generation"

$$\Delta f \Delta l \Delta x = [(fv)|_m - (fv)|_{l+\Delta l}]\Delta x \Delta t + [(fu)|_x - (fu)|_{x+\Delta x}]\Delta l \Delta t + G\Delta l \Delta x \Delta t \qquad (3.34)$$

Dividing 3.34 by $\Delta l \Delta x \Delta t$ e and taking the limit $\Delta l \Delta x \Delta t \rightarrow 0$, we obtain Equation 3.35:

$$\frac{\partial f}{\partial t} = \frac{-\partial(fv)}{\partial m} - \frac{\partial(fu)}{\partial x} + G \qquad (3.35)$$

It is noteworthy that this equation can be generalized to three dimensions x, y, z, replacing the term in space by the divergence of the product of the number of crystals by the velocity in the direction of interest, that is $\nabla \cdot (f\,\vec{u})$. In this balance, it was considered that the particle velocity is equal to the fluid velocity. When this assumption is not valid, a momentum

balance must be included in both the fluid and the particle to describe the differences between the velocity fields.

The balance above only represents the number of crystals locally, only on the defined control surface. It is convenient to define a macroscopic balance using the average properties over the entire physical space, the inlet and outlet streams, defined in Equation 3.36-3.38.

$$\overline{f} = \frac{1}{V}\iiint_0^V f dV \tag{3.36}$$

$$Q_{ent}f_{ent} = \iint ufdS \tag{3.37}$$

$$Q_{out}f_{out} = \iint ufdS \tag{3.38}$$

Integrating Equation 3.35 over space and dividing by V and applying the Gauss divergence theorem yields Equation 3.39:

$$\frac{1}{V}\frac{\partial(\overline{f}V)}{\partial t} = \frac{-\partial(\overline{f}v)}{\partial m} - \frac{1}{V}(Q_{sai}f_{sai} - Q_{ent}f_{ent}) + G_{av} \tag{3.39}$$

If the size distribution is not uniform in the control volume, it is more interesting to evaluate the local balance in a grid defined in x, y, z intervals for a better evaluation of the population balance (RASMUSSON *et al*., 2014).

Equation 3.39 represents a non-linear hyperbolic differential equation with a complex analytical resolution. In most cases it is impossible, thus requiring efficient numerical techniques for its solution and subsequent use as a prediction tool (COSTA; MACIEL; FILHO, 2007).

3.2.2 Method of classes

There are several methods in the literature to solve hyperbolic differential equations. Costa *et al.* (2007) reviewed studies on methods that can be used to solve population balances in crystallizers. One of the highlighted methods is the method of classes, proposed by Marchal *et al.* (1988), which can be applied to a generalized case with agglomeration and growth depending on the crystal size, characteristics present in the calcium carbonate system

(RODRIGUEZ-BLANCO; SHAW; BENNING, 2011; WALKER; MARZEC; NUDELMAN, 2017). The method of classes discretizes the crystal size domain in a grid, generating classes of size L_i, thus transforming the partial differential equation into an ordinary differential equation, dependent only on time based on the consideration of perfect mixing in the volume of control.

Defining as L_0 the smallest size class that is the size of the crystal produced by nucleation and Ln the largest possible crystal from which there is no further growth, one can define the grid as L = [L_0 .... L_n]. These sizes define n classes, each one defined as C_i, where the size range of class C_i is between $\Delta C_i = L_i - L_{i-1}$ and the characteristic size of this class is represented by $S_i = (\frac{L_{i-1}+L_i}{2})$.

From this discretization, N_i (t) can be defined in Equation 3.40 as the number of crystals in class C_i at time t per volume of suspension:

$$N_i(t) = \int_{L_{i-1}}^{L_i} \bar{f} dL \tag{3.40}$$

Integrating Equation 3.40 from the knowledge of $\bar{f}$ obtained in Equation 3.39 and defining the crystal size l as a measure of crystal length. For a flowing system, we obtain Equation 3.41:

$$\frac{dN_i}{dt} + \frac{1}{V}\frac{dV}{dt}N_i + \left[\nu(L_i)\bar{f}(L_i) - \nu(L_{i-1})\bar{f}(L_{i-1})\right] + \frac{Q_s N_i - Q_e N_{i,e}}{V} = \overline{G_i} \tag{3.41}$$

Defining $\bar{G}_i$ as $\overline{G_i} = R_{N,i} + R_{A,i} - R_{D,i} + R_{trans,i}$, nucleation, appearance, and disappearance by agglomeration, and polymorphic transition rates can be defined, respectively in Equations 3.42-3.45:

$$R_{N,i} = r_n \; with \; i = 1, as \; only \; the \; first \; class \; nucleates \tag{3.42}$$

$$R_{A,i} = \int_{L_{i-1}}^{L_i} r_a \, dL \tag{3.43}$$

$$R_{Di} = \int_{L_{i-1}}^{L_i} r_D \, dL \tag{3.44}$$

$$R_{trans,i} = \int_{L_{i-1}}^{L_i} r_t \, dL \tag{3.45}$$

As can be seen in Equation 3.41, it is necessary to obtain the value of $\bar{f}$ in class C_i. To resolve that, it can be assumed that $\bar{f}$ has a constant value Φ_i with the size range of class C_i, and that value of $\bar{f}$ at the L_i is the arithmetic mean of Φ_i and Φ_{i+1}. To facilitate the understanding of these considerations Figure 3.3 is presented, which elucidates the discretization of $\bar{f}$ as a function of L.

Figure 3.3 - Discretization of the number density function with the classes.

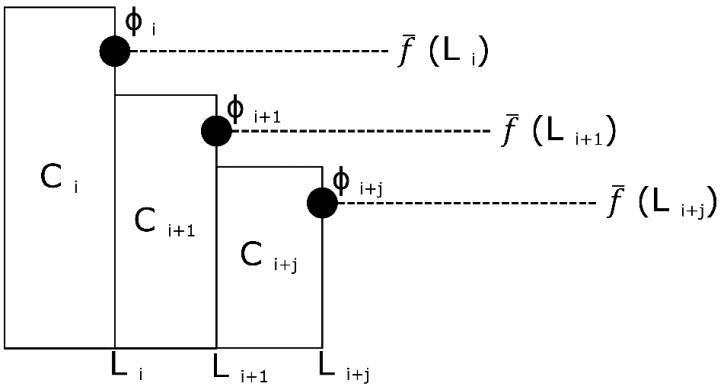

Source: Own authorship

From the discretization and the consideration that are no volumes changes with time, Equation 3.41 can be rewritten for three class categories, the first with index 1, representing the crystals within the first class size, the intermediate ones and the last with index N_c, representing the crystals within the last class size; obtaining the Equations 3.46-3.48, for growing crystals, that are supersaturated in relation with the solution, and Equations 3.49-3.51 for dissolving crystals, that are undersaturated in relation with the solution.

Growing crystals

$$\frac{dN_1}{dt} = -\frac{N_2}{2*w_2}\nu(L_1) - \frac{N_1}{2*w_1}\nu(L_1) + R_n - R_{Di} + R_{trans} + \frac{Q_S N_1 - Q_e N_{1,e}}{V} \tag{3.46}$$

$$\frac{dN_i}{dt} = -\frac{N_{i+1}}{2*w_{i+1}}\nu(L_i) + \frac{N_{i-1}}{2*w_{i-1}}\nu(L_{i-1}) + \frac{N_i}{2\,w_i}\nu(L_{i-1}) - \nu(L_i) + R_{A,i} - R_{D,i} + R_{trans} + \frac{Q_S N_i - Q_e N_{i,e}}{V} \tag{3.47}$$

$$\frac{dN_{nc}}{dt} = \frac{N_{nc-1}}{2*w_{nc-1}}\nu(L_{nc-1}) + \frac{N_{nc}}{2*w_{nc}}\nu(L_{nc-1}) + R_{A,nc} + R_{trans} + \frac{Q_S N_{nc} - Q_e N_{nc,e}}{V} \tag{3.48}$$

Dissolving crystals

$$\frac{dN_1}{dt} = -\frac{N_1}{2*w_1}\mathrm{D}(L_1) - \frac{N_2}{2*w_2}\mathrm{D}(L_1) + \frac{N_2}{2*w_2}\mathrm{D}(L_2) + \frac{N_3}{2*w_3}\mathrm{D}(L_2) - R_{Di} + \frac{Q_S N_1 - Q_e N_{1,e}}{V} \quad (3.49)$$

$$\frac{dN_i}{dt} = \frac{N_{i+1}}{2*w_i+1}\mathrm{D}(L_i) - \frac{N_{i-1}}{2*w_{i-1}}\mathrm{D}(L_{i+1}) - \frac{N_i}{2\,w_i}\mathrm{D}(L_{i-1}) - \mathrm{D}(L_i) + R_{A,i} - R_{D,i} + \frac{Q_S N_i - Q_e N_{i,e}}{V} \quad (3.50)$$

$$\frac{dN_{nc}}{dt} = -\frac{N_{nc-1}}{2*w_{nc-1}}\nu(L_{nc-1}) - \frac{N_{nc}}{2*w_{nc}}\nu(L_{nc-1}) + R_{A,nc} + \frac{Q_S N_{nc} - Q_e N_{nc,e}}{V} \quad (3.51)$$

With ordinary differential equations defined, the nucleation, growth, dissolution, agglomeration rates must be defined to solve the system numerically. Although more fundamental theories exist, such as the Volmer theory of nucleation or the Burton-Cabrera-Franck theory of growth, it is more common to use a power-law-like model for the rates calculations (GARSIDE, 1985; CHAKRABORTY; BHATIA, 1996a; TRAMPUŽ; TESLIĆ; LIKOZAR, 2019). Accordingly, in the present work, it was considered appropriate to use such an empirical approach in interpreting the nucleation, growth, agglomeration, and transformation parameters for fits of cumulative over size number density data in the experimental conditions that will be presented in section 4.4.

3.3 STEP RULE CALCULATION

The precipitation of calcium carbonate can involve more than one polymorph. Thus, the polymorphism present in that crystal requires the formulation of more than one population balance. Besides that, as the calcium carbonate is known to present an example of the already discussed heuristic rule of Ostwald-Lussac, it is necessary to define the order of stability that the solids phases may present and with it define the multistep phase transition that may occur during crystallization. The change in Gibbs free energy caused by forming a polymorph with size L, representing its thermodynamic stability, can be obtained with Equation 3.52.

$$\Delta G_{ex}(\tilde{n}, SS) = -\frac{3}{2}\frac{k_v\, R\, T}{N_a}\ln(SS)\; L^2 + \frac{2\,\gamma\, k_a\, V_m}{N_a}\; L \quad (3.52)$$

With the calculations of Equation 3.52, it is possible to define the less stable form that will appear first and then subsequently transform into a more stable phase, following a similar pattern as shown in Figure 2.7.

3.4 KINETIC RATES

The nucleation rate (Rn), which only applies in the balance for the first class, is calculated by Equation 3.53. A parameter that includes the total mass of crystals is also included to capture the secondary nucleation influence on the appearance of new solids. The nucleation rate is set to zero when the solid supersaturation becomes less than 1. It should be noted that the proposed nucleation rate represents the appearance of crystals with a size small or equal to the first size class; that is if the first size the equipment was able to measure is much larger than the critical size, these rates can englobe the formation of crystal in the critical size, its growth, and polymorphic transformation (GEBAUER; VÖLKEL; CÖLFEN, 2008; D.U.; AMSTAD, 2019). In Equation 3.53, k_n represents the kinetic constant of nucleation, m_{cr} is the crystal mass, n1 is the secondary nucleation parameters, V_{sol} is the solution volume and n represents the influence of the supersaturation in the nucleation.

$$R_n = k_n {m_{cr}}^{n1} V_{sol} (SS - 1)^n \tag{3.53}$$

The growth rate for each size class ($\nu_{(i)}$) is calculated by Equation 3.54, which uses a size-dependent growth rate incorporating the size influence in the crystal solubility by using an adaptation of Equation 2.45. Besides that, a two-step mechanism is present consisting of the solution mass transfer to the solid-liquid interface and its mass integration to the crystal structure (DONNET; BOWEN; LEMAÎTRE, 2009; VETTER *et al.*, 2013b; TRAMPUŽ; TESLIĆ; LIKOZAR, 2019).

$$\nu_{(i)} = \frac{k_a k_g \rho_{sol} \eta_i}{3\, \rho_{cr} k_v} \left(SS - \exp\left(\frac{\alpha}{L}\right)\right)^g \tag{3.54}$$

Where k_g represents the kinetic constant of growth, k_a is the area shape factor, ρ_{sol} is the solution specific mass, k_v is the volume shape factor and ρ_{sol} is the crystal specific mass. The term η_i represents the crystalline external effectiveness factor, calculated for each class according to Equation (3.55).

$$\eta_i = (1 - \frac{k_g}{k_{d,i}}\left(SS - \exp\left(\frac{\alpha}{L}\right)\right)^{g-1} \eta_i)^g \quad (3.55)$$

Equation 3.56 represents the Froessling Equation used to calculate the convective mass transfer coefficient for each class ($k_{d,i}$), with the respective characteristic length associated with the polymorph crystalline habit.

$$k_{d,i} = \frac{D_{ff}}{L_{ci}}\left(2 + 1.10\ Re_{p,i}^{\frac{1}{2}} Sc^{\frac{1}{3}}\right) \quad (3.56)$$

With D*ff* for the diffusion ions calculated from the Nernst-Einstein (BREČEVIĆ; KRALJ, 2008; ZEEBE, 2011), the Reynolds' number, calculated based on the crystal length, for the flow over the particle and Sc the Schmidt's number were calculated from the correlations presented by Trampuž et al. (2019). When the solid no longer shows supersaturation concerning the medium, i.e., it has a size smaller than the critical stability size, the phenomenon of dissolution takes place. Size-dependent crystal dissolution may be written on an equal basis as the growth rate was obtained (Equation 3.57), except that the power-law for dissolution is considered equal to 1 (GARSIDE, 1971; TRAMPUŽ; TESLIĆ; LIKOZAR, 2019).

$$\mathrm{D}_{(i)} = \frac{k_a k_D \rho_{sol} \mathrm{k}_{d,i}}{3\ \rho_{cr} k_v (\mathrm{k}_{d,i} + k_D)} (\exp\left(\frac{\alpha}{L}\right) - SS) \quad (3.57)$$

Equations 3.58 and 3.59 describe the agglomeration rate of crystals of the classes j and k (MARCHAL *et al.*, 1988), where $R_{A.,n}$ indicates the crystal formation rate of the class n and $R_{D.,n}$ indicates the crystal disappearance rate of the class n due to agglomeration. Crystals from the largest size class do not agglomerate, however the agglomeration of smaller crystals may produce them.

$$R_{A,n} = \sum_m^{m_{max}} \beta_{j,k} N_j N_k V_{sol} (\frac{S_j^3 + S_k^3}{S_l^3} \delta_{il}\ ) \quad (3.58)$$

$$R_{D,n} = \sum_m^{m_{max}} \beta_{j,k} N_j N_k V_{sol} (\delta_{ij} + \delta_{ik}\ ) \quad (3.59)$$

The coefficients δ_{ij}, δ_{ik}, and δil are equal to 1 when i = j or i = k or i = l, with j and k representing the pair of agglomerating classes and l the resulting class produced by agglomeration. The index m represents the number of possible agglomeration pairs, varying from 1 to $m_{max} = 0{,}5\ N_{nC}(N_{nC} - 1)$.

The clustering kernel $\beta_{j,k}$ represents the product between the frequency of collisions between solids with the efficiency of these collisions, thus quantifying which of the collisions produces a new particle. This parameter was calculated by Equation 3.60, chosen to represent this kernel since the solid size range produced by the experiments were between the Batchelor scale and Kolmogoroff microscale presented, similar to the work of David *et al.* (2003)

$$\beta_{j,k} = k_A v_k \left(S_j + S_k\right)^3 \left(\frac{P}{\mu_r}\rho_r\right) \tag{3.60}$$

The total mass balance for crystals (m_{cr}) was calculated as the sum of masses of crystals with individual classes for each polymorph (Equation 3.61).

$$m_{cr} = \sum_{np=1}^{np} k_{v,np}\rho_{cr,np} \sum_{i=1}^{nc} N_i S_i^3 \tag{3.61}$$

Equation 3.62 demonstrates the aqueous solution ionic concentration calculation with the total mass of crystal produced at time t.

$$C(t) = \frac{m_0 - m_{cr}(t)}{m_{sol}} \tag{3.62}$$

It is now proposed a transformation term representing the rates that one polymorph rearranges into the other, also relating with the populational balances for each possible polymorph. This transformation is defined to be calculated by a constant kinetic k and a reaction order term, ro, adjusted with the experimental data (CHAKRABORTY; BHATIA, 1996). This term (Equation 3.63) was calculated similarly as a rate of nucleation showed in Gebauer *et al.* (2014), with the contributions of the kinetic barrier being neglected for simplicity. The thermodynamic barrier is calculated with the free energy profiles obtained in Equation 3.52.

$$R_{trans,n} = k \left(\frac{N_i}{V}\right)^{ro} = A\, e^{\frac{-\Delta G_{ex}}{k_b T}} \left(\frac{N_i}{V}\right)^{ro} \tag{3.63}$$

In the present equation, the Gibbs free energy for the transition solids associated with their respective size is calculated to obtain the thermodynamic barrier. The pre-exponential factor A is associated with the solid rearranging itself to a more stable form. In the proposed populational balance, this term had a negative value for the polymorph in transition and a positive value for the more stable form predicted by the step rule calculation.

An empirical linear correlation was chosen to include the kinetics effect that external bivalent cations could cause in the calcium carbonate precipitation. The theoretical determination of all kinetic phenomena associated with the presence of others would be difficult and possibly bring a high number of parameters to the model. The estimative of how the ions affect the kinetic rates is presented in Equation 3.64.

$$eff_{(Mg,Sr,Ba)} = a_{eff} + \frac{(Sr,Ba,Mg)}{Ca} b_{eff} \tag{3.64}$$

Equation 3.64 allows the observed effects on rates to be evaluated multiplicatively in the population balance equations and are settled to 1 when the concentration of the external ion is zero. It should be noted that the effect shown above is specific for each external ion and has specific parameters for the affected rate. The observed effects can be included in the kinetic rates depending on the external ion and its observed effects in the polymorphs produced. (KITANO, 1962; ASTILLEROS *et al.*, 2000; RODRIGUEZ-BLANCO *et al.*, 2011; NIELSEN *et al.*, 2016; SANJIV RAJ; DEVI; SUBRAMANIAN, 2020).

The values of properties, of both crystallization mixture and individual components, and equations for calculating dimensionless numbers are given in APPENDIX A – Table A4.

4 MATERIALS AND METHODS

4.1 ALGORITHM FOR THE MODEL SOLUTION

The presented kinetic and thermodynamic models have to be solved together, as one requires the information produced by the other, which encompasses both supersaturation and order of appearance for the polymorphs. Thus, it was necessary to produce a routine that provides solutions for the equations and connects its outputs to obtain a continuous response.

The first routine is called “Paramfit_Bpop”, which accepts as input the vector of parameters presented in Table 4.1, adjusted with the experimental data. After that operation, it loads the necessary entry data, the ionic concentration in water, the temperature, pressure, volume of reaction, and if the system is closed or open. If the system is closed, the composition of the gas phase is also informed.

If it is necessary to adjust the parameters from experiments, it loads the experimental data composed of the volumetric distribution of the produced solids, the total crystalline mass

and the polymorphic proportion with the reaction time and its experimental variance. The routine calls the optimization step with the information correctly loaded, which subsequently calls the function SfunD.

Table 4.1 - Vector of the model parameters.

Parameter	Representation
kn_{vat} [1/m³ kg s]	kinetic constant of nucleation
n_{vat}[-]	nucleation relation with SS
kg_{vat} [m/s]	kinetic constant of growth
g_{vat}[-]	growth relation with SS
n_{1vat}[-]	influence of secondary nucleation
kd_{vat} [m/s]	kinetic constant of dissolution
ka_{vat} [s/m^7]	kinetic constant of agglomeration
$ro_{vat\text{-}calc}$[-]	order of transformation reaction
$A_{vat\text{-}calc}$ [1/s]	pre-exponential factor for transformation reaction
$a_{effMgNuVat}$[-]	Linear coefficient of external ion effect
$b_{effMgNuVat}$[-]	Angular coefficient of external ion effect

Source: Own authorship

The choice to adjust the presented parameters instead of utilizing those on literature was based on the fact that the parameters obtained in the works of Trampuz et al. (2019), Brecevic and Kralj (2008) and Chakraborty and Bhatia (1996) were not directly compatible with the present model. Trampuz et al. (2019) adjusted the populational model with fesoterodine fumarate crystallization data, Brecevic and Kralj (2008) adjusted the growth, dissolution and nucleation $CaCO_3$ rates individually with different equations than those proposed in section 3.4 and Chakraborty and Bhatia (1996) adjusted the growth, nucleation, agglomeration rates based on direct power law correlations instead of the semi-empirical equations in 3.4.

The function “SfunD” computes an error function for the proposed model. This function does the numerical integration of the model, stored in the function “BpopModel”, saves its results, and then compares with the experimental data, returning the error to the function “Paramfit_Bpop”.

The "BpopModel" provides the routine with the actual model, with all the thermodynamic and kinetic calculations, producing a matrix with the values for the differential equations presented in Equations 3.21-3.24 for each integration step. For clarity, Figure 3.4 represents a scheme of the algorithm flow together with the calculations of "BpopModel".

Figure 4.1 - Solution algorithm flowchart.

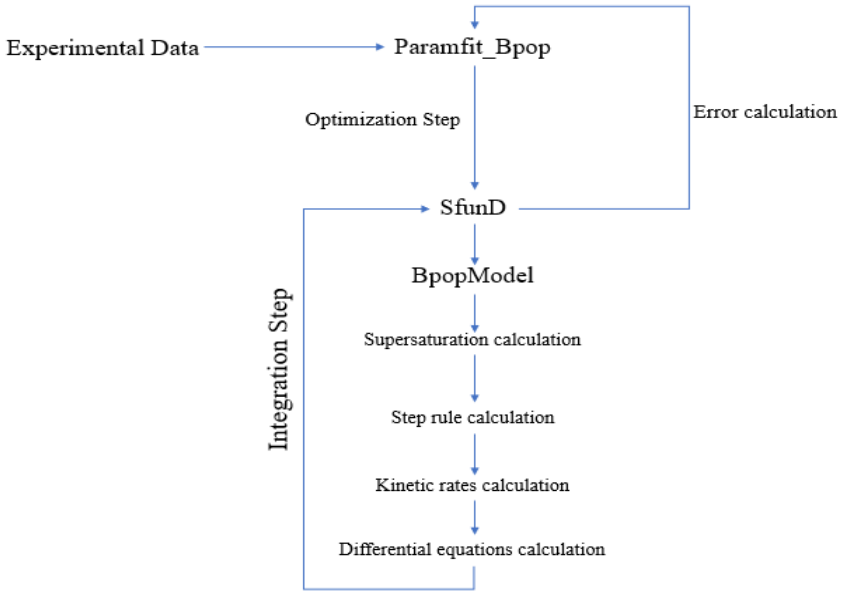

Source: Own authorship

4.2 INTEGRATION STEP

The system of equations was solved in the GNU Octave environment using the ode15s routine. This routine is a variable-step, variable-order (VSVO) solver based on the backward differentiation formulas (BDF) of orders 1 to 5. The variation in the numerical steps or the method order is associated with the tolerances, relative or absolute, defined in the routine. The relative tolerance was set to 3%. When the method compares different steps or orders, the difference between the obtained values has to be less than 3% or the method will increase the order or decrease the integration step size.

The backward differentiation formula (BDF) is a family of implicit methods for the numerical integration of ordinary differential equations (SHAMPINE; REICHELT, 1997; BEERS, 2006). The specific formulas for the BDF method are presented in Equations 4.1-4.5, with h representing the step size, f the differential equation system and n the step number.

$$y_{n+1} - y_n = h\, f(t_{n+1}, y_{n+1}) \tag{4.1}$$

$$y_{n+2} - \frac{4}{3}y_{n+1} + \frac{1}{2}y_n = \frac{2}{3}h\, f(t_{n+2}, y_{n+2}) \tag{4.2}$$

$$y_{n+3} - \frac{18}{11}y_{n+2} + \frac{9}{11}y_{n+1} - \frac{2}{11}y_n = \frac{6}{11}h\, f(t_{n+3}, y_{n+3}) \tag{4.3}$$

$$y_{n+4} - \frac{48}{25}y_{n+3} + \frac{36}{25}y_{n+2} - \frac{16}{25}y_{n+1} + \frac{3}{25}y_n = \frac{12}{25}h\, f(t_{n+4}, y_{n+4}) \tag{4.4}$$

$$y_{n+5} - \frac{300}{137}y_{n+4} + \frac{300}{137}y_{n+3} - \frac{200}{137}y_{n+2} + \frac{75}{137}y_{n+1} - \frac{12}{137}y_n = \frac{60}{137}h\, f(t_{n+5}, y_{n+5}) \tag{4.5}$$

4.3 OPTIMIZATION STEP

With the numerical resolution of these equations defined, the next step estimates the kinetic parameters from the experimental data. The problem of parameter estimation consists of three stages: formulation of the objective function, minimization of the objective function, and interpretation of the results obtained (M. SCHWAAB AND J.C. PINTO, 2007). The objective function formulation was applied with the maximum likelihood method (ML) in this work. This method estimates the probability distribution parameters by maximizing a likelihood function under the assumed statistical model, that the observed data is most probable (M. SCHWAAB AND J.C. PINTO, 2007; ROSSI, 2018).To produce an objective function, it is possible to assume normal error distribution, the model predicts the real experimental values and the experimental measures are uncorrelated. Then, it is possible to define an equation that serves as the estimation problem metric, i.e., the objective function (Equation 4.6), with NE representing the number of experiments and NY the number of dependent variables.

$$F_{obj} = \sum_{i=1}^{NE} \sum_{j=1}^{NY} \frac{(y_{i,j}^{e} - y_{i,j}^{m})^2}{\sigma_{yij}^2} \tag{4.6}$$

The minimization of Equation 4.6 was made with a hybrid algorithm that first searches for the global best F_{obj} value with inertia-controlled Particle Swarm algorithm (PSO). This search is followed by a Nelder-Mead Simplex method, with both methods implemented in GNU Octave. The Particle Swarm method is a stochastic optimization algorithm inspired by Reynolds (1987) simple equations for simulating the interactions of individuals in flying swarms (M. SCHWAAB AND J.C. PINTO, 2007; MIRJALILI, 2019). The Nelder-Mead Simplex method is a heuristic direct search method using the concept of a simplex and approaches the local

optimum based on a series of steps that can move, expand and contract the geometrical simplex (LAGARIAS *et al.*, 1998; WANG; SHOUP, 2011).

The combination of PSO with a Nelder–Mead method can improve the estimation based on the best solution found, providing excellent and robust results for the parameter estimation in populational models as shown in Besenhard *et al.* (2015).

4.4 EXPERIMENTAL DATA

There were two different sets of experimental data utilized in the optimization step of the algorithm presented in Figure 4.1. The first set of data was produced in the Center for Studies on Colloidal Systems (NUESC), from the Institute of Technology and Research (ITP), in Aracaju-SE. The second set of data was obtained in a partnership with the Laboratory of Chemical Process and Bionano Particle Technology (LPP), from the Institute of Technological Research (IPT), in São Paulo-SP. The third set of experimental data obtained from Petrobras was utilized only in the integration step of Figure 3.4. For the sake of clarity, the first set of data will be named Data Set 1, the second set Data Set 2 and the third set Data Set 3 from now on.

4.4.1 Methodology for Data Set 1

4.4.1.1 Methodology and conditions of the experiments

Calcium chloride dihydrate ($CaCl_2 \cdot 2H_2O$, 99.9 wt.%.) and sodium bicarbonate ($NaHCO_3$, 99.9 wt.%.) were purchased from Synth. Water was doubly distilled and deionized using an ultrapure water purification system (Megapurity).

The methodology used in the experiments was based in the work of Serpa (2015). The precipitation experiments were carried out in a jacketed reactor (600 mL) coupled with an ultra-thermostatic bath (Quimis, model Q214M4, accuracy of ± 0.1 ºC). Solutions were stirred at 1100 rpm using a magnetic stirrer (IKA, model RCT basic). The FBRM probe (Mettler Toledo, model G400) was inserted into the reactor at an inclination angle of 45º. This position minimizes the formation of scales at its extremity, ensured by the equipment's maximum allowable error (fouling index <10%). Data acquisition (chord length and number) and analysis were performed by the software iC FBRM™. FBRM technique was used to monitor the precipitation evolution and the growth kinetics of $CaCO_3$ particles. The minimum chord size detected by FBRM is about 0.5 µm. The scheme of the experimental unit is presented in Figure 4.2.

Figure 4.2 - Schematic diagram of the experimental unit precipitation of salts in water mixtures using the FBRM: (1) computer, (2) FBRM probe, (3) reactor, (4) magnetic stirrer and stirring plate, (5) water bath and (6) pHmeter.

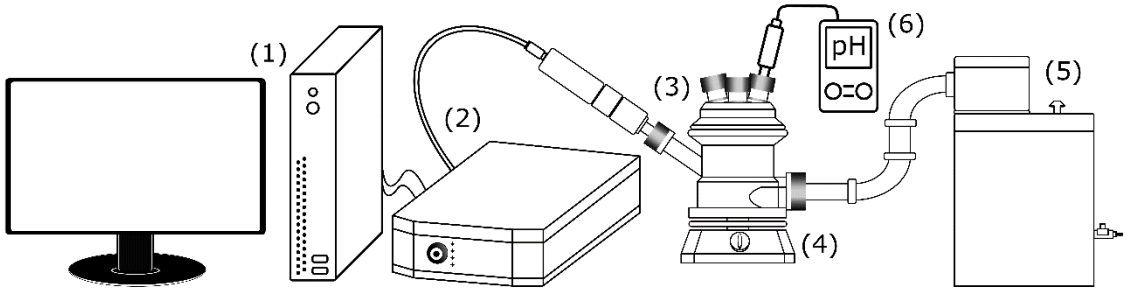

Source: Own authorship

$CaCl_2$ and $NaHCO_3$ solutions with 50, 40, 30, and 20 mmol.L^{-1} were prepared by agitation at 100 rpm for 1 h, followed by filtration (Vidrolabor filtration system) using a 0.45 μm nylon filter (Allcrom). 250 mL of the bicarbonate solution was added to the glass cell under stirring and temperature control. After that, 250 mL of the calcium solution was added, and the measurement of the crystal populations was initiated by the FBRM probe (sampling rate of 2 s). The measurements were obtained in triplicates, and the analysis was performed considering the mean value of the experimental replicates and the moving average for 1-minute intervals.

The pH was monitored along the reaction using an *in-line* Mettler Toledo pHmeter, with the obtained value being registered in 1-minute intervals. Crystal mass samples were collected every 10 min and the mass of the crystals produced were dried and weighted gravimetrically.

A metallic coating was performed for SEM analysis using a Sputter Coater EMITECH Model: K450 with an Au layer thickness estimated at 200 Å. The sample was placed on a glass slide, collected on a double-sided carbon tape fixed to the stub and then metalized for 2 min before the analysis. A scanning electron microscope with the X-ray dispersive energy detector model Leo 440i (SEM), brand: LEO Electron Microscopy/Oxford, was used for the analysis. A voltage of 20 kV, current of 100/600 mA, and magnification of 5000x and 10,000x were also defined.

XRD analyses were performed on a PANalytic EMPYREAN diffractometer, using a Cu Kα source (40 kV and 40 mA), in the range of $5\ ° < \theta < 40°$, with a step of 0.013° and a 2 min^{-1} count time. Phase identification was performed using the Joint Committee on Powder Diffraction Standards (JCPDS) database standard. The polymorphs produced were calculated

with the XRD intensity peak analysis methodology proposed by Kontoyannis and Vagenas (2000), based on the intensity of the calcium carbonate characteristics peaks .

4.4.1.2 Methodology of the simulations

The supersaturation of the calcium carbonate forms was calculated by Equations presented in section 3.1.2.1 as the experiments were done in an open atmosphere, at standard temperature and pressure conditions. The activity and fugacity calculations of the species were made by Equations presented in section 3.1.1.

The kinetic model utilized is represented in Equations 3.46-3.63 with 75 equations for each polymorph, within a size range of 1.036-171.79 μm; this class distribution was produced by the FBRM's software and utilized directly in the model. The flow rates Q set to null values producing the cumulative volumetric solid distribution, the crystal mass, and the final polymorphic associated with the batch conditions. These variables were inputted in Equation 4.6 together with the experimental cumulative volumetric distribution, calculated assuming that the chord size was equivalent to the crystal diameter, crystal mass, final polymorphic proportion, and the variance of all these measurements. The obtained modeling error was checked by comparing the modeling errors obtained with the allowable experimental deviations to evaluate the quality of the model. The likelihood confidence region for the obtained parameters were obtained considering on the elliptic form for the confidence region and then checking which PSO+Nelder particles passed the Chi-Squared test that represents the region.

The residuals, obtained from subtracting the model and experiments values, were also tested by a t-test to see if the residual's average were equivalent to zero.

4.4.2 Methodology for Data Set 2

4.4.2.1 METHODOLOGY AND CONDITIONS OF THE EXPERIMENTS

The IPT-SP experimental procedures and the results were retired from a technical report produced by Wagner Aldeia, Rafael Loureiro de Mello Gallo and Larissa Ribeiro Leite de Araujo (technical report to Petrobras, 2018). Their report focused on an experimental study on the effects of divalent ions on calcium carbonate precipitation.

The experiments were performed in a 5.5 L reactor with a blade turbine impeller. The experiments were carried out at atmospheric pressure and room temperature, using precursor

solutions with a nominal concentration of 40.000 mg.L^{-1} of $CaCl_2$, 2.000 mg.L^{-1} of $NaHCO_3$, and different concentrations of Mg^{2+}, Sr^{2+}, Ba^{2+} (indicated in Table 4.2), with sampling intervals of 1, 5, 15, 30, 45, 60, 75, 90, 105 and 120 min. The ionic concentrations were chosen based on the conditions found in wells explored by Petrobras.

Table 4.2 - List of experiments for crystallization kinetics determination

Exp.	**Addition Ion [mg.L^{-1}]**	
Ion Free (IF)	-	-
Mg-30	Mg^{+2}	30
Mg-144	Mg^{+2}	144
Ba-28	Ba^{+2}	28
Ba-280	Ba^{+2}	280
Sr-33	Sr^{+2}	33
Sr-1500	Sr^{+2}	1500

Source: Own authorship

The X-ray diffractometry technique was adopted for crystallographic characterization of the calcium carbonate forms using a model LabX XRD-6000 equipment from Shimadzu Corporation Japan Ltd. operating with a radiation source of the type CoKα. The voltage and current values for the equipment operation were set at 40.0 kV and 30.0 mA, respectively. The tests were carried out considering an angled sweep in the range of 25 to 65º, with a 2º/min angular feed rate of 0.02º step. The data obtained were treated by the Rietveld Method for better resolution of the experimental data. The polymorphs produced were calculated with the XRD intensity peak analysis methodology similar to the proposed by Kontoyannis and Vagenas (2000).

The samples of calcium carbonate crystals produced in the precipitation processes were analyzed by scanning electron microscopy (HRSEM-FEG), using an FEI QUANTA 3D FEG microscope. Image acquisition was performed with the equipment operating in the secondary electron detection mode and high vacuum conditions. The preparation of the samples was restricted to the arrangement on a double-sided copper tape and covered with a thin Au/Pd film. The imaging was done by applying an acceleration voltage of the electrons equal to 20 kV, aiming to reduce any charging effect of the samples without compromising the resolution. Images were obtained with magnifications (magnitude) of 500x, 2,000x, 5,000x, 10,000x, and 25,000x. The laser diffraction technique was adopted using a MasterSizer 2000 model

equipment from Malvern Instruments Ltd to determine the size distribution of crystals (CSD) generated in the precipitation process. The dispersion of the particles was made in an aqueous medium with the aid of ultrasound before the experiments, and the readings were taken at regular intervals of 5 minutes until the variation of the mean diameter in volume between two consecutive readings periods was less than 2%. Samples of dried crystalline mass were collected in 1, 5, 15, 30, 45, 60, 75, and 90 min. The readings were taken at regular intervals until the variation of mass between two consecutive readings periods was less than 2%.

4.4.2.2 METHODOLOGY OF THE SIMULATIONS

The supersaturation of the calcium carbonate forms was calculated by Equations presented in section 3.1.2.1 as the experiments were done on an open atmosphere at standard temperature and pressure conditions. The activity and fugacity calculations of the species were made by the Equations presented in section 3.1.1.

The kinetic model utilized is represented in Equations 3.46-3.64 with 75 equations for each polymorph, within a size range of 0.01-532.77 μm; this class distribution was produced by the DLS's software and utilized directly in the model. The flow rates Q were also set to null values, producing the cumulative volumetric solid distribution, the crystal mass, and the final polymorphic associated with the batch conditions. Unfortunately, it was not possible to use the maximum likelihood method in the parameter estimation for this data set, as not all experimental measures could be performed in triplicate tests. Thus, the objective function used had the form of the classical least-squares objective function, presented in Equation 4.7.

$$F_{obj} = \sum_{i=1}^{NE} \sum_{j=1}^{NY} ({y_{i,j}}^{exp} - {y_{i,j}}^{m})^2 \quad (4.7)$$

The model output was normalized and then inputted in Equation 4.7 together with the also normalized experimental cumulative crystal volume, crystal mass, and polymorphic proportion.

The selection of rates affected by the divalent ions (Mg^{2+}, Ba^{2+}, and Sr^{2+}) was made automatically by a programmed routine. It can put Equation 3.39, before the optimization step, in the kinetic rates, run five times the minimization, and evaluate the objective function all for possible combinations, i.e., the effect on the nucleation and growth, then the effect on the nucleation and transformation, and with all the subsequent combinations. After it concluded to

test all the possible combinations, a Wilcoxon Rank Sum Test was made to obtain the group of parameters that produced the smallest value of F_{obj}. This was made for each ion, with the pair of affected rates for each ion that produced the smallest F_{obj}; a final optimization was run, also five times, and the best F_{obj} was obtained. The programmed routine also formats all the parameters to the same magnitude in both, the PSO and Nelder Mead methods to avoid the higher-magnitude parameters having more influence than the lower ones (M. SCHWAAB AND J.C. PINTO, 2007).

To simulate the incorporation of the divalent ions in the produced solids along the process, the distribution coefficients of Sr^{2+}, Ba^{2+}, and Mg^{2+} in the polymorphs, were used to calculate the aqueous concentration profile of these ions along the crystallization time from the coefficient estimations made by Kitano *et al.* (1971) and Sawada *et al.* (1990).

4.4.3 Methodology for Data Set 3

4.4.3.1 METHODOLOGY AND CONDITIONS OF THE EXPERIMENTAL DATA

Petrobras provided experimental information around a choke valve region to investigate the effect of the valve's presence with the calcium carbonate formation for a range of topside well conditions. Tables 4.3 and 4.4 present the information corresponding to the operating conditions of flow, temperature, pressure, and salinity in the inlet and outlet regions of the valve for two different wells.

Table 4.3 - Operating conditions in the inlet and outlet region around the choke valve.(Continues on next page)

	Inlet	**Outlet**
Well-1		
Temperature [ºC]	31.13	31.01
Pressure [kPag]	2,170	2,000
Aqueous flow rate[m³/day]	1,722	1,722
Oil flow rate [m³/day]	1,808	1,801
Gas flow rate [m³/day]	21,920	23,960

	Inlet	Outlet
Well-2		
Temperature [ºC]	24.13	23.56
Pressure [kPag]	2,243	2,000
Aqueous flow rate [m³/day]	31	31
Oil flow rate [m³/day]	3,877	3,859
Gas flow rate [m³/day]	29,350	33,310

Source: Own authorship

Table 4.4 - Water composition around the choke valve.

Ion	Well-1	Well-2
	Concentration [ppm]	*Concentration [ppm]*
Na^{1+}	13,394	78,780
K^{1+}	953	4,188
Mg^{2+}	271	1,900
Ca^{2+}	1,029	10,120
Ba^{2+}	2	21
Sr^{2+}	0	2,666
Cl^{1-}	22,485	147,488
Br^{1-}	80	140
SO_4^{2-}	175	232
HCO_3^{1-}	3,446	697
pH	8,1	6

Source: Own authorship

4.4.3.2 METHODOLOGY OF THE SIMULATIONS

The supersaturation of the calcium carbonate forms was calculated by Equations presented in section 3.1.2.2 as the simulations were made on a closed atmosphere with specified temperature and pressure. The activity and fugacity calculations of the species were made by the Equations presented in section 3.1.1. In this case, the presence of an oil phase was considered to calculate the partition of CO_2 among the aqueous and oil phase with Equation 4.8, developed based on Carrazana (2012). In Equation 4.8, the CO_2 in the aqueous phase is

calculated and then corrected by the influence of an oil phase based on the ratio between the aqueous and oil phase molar flow.

$$CO_{2(aq)}^{with\ oil\ presence} = \frac{R_{W/O}\ \ CO_{2(aq)}^{without\ oil\ presence}}{R_{W/O}+44.45} \tag{4.8}$$

To calculate the influence of the temperature and pressure on the equilibrium constant, a methodology similar to Cosmo (2013) was utilized. The author calculated the standard values for calcite formation according to Equation 3.30 and later applied the van't Hoff equations to obtain an equilibrium constant equation for conditions up to 100 atm and 100 °C. The results obtained were used and expanded to other calcium carbonate polymorphs, vaterite and aragonite, under formation conditions up to 100 °C and 200 atm. First, equilibrium constants for the calcium carbonate solids in the reference condition, 25ºC and 1 atm, were calculated. As indicated in Equation 3.30, the value of the Gibbs energy change in the reaction under these conditions must be known for the calculation of $K_{eq,ref}$. Thus, the values were calculated from each reaction species respective formation values.

Figure 4.3 outlines the methodology used to the calculations described in Equations 3.31 and 3.32. For the use of Equation 3.32, it was necessary to know the enthalpy of formation and heat capacity for each species in the reaction. In this step, it was considered that the reaction enthalpy and heat capacity did not change with the temperature, based on the results of Cosmo (2013) which calculated that this consideration only produced an error of 2% when compared to considering the changes for the range of T utilized in the present thesis and the work of Cosmo (2013).

As for the integration of Equation 3.32, it was obtained the variations of the standard molar volumes, in the pressure of interest and the reference temperatures (0, 25, 50, 75, and 100 °C). As for the pressure effect in molar volumes, it was considered that change in the molar volume of the reaction is captured by calculating the compressibility of the solvent for each pressure of interest and that the change in compressibility for each component can be ignored for pressures up to 700 atm (COSMO *et al.*, 2019).

All the necessary thermodynamic information was obtained from Cosmo (2013), Krupka *et al.* (2010), and Apps & Wilkin (2015). The obtained tables with Gibbs energy change, formation enthalpy, heat capacity and molar volumes will be presented in the Results and Discussion section.

Figure 4.3 - Methodology to obtain K_{eq} for each Temperature and Pressure pair.

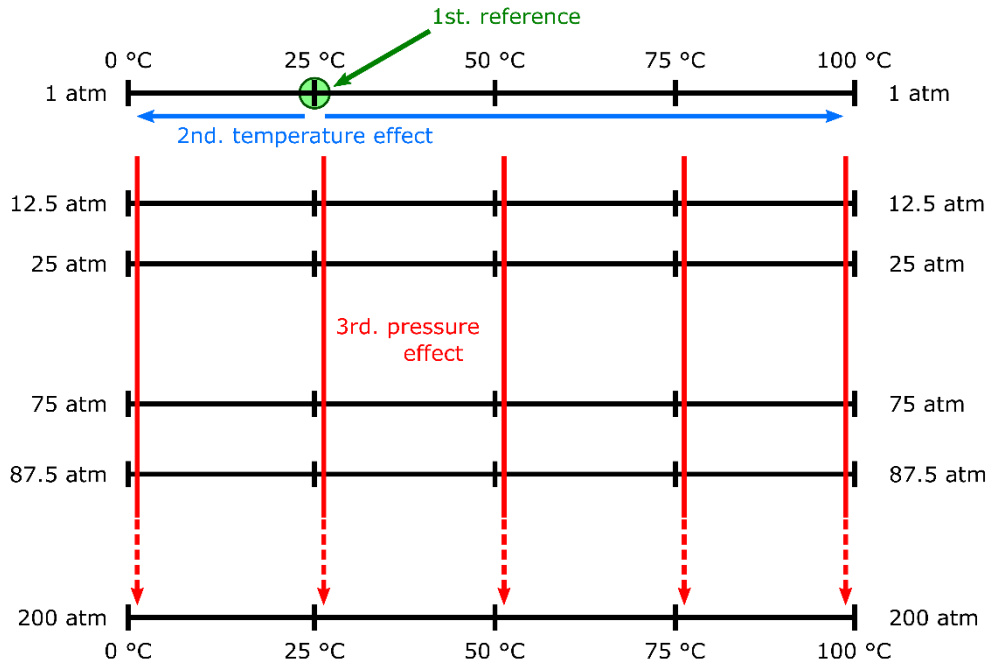

Source: Own authorship

Thus, it was possible to determine the equilibrium constant values for any pressure at the temperatures used as reference. The various values calculated for the equilibrium constant of the k_{eq} reaction were obtained. The regression of the data was performed to obtain the constant as a function of pressure and temperature. The values calculated with the final expression obtained were compared to those reported by the Multiscale® 6 (version 7.1) and SUPCRT92 software.

For the kinetic analysis of the impact caused by the choke valve on the precipitation of salts, two regions of interest were defined in the data simulation: one meter before the choke valve defined as Inlet and one meter of piping after defined as Outlet (Figure 4.4). Such separation seeks to compare the differences associated with solid formation before and after valve positioning through the results of the model.

Figure 4.4 - Schematic representation of the choke valve region used in the simulations.

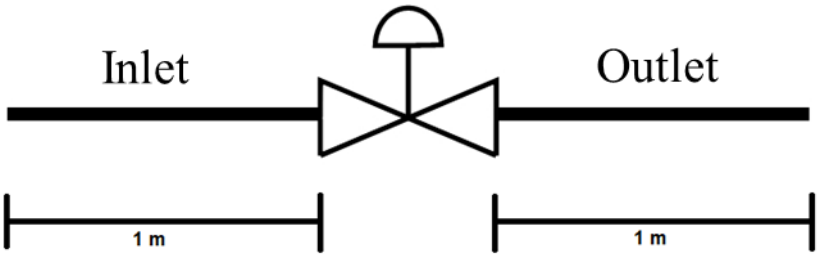

Source: Own authorship

As it is a simulation along with a flow, the macroscopic balance using the average properties around the entire control volume would not bring relevant information since there would be no spatial separation in the flow direction, but only calculation of the average properties in the entire control volume. Thus, a discretization in the X-axis direction was performed, based on the consideration that there are only variations in this direction. Upstream and downstream piping were discretized into 50 finite volumes. Thus, each of these volumes is represented by the Equations (3.46) to (3.51), totaling 100 systems of equations. Figure 4.5 represents a schematic of this discretization.

Figure 4.5 - Representation of finite volumes and terms associated with each region.

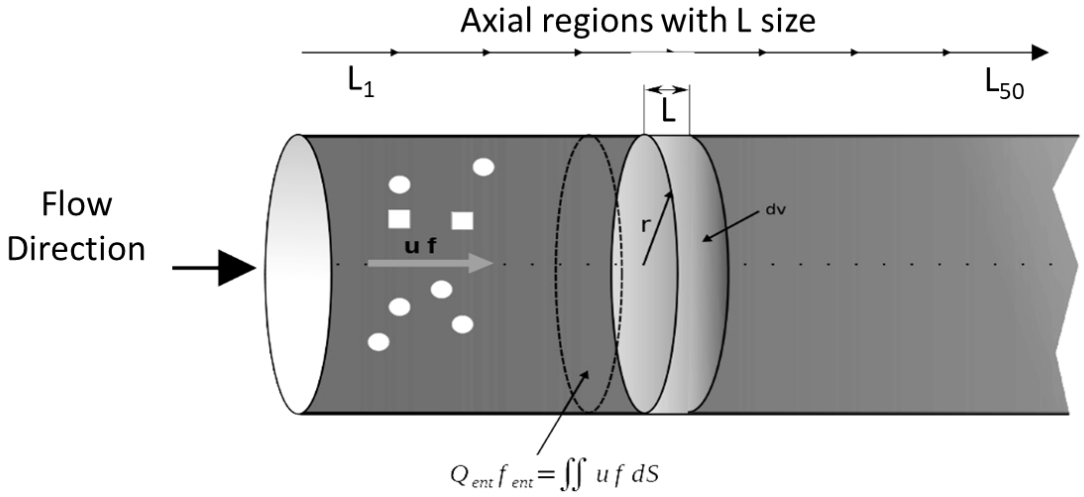

Source: Own authorship

It can be seen that the term Q/V in Equations 3.46-3.51 represents the residence time of the crystals in the control volume, as it flows in a cylindrical pipe. It was considered that all particles could be represented by the average residence time Q/V, with no need to calculate the distribution of residence time in populations (FOGLER, 2004).

Besides, the following assumptions were accepted in the model for the elaboration of the simulations:

- The flow, pressure, and temperature were considered constant along the pipeline;
- There are no crystals in the stream that enters the tubulation on both inlet and outlet regions;
- The creation of fluctuations and turbulence in the flow caused by the presence of the valve was not considered;
- That all phases flow with the same axial velocity;
- The effect of the oil phase was considered only in the phase equilibrium, not considering the kinetic effects that these may cause in the system;
- Piston-type flow and perfect radial mixing;
- There is no fouling, every particle formed flows along with the system at a velocity equal to the fluid;
- The energy of activation for the kinetic rates, nucleation, growth, and dissolution are similar to those of Brečević and Kralj (2008).

In addition, the calculation of the Reynolds' number used to obtain the convective mass transfer coefficient must be modified to the form of Equation 4.9. For a flowing system the shear velocity calculated from the consideration of flow without wall interference is a better representation of the inertial influence on the flowing particle (LIVK; ILIEVSKI, 2007; PERRY *et al.*, 2007). With u_{shear} *e* d_{part}, representing the shear rate and the diameter of the crystalline particle calculated using the area shape factor for the non-spherical polymorphs.

$$Re_{par} = \frac{-\rho * u_{shear} * d_{part}}{\nu} \tag{4.9}$$

In addition to this modification, the agglomeration kernel is adjusted for a flow-through system. In this step, Livk (2007) work was used to estimate the kernel for gypsum in laminar and turbulent flows. Thus, a similar behavior was assumed for the calcium carbonate polymorphs.

With that, it was possible to obtain a new set of equations that requires the following inputs to produce the crystal size distribution, the total crystal mass, and the polymorphic proportions along the tubular region:

- The volumetric flow of each phase present in the flow that is, the flows of water, oil, and gas;
- The temperature and pressure in each region of the system;
- The salinity at some point of the flow (inlet or outlet);
- The physical dimensions of the piping in each region of the system;
- The composition of the gaseous, aqueous, and oil phases, if this is not possible, at least the content of carbon dioxide in the gas phase must be known to calculate the concentration of this component in the aqueous phase.

Thus, the system represents a tool capable of evaluating the formation of calcium carbonate solids upstream and downstream of the choke valve under different operating conditions.

5 RESULTS AND DISCUSSION

5.1 RESULTS FROM DATA SET 1

The first step in the model calculation was estimating which calcium carbonate forms presented thermodynamic stability in the range of experimental conditions, from 50 mmol.L^{-1} to 20 mmol.L^{-1} of calcium and bicarbonate.

Both vaterite and calcite showed thermodynamic stability in the studied conditions. The change in the Gibbs free energy caused by vaterite and calcite polymorphs, within the first class characteristic size(0.518 μm), formation was -1.35 x 10^{-10} J.mol^{-1} and -1.54 x 10^{-9} J.mol^{-1}, respectively, for the system with 50 mmol.L^{-1} of calcium and bicarbonate. The higher value of ΔG for vaterite is due to its lower interfacial tension with water and higher solubility, thus having a lower bulk and surface energy relation (GEBAUER *et al.*, 2018). As the system can produce both polymorphs, the model predicted that the less stable vaterite appeared first and consequently was transformed in the more stable calcite, as the Ostwald step rule states (NAVROTSKY, 2004; GOWER, 2008). The model will only predict calcite nucleation if the system achieves vaterite equilibrium, i.e., the supersaturation of these polymorphs becomes equal to one. The aragonite polymorph also presented stability, although its change in the Gibbs free energy value was close to the calcite, 94.56% of the calcite value. The formation of aragonite was not included in the calculations, since the system did not include magnesium ions nor high temperatures, experimental conditions that favor the aragonite formation (NAVROTSKY, 2004; ROSA; LUNDAGER MADSEN, 2011; BLUE *et al.*, 2017). The supersaturation values calculated for the possible forms, calcite and vaterite (Table 5.1), show that SS increases with ionic concentration, using the same carbonate and bicarbonate proportions.

Table 5.1 - Calculated system supersaturation (SS) at different calcium and bicarbonate ionic concentrations.

Ionic concentration [mmol.L^{-1}]	**SS calcite**	**SS vaterite**
50	8.87	6.24
40	7.72	5.42
30	6.43	4.47
20	4.97	3.49

Source: Own authorship

It should be noted that, with the supersaturation values obtained in Table 5.1, not all calcium and bicarbonate ions are available to produce calcium carbonate. Due to the system non-ideality, its activity coefficients vary between 0.34-0.43 for the calcium-carbonate ionic pair. To evaluate the differences between the real and ideal solution behavior is possible to consider that the activity coefficients are equal to one, and that all ions are available for precipitation, the supersaturation value for a system with 50 mmol.L^{-1} would be 13.81 and 9.71, for calcite and vaterite, respectively.

With the supersaturation and step rule calculation, the experimental data concerning the particle size distribution and crystalline mass throughout the $CaCO_3$ precipitation process were used as input information in the optimization step, to produce the parameters necessary for the model to be able to represent the experimental data.

Figures 5.1-5.4 show the results of the parametric estimation step for the experimental conditions, from 50 mmol.L^{-1} to 20 mmol.L^{-1} of calcium and bicarbonate ions. It is important to note that the volumetric distributions represent all the particles produced, for both vaterite and calcite populations balances together. From the results, it is possible to observe how the maximum likelihood method uses the experimental variance information as a weighting factor. It can be observed that the methodology allowed in its majority more significant modeling errors in the points that presented higher experimental variances and restricted high model errors when lower variances were present.

Figure 5.1 - Particle size distribution and crystal mass experimental and predicted by the system model, for experiment with 50 mmol.L^{-1} of calcium and bicarbonate ions.

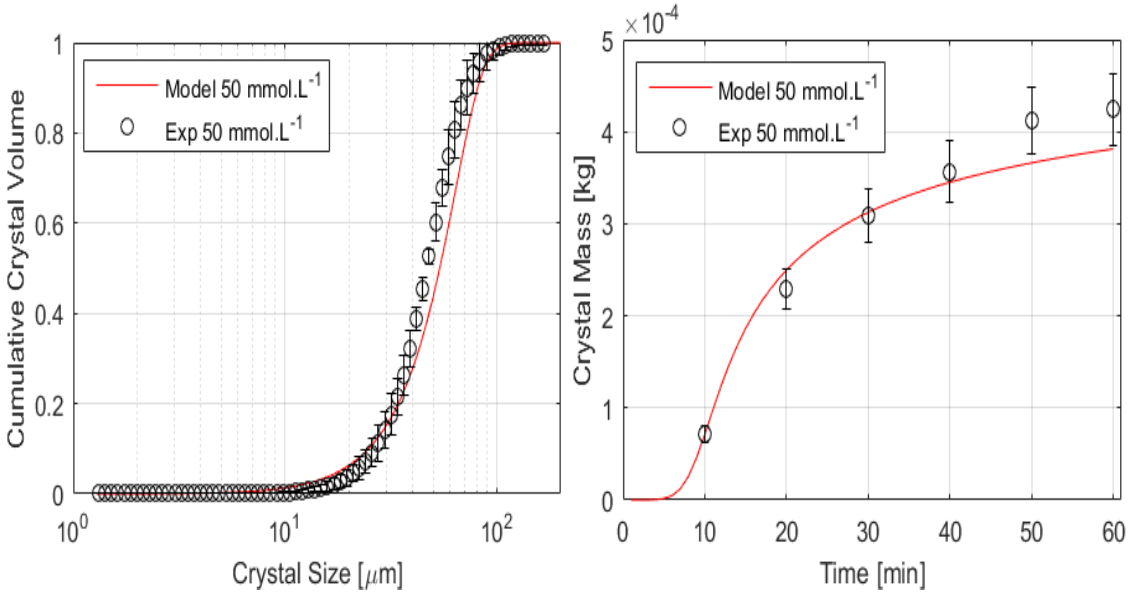

Source: Own authorship

Figure 5.2 - Particle size distribution and crystal mass experimental and predicted by the system model, for experiment with 40 mmol.L^{-1} of calcium and bicarbonate ions.

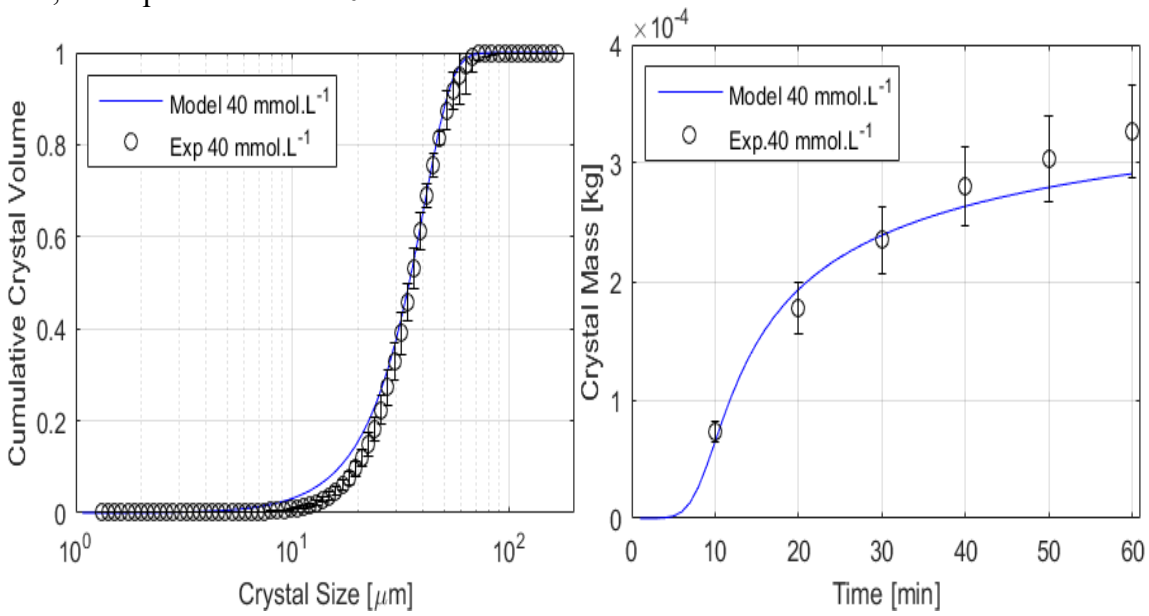

Source: Own authorship

Figure 5.3 - Particle size distribution and crystal mass experimental and predicted by the system model, for experiment with 30 mmol.L^{-1} of calcium and bicarbonate ions.

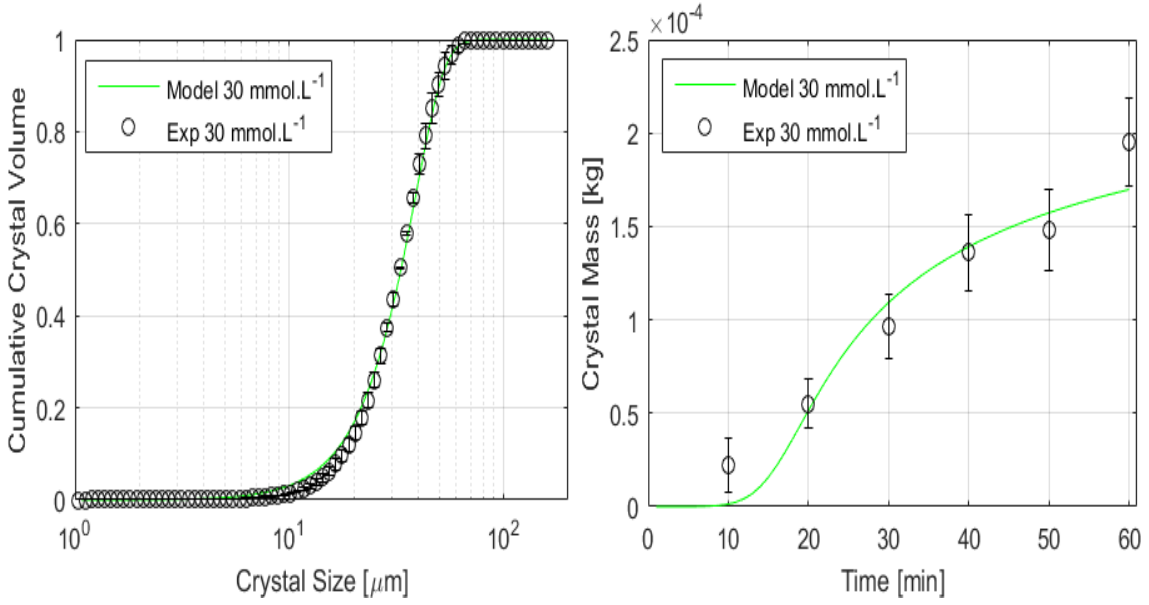

Source: Own authorship

Figure 5.4 - Particle size distribution and crystal mass experimental and predicted by the system model, for experiment with 20 mmol.L^{-1} of calcium and bicarbonate ions.

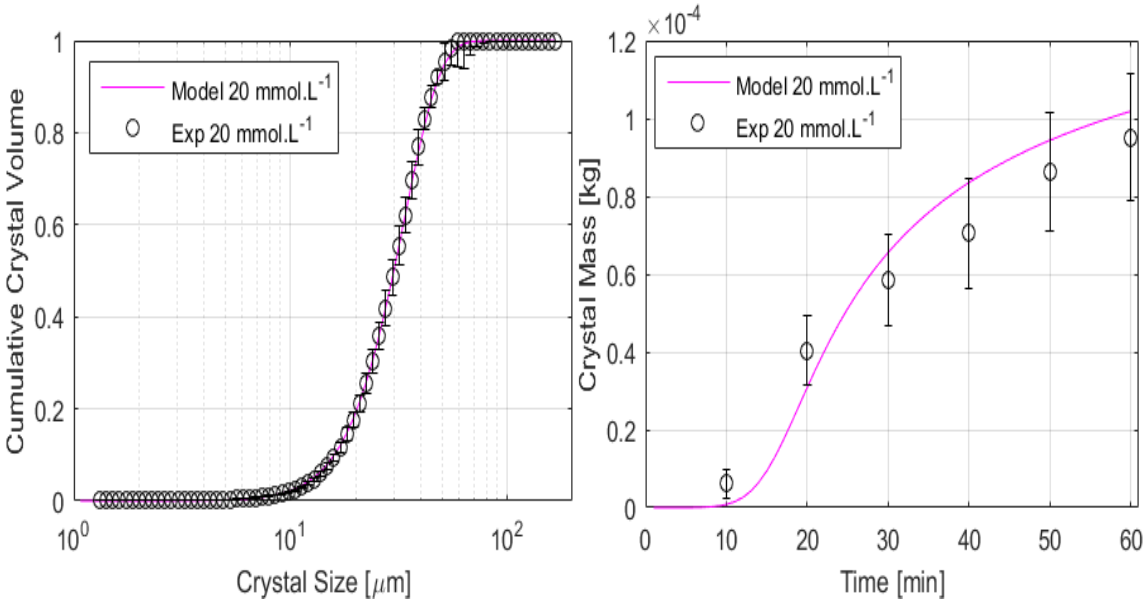

Source: Own authorship

It can be seen that the maximum likelihood approach is helpful for an experimental system with a variable experimental error (PRESS *et al.*, 2007). The hypothesis that the modeling errors are only due to experimental random errors can be checked by comparing the modeling errors obtained with the allowable experimental deviations. If the modeling errors are compatible there is no way to reject the perfect model hypothesis. Otherwise, there is enough argument for the user to continue investing in improving the model. In this case, the model can successfully represent the experimental data if:

$$\chi 2_{min} < F_{obj} < \chi 2_{max}$$

Performing the calculations for the studied conditions and with the respective degree of freedom with 95% confidence:

$$264.9 < 329.56 < 360.6$$

Thus, one cannot reject the perfect model hypothesis since the modeling errors are comparable to the experimental errors. The linear correlation coefficient between experimental and model values can also be evaluated in the form of R^2 to quantify the agreement of these values (Table 5.2).

Table 5.2 - Linear correlation coefficient between the model and the experiments studied: R^2 size represents the relation between the experimental and simulated cumulative volumetric distribution and R^2 mass between the experimental and simulated crystalline mass along the time.

Experimental Condition	R² Size	R² Mass
50 mmol.L^{-1}	0.911	0.932
40 mmol.L^{-1}	0.964	0.973
30 mmol.L^{-1}	0.981	0.968
20 mmol.L^{-1}	0.974	0.915

Source: Own authorship

As the correlation coefficient for both size distribution and crystalline mass (Table 5.2) presented values greater than 0.9, the correlation between the values predicted by the model and the experimental measures can be considered satisfactory, varying approximately linearly and proportionally.

The residues average and standard deviation for the model to the volumetric distribution and crystalline mass was equal to $-4.07 \times 10^{-4} \pm 3.77 \times 10^{-3}$ and $2.44 \times 10^{-6} \pm 1.03 \times 10^{-5}$. Applying a t-test with this result, it can be concluded that both means of the residuals of the two variables are equivalent to zero with 95% confidence; that is another indication that the adjustment can be considered satisfactory. Besides that, the residuals for both variables presented random behaviors indicating no systematic error (M. SCHWAAB AND J.C. PINTO, 2007).

Besides the objective function and residuals analysis being necessary, the estimated parameters should also be analyzed. Table 5.3 presents the confidence interval obtained for all parameters for the PSO+Nelder particles that are in the likelihood confidence region.

The obtained growth parameters agreed with Brecevic and Kralj (2008) that the vaterite presents higher initial growth rates than the calcite. Although, when comparing the initial calculated growth rates for both polymorphs with Brecevic and Kralj (2008), the average vaterite growth rate was slower in this work, 1.23×10^{-8} m.s^{-1} in comparison with the 1.67×10^{-8} m.s^{-1} obtained by the Brecevic and Kralj (2008), and the average calcite growth rate was also slower in the present model, 3.04×10^{-10} m.s^{-1} in comparison with the 9.44×10^{-10} m.s^{-1} obtained by Brecevic and Kralj (2008).

However, the authors studied the growth rates on seeded batch experiments with higher ionic strengths than the present work, 0.19 mol.L^{-1} for this work and up to 0.315 mol.L^{-1} and

found that an increase in the ionic strength can increase the rate constants. Also, they observed g_{calc} and g_{vat} equal to 2 instead of 4.96 and 1.27 for the vaterite and calcite relation with supersaturation, which could also cause the differences observed. The initial nucleation rate was higher than the obtained by Chakraborty and Bhatia (1996b), $1.35x10^{-1}$ $L^{-1}.s^{-1}$ in comparison with $4.02x10^{-2}$ $L^{-1}.s^{-1}$. Although, the authors used different precipitation conditions to estimate its nucleation rate (250 rpm, 6 min of residence time, and SS_{vat}=9.15), which could have produced the different kinetic rates observed. For the agglomeration rates, it was possible to observe that the calcite polymorph presented 18.34 times higher agglomeration tendency. Chakraborty et al. (1996) also observed this behavior, although to a lesser extent.

Table 5.3 - Likelihood confidence region for the obtained parameters.

Parameter	**Estimated Value**	**Inferior Limit**	**Superior Limit**
kn_{vat} [$1.m^3 kg^{-1} s^{-1}$]	9.88×10^{4}	8.79×10^{4}	9.97×10^{4}
n_{vat}	1.75	1.36	2.13
kg_{vat} [$m.s^{-1}$]	2.07×10^{-16}	1.06×10^{-16}	2.69×10^{-16}
g_{vat}	4.96	4.41	4.98
n_{1vat}	0.39	0.32	0.43
kg_{calc} [$m.s^{-1}$]	5.22×10^{-10}	1.24×10^{-10}	9.01×10^{-10}
g_{calc}	1.27	0.7	1.86
kd_{vat} [$m.s^{-1}$]	4.09×10^{-8}	3.77×10^{-8}	4.4×10^{-8}
kd_{calc} [$m.s^{-1}$]	7.34×10^{-7}	6.98×10^{-7}	7.71×10^{-7}
ka_{vat} [$s.m^{-7}$]	2.17×10^{5}	3.12×10^{3}	3.62×10^{3}
ka_{calc} [$s.m^{-7}$]	3.89×10^{6}	2.21×10^{3}	2.88×10^{3}
$A_{vat\text{-}calc}$ [$m^{4.5} \cdot s^{-1}$]	$3.05 x10^{-7}$	1.83×10^{-7}	7.32×10^{-7}
ro	1.5	1.3	1.71

Source: Own authorship

The likelihood confidence region did not include zero with 95% of confidence for all parameters. Indicating that the parameters were significant although they are somewhat correlated presenting correlation coefficients between -0.831 and 0.7150, which can be due to the model nonlinearity. This characteristic makes a precise parameter estimation difficult, however this is an intrinsic characteristic of the kinetic models with many estimated parameters

simultaneously (M. SCHWAAB AND J.C. PINTO, 2007, PRESS *et al.*, 2007). With the estimation processes concluded, it is possible to use the model simulations to understand the experimental data and their behavior.

It is common among the articles that studied this crystallization to use the SEM images analysis of the crystal habit of the crystalline forms and to identify potential transformations between polymorphs (BECK; ANDREASSEN, 2010; RODRIGUEZ-BLANCO; SHAW; BENNING, 2011; BOTS *et al.*, 2012; MAYORGA; ASTILLEROS; FERNÁNDEZ-DÍAZ, 2019). Although to fully evaluate which forms were present in the proposed experimental system, the X-ray diffraction can determine each polymorph characteristic unit cells, allowing to evaluate its mineralogy and calculate the different molar proportions between the polymorphs.

Figure 5.5 presents the SEM images for the 50, 40, 30, and 20 mmol.L^{-1} experimental conditions at the end of the process. It is possible to notice the predominance of the spherical and cauliflower-like crystalline habits that can be associated with the vaterite polymorph. The difference between these two habits can be a function of particle production, the cauliflower particles appear to have a significant agglomeration of solids. Instead, the spherical particles showed a more clean surface (RODRIGUEZ-BLANCO; SHAW; BENNING, 2011; BOTS *et al.*, 2012).

The presence of cubic-like solids, crystalline habit usually associated with the calcite polymorph can only be noted in the experiments with 50 and 40 mmol.L^{-1}. This can demonstrates that the supersaturation is a determining variable in the polymorph selection for the crystalline system (RODRIGUEZ-BLANCO; SHAW; BENNING, 2011; BLUE *et al.*, 2017). Figure 5.6 shows a vaterite particle in a dissolution process, with the reprecipitation of a new solid on its surface. This dissolution-reprecipitation process was also reported in the literature for its representation of the step rule proposed kinetic pathway (BECK; ANDREASSEN, 2010; RODRIGUEZ-BLANCO; SHAW; BENNING, 2011; BOTS *et al.*, 2012; BLUE *et al.*, 2017; MAYORGA; ASTILLEROS; FERNÁNDEZ-DÍAZ, 2019).

The SEM images indicate that the model thermodynamic calculations are correct, as the step rule calculations defined that the vaterite particles were the first to appear, and later rearrange in the more stable calcite. This pathway produces a kinetically favorable step system. The vaterite presented supersaturation with the process, offering a lower energy barrier option for the crystallization to initialize its solid production (GOWER, 2008).

Figure 5.5 - SEM images of the solid phases from all experiments at the final crystallization moments. The picture on the top left represents the more concentrated and the picture on the lower right, the less concentrated batch with C and V indicating possible calcite and vaterite crystalline habits.

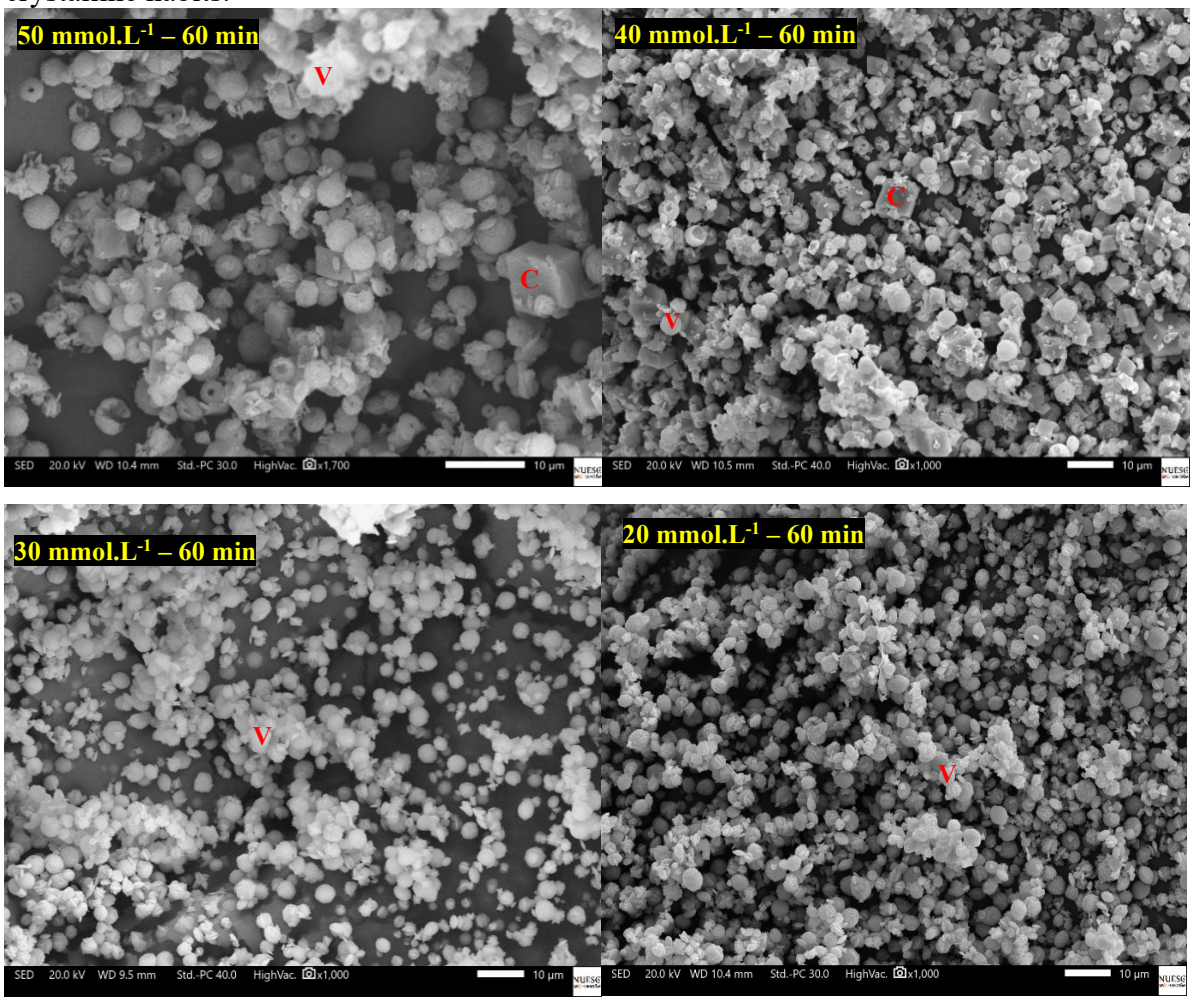

Source: Own authorship

Figure 5.6 - SEM image of a possible vaterite-calcite transformation process.

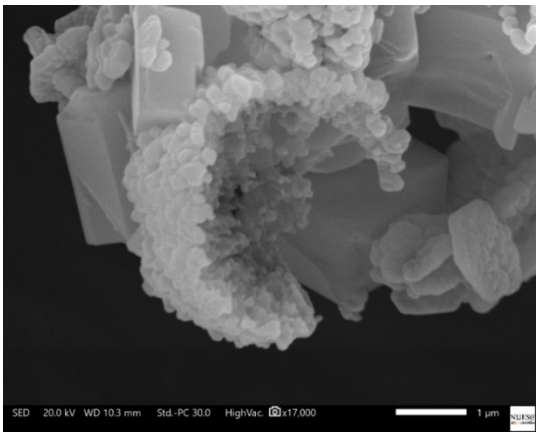

Source: Own authorship

In the XRD diffractogram, presented in Figure 5.7, it is possible to confirm that both vaterite and calcite polymorph compose the crystalline mass, as the characteristic planes for these polymorphs can be identified in the diffraction peaks.

Figure 5.7 - XRD diffractogram of the particles obtained at the end of the experiments (with 50, 40 and 30 mmol.L^{-1}), showing the intensity of the characteristics vaterite(V) and calcite(C) diffraction peaks along 20º and 70º.

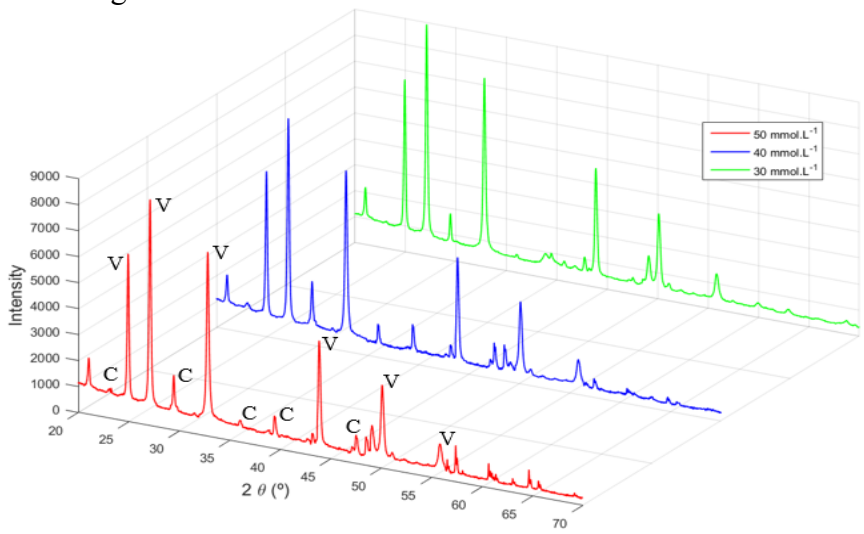

Source: Own authorship

Using the methodology of Kontoyannis and Vagenas (2000), it is possible to obtain the molar composition of the crystalline mass, using the proportion between the peaks (110), that appears close to 25º, for vaterite and (104), that appears close to 30º, for calcite. It is possible to obtain experimental crystalline proportion and compare with the model calculation (Table 5.4). Although, for 20 mmol.L^{-1}, it was not possible to identify calcite, only the vaterite polymorph; its diffractogram was not displayed in Figure 5.7 as it was very similar to the 30 mmol.L^{-1}.

Table 5.4 - Final polymorphic proportion experimental and predicted by the model.

Condition	**Exp. Calcite/Vaterite [%wt.]**	**Model Calcite/Vaterite [%wt.]**
20 mmol.L^{-1}	0/100	1.02/99.18
30 mmol.L^{-1}	1.80/98.20	2.78/97.22
40 mmol.L^{-1}	4.72/95.28	5.85/94.15
50 mmol.L^{-1}	3.31/96.69	4.74/95.53

Source: Own authorship

It is possible to notice that the model represented well the experimental results: the highest production of calcite in experiment with the 40 mmol.L^{-1} and the lowest production of calcite in the experiment with 20 mmol.L^{-1}; with a global average error of 1.4% ± 0.51%.

To better evaluate the results, one can use the rates of calcite production in proportion to those of vaterite. The higher is the proportion, the more favorable is the production of calcite, in comparison with vaterite. For clarity, the proposed calculation is presented in Equation 5.1.

$$R_{\frac{calc}{vat}} = \frac{\sum G_{calc} + Trans_{vat-calc}}{\sum G_{vat} + N_{uvat} - Trans_{vat-calc}} \quad (5.1)$$

Table 5.5 presents the mean ratio of Equation 5.1 to the simulations up to 60 minutes, i.e., the last crystallization time. It can be noted that the ratio values, for all conditions, were smaller than one. Thus, it can be observed that the rates of vaterite production were higher for all the studied reactions. Besides that, the condition of 40 mmol.L^{-1} indeed had a higher proportion, indicating that proportionally with vaterite rates it had more calcite production than its counterparts.

Table 5.5 - Ratio of the rates that produced calcite with vaterite.

Ionic concentration	$\boldsymbol{R_{\frac{calc}{vat}}}$
50 mmol.L^{-1}	0.0302
40 mmol.L^{-1}	0.0540
30 mmol.L^{-1}	0.0143
20 mmol.L^{-1}	0.0072

Source: Own authorship

Analyzing the individual components of this ratio, it was possible to see that the experiment with 50 mmol.L^{-1} of ions presented a nucleation and vaterite growth rate 2.84 times and 4.27 higher than the experiment with 40 mmol.L^{-1}, in contrast with higher calcite growth rate and transformation rates only 1.46 and 3.41 higher in the experiment with 50 mmol.L^{-1} in comparison with the rates of the 40 mmol.L^{-1}. Thus, it is possible to see that the supersaturation and initial ionic concentration affected more the rates for vaterite, than those for calcite, which agrees with the adjusted parameters, as both g_{vat} and nu_{vat} are higher than g_{calc}. Besides that, the higher mass produced in the experiment with 50 mmol.L^{-1} was consequence of the higher

secondary nucleation (15.2% higher than 40 mmol.L^{-1}). Although, for the 30 mmol.L^{-1} the transformation rate of 50 mmol.L^{-1} was 16.4 times higher than this concentration with this increase being sufficient to maintain the more concentration ratio higher calcite favoring than 30 mmol.L^{-1}.

All simulations required at least 15 hours to have the predominance of calcite, which is slower than the results of Rodriguez-Blanco *et al.* (2011) and Bots *et al.* (2012); though both had a more supersaturate system at least 30 times more as both authors added 1 mol.L^{-1} of the necessary calcium and carbonate ions.

The graphs in Figures 5.1-5.4 were combined to produce Figure 5.8, seeking to evaluate the size distribution simulations and experiments better. The model calculations obtained an average error of 3% ± 5%, indicating a generally good agreement with the experiments. It is also possible to see that the model was able to capture the right shift on the size distributions caused by the increase in the supersaturation, favoring the production of larger particles than its less concentrated counterparts.

Figure 5.8 - Simulated and experimental cumulative volumetric distribution for all experimental conditions.

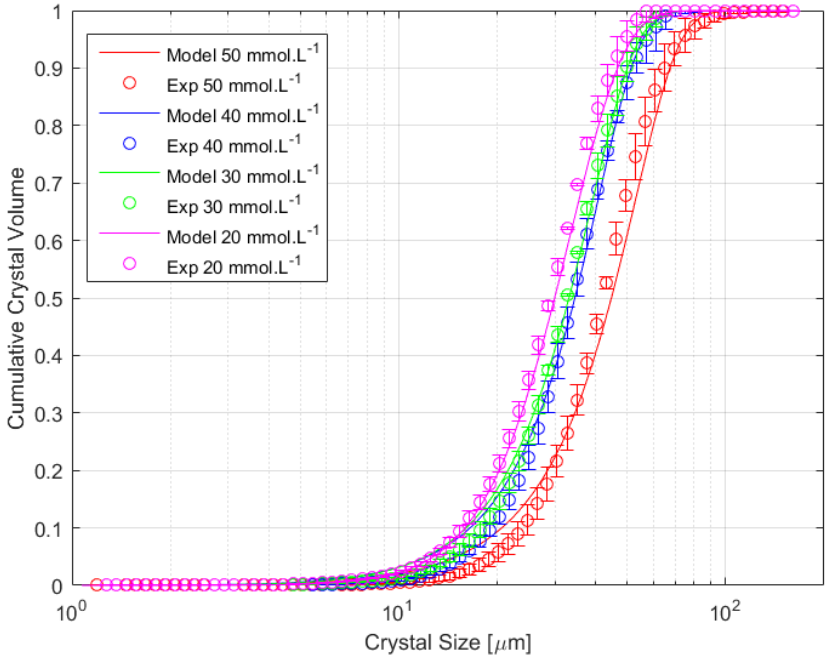

Source: Own authorship

To evaluate the size increasing effect that the supersaturation caused on both simulation and experiments, Figure 5.9 compares the simulated and experimental average volumetric diameter of the crystal populations. It is possible to notice that the concentration of 50 mmol.L^{-}

[1], on both experimental and simulation, produced larger crystals, in average, than those of experiments 40, 30, and 20 mmol.L^{-1}.

Figure 5.9 - Simulated and experimental average volumetric diameter for all conditions.

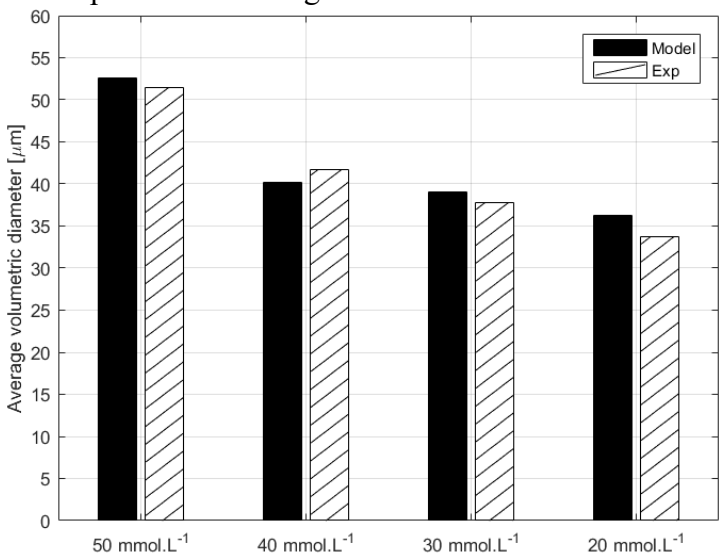

Source: Own authorship

The kinetic rates can be used to discuss the observed results. For this, the ratio between the terms in population balance that increases the particle size, i.e., growth and agglomeration, and the terms that produce that smallest size, i.e., nucleation and dissolution, , has to be evaluated.

This calculation was made for all 150 differential equations, enabling the mean ratio calculation along all reaction times (Table 5.6). Comparing this ratio for all the experimental conditions, experiment with 50 mmol L^{-1} presented the highest value. Thus, this system produces the larger particles, as this reaction presented more intense growth and agglomeration processes than the nucleation and dissolution for all experimental conditions. With the decrease of the calcium content, the ratio also decreases, showing a system that produces smaller particles, as the rates of growth and agglomeration were more affected than the nucleation and dissolution terms. Besides that, the values of these ratios for the systems with 40, 30, and 20 mmol.L^{-1} were close to each other, showing that these systems had similar proportions between the mathematical terms that account for the increase and decrease of the particle sizes, thus producing similar distributions mean particle size.

Table 5.6 - Average ratio of the mathematical terms in the population balances: with G, Agg, Nu e D, representing the population particles' overall growth, agglomeration, nucleation, and dissolution rate.

Ionic concentration	G+Agg /Nu + D
50 mmol.L^{-1}	53.31
40 mmol.L^{-1}	31.48
30 mmol.L^{-1}	28.46
20 mmol.L^{-1}	24.28

Source: Own authorship

Along with the volumetric size distribution, it is also possible to use model calculations to evaluate the differences between crystalline mass profiles. Figure 5.10 shows the simulated and experimental crystalline profiles for all conditions. It can be seen that the increase in the supersaturation resulted in higher crystal production, and that tendency was well represented by the model, with an average error of -8% ± 6%

Figure 5.10 - Simulated crystalline mass profiles for all experimental conditions.

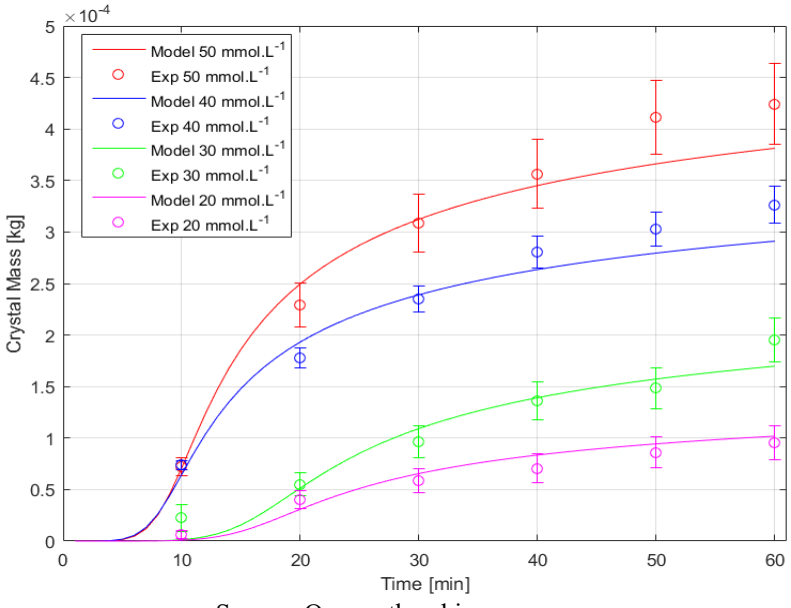

Source: Own authorship

It is possible to investigate the crystalline production, using the sum of the rates that produce mass, (growth and nucleation rates), minus the rate that reduces the crystal mass (the dissolution rate), along the time, as shown in Table 5.7.

Table 5.7 - Mean, for all size classes, of the sum of the growth and nucleation rates, minus the dissolution rate, for both calcite and vaterite, along the crystallization time.

Ionic concentration	**G+Nu- D**
50 mmol.L^{-1}	833.77
40 mmol.L^{-1}	618.75
30 mmol.L^{-1}	143.23
20 mmol.L^{-1}	85.93

Source: Own authorship

The values presented in Table 5.7 show that the more concentrated condition resulted in a higher value of the actual crystalline production, followed by the more diluted systems. This proportion among the sum is in accordance with the results in Figure 5.10, in which the system with 40 mmol.L^{-1} presented a behavior close to the system with 50 mmol.L^{-1}, whereas the system with 30 mmol.L^{-1} had a crystalline mass profile closer to the system with 20 mmol.L^{-1}.

5.2 RESULTS FROM DATA SET 2

The first step in the model calculation was also estimating which calcium carbonate forms presented thermodynamic stability, in the range of experimental conditions.

Similar to the results presented above (section 5.1), both vaterite and calcite showed thermodynamic stability in the studied conditions. The changes in the Gibbs free energy caused by the formation of vaterite and calcite polymorphs, within the first class characteristic size (0.005 μm), were -8.21 x 10^{-14} J.mol^{-1} and -2.61 x 10^{-12} J.mol^{-1}, respectively, in the system with only calcium and bicarbonate. It can be noted that the changes in the Gibbs free energy in this system were smaller than in Data Set 1, this happened as the first class size is much smaller in this data than in Data Set 1 (0.005 in comparison with 0.536 μm); consequently, the Data Set 2 is closer to the critical size for both polymorphs, that are 9.76x10^{-4} μm and 5.42x10^{-4} μm for vaterite and calcite respectively.

The supersaturation values calculated for the possible forms, presented in Table 5.8, were all higher than those values obtained for experimental data from Data Set 1 (section 5.1). This was due to the different calcium content, as instead of 50 mmol.L^{-1} of calcium, the Data Set 2 added 1 mol.L^{-1} of calcium.

Table 5.8 - Supersaturation computed at different calcium and bicarbonate ionic concentrations.

Exp.	SS calcite	SS vaterite
Ion Free(IF)	26.12	18.37
Mg-30	24.04	16.91
Mg-144	29.98	21.08
Ba-28	26.12	18.37
Ba-280	26.06	18.33
Sr-33	26.12	18.37
Sr-1500	25.59	18.00

Source: Own authorship

Besides that, as the Pitzer calculations have ion-specific interaction parameters, the impact of the ion presence is specific to its characteristics. The interaction of Mg^{2+} with HCO_3^{1-} presented parameters 1.48 times higher than those of Sr^{+2}. For the Mg^{2+} decreasing the supersaturation in the less concentrated system and after that increasing the SS value shows the non-linear dependence of the activity calculation with the ionic concentration and strength. The simulations with 30 ppm produce calcium activity coefficients 18.6% smaller than those of simulations with 144 ppm of Mg^{2+}.

It is important to emphasize that the kinetic results of model simulations obtained in the above section (5.1) cannot quantitatively predict the results of other particle sizing techniques, such as dynamic light scattering utilized in the Data Set 2. Due to the different physical principles of the measurements, different representative sizes may be measured by different techniques (HEATH *et al.*, 2002; TRAMPUŽ; TESLIĆ; LIKOZAR, 2019). This effect can be seen in the different size classes that both types of equipment produced. the size distribution classes for the Data Set 1 and 2 are plotted in Figure 5.11. It is possible to observe that the FBRM (Data Set 1) obtained size classes with diameters in average 1731% larger than the DLS equipment (Data Set 2). However, it should be noted that the Data Set 2 presented larger diameters for the classes 60 to 75.

Figure 5.11 - Comparison of the granulometric size class for the Data Set 1 and 2.

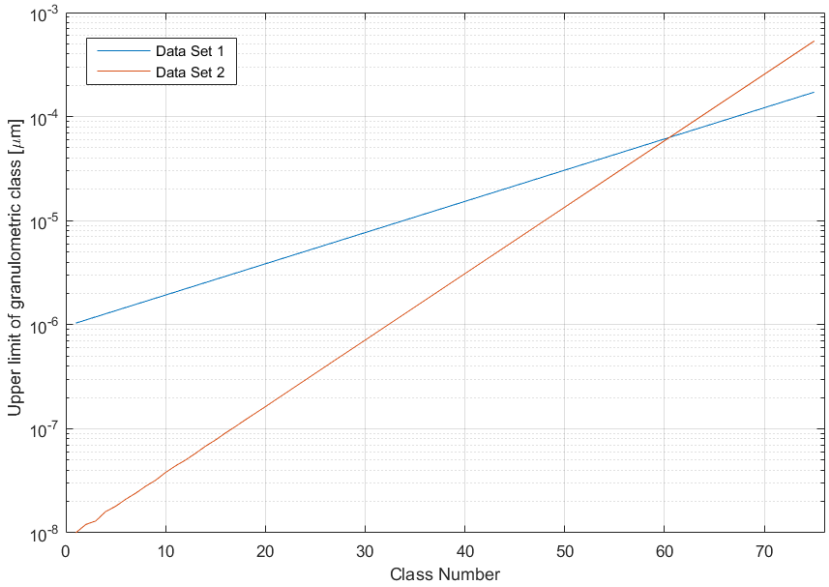

Source: Own authorship

Accordingly, the model parameter estimated for the Data Set 1 based on a particle chord distribution, as opposed to a conventional diameter-based distribution (DLS, used in the Data Set 2), is better used to predict the crystal size distributions determined by FBRM (HEATH *et al.*, 2002; TRAMPUŽ; TESLIĆ; LIKOZAR, 2019). Thus, the set of the Data Set 2 utilized in the optimization step, produced a different set of parameters (Tables 5.7 and 5.9) than those obtained from Data Set 1.

The obtained growth parameters (Table 5.9) agreed with those reported by Brecevic and Kralj (2008); that the vaterite presents higher initial growth rates than the calcite. It is also possible to compare the simulated growth rates for each polymorph with the results obtained by these authors, observing that the present work obtained average higher growth rates for the vaterite polymorph, 4.14×10^{-7} m.s^{-1} in comparison with 1.69×10^{-7} m.s^{-1} obtained in Brecevic and Kralj(2008), and average lower growth rates for the calcite, 1.06×10^{-9} m.s^{-1} compared to the 8.83×10^{-9} m.s^{-1} obtained by Brecevic and Kralj(2008). Both initial growth rates were also higher than those obtained with Data Set 1 (Table 5.3), as both polymorphs were more supersaturated in this case. Furthermore, it can be determined, based on Teng et al.(2000), from the g_{calc} and $g_{vat,}$ that the Data Set 1 and 2 growth rates presented relation with supersaturation closer to those mechanisms of rough and simultaneous spiral-polynuclear growth, respectively.

The initial nucleation rate observed was smaller than those obtained by Chakraborty and Bhatia (1996b), 1.81×10^{-3} L^{-1}.s^{-1} compared to 3.38×10^{-1} L^{-1}.s^{-1} and those obtained from the Data Set 1. This slower initial nucleation rate is a direct function of the secondary nucleation

influence. Table 5.9 presents a n_{1vat} = 0.8, producing a higher influence of the secondary nucleation in this data than in Data Set 1 and Chakraborty and Bhatia (1996b), as these obtained n_{1vat} = 0.35 (Data Set 1) or did not include a specific secondary nucleation term(Chakraborty and Bhatia (1996b)). Thus even with a higher supersaturation, that Data Set 2 had over Data Set 1 it still was produced an initial smaller value of that the obtained with the Data Set 1.

It was also possible to observe that the calcite polymorph presented an agglomeration tendency 6.76 times higher than vaterite, more similar to those from Chakraborty *et al.* (1994) than the Data Set 1. Though, the actual agglomeration parameters (Table 5.9) were smaller than those obtained from Data Set 1, probably related to the fact that the Data Set 1 presented larger solids, as shown in Figure 5.11.The discussed differences in the experimental conditions from the literature conditions discussed in 5.1 were also presented here, with the more notable differences being the supersaturations, ionic strength, 2.35 mol.L^{-1} in comparasion with 0.19 mol.L^{-1}, and reactor configuration that the Data Set 2 had over Data Set 1.

Table 5.9 - Kinetic Parameters obtained through optimization.

Parameter	**Estimated Value**
kn_{vat} [1.m^{-3} kg^{-1} s^{-1}]	2.6 x 10^{2}
n_{vat}	4.3
kg_{vat} [m.s^{-1}]	3 x 10^{-21}
g_{vat}	7.2
n_{1vat}	0,8
kg_{calc} [m.s^{-1}]	1.5 x 10^{-12}
g_{calc}	1,5
kd_{vat} [m.s^{-1}]	6.7 x 10^{-9}
kd_{calc} [m.s^{-1}]	3.1 x 10^{-8}
ka_{vat} [s.m^{-7}]	3.3 x 10^{4}
ka_{calc} [s.m^{-7}]	2.56 x 10^{5}
$ro_{vat-calc}$	1.8
$A_{vat-calc}$ [$m^{5.4}$.s^{-1}]	2 x 10^{-13}

Source: Own authorship

The results of the routine responsible for the selection of rates affected by the divalent ions (Mg^{2+}, Ba^{2+}, and Sr^{2+}) are presented in Table 5.10. This table shows the median and standard deviation value of the objective function obtained by the inclusion of Equation 3.64 in the mentioned rates for each divalent cation in all possible pairs of kinetic rates.

Table 5.10 - Statistical results of affected rates inclusion in the objective function for the experiments with the specific divalent ion. The smallest F_{obj} obtained for each ion was colored in red, blue, and green for Mg, Ba, and Sr, respectively.

Affected rates	Fobj Mg^{2+}	Fobj Ba^{2+}	Fobj Sr^{2+}
Nucleation and Vaterite Growth	61.3 ± 15.2	158.5 ± 52.1	85.2 ± 38.5
Nucleation and Calcite Growth	48.7 ± 13.9	132.2 ± 43.5	70.5 ± 47.4
Nucleation and Transformation	**15.1 ± 3.28**	168.9 ± 58.9	105.2 ± 46.5
Nucleation and Vaterite Agglomeration	80.2 ± 7.6	156.4 ± 51.4	126.2 ± 27.7
Nucleation and Calcite Agglomeration	55 ± 20.4	70.3 ± 23.1	168.2 ± 18.6
Nucleation and Vaterite Dissolution	72.8 ± 20.6	160.6 ± 52.8	91.5 ± 21.6
Nucleation and Calcite Dissolution	41.3 ± 6.9	125.9 ± 41.4	95.7 ± 48.5
Vaterite Growth and Calcite Growth	161.0 ± 8.9	68.2 ± 22.4	181.8 ± 38.5
Vaterite Growth and Transformation	80.2 ± 15.8	71.3 ± 23.4	174.5 ± 29.7
Vaterite Growth and Vaterite Agglomeration	120.1 ± 25.4	155.3 ± 51.1	141.9 ± 46.5
Vaterite Growth and Calcite Agglomeration	76.0 ± 16.1	79.7 ± 26.	113.6 ± 22.7
Vaterite Growth and Vaterite Dissolution	67.6 ± 17.4	53.0 ± 14.4	159.8 ± 45.6
Vaterite Growth and Calcite Dissolution	165.2 ± 22	85.0 ± 27.9	149.3 ± 15.9
Calcite Growth and Transformation	49.7 ± 10.3	**22.0 ± 7.2**	**30.6 ± 8.6**
Calcite Growth and Calcite Agglomeration	135.8 ± 21.1	65.6 ± 18.3	60.6 ± 27.1
Calcite Growth and Vaterite Agglomeration	98 ± 27.5	61.9 ± 13.8	68.4 ± 25.9
Calcite Growth and Vaterite Dissolution	42.4 ± 16.9	57.7 ± 12.4	89.4 ± 19.1
Calcite Growth and Calcite Dissolution	74.9 ± 11.51	86.0 ± 28.3	48.5 ± 14.4
Transformation and Vaterite Agglomeration	44.5 ± 6.3	57.7 ± 19	80.0 ± 24.7
Transformation and Calcite Agglomeration	40.3 ± 5.5	96.5 ± 31.7	61.1 ± 14.7
Transformation and Vaterite Dissolution	88.6 ± 7.6	46.7 ± 11.4	77.9 ± 25.9
Transformation and Calcite Dissolution	26.6 ± 8.3	99.7 ± 32.8	65.3 ± 21.5
Calcite Agglomeration and Vaterite Dissolution	134.8 ± 28.8	155.3 ± 51.1	89.4 ± 12.1
Vaterite Agglomeration and Vaterite Dissolution	83.3 ± 22.4	70.3 ± 23.1	64.2 ± 11.5
Calcite Agglomeration and Calcite Dissolution	135.8 ± 36.8	103.9 ± 34.1	50.6 ± 14.4
Vaterite Agglomeration and Calcite Dissolution	76.0 ± 13.4	141.7 ± 46.6	76.8 ± 15.6

Source: Own authorship

For all possible combinations in Table 5.10, a Wilcoxon Rank Sum Test was made for each pair of combinations obtaining with 95% confidence, that the best adjustment was obtained through the routine inputting the Mg effect with the nucleation rate of the vaterite and transformation rate. As for Sr and Ba, their effects were put with the calcite growth and transformation rates. With the location of the effects defined, a final optimization was run with all experiments and the estimated parameters responsible for these results are presented in Table 5.11.

Table 5.11 - Obtained empirical effects parameters for each divalent ion.

Parameter	Estimated Value
$a_{MgNuVat}$	-2.85
$b_{MgNuVat}$	0.38
$a_{MgTrans}$	-2.52×10^3
$b_{MgTrans}$	26.36
$a_{SrGCalc}$	23.4
$b_{SrGCalc}$	1.09
$a_{SrTrans}$	2.3×10^2
$b_{SrTrans}$	1.4×10^3
$a_{BaTrans}$	3.3×10^3
$b_{BaTrans}$	1.9×10^3
$a_{BaGCalc}$	74.5
$b_{BaGCalc}$	1.07

Source: Own authorship

The presence of Magnesium resulted in an inhibition of the nucleation of vaterite and acceleration of the polymorphic transformation, vaterite-calcite, in the conditions of experiments Mg-30 and Mg-144. However, both effects decreased with increasing the concentration of Magnesium. For the Strontium and Barium both calcite growth rate and vaterite-calcite transformation rate were accelerated, with the effect intensity being higher with higher concentration.

The SEM micrographs for the samples obtained during the experiments (Figure 5.12) present crystalline habits consistent with vaterite, spherical or in cauliflower-like aggregates, and the calcite cubic for all conditions (RODRIGUEZ-BLANCO; SHAW; BENNING, 2011;

BLUE *et al.*, 2017; MAYORGA; ASTILLEROS; FERNÁNDEZ-DÍAZ, 2019; SANJIV RAJ; DEVI; SUBRAMANIAN, 2020). With the solid distribution characteristics presented in Fig. 5.12, it is possible to notice the influence of the secondary nucleation and agglomeration in the process, as can be noted in the presence of smaller crystals on the larger solids surface. Besides, it is possible to note that the polymorphic transformation, either solid-state or solution mediated, was highly influenced by the presence of external ions, especially for the experiments with Ba and Sr (BOTS *et al.*, 2012; MAYORGA; ASTILLEROS; FERNÁNDEZ-DÍAZ, 2019).

Figure 5.12 - SEM micrographs of the precipitates recovered from solutions with different ionic compositions, after a range of elapsed times of 5-90 minutes. (Continues on next page)

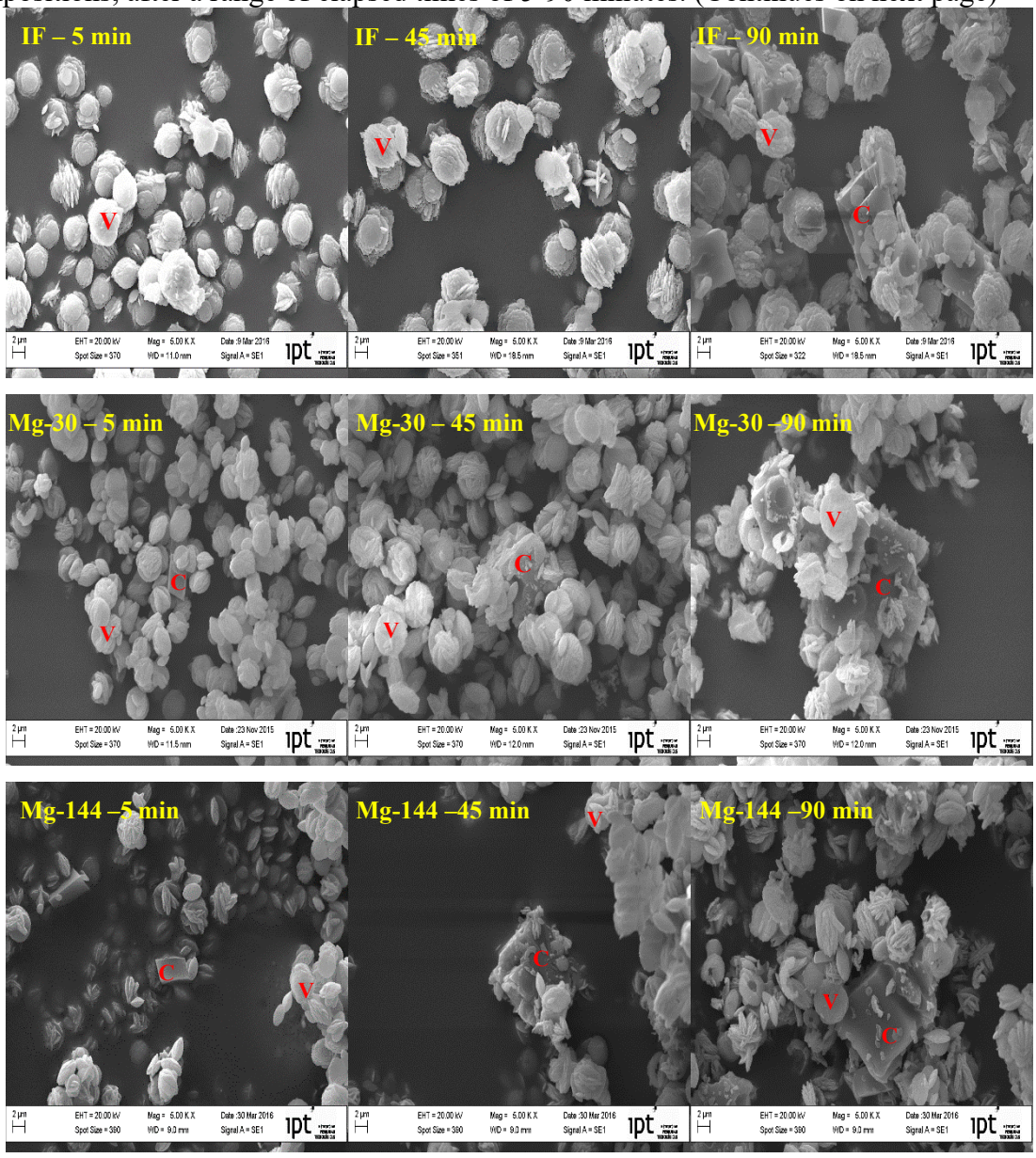

Figure 5.12 - SEM micrographs of the precipitates recovered from solutions with different ionic compositions, after a range of elapsed times of 5-90 minutes.

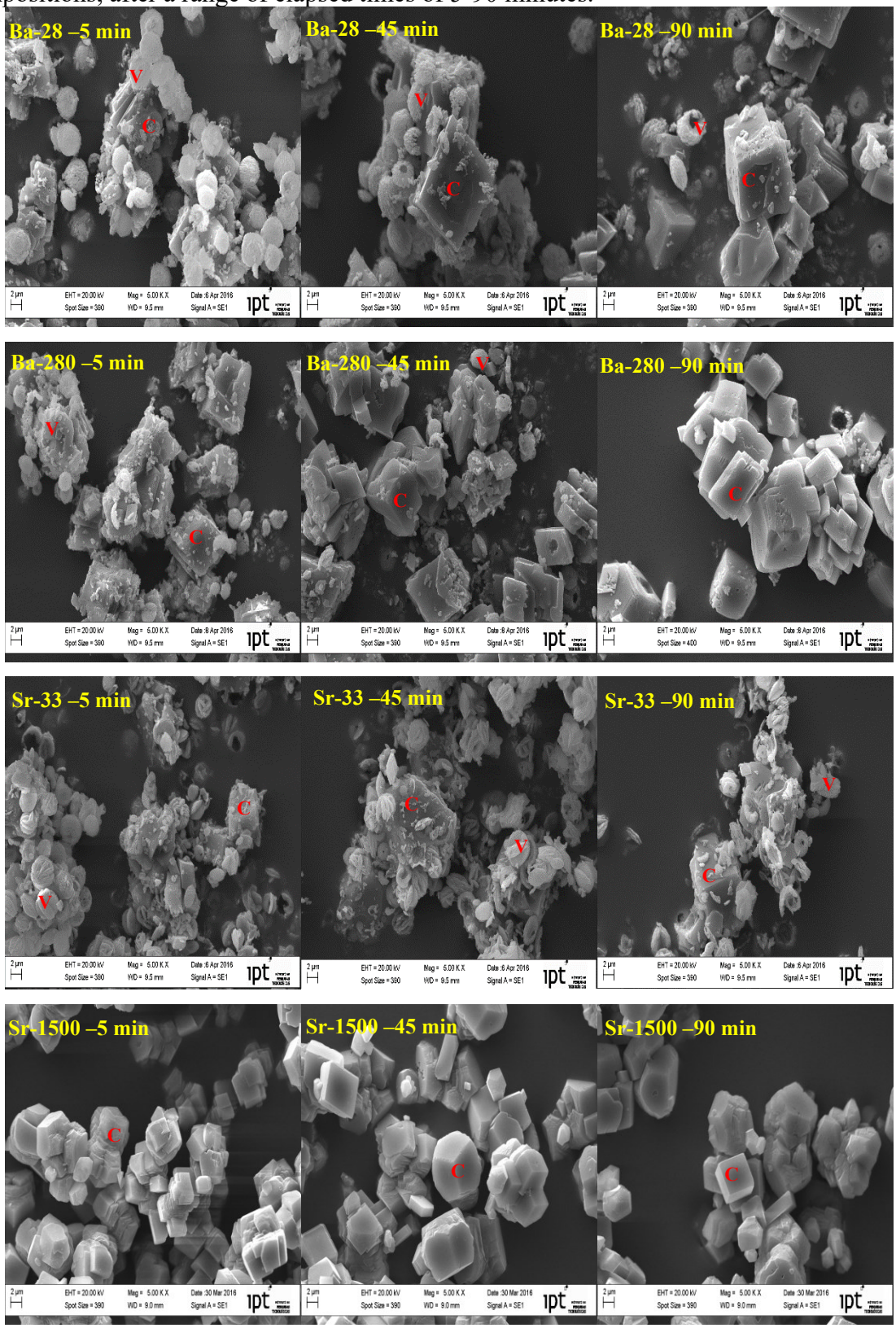

Source: Own authorship

The XRD profile with time for the Ion Free experiment (Figure 5.13) was similar to vaterite-calcite transition profiles observed by Rodriguez-Blanco *et al.* (2011) and Bots *et al.* (2012), and presented calcite production in higher proportions than the Data Set 1 . The ionic concentrations of the Data Set 2 are closer to these experiments, as it also worked with 1 $mol.L^{-1}$ of calcium. Thus, it presented the necessary supersaturation to produce similar calcite profiles.

It is also possible to do a calculation similar to those of Table 5.3 to evaluate the ratio of the calcite and vaterite production rates, obtaining a value of 0.127, which is a higher calcite/vaterite ratio of production than the most calcite producing system(Data Set 1), 40 $mmol.L^{-1}$, that obtained 0.054. In this comparison Data Set 2-1, the increase in supersaturation with a different reaction system caused the production of a higher number of vaterite particles per liter, 2.849 x 10^9 $particles.L^{-1}$ (Data Set 2) instead of 1.37 x 10^7 $particles.L^{-1}$ (Data Set 1). This number of vaterite particles per liter produced an increase of 3,634% on transformation rate that carried the system to produce higher calcite ratios in Equation 5.1.

As for the calcite appearance rates, Brecevic and Kralj (2008) concluded that the calcite growth was the rate-determining process for the overall transformation of vaterite to calcite based on a mathematical model of Davey *et al.* (1986). Similar observations can be made with the populational balance proposed in this work, in which the calcite growth rate was increased by 20%, the final calcite content increased by 8% a value higher than when the transformation rate was increased by 60%, increasing only 3% of the calcite content. The transformation rates calculated by all vaterite size classes were similar to the obtained by Chakraborty and Bhatia (1996a, 1996b). However, the present model obtained a reaction order of 1.8, instead of a first-order reaction obtained in this work. In consonance with the works mentioned above, the reaction on the crystal surface was the rate-determining step for the growth of both polymorphs, as the crystalline external effectiveness factor was always higher than 0.9 for all class sizes. It was also possible to notice, in Figure 5.13, that the model described well the kinetics of the polymorphic distribution for the Ion Free conditions, presenting an absolute average error of 2 ± 3% in relation to the mass proportion of both polymorphs.

Figure 5.13 - Polymorphic proportion along the time for the Ion Free experiment, determined from vaterite peak (101) and calcite peak (104) from the XRD diffractogram, after the Rietveld treatment.

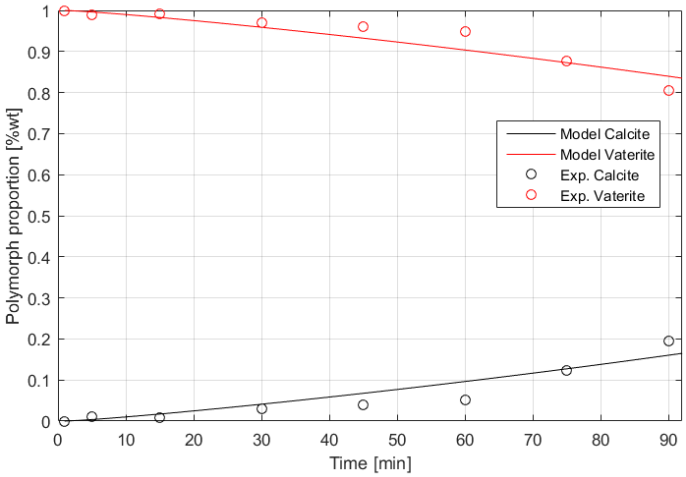

Source: Own authorship

The effect of external ions, Mg^{2+}, Ba^{2+} and Sr^{2+} , in the formation of vaterite and calcite, can be observed on the polymorphic proportion, presented in Figures 5.14 to 5.16. The polymorphic proportion, for the rhombohedral calcite and hexagonal vaterite in comparison with the Ion Free experiment, was calculated by integration of the XRD results, using the a methodology similar with the work of Kontoyannis and Vagenas (2000) (KONTOYANNIS; VAGENAS, 2000; BECK; ANDREASSEN, 2010; MAYORGA; ASTILLEROS; FERNÁNDEZ-DÍAZ, 2019). For the Magnesium ions (Figure 5.14), the appearance of calcite crystals did not increase proportionally with the concentration of Mg; Mg-144 resulted in a final calcite content (41.9 wt.%) lower than Mg-30 (59 wt.%), although it still produced higher contents than the Mg-free experiment at the end of its crystallization (19.4 wt.%). For the Barium ions (Figure 5.15) and Strontium ions (Figure 5.16), the calcite crystals were already predominant in the initial moments of the experiment. The consequent increase in the concentration of external ions intensified this effect, even though the highest concentration of the Sr ions resulted in a similar increase in the calcite production.

Figure 5.14 - Comparison between the simulated and experimental data for the polymorphic proportions obtained in the experiments: Ion Free, Mg-30, and Mg-144, along the crystallization time.

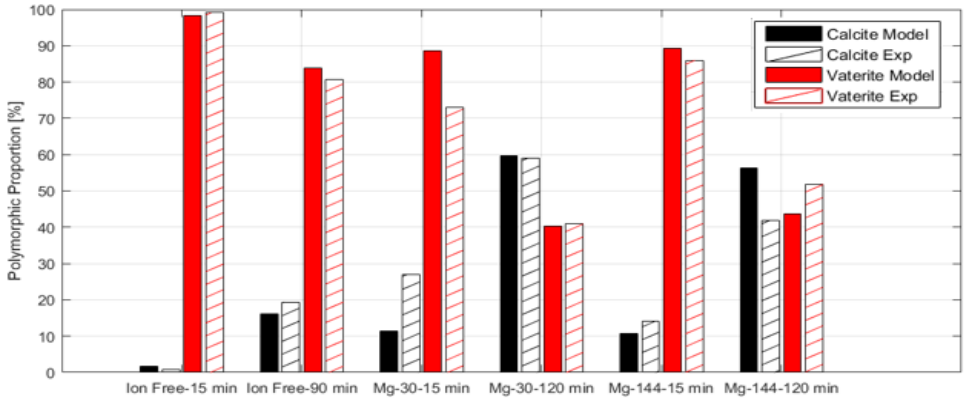

Source: Own authorship

For the Mg experiments, it was possible to noticed that an early appearance of calcite was observed for both concentrations in Figure 5.14. It is possible to observe that this phenomenon was well represented by the model, obtaining an average error of -7% ± 12% for Mg-30 and 5% ± 13% for Mg-144. To better evaluate this effect, it is better to discuss both rates influenced by Mg addition: the nucleation rate of vaterite and its transformation to calcite. The possible inhibition of vaterite by Magnesium was also observed by Bots *et al.* (2011), which was associated with changes in the crystal structure caused by the Mg incorporation. Du and Amstad (2019) discussed that the Mg could increase the amorphous calcium carbonate lifetime by slowing the kinetic dehydrations necessary to its transition to vaterite, thus slowing its appearance rate. The model calculations obtained a nucleation rate 57,9% slower for Mg-144 and 62,3% slower for Mg-30 (compared to the ion free experiment); the increase in the Magnesium content that did not produce a higher inhibition can show the complex mechanisms that underline these ionic contributions.

The interrelation between the solution conditions and crystalline characteristics can play a decisive role in the ionic incorporation of external ions into calcium carbonate solids. As the distribution coefficient of the Magnesium in the vaterite/solution and amorphous calcium carbonate/solution were shown to increase with the decrease in the Mg concentration (SAWADA; OGINO; SUZUKI, 1990). Thus, the conditions in the experiment Mg-30 can favor the incorporation of this ion in the amorphous/vaterite structure more than for the experiment Mg-144. An increase in the transformation rates calculated by the model was also observed, with kinetic rates 12.1 (Mg-144) and 23.42 (Mg-30) times higher than the Mg-Free experiment. Rodriguez-Blanco *et al.* (2011) also obtained a higher content in the calcite formation in the

presence of Magnesium. The authors concluded that Mg incorporation could decrease the kinetic barrier for the transition from vaterite to calcite, favoring the calcite formation. (CHEN; NEVILLE, 2004; GOWER, 2008; RODRIGUEZ-BLANCO *et al.*, 2011; BOTS *et al.*, 2012; BLUE *et al.*, 2017). Higher rates for the experiment with less Magnesium can be associated with the inhibition that Mg can cause in the calcite growth rate, slowing the appearance rate of this polymorph, as this growth rate was shown to be the rate-determining of the transformation (SAWADA; OGINO; SUZUKI, 1990; CHEN; NEVILLE, 2004; BREČEVIĆ; KRALJ, 2008; ASTILLEROS; FERNÁNDEZ-DÍAZ; PUTNIS, 2010). Mg incorporation could cause a change in the polymorphic appearance, as observed by Davis *et al.* (2000), with the aragonite becoming the more stable solid. However, it did not happen in the present work, since the Mg to calcite proportion was smaller than the 1.8% mol, concentration identified as when aragonite became the more stable polymorph.

In the experiments with Strontium and Barium ions, similar effects were observed in Figures 5.15 and 5.16. The obtained error was of 6% ± 11% for Ba-28 and -12% ± 11% for Ba-280, as for Sr-33 and Sr-1500 were 5% ± 14% and -8% ± 9%. The presence of these ions favored the formation of calcite , increasing the vaterite-calcite transformation and calcite growth rate. Astilleros *et al.* (2000) discussed that the calcite crystal presents an inability to accommodate the Sr and Ba ions, which have different physicochemical properties than Ca. This limitation can also be expected in the vaterite polymorph based on the crystalline properties of its crystal structure (WANG; BECKER, 2009).

Figure 5.15 - Comparison between the simulated and experimental data for the polymorphic proportions obtained in the experiments: Ion Free, Ba-28, and Ba-280 along the crystallization time.

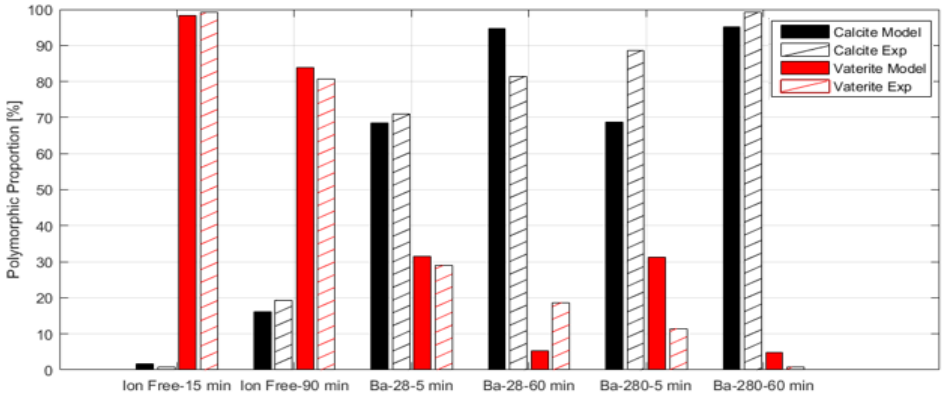

Source: Own authorship

Figure 5.16 - Comparison between the simulated and experimental data for the polymorphic proportions obtained in the experiments: Ion Free, Sr-33, and Sr-1500 along the crystallization time.

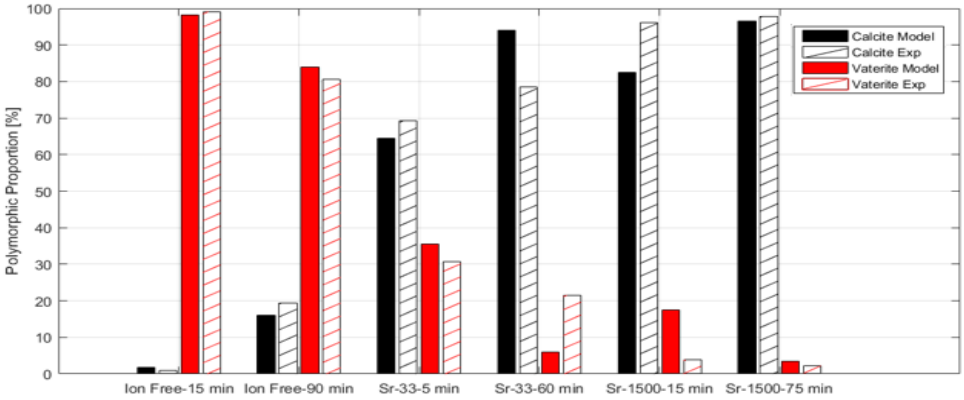

Source: Own authorship

Although, from similar conditions used in this present work, Kitano *et al.* (1971) observed that these ions could present high distribution coefficients within the calcite polymorph, producing crystals with high Sr and Ba content especially in the initial moments of the crystallization. This incorporation could be responsible for the obtained increase by 9% (Ba-28), 24% (Ba-280), 8% (Sr-33), and 52% (Sr-1500) in the calcite growth rate by the adjusted model. It also interfered with the vaterite-calcite transition, which produced significant increases of 94.2 (Ba-28), 96.6 (Ba-280), 51.7(Sr-33), and 54.3 (Sr-1500) times following the parameter estimation. As these ions are incorporated into the calcite structure, modification with the supersaturation of the crystal structures will not be a single value but a function of the solid composition (PRIETO *et al.*, 1997; ASTILLEROS *et al.*, 2000). As both strontium carbonate ($K_{sp} = 2.58 \times 10^{-9}$ at 25ºC and 1 atm), and barium carbonate ($K_{sp} = 1.3 \times 10^{-9}$ at 25ºC and 1 atm) are less soluble than the calcium carbonate calcite ($K_{sp} = 3.33 \times 10^{-9}$ at 25ºC and 1 atm), the incorporation of Sr and Ba ions could cause an increase of the calcite supersaturation. It would have increased its growth rate, which is the direct function of calcite supersaturation and potentially its transformation rate, producing faster growth and transformation rates than more soluble calcite. (BREČEVIĆ; KRALJ, 2008; RODRIGUEZ-BLANCO *et al.*, 2011; BOTS *et al.*, 2012; GEBAUER *et al.*, 2014; BLUE *et al.*, 2017; LASSIN *et al.*, 2018).

Sr and Ba favored the production of calcite, as the model attempted to increase both of its rates that produce this polymorph. This effect was noted by Kitano (1962) for a range of Ba and Sr contents in proportion with Ca concentration. In the experiments with Ba, with proportions similar to Ba-28 and Ba-280, an increase in calcite production was observed. However, with the Ba:Ca ratio in concentration increasing at least 100 times above Ba-280, the

formation of vaterite polymorph seemed to be favored, an effect also observed by Sanjiv *et al.* (2020). For the Strontium ions, both Sanjiv *et al.* (2020) and Kitano (1962) observed that formation of aragonite was favored with Sr addition, although the latter observed that in concentrations close to the experiments Sr-33 and Sr-1500, with the presence of chloride ions, the aragonite production was inhibited and the calcite was the more stable polymorph.

However, in concentrations at least 20 times higher than Sr-1500, Sanjiv *et al.* (2020) continued to observe that aragonite formation was favored by kinetic reasons linked with the concentration gradient of the Sr ions in the media. This different behavior observed with different concentrations can illustrate the complexity of the studied phenomena, demonstrating that the obtained model correlation and experimental results apply to conditions similar to the present work.

It is also possible to notice that the model correctly predicted that vaterite was first formed and then, subsequently transformed in calcite for all experimental conditions, as expected by the Ostwald-Lussac rule of stages calculations made in the model. For the actual proportion of polymorphs presented in the crystallization media along the time, it can be seen that the simulated calculations had a general agreement with the experimental data, with an average error of 7.9% ± 7%. It is also possible to see that the model represented the influence of the external ions in the polymorphic changes. The model predicted the observed acceleration and the different magnitudes produced by each ion. Although the model did not describe the influence of the ionic concentration increase, the difference in calcite proportion at the final moments in the magnesium experiments was predicted as 3.2%, a value smaller than the experimentally observed (17.1%). This problem also applied for experiments with Barium and Strontium , as the difference in calcite predictions was 0.4% and 2.5% compared to the 17.9% and 19.3% that experimental data indicated. This could be caused by linearity of the equations chosen to model these effects, as such complex mechanisms can have non-linear behaviors as shown by the Sanjiv *et al.* (2020) and Kitano (1962).

The crystalline mass profiles obtained in the crystallization experiments with Mg, Sr, and Ba are presented in Figures 5.17 to 5.19, respectively. The addition of Mg caused an average, in relation with time, reduction of 12% and 8% (Mg-30 and Mg-144) in the production of crystalline mass, presenting final average mass values of 7.62, 7.81 and 7.95g (Mg-30, Mg-144 and IF) at 90 minutes. The experiments with Ba and Sr also presented this limitation, with an average, in relation with time, reduction, in relation with time, in the crystalline mass of

18%, 16%, 11% and 13% (Ba-28, Ba-280, Sr-33, Sr-1500) and final average mass values of 7.38, 7.58, 7.76 and 7.60g (Ba-28, Ba-280, Sr-33, Sr-1500).

The model calculations for crystalline mass produced with experimental conditions (Figure 5.17 to 5.19) presented a general agreement with the experimental values, with an average error of 14% ± 8% in the crystalline mass obtained. It is important to notice that the main discrepancies appeared in the first moments of the crystallization, so that calculating the error without these values resulted in an average value of 8% ± 3%. Besides that, it is possible to see that the simulations can predict the reduction in the mass profile along the reaction caused by the presence of the external ions, producing in average 6% (Mg-30), 4% (Mg-144), 16.2% (Ba-28), 13.8% (Ba-280), 14.1% (Sr-33) and 7% (Sr-1500) smaller masses than those of the simulations for Ion Free conditions. However, it can be noted that the simulations for both Ba-280 and Sr-1500 produced 3% and 16% higher final mass than the Ion Free condition.

With both experimental and simulated data is possible to observed that the experiments achieved crystal masses closer to the thermodynamic equilibrium, close to 8.1g for all experiments, sooner than the simulations; with the experimental data presenting crystalline masses closer to each other than the calculated ones. In the Mg data, the simulations needed 105 minutes to achieve the same percentual difference in the final mass obtained by the experiments at 90 minutes; indicating that the simulated rates develop somewhat slower than the experimental ones.

It is also possible to do a calculation similar to that presented in Table 5.5, using the sum of growth and nucleation rate, minus the dissolution, for both calcite and vaterite. The calculated value is $7.294 \times 10^{4,}$ which is higher than that obtained with Data Set 1 (section 5.1, with 50 $mmol.L^{-1}$ of calcium) obtained value equal to 833.7. This higher value can be associated with the higher nucleation (781%) and polymorphic growth rate (125.6% higher) that the Data Set 2 system presented over Data Set 1.

The results presented in Figure 5.17 to 5.19 can be also evaluated by the influence of the ions in the kinetic rates responsible for the crystalline mass production, i.e., nucleation and growth rates. Though it should be noted that polymorphic transformation does not produce an increase in the total mass, it rearranges the crystal structure and the calcite and vaterite polymorphs have different growth rates.

Starting with the Magnesium experiments, as already mentioned before, both systems produced in average, in relation with time, smaller crystal masses in comparison with Ion Free, although the Mg experiments produced similar crystalline mass, with the Mg-144 being only,

in average, 2% higher than Mg-30. As evaluated in the polymorphic discussion, this ion affected the vaterite nucleation rate and its transformation rate, two phenomena that can cause a reduction in the crystalline mass. The 57.9% reduction in the nucleation rate calculated in Mg-144 represents less production of new vaterite crystals, directly affecting the crystal mass. However, the same could be said by the 62.3% reduction observed in Mg-30, affecting the nucleation rate about 4.4% more than Mg-144. Thus, this contributed to the smaller crystal production, along the experimental time, observed in the experiment with 30 ppm of magnesium.

The 11.2 times (Mg-144) and 23.4 (Mg-30) acceleration in the vaterite-calcite transformation also influenced the mass profiled obtained with these reactions. As calcite grows on average 82.17% slower than vaterite along the reaction time, the higher its presence, the fewer crystalline mass was produced, as its crystals do not integrate new ions as fast as vaterite. Therefore, this also contributed to the higher crystal production as the Mg-144 predicted a smaller calcite content.

Figure 5.17 - Comparison of experimental and simulated results for the crystal mass obtained in experiments with Mg.

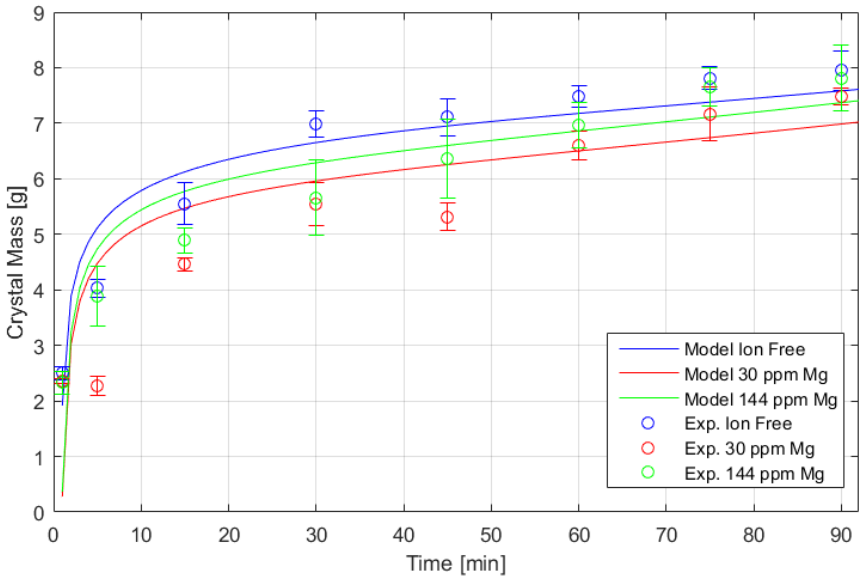

Source: Own authorship

The same time-average analysis in comparison with IF can be made to Barium and Strontium experiments, with the difference that those increased the calcite growth rate and accelerated its transformation from vaterite. Although, it can also be noted that the Ba and Sr simulations, and experiments, also presented closer crystalline mass between each other, 2.4% and 7.1% average differences, than with those discussed in comparison with IF.

The difference between the growth rate of the polymorphs was, on average, 72% (Ba-28), 65% (Ba-280), 73% (Sr-33) and 32% (Sr-1500) of those of Ion Free. Although, it is possible to see that the calcite still presented slower rates, in average, than vaterite in these experiments. As Ba and Sr ions also highly influenced the vaterite-calcite transformation rates and produced higher calcite contents than Ion Free, the slower time-average crystalline production is a function of the more significant presence of a polymorph that still grows, at average, slower than its counterpart.

Though calcite presented a lower average growth rate than vaterite for the Sr and Ba experiments, there was a moment in the crystallization that the Ba-280 (54 min) and Sr-1500 (43 minutes) started to obtain higher growth rates for the calcite instead of vaterite. This moment happened by the acceleration produced by both Sr and Ba ions in this rate and the depletion of the supersaturation; the latter affects more the vaterite rate than the calcite, as it presented a much higher dependence of this variable, 7.2 in comparison of 1.5 that calcite presented. This acceleration is associated with the moment when Ba-280 and Sr-1500 produced more mass than the simulations with the ion free conditions. As when the calcite started to grow faster than vaterite, the difference between these rates only increased up to a point where the more stable polymorphs started growing approximately 100, Ba-280, or 1000, Sr-1500, times faster.

Figure 5.18 - Comparison of experimental and simulated results for the crystal mass obtained in experiments with Ba.

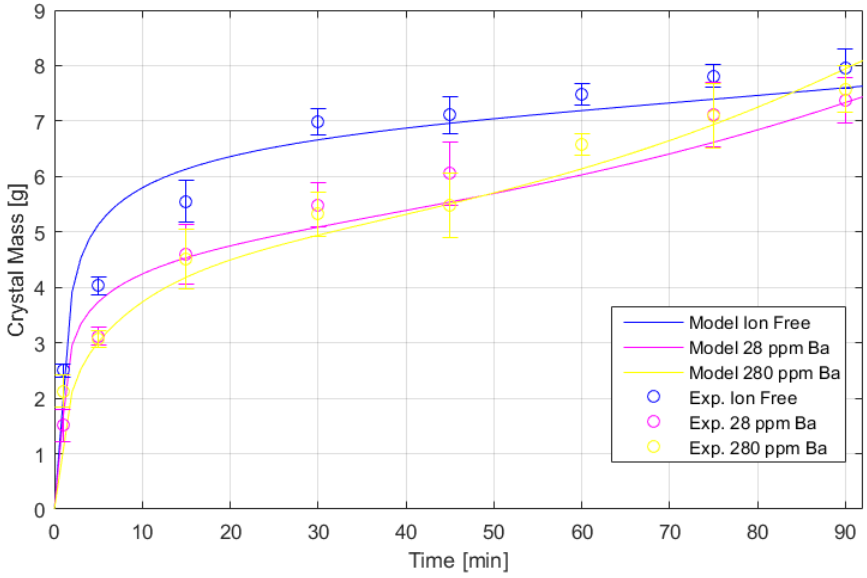

Source: Own authorship

Figure 5.19 - Comparison of experimental and simulated results for the crystal mass obtained in experiments with Sr.

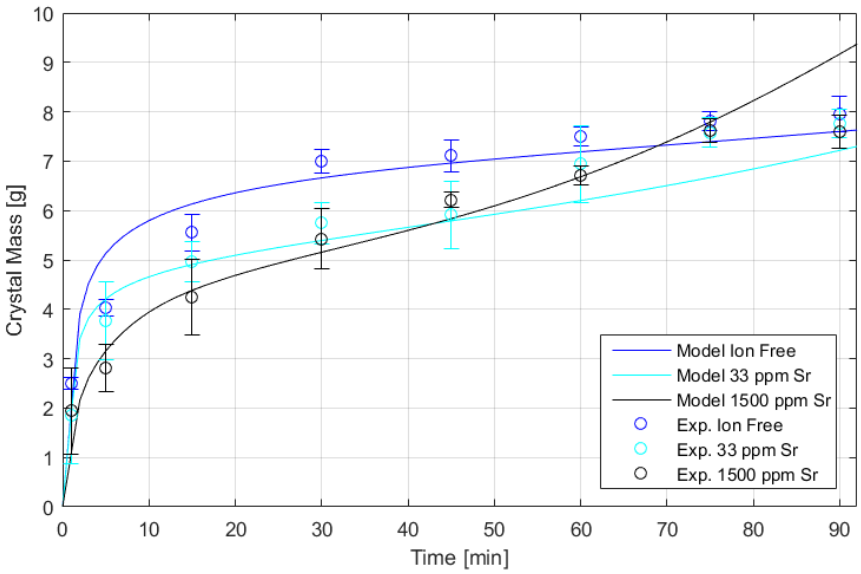

Source: Own authorship

The sequence of graphs presented in Figures 5.20 to 5.22 compares the simulated data with the experimental data for the final size distribution. The model calculations obtained an average error of 8% ± 7%, indicating a generally good agreement with the experiments.

Figure 5.20 - Comparison of experimental and simulated results for the cumulative crystal volumetric size distribution, at 90 minutes, for Mg-30, Mg-144, and Ion Free conditions.

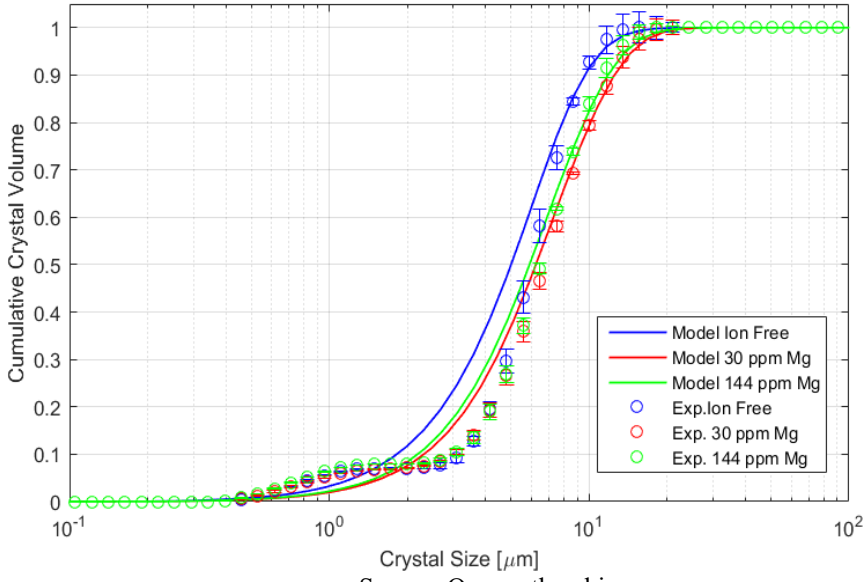

Source: Own authorship

Figure 5.21 - Comparison of experimental and simulated results for the cumulative crystal volumetric size distribution at 90 minutes for Ba-28, Ba-280, and Ion Free conditions.

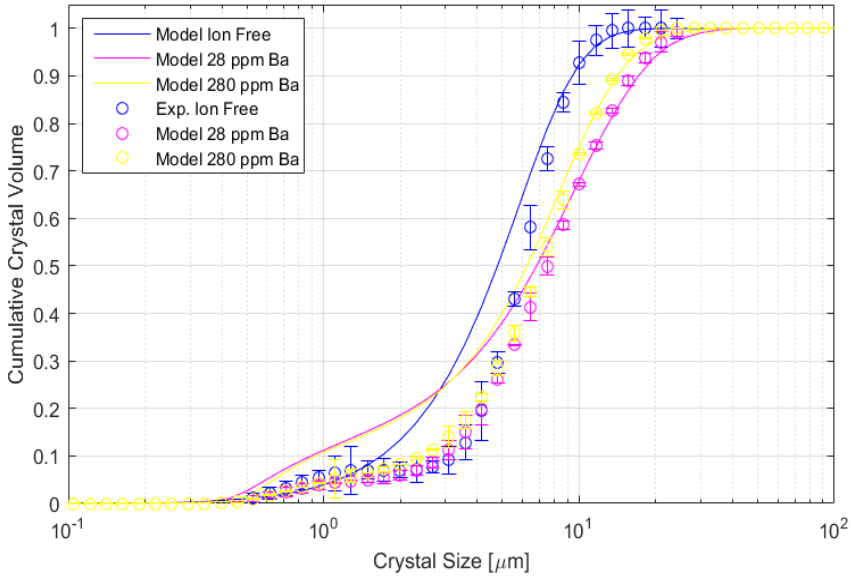

Source: Own authorship

Figure 5.22 - Comparison of experimental and simulated results for the cumulative crystal volumetric size distribution at 90 minutes for Sr-33, Sr-1500, and Ion Free conditions.

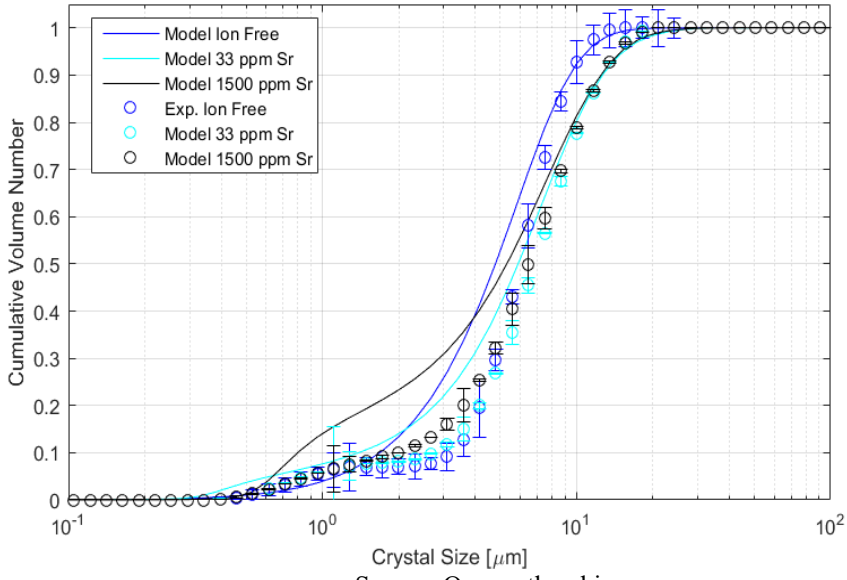

Source: Own authorship

Although it should be noted that the model error presented different behavior along the experimental data presented, different errors were obtained for the smaller and larger particles. In the first three experiments, IF, Mg-30 and Mg-144, the model calculations obtained an average error of -2% ± 2% for the smaller particle with 0.3 µm - 1.7 µm and an average error of 6% ± 7% for the larger particles with 2.3 µm - 18 µm. Such as for the last four experiments,

Ba-28, Ba-280, Sr-33 and Sr-1500, the average errors were 13% ± 8% and 6% ± 4% for the smaller and larger particles, respectively.

It is also possible to compare the simulated and experimental average volumetric diameter, as presented in Figure 5.23. It is possible to observe that the addition of the external ions produced larger average volumetric diameters than the Ion Free condition. The model obtained an average error of -6 ± 7% with all conditions, predicting smaller diameter sizes than the experimental data for all experiments, except for Ba-280.

Figure 5.23 - Comparison between experimental and simulated average volumetric diameter for all the studied conditions.

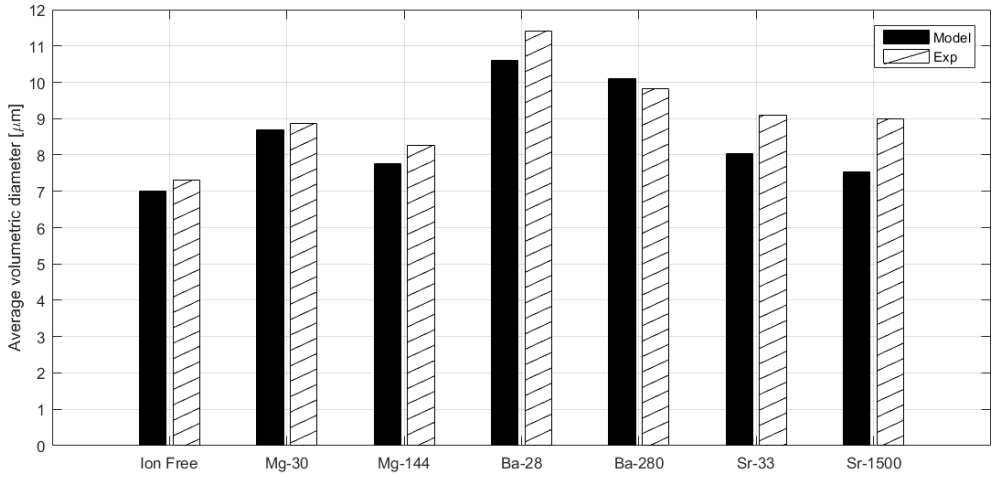

Source: Own authorship

The results of Figure 5.23 can be compared with those of Figure 5.5, observing that the Data Set 1 appears to produce much larger solids than the Data Set 2 for both simulation and experimental data. Although, this is associated with the discussion of Figure 5.11 and the discussion of Trampuž *et al.* (2019) that is due to different physical principles of measurement, as the FBRM is based on the reflectance measurement of the particle chord distribution instead of the Brownian motion of the dispersed particles, that is the base of the DLS measurement. With both experimental and simulation estimated parameters from these different sources, sizes cannot be direct quantitatively compared.

Though, with the Data Set 2, it can be noted that the model was able to simulate the size-increasing effect that the addition of the external ions caused in the crystalline system. Besides, the calculations also indicated that the increase in concentration did not increase the production of larger particles, the same as observed in the experimental data. To discuss the

effects of external ions on crystal size distribution, one can evaluate how these influenced the nucleation, growth, and agglomeration, as can be more than one polymorph rate.

The experiments with Magnesium produced larger volumetric average diameters than Ion Free due to a combination of the nucleation, growth and agglomeration rates. The reduction in the homogeneous nucleation rate by the Mg presence, 62.3% in Mg-30 and 57.9% in Mg-144, together with smaller secondary nucleation, 6% and 2% than Ion Free, produced overall nucleation rates 65.4% (Mg-30) and 59.5% slower than Ion Free. This reduction was sufficient to shift the size distribution to the right side. Besides that, no limitations for vaterite growth included Mg-30 and Mg-144, although this ion accelerated the transition rates between vaterite-calcite. Thus, the calcite still grows slower, for the majority of the reaction, than its more soluble counterpart, vaterite. However, it presents a higher agglomeration rate constant, 6.76 times the vaterite, producing 130% and 128% higher agglomeration rates than those in Ion Free experiment, contributing to a higher production of larger particles.

A similar behavior among the effects in the size distribution calculations was observed for experiments with Barium and Strontium. Both ions also influenced the crystalline mass produced. They presented average nucleation rates representing 78.8%, 82.7%, 81.8%, and 87.67% of the Ion Free experiment, producing fewer crystals with the smallest possible size, shifting the size distribution to the right side. Besides that, the Ba and Sr ions also resulted higher calcite content than those of Ion Free, obtaining agglomeration rates 368%, 393%, 317%, and 382% higher than for the experiment without Ba or Sr, therefore, also contributing to the observed shift to the right on the simulated size distribution.

The increase of the smaller particles, close to 1 μm that seems to appear on Ba-28, Ba-280, and Sr-1500 final size distributions, were associated with the calcite growth acceleration. There was a moment in which calcite started to grow faster than vaterite, 60 (Ba-28), 54 (Ba-280), 43 (Sr-1500) minutes, increasing the crystalline mass production and consequently, accelerating the secondary nucleation phenomena. This influence can be observed by plotting the final size distribution against the moment before that calcite became the faster-growing polymorph. Figure 5.24 shows that the size distribution was shifted to the right with this time for the Ba-28, Ba-280 and Sr-1500 conditions in comparison with the final moments of the volumetric size distribution.

The graphs in Figure 5.24 indicate that the parameter estimation process tried to increase the calcite acceleration effect to represent the larger sizes on Ba and Sr experiments, causing the increase in the crystalline mass and, consequently, in the smaller particles, by the secondary

nucleation mechanism, on the size distribution. If the agglomeration of this polymorph were to be affected instead, the larger sizes that these ions presented could be simulated without modifications with the crystalline mass, not producing the smaller particles that we observed. This observation can be used to demonstrate the complexity of the parameter estimation process with various simultaneous rate calculations and adjustments.

Figure 5.24 - Cumulative crystal size distributions for experiments Ba-28, Ba-280, and Sr-1500, in specific times: before and after the faster calcite growth rate.

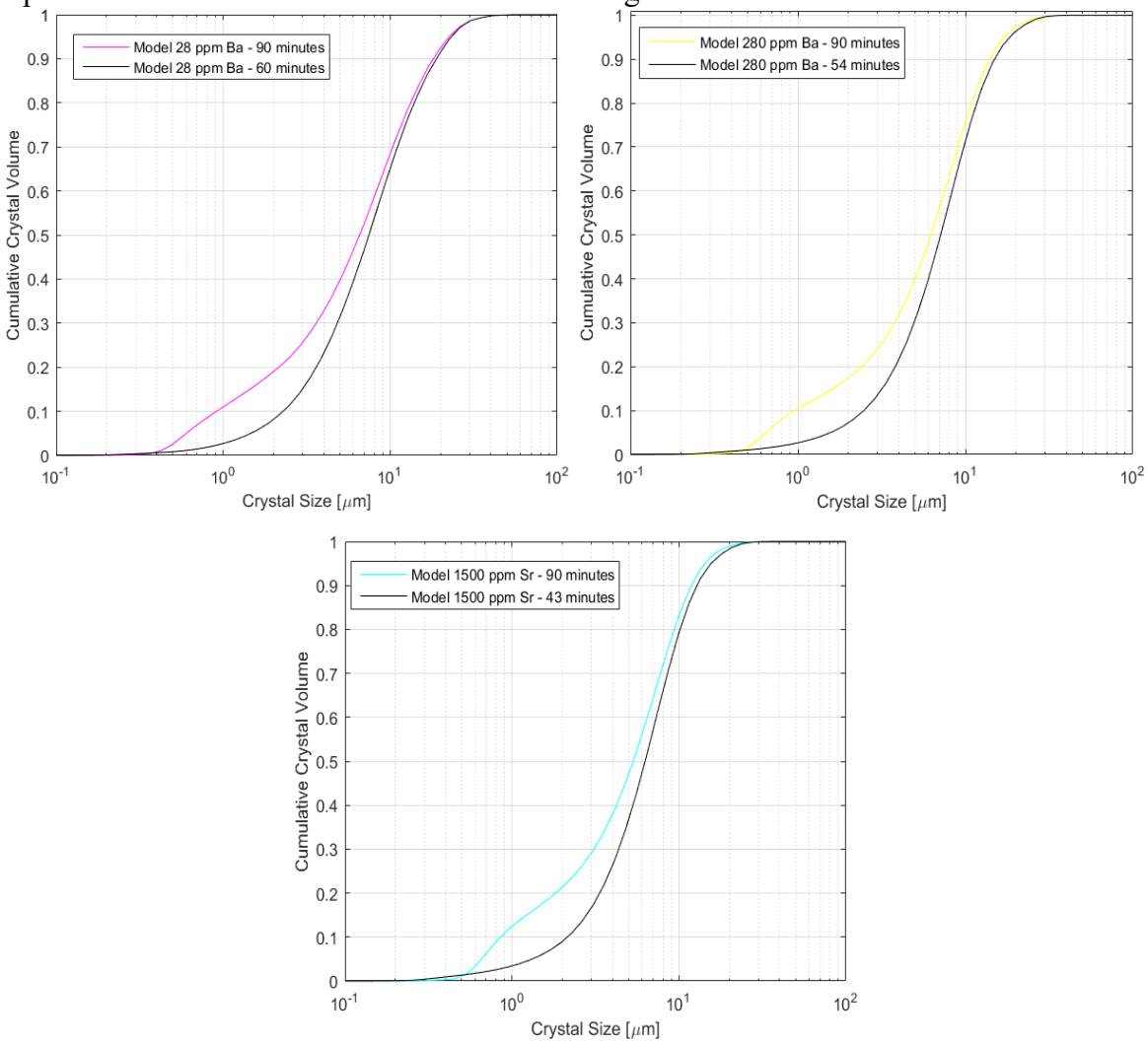

Source: Own authorship

5.3 RESULTS FROM DATA SET 3

The first step for the simulations using the Petrobras data was to obtain the equilibrium constants for the calcite, vaterite, and aragonite global reaction, at 100ºC and 200 atm. These constants provide important information about the system to be investigated, such as the saturation and mass of the precipitated crystal in a given condition of temperature, pressure, and salinity.

To obtain the value of K_{eq} at standard conditions for calcite, vaterite, and aragonite, the information presented in Table 5.12 was utilized in Equation 3.30, obtaining Keq = 3.09 x 10^{-5} (calcite), 1.29 x 10^{-4} (vaterite), and 5.12 x10^{-5} (aragonite); which agrees with the expected order of solubility of these polymorphs: vaterite presented the higher solubility, followed by aragonite and then calcite.

Table 5.12 - Gibbs free energy for the formation of species involved in the calcium carbonate reaction

T = 25 ºC **P = 1 atm**	ΔG_f^0 **(cal/mol)**
$CaCO_{3calcite}$	-269,851.1 [1]
$CaCO_{3vaterite}$	-269,010.5 [2]
$CaCO_{3aragonite}$	-269,550.0 [3]
$CO_{2(aq)}$	-92,256.2 [1]
$H_2O_{(l)}$	-56,690 [1]
$Ca^{2+}{}_{(aq)}$	-132,123.9 [1]
$HCO_3{}^{1}{}_{(aq)}$	-140,260.5 [1]

Fonte: Cosmo (2013) [1]; Krupka *et al.* (2010) [2]; Apps & Wilkin (2015) [3]

With the standard values for the equilibrium constants, it is possible to use Equations 3.31 and 3.32 to evaluate the effects of temperature and pressure on the equilibrium. The enthalpy of formation and heat capacity of the species presented in the calcium carbonate reaction (Table 5.13) enable the calculation of the equilibrium constant with temperature changes (Equation 3.31). The results of standard chemical equilibrium for calcite, vaterite, and aragonite to temperatures from 0ºC to 100ºC are presented in Table 5.14.

Table 5.13 - Enthalpy and Heat capacity of the species involved in the calcium carbonate reaction.

T = 25ºC **P = 1 atm**	ΔH_f^0 **(cal/mol)**	C_p^0 **(cal/mol K)**
$CaCO_{3calcite}$	-288,610.1 [1]	19.57[1]
$CaCO_{3vaterite}$	-288,074.6 [2]	19.59[2]
$CaCO_{3aragonite}$	-288,510.2 [3]	19.42[3]
$CO_{2(aq)}$	-98,900.6 [1]	50.87[1]
$H_2O_{(l)}$	-68,315.0 [1]	17.99[1]
$Ca^{+2}{}_{(aq)}$	-129,739.5 [1]	-7.53[1]
$HCO_3^-{}_{(aq)}$	-164,897.2 [1]	-5.23[1]

Source: Cosmo (2013) [1]; Krupka *et al.* (2010) [2]; Apps & Wilkin (2015) [3]

Table 5.14 - Equilibrium constant for the calcite, vaterite and aragonite for the temperatures of 0, 25, 50, 75 and 100ºC.

T (°C)	**0**	**25**	**50**	**75**	**100**
$-\log_{Keq}$ calcite	4.35	4.51	4.79	5.16	5.60
$-\log_{Keq}$ vaterite	3.57	3.89	4.21	4.60	5.06
$-\log_{Keq}$ aragonite	4.01	4.29	4.58	4.95	5.39

Source: Own authorship

With the calculation for variation with temperature already performed, it is possible to calculate the influence of pressure in the equilibrium constant. Using Equation 3.32, the molar volume of the species for the desired temperature values(0, 25, 50, 75 and 100ºC) was obtained (Table 5.15). With both calculations, it was possible to determine the equilibrium constant value for the temperature and pressure range of 0-100ºC and 1 to 200 atm, with the combined use of Equations 3.8 and 3.9, using the methodology shown in Figure 4.3. Figures 5.25 to 5.27 present the obtained profiles of the equilibrium constants of calcite, vaterite, and aragonite as a function of temperature and pressure. With this, the influence of temperature and pressure with the equilibrium can be evaluated with the Le Chatelier principle.

Table 5.15 - Molar volume for the species involved in the calcium carbonate formation for temperatures of 0, 25, 50, 75 and 100ºC.

V (cm³/mol)	**0ºC**	**25ºC**	**50ºC**	**75ºC**	**100ºC**
$V°_{CaCO3(calcite)}$ [1]	36.91	36.93	36.95	36.97	36.99
$V°_{CaCO3(vaterite)}$ [2]	37.68	37.78	37.91	37.96	38.14
$V°_{CaCO3(aragonite)}$ [3]	32.23	32.31	32.43	32.47	32.62
$V°_{H2O(l)}$ [1]	18.02	18.06	18.23	18.48	18.79
$V°_{CO2\ (aq)}$ [1]	34.36	32.89	32.75	33.33	34.47
$V°_{Ca^{2+}(aq)}$ [1]	-19.84	-17.85	-18.22	-19.1.	-20.00
$V°_{HCO3^{1-}(aq)}$ [1]	21.73	24.60	25.47	25.38	24.57

Source: Cosmo (2013) [1]; Krupka *et al.* (2010) [2]; Apps & Wilkin (2015) [3]

Figure 5.25 - Equilibrium constant profile as a function of temperature and pressure, obtained for the mineral calcite

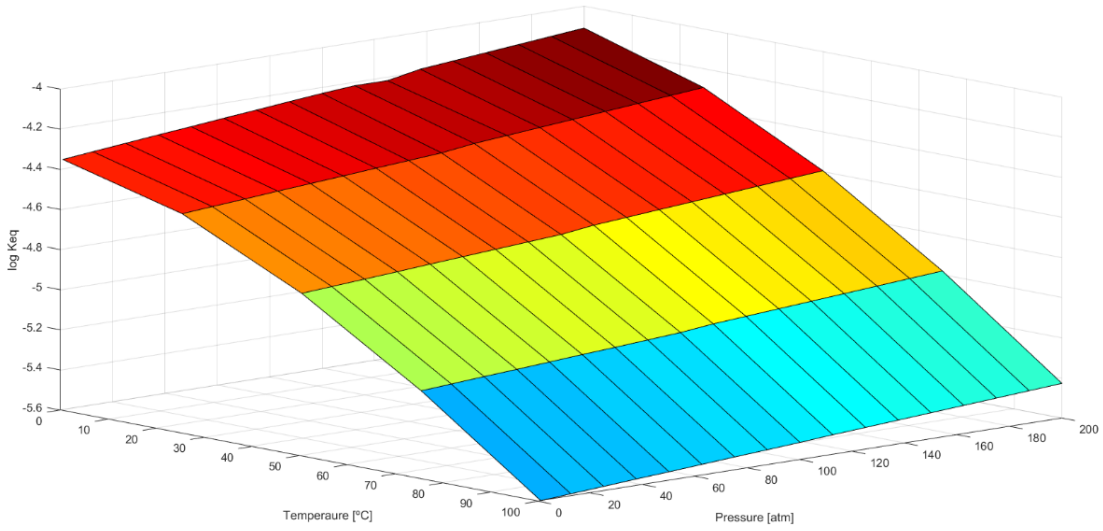

Source: Own authorship

Figure 5.26 - Equilibrium constant profile as a function of temperature and pressure, obtained for the mineral vaterite

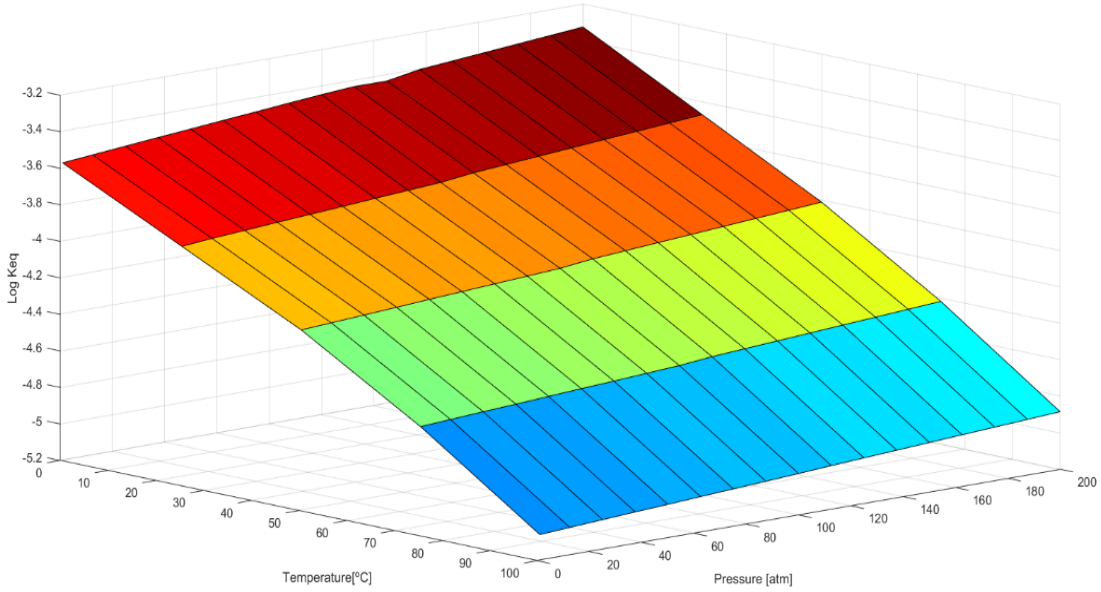

Source: Own authorship

Figure 5.27 - Equilibrium constant profile as a function of temperature and pressure, obtained for the mineral aragonite

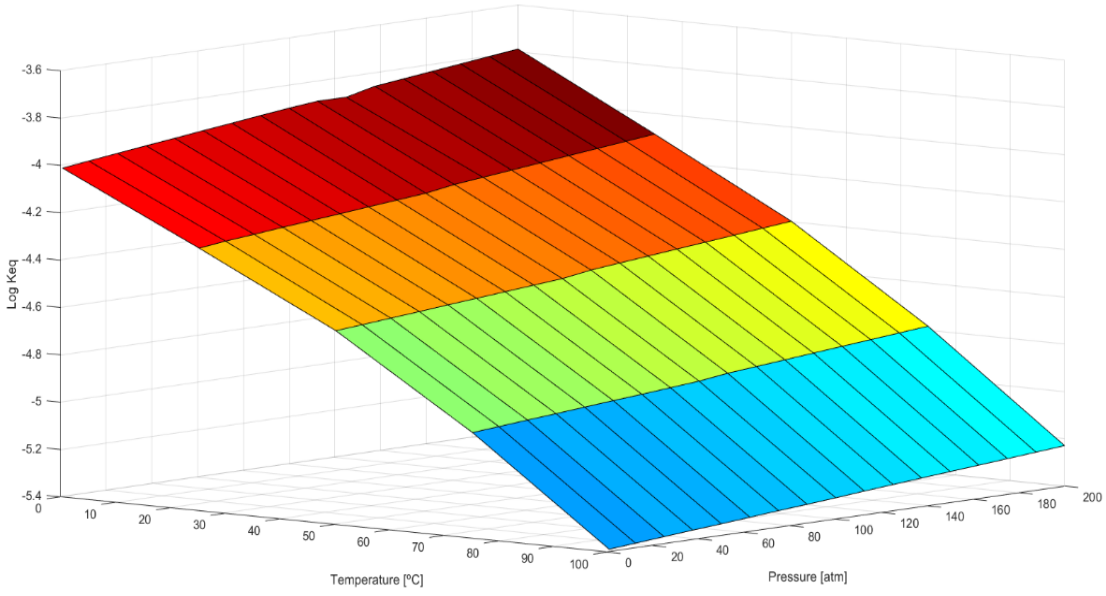

Source: Own authorship

The increase in temperature led to the reduction of the equilibrium constant. The production of the three crystalline forms presents standard enthalpy of positive reaction: 3,708.3, 4,243.7, and 3,808.1 cal.mol^{-1} for calcite, aragonite, and vaterite, respectively. Thus, the increase in temperature shifts the equilibrium in favor of solid production to reduce the system temperature to maintain equilibrium.

On the contrary, increasing the pressure resulted in increased values of the equilibrium constant. The production of the three crystalline forms shows a positive standard molar volume variation: 65.7, 66.5, and 61.1 $cm^3.mol^{-1}$ for calcite, vaterite, and aragonite, respectively. Therefore, the increase in pressure shifts the equilibrium in favor of the reactants (calcium and bicarbonate ions) to reduce the pressure of the system. In addition, it is possible to notice that the equilibrium constant is more sensitive to changes concerning temperature when compared to pressure. This occurrence is due to the magnitude differences that are observed between the standard enthalpy variations when compared with the standard molar volume variations, because, as it is possible to observe in the van't Hoff equations, the derivative of the equilibrium constant is a direct function of ΔH_r^0 e ΔV_r^0 against variations in temperature and pressure, respectively.

The equilibrium constant values obtained for calcite were compared with the data available by the Multiscale® software. In general, the observed deviation ranged from -2.09 to -1.27%, with a mean deviation of -1.56%. The equilibrium constant values obtained for aragonite and vaterite were validated using the free software SUPCRT92 (JOHNSON; OELKERS; HELGESON, 1992). The observed deviation varied between 1.6 and 2.8%, with a confidence interval of 95%. The mean deviation was 2.2%. Thus, it can be said that the equilibrium constants obtained for calcite, vaterite, and aragonite as a function of temperature and pressure showed agreement with the reference software and can be used to calculate the supersaturation of these solids.

The values obtained using the software were compared with the values calculated by the proposed thermodynamic model. Table 5.16 presents temperature, pressure, and salinity conditions close to those found in three different operations found in platforms operating in the pre-salt region. Unfortunately, only a comparison with the calcite precipitate mass can be made, as Multiscale® only considered this polymorph, and a simulation in SUPCRT92 was not possible with the studied conditions.

It is possible to observe that the proposed model produced values close to those obtained through the commercial program Multiscale®, with deviations varying between -3 and -7% for the mass of precipitated calcite per volume of solution. In addition, the thermodynamic model was able to predict the tendency of precipitation to decrease with the reduction of temperature and pressure of the system. The good agreement between the results offers a solid thermodynamic base to kinetic investigations concerning the choke valve region.

Table 5.16 - Calcite crystal mass precipitated by volume of solution, at different operating conditions.

Water ionic composition	**Concentration (ppm)**
Na^{+1}	39,680.74
Mg^{2+}	8,498
Ca^{2+}	27,549.62
K^{+1}	774.1404
Ba^{2+}	39,660.04
Sr^{2+}	1,244.204
Cl^{1-}	111,322.6
HCO_3^{-1}	41,931.4

Pressure (bar)/ Temperature (ºC)	Multiscale®	Model	Deviation (%)
306 and 92	34.6 $g.L^{-1}$	33.5 $g.L^{-1}$	-3
151.8 and 90	32.6 $g.L^{-1}$	30.3 $g.L^{-1}$	-7
21 and 28	30.4 $g.L^{-1}$	29.1 $g.L^{-1}$	-4

Source: Own authorship

The parameters obtained with the Data Set 1 were used for the kinetic simulations. The choice was made because the experimental conditions could present different supersaturations. Thus, even with the presence of divalent ions with the water composition, the simulations focusing on understanding the effects caused by different thermodynamic potential were chosen to be the first step.

Initially, similar to the cases before, the kinetic model estimated the polymorphs that presented thermodynamic stability favorable to their precipitation under the experimental conditions. Only vaterite and calcite presented thermodynamic stability concerning the other solids tested, that were magnesium chloride ($MgCl_2$), calcium chloride ($CaCl_2$), barium sulfate ($BaSO_4$), strontium carbonate ($SrCO_3$), among others, under the tested conditions. The change in Gibbs free energy caused by the formation of vaterite and calcite polymorphs was -1.83 x 10^{-9} J mol^{-1} and -4.21 x 10^{-8} J mol^{-1}, respectively for the conditions in Well-1; similar results were obtained for Well-2.

Here, it should be said that in Well-2, the proportions of Sr^{2+}/Ca^{2+} and Mg^{2+}/Ca^{2+} were close to Sanjiv (2020), and the more concentrated of Kitano (1962) that noted both Sr^{2+} or Mg^{2+}

favored aragonite formation. Unfortunately, no kinetic parameter was adjusted to aragonite formation, so its formation was not considered at the moment for the simulations.

Thus, it was possible to calculate the supersaturation for calcite, vaterite, and the thermodynamic potential of precipitation of both wells concerning the formation of calcium carbonate solids both inlet and outlet of the valve (Table 5.17). It is possible to notice that both wells presented supersaturation between Data Set 1 and Data Set 2, with these wells presenting calcium and bicarbonate concentration with the range of those of sections 5.1 and 5.2. Although, it should be noted that the calculations of Table 5.16 were made with the obtained above K_{eq}, and not by the direct solubility constant, of the polymorphs that presented values of 1.36×10^{-4} and 3.27×10^{-5} for vaterite and calcite in the conditions of Well-2.

Table 1.17 - Thermodynamic calculations for both wells in the choke valve regions.

Inlet		**Outlet**	
Well-1			
SS_{calc}	14.99	SS_{calc}	15.48
SS_{vat}	7.35	SS_{vat}	7.59
Thermodynamic potential [kg/day]	8.45	Thermodynamic potential [kg/day]	8.73
Well-2			
SS_{calc}	13.13	SS_{calc}	13.61
SS_{vat}	6.52	SS_{vat}	6.77
Thermodynamic potential [kg/day]	0.44	Thermodynamic potential [kg/day]	0.46

Source: Own authorship

It is observed that the Well-1 presented higher supersaturations and thermodynamic potentials of precipitation compared to the Well-2. Several factors affected the system supersaturation for the two investigated wells, namely:

Ionic concentration: The Well-1 has a higher ratio of bicarbonate/calcium when compared to the Well-2. Analyzing the global equation of calcium carbonate formation, Equation 1.35 states that a mol of calcium reacts with 2 mols of bicarbonate. Thus, even with the higher calcium content, the Well-2 is limited by its bicarbonate content.

Temperature and pressure: The Well-1 have a higher temperature and lower operating pressure. As observed in Figures 5.25-5.27, which described the equilibrium constant of the polymorphs, the precipitation favoring effect of temperature is more pronounced than precipitation reduction effect of pressure, thus producing an increase in the calcium carbonate precipitation potential in the face of the conditions presented by the Well-2.

Furthermore, the temperature and pressure conditions indicate that the Well-1 has a lower concentration of carbon dioxide in the aqueous phase. However, the difference in salinities should be observed, especially in the levels of sodium and chloride ions between the two wells, which have a known effect on the solubility of CO_2, reducing it significantly at concentrations greater than 100,000 ppm of the ion pair (DUAN; SUN, 2003; DUAN; LI, 2008). Besides that, it can be noted in Table 4.1 that Well-2 had a higher ratio of oil to water flow rate, favoring the partitioning of dioxide carbon with the oil phase more than Well-1, as Equation 4.8 shows.

Fortunately, the methodology of calculating the solubility of carbon dioxide in the aqueous phase present in the model covered all these factors. It is noteworthy that the model predicted with a 12% error that the Well-2 had 30% lower CO_2 content than Well-1, based on chromatography measurements made by Petrobras. A lower concentration of carbon dioxide favors precipitation, but such favoring was not enough to compensate for the first two items that reduce the supersaturation of this well.

The observed differences in the thermodynamic potential can relate to the different volumes of water presented for each well. The Well-2 presented a water flow rate 98.2% smaller than that for Well-1, thus even with similar supersaturation, the actual mass of calcium and bicarbonate were much lower than those of Well-1, and consequently the possible mass of calcium carbonate formed. It is noteworthy that operations in Well-2 are recent when compared to those in Well-1, so it is expected that this difference in water content will decrease over time, and the value of the potentials will approach with the continuity of the operation in Well-2 (ROSA; CARVALHO; XAVIER, 2011).

From the supersaturation values, the kinetic simulations provided by the model can be discussed. These are represented in the mass curves of the most stable polymorph along the pipe (Figure 5.28) and the solids distribution at the pipe's end (Figure 5.29).

Figure 5.28 - Calcite crystal mass profiles along the tubulation in the inlet and outlet conditions around the valve, for Well-1 (left side) and Well-2 (right side) conditions.

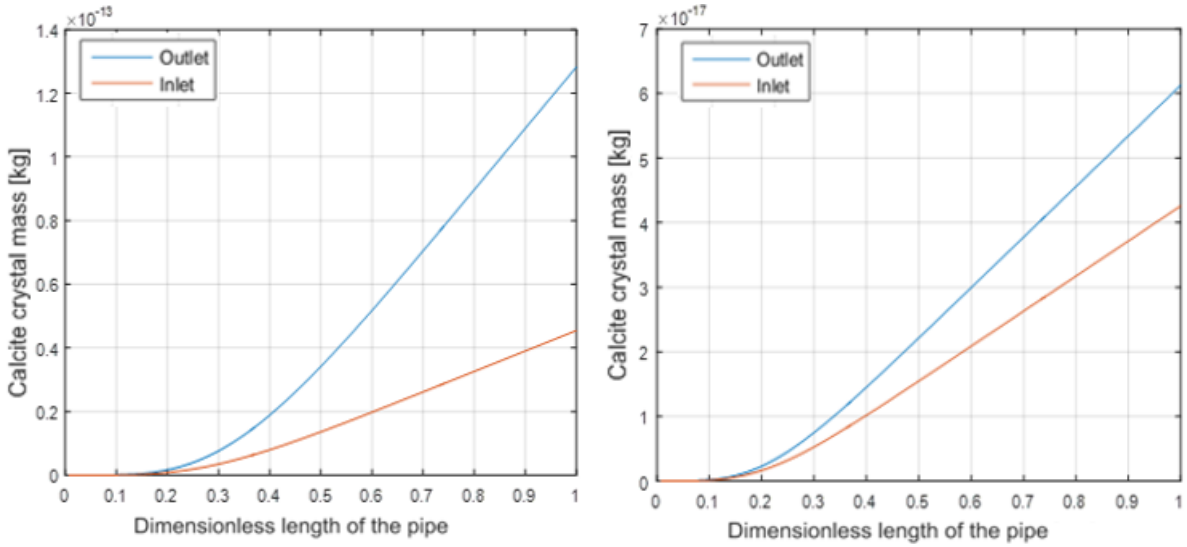

Source: Own authorship

The simulations provided by the kinetic model showed the impact that the choke valve had on the system. The increase in supersaturation caused by the localized pressure drop accelerated the process kinetics, which is faster in the Well-1 as it has higher supersaturation. This well showed faster kinetics due to higher supersaturations, producing faster growth (94%) and nucleation (803%), than the Well-2 conditions. A comparison between the two profiles indicates that the curve of the Well-2 is further away from the equilibrium given by the thermodynamic potential. This effect is related to the residence time, 43% shorter that Well-2 presented over Well-1. Consequently, the flowing particles that already have slower kinetic rates also had a shorter time to nucleate, grow, agglomerate, and rearrange themselves. For all simulations, the dimensions of the tube were considered constant, one meter in length and eight inches in diameter.

The low residence times, both Wells presented $\tau<1s$, significantly influenced the polymorphic transformation, with the calcite mass representing only 1.17% and 0.10% of the vaterite crystalline mass, the major polymorph formed along the tube. Thus, it is essential to carry out a study about the kinetic behavior of the system allied to the thermodynamic study, since thermodynamics indicates which solid is more stable and the order of their appearance; at the same time, the kinetics can determine the velocity of occurrence of these events.

Observing Figure 5.29 is also possible to evaluate the impact of the different operating conditions around the choke valve with solid size distribution. It is observed that the Well-1

produced solids with approximate sizes of 0.2 µm, compared to the 0.08 µm from the Well-2. This difference can also be associated with the kinetic rates and the time that these had to develop themselves. At the initial moments, in the first 10 finite volumes, the nucleation rates presented higher values, 84% and 96% higher than the initial populational growth and agglomeration rates, in Well-1 and Well-2, respectively. Although, this difference became 62% and 54% smaller per second within the tube. The same calculations presented in Table 5.6 can also be made here, obtaining that the Well-1 presents an average, along the axial direction, ratio between growth and agglomeration over nucleation and dissolution equal to 0.164, while a value equal to 0.0117 is obtained for Well-2. Thus, considering the fact that the Well-2 had less time to develop its kinetics rates, smaller crystal sizes will be produced by Well-2, in relation to Well-1.

Figure 5.29 - Volumetric size distribution for the solids produced around the choke valve region, at Well-1 (left side) and Well-2 (right side) conditions.

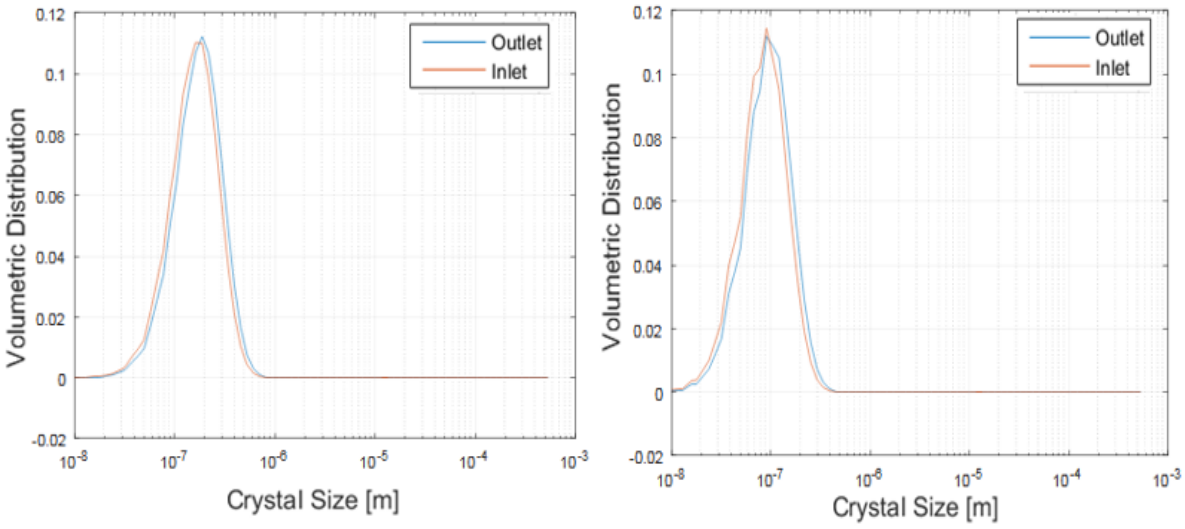

Source: Own authorship

It is also possible to evaluate the difference in the impact that the choke valve presented in the two types of output produced by the model, the thermodynamic potential of $CaCO_3$ formation and the mass that kinetically formed during the flow in the pipe (Table 5.18). Results presented in Table 5.18 show the differences between the purely thermodynamic simulation and that considering the influence of the kinetic component. The values obtained by the thermodynamic calculations assume equilibrium. The predicted values informed the total amount of calcium carbonate that must precipitate for the system to reach a new equilibrium without considering the time required to reach this level.

Table 5.18 - Comparison between the kinetic and thermodynamic prediction of the total crystalline mass produced in the regions around the choke valve for Well-1 and Well-2.

Thermodynamic Model				**Kinetic Model**			
	Inlet [kg/day]	Outlet [kg/day]	Diff. [%]		Inlet [g/day] x10^4	Outlet [g/day]x10^4	Diff. [%]
Well-1	8.45	8.73	3	Well-1	250	469	88
Well-2	0.44	0.46	5	Well-2	1.06	1.27	20

Source: Own authorship

On the other hand, the kinetic values can consider the time the system has to produce these solids, a fundamental quality for a flowing system like the one presented in this case study. Thus, the difference obtained in the Table 5.18 is directly related to the fact that both wells have residence times notably shorter than the time required for thermodynamic equilibrium. This observation underscores the previous conclusion that both systems are far from equilibrium. Therefore, it can be concluded that the purely thermodynamic prediction is not able to inform values close to those obtained in the field, because the chemical equilibrium will not be reached in the flow conditions, being necessary the introduction of the kinetic components in order for a simulator to be able to recognize the different conditions of this process.

In addition, Table 5.18 provides the difference in the impact of the choke valve presence on the two types of predictions. The thermodynamic prediction has its increase associated with pressure drop and consequent release of carbon dioxide from the system, thus increasing the predicted value. On the other hand, the kinetic prediction recalculates all the rates referring to kinetics, nucleation, growth, agglomeration, and transformation, for this new condition, observing a higher impact than the thermodynamic one. This higher impact is because the rates quoted are not linearly dependent on supersaturation. Nucleation, for example, has a power of 1.75 concerning supersaturation and increases with the root of the crystal mass. Thus, the higher the process rates, the more pronounced this impact. Well-1 had a higher impact, almost four times greater when compared to Well-2.

As can be seen in the tables with the composition of the phases for both Well-1 and Well-2, the water content varies significantly. This water content directly influences the calculations, changing the total mass of solids produced and consequently, the kinetics of this process. The wells that presented lower water contents are in operation for less time than the wells with the higher water proportion, the Well-1, and Well-5, thus being considered less developed wells. This definition is based on the fact that a well at the beginning produces higher

levels of oil and gas, and with the continuity of the operation, it starts to produce more water since the first phases, with lower specific mass, flowed at greater intensity in the first moment (ROSA; CARVALHO; XAVIER, 2011).

Thus, it becomes interesting to evaluate the production of solids, both by thermodynamic and kinetic prediction, in proportion to the water content of each well. With this, it becomes possible to identify which wells present the potential for the problem of precipitation in comparison to other wells, comparing all wells on the same basis per million cubic meters of water (Table 5.19).

Table 5.19 - Thermodynamic and kinetic predictions for all the wells around the valve region, per million cubic meters of water.

	Thermodynamic model				**Kinetic model**		
	Entrada [kg/Mm³]	Saída [kg/Mm³]	Dif. [%]		Entrada [g/Mm³]	Saída [g/Mm³]	Diff. [%]
Well-1	4,907	5,062	3	Well-1	14.5	27.2	88
Well-2	14,200	14,800	5	Well-2	3.42	4.10	20

Source: Own authorship

From the proportion by volume of water, it is noted that the two wells with the lowest daily potentials had the highest values. Thus, proportionally, they are wells with potential future problems, because as they develop, the produced water presents favorable conditions for forming calcium carbonate solids. In addition, it can be seen that the Well-6 presented values higher than two wells more supersaturated than it, the Well-1 and the Well-5, demonstrating that the proportion per mass of water must also be analyzed, not only the absolute value of the crystalline masses formed.

In Tables 5.18 to 5.19, it is possible to notice that the greater the supersaturation of the well, the greater the influence of the choke valve on the formation of solids. This relation is since the relationship of kinetic rates is not linear with supersaturation, nor with crystalline mass. Thus, increase in the supersaturation variable caused by the localized pressure drop of the choke causes more significant kinetic impact than a thermodynamic one. Thus, wells further away from chemical equilibrium and with higher crystal production require greater care in the choke region due to the possible acceleration of their kinetic phenomena.

The present results show the importance of kinetic analysis in oil and gas production systems. As crucial as thermodynamic prediction is, it alone cannot include fundamental

variables in the discussion of flow systems, such as time in the prediction closer to operation reality. Although it is necessary to point out that the tool presented in this document is preliminary, it is still based on experimental data and considerations far from the field reality. However, it is possible to observe its potential as an analysis and prediction tool for calcium carbonate-forming systems.

6 CONCLUSION

A mathematical model which sought to represent both thermodynamic and kinetic aspects of the calcium carbonate precipitation was developed based on the theoretical and experimental observations available in the present literature. The thermodynamic calculations were centered on the equilibrium constant, responsible for quantifying the distance from chemical equilibrium that the conditions of the produced water are, and the energy associated with the formation of each polymorph. Together with the thermodynamic aspect, it became possible to evaluate the kinetic model, in which the rates of nucleation, growth, dissolution, agglomeration, and polymorphic transformation can be obtained. For the correct quantification of these kinetic events, the concepts of step rule and ripening associated with these phenomena were included with the calculations. With both aspects covered, it was possible to add the numerical tools responsible for the model simulation, a numerical integrator capable of working with this complex system of equations, of the type of back differentiation formula with order 5, together with a hybrid algorithm that combines a particle swarm optimizer with adaptive inertia together with a Nelder-Mead optimizer. The produced routine was used with different three sets of experimental data.

The first set of data, namely Data Set 1, was obtained from the ITP/NUESC that measured the total crystalline mass produced, the size, and the polymorphic distribution of the precipitated crystals by a range of initial calcium and bicarbonate concentrations 50 $mmol.L^{-1}$ to 20 $mmol.L^{-1}$, with a batch reactor at 25ºC and 1 atm. The model was adjusted for crystal size distribution, total crystalline mass, and polymorphic proportion prediction for the range of crystallization conditions, obtaining an average error of 4% per variable that successfully passed the chi-squared test attesting the quality of the parameter estimation process. The model described the increase that the elevation in supersaturation caused on both total mass and size distribution of crystals obtained, with a -8% ± 6% and 3% ± 5% error, respectively; being capable of evaluating the SS effect on the kinetic rates that produced the observed effects. The calculations correctly represented the final polymorphic distribution, matching the higher calcite content that 40 $mmol.L^{-1}$, 5.35 wt.%, had over the other tested conditions.

The second set of data, namely Data Set 2, used was obtained from IPT/LPP, presenting the crystallization results of experiments with a range of external ions concentration, Mg (30 to 144 ppm), Ba (28 to 280 ppm), and Sr (33 to 1500 ppm) with a 5.5 L reactor with 1 and 0.297 $mol.L^{-1}$ of calcium and bicarbonate at 25ºC and 1 atm. The model was also adjusted for crystal

size distribution, total crystalline mass, and polymorphic proportion prediction for range crystallization conditions, obtaining a good general agreement with a mean squared error of 12%. The programmed routine responsible for optimizing the model imposed a reduction on vaterite nucleation and acceleration of the polymorphic transformation rate with the Mg experiments to model the 21 and 13% higher volumetric diameter, 12 and 8% smaller total crystalline mass, and 40% and 23% higher calcite contents that the Magnesium experiments had over the external free experiment. As for the Barium and Strontium conditions, the routine imposes an increase on calcite growth and polymorphic transformation rates to the model the 56%, 34%, 24%, 23% increase on the average volume diameter, 18%, 16%, 11% and 13% average reduction, in relation with time, on the crystal mass production and 62%, 80%, 50%, 69% higher calcite content that the Ba and Sr experiments obtained in comparison with the experiment without these ions.

With the parameter estimation process made with the Data Set 1, a case study was carried out with the proposed tool. The object of the study was the region of a choke valve. The objective of the simulations was to simulate the valve's influence in the thermodynamic potentials and crystallization kinetics before and after this component. From the results, it was possible to observe the 18.2 times higher kinetic and thermodynamic precipitating potential that the Well-1 presented compared to the Well-2, based on 4,762% higher bicarbonate/calcium rates, 29% higher temperatures, 43% longer residence time, and 5,455% higher water flow rate that Well-1 had over Well-2. Besides that, it was noted how the presence of the valve influenced the higher kinetic rates of Well-1, 4.4 times more of that in Well-2. Besides, the polymorph calcite, although presenting higher thermodynamic stability, was not the most phase present in all simulated wells due to lack of time for its transition phenomenon. At the end of the simulations, the thermodynamic and kinetic potential of the wells were compared concerning the water content, as it was observed that this had a strong influence on the values obtained. Being possible to observe that less developed fields can present proportionally higher formation potentials, highlighting the problem that such wells can present in the continuity of their operation.

Thus, it can be seen that a complete population balance can provide a valuable tool to evaluate the thermodynamic and kinetic mechanisms of calcium carbonate formation. While the model was adjusted only to a specific range of concentrations, it may be helpful in the calcium carbonate crystallization process as a practical study tool to evaluate the effects of supersaturation, external ions on, and temperature, pressure, and time residence variations with

$CaCO_3$ formation for both academia and industry applications. The same modeling framework can be used for different concentration ranges, adjusting the crystalline production effects with other operating conditions. Even though complete generalization of $CaCO_3$ crystallization modeling is not yet possible, the use of the present model may also be extended to other similar crystallization systems with modifications on the base model. These include additions of other ions, such as SO_4^{2-}, other salts that can also precipitate, as $BaSO_4$, the study of synergic effects that simultaneous ions can have, the kinetic effects of high temperature, pressures, and different oil compositions presence, together with different reactors conditions which could significantly increase the model application. Further upgrade of the model could also extend its applicability to continuous systems, developing a more robust and accurate fluid dynamic model to evaluate better the velocity gradients and the multiphase flow, which are essential in industry and academia.

REFERENCES

ABBAS, A.; ROMAGNOLI, J. A. Multiscale modeling, simulation and validation of batch cooling crystallization. **Separation and Purification Technology**, v. 53, n. 2, p. 153–163, 2007.

AGGARWAL, P. K.; GUNTER, W. D.; KHARAKA, Y. K. Effect of Pressure on Aqueous Equilibria. **American Chemical Society Symposium Sei**, p. 87–101, 1990.

AL-ANEZI, K.; JOHNSON, D. J.; HILAL, N. An atomic force microscope study of calcium carbonate adhesion to desalination process equipment: effect of anti-scale agent. **Desalination**, v. 220, n. 1–3, p. 359–370, 1 mar. 2008.

ALDEIA, W. et al. Efeito do campo magnético na formação, incrustação e transporte de partículas de carbonato de cálcio. **Workshop sobre métodos físicos de combate à incrustação em Poços**, n. 1, 2019.

ANDERSON, G. M.; CRERAR, D. A. **Thermodynamics in geochemistry: The equilibrium model**. 1st ed. New York, EUA: Oxford University Press, 1994.

APPS, J. A.; WILKIN, R. T. Thermodynamic Properties of Aqueous Carbonate Species and Solid Carbonate Phases of Selected Trace Elements pertinent to Drinking Water Standards of the U.S. Environmental Protection Agency. 2015.

ASTILLEROS, J. M. et al. The effect of barium on calcite {10$\bar{1}$4} surfaces during growth. **Geochimica et Cosmochimica Acta**, v. 64, n. 17, p. 2965–2972, 2000.

ASTILLEROS, J. M.; FERNÁNDEZ-DÍAZ, L.; PUTNIS, A. The role of magnesium in the growth of calcite: An AFM study. **Chemical Geology**, v. 271, n. 1–2, p. 52–58, 2010.

AZIMI, G. et al. Scale-resistant surfaces: Fundamental studies of the effect of surface energy on reducing scale formation. **Applied Surface Science**, v. 313, p. 591–599, set. 2014.

BECK, R.; ANDREASSEN, J. P. The onset of spherulitic growth in crystallization of calcium carbonate. **Journal of Crystal Growth**, v. 312, n. 15, p. 2226–2238, 2010.

BECK, R.; SEIERSTEN, M.; ANDREASSEN, J. P. The constant composition method for crystallization of calcium carbonate at constant supersaturation. **Journal of Crystal Growth**, v. 380, p. 187–196, 2013.

BEERS, K. J. **Numerical Methods for Chemical Engineering**. 1st ed. Cambrigde, UK: Cambridge University Press, 2007.

BESENHARD, M. O. et al. Evaluation of Parameter Estimation Methods for Crystallization Processes Modeled via Population Balance Equations. **Chemical Engineering**

Research and Design, v. 94, n. August, p. 275–289, 2015.

BLUE, C. R. et al. Chemical and physical controls on the transformation of amorphous calcium carbonate into crystalline CaCO3 polymorphs. **Geochimica et Cosmochimica Acta**, v. 196, p. 179–196, 2017.

BOTS, P. et al. The role of SO4 in the switch from calcite to aragonite seas. **Geology**, v. 39, n. 4, p. 331–334, 2011.

BOTS, P. et al. Mechanistic insights into the crystallization of amorphous calcium carbonate (ACC). **Crystal Growth and Design**, v. 12, n. 7, p. 3806–3814, 2012.

BREČEVIĆ, L.; KRALJ, D. ChemInform Abstract: On Calcium Carbonates: From Fundamental Research to Application. **ChemInform**, v. 39, n. 5, p. 467–484, 2008.

BREČEVIĆ, L.; NIELSEN, A. E. Solubility of amorphous calcium carbonate. **Journal of Crystal Growth**, v. 98, n. 3, p. 504–510, 1989.

CARRAZANA, L. G. **Coeficiente de Partição do CO ₂ no Processo de Injeção de Água Carbonatada**. 2012. Universidade Estadual de Campinas, 2012.

CHAKRABORTY, D. et al. Steady-State Transitions and Polymorph Transformations in Continuous Precipitation of Calcium Carbonate. **Industrial and Engineering Chemistry Research**, v. 33, n. 9, p. 2187–2197, 1994.

CHAKRABORTY, D.; BHATIA, S. K. Formation and aggregation of polymorphs in continuous precipitation. 1. Mathematical modeling. **Industrial and Engineering Chemistry Research**, v. 35, n. 6, p. 1985–1994, 1996a.

CHAKRABORTY, D.; BHATIA, S. K. Formation and aggregation of polymorphs in continuous precipitation. 2. Kinetics of CaCO3 precipitation. **Industrial and Engineering Chemistry Research**, v. 35, n. 6, p. 1995–2006, 1996b.

CHANG, R. et al. Calcium carbonate precipitation for CO 2 storage and utilization: A review of the carbonate crystallization and polymorphism. **Frontiers in Energy Research**, v. 5, n. JUL, p. 1–12, 2017a.

CHANG, R. et al. Tuning crystal polymorphisms and structural investigation of precipitated calcium carbonates for CO2 mineralization. **ACS Sustainable Chemistry and Engineering**, v. 5, n. 2, p. 1659–1667, 2017b.

CHEN, J.; XIANG, L. Controllable synthesis of calcium carbonate polymorphs at different temperatures. **Powder Technology**, v. 189, n. 1, p. 64–69, 2009.

CHEN, T.; NEVILLE, A. Influence of Mg^{2+} on the kinetics and crystal morphology of caco3 scale formation on the metal surface and in bulk solution. **Corrosion**, n. 04059, p. 1–

13, 2004.

CHEN, T.; NEVILLE, A.; YUAN, M. Calcium carbonate scale formation - Assessing the initial stages of precipitation and deposition. **Journal of Petroleum Science and Engineering**, v. 46, n. 3, p. 185–194, 2005.

CHIEN, C.-W.; LEE, C.-C.; TAI, C. Y. Heterogeneous nucleation rate of calcium carbonate derived from induction period. **Industrial and Engineering Chemistry Research**, v. 46, p. 6435–6441, 2007.

CHRISTOFFERSEN, M. R.; DOHRUP, J.; CHRISTOFFERSEN, J. Kinetics of growth and dissolution of calcium hydroxyapatite in suspensions with variable calcium to phosphate ratio. **Journal of Crystal Growth**, v. 186, n. 1–2, p. 283–290, 1998.

CHRISTOV, C.; MOLLER, N. A chemical equilibrium model of solution behavior and solubility in the H-Na-K-Ca-OH-Cl-HSO4-SO4-H2O system to high concentration and temperature. **Geochimica et Cosmochimica Acta**, v. 68, n. 18, p. 3717–3739, 2004.

COLLIER, A. P.; HOUNSLOW, M. J. Growth and aggregation rates for calcite and calcium oxalate monohydrate. **AIChE Journal**, v. 45, n. 11, p. 2298–2305, 1999.

COSMO, R. D. P. **Modelagem e Simulação Termodinâmica da Precipitação de Calcita em Condições de Poço**. 2013. Universidade Federal do Espírito Santo,Centro Universitário Norte, 2013.

COSMO, R. de P. et al. Estimating CO2 degassing effect on CaCO3 precipitation under oil well conditions. **Journal of Petroleum Science and Engineering**, v. 181, n. March, 2019.

COSTA, C. B. B. **Modelagem e Controle Ótimo do Processo de Cristalização do Ácido Adípico**. 2003. Universidade Estadual de Campinas, 2003.

COSTA, C. B. B.; MACIEL, M. R. W.; FILHO, R. M. Considerations on the crystallization modeling: Population balance solution. **Computers and Chemical Engineering**, v. 31, n. 3, p. 206–218, 2007.

CRABTREE, M., ESLINGER, D., FLETCHER, P., MILLER, M., JOHNSON, A., KING, G. Fighting scale — Removal and prevention. **Oilfield Review**, p. 30–45, 1999.

DALAS, E.; KOUTSOUKOS, P. G. Calcium Carbonate Scale Formation on Heated Metal Surfaces. **Geothermics**, v. 18, n. 1–2, p. 83–88, 1989.

DAVEY, R. J. et al. Rate controlling processes in solvent-mediated phase transformations. **Journal of Crystal Growth**, v. 79, n. 1- 3 PART 2, p. 648–653, 1986.

DAVID, R. et al. Modelling of multiple-mechanism agglomeration in a crystallization

process. **Powder Technology**, v. 130, n. 1–3, p. 338–344, 2003.

DAVID, R.; MARCHAL, P.; MARCANT, B. Modelling of agglomeration in industrial crystallization from solution. **Chemical Engineering & Technology**, v. 18, n. 5, p. 302–309, 1995.

DAVIS, J. K.; DOVE, P. M.; DE YOREO, J. J. The Role of Mg+2 as an impurity calcite growth. **Science**, v. 290, p. 1134–1137, 2000.

DE SOUZA, A. V. A.; ROSÁRIO, F.; CAJAIBA, J. Evaluation of calcium carbonate inhibitors using sintered metal filter in a pressurized dynamic system. **Materials**, v. 12, p. 1849–1862, 2019.

DEYHIMI, F.; GHALAMI-CHOOBAR, B. Potentiometric determination of activity coefficients for NH4Cl in the ternary NH4Cl/LiCl/H2O mixed electrolyte system. **Journal of Electroanalytical Chemistry**, v. 584, n. 2, p. 141–146, 2005.

DICKENS, B.; BOWEN, J. S. Refinement of the crystal structure of the aragonite phase of CaCO3. **Journal of Research of the National Bureau of Standards Section A: Physics and Chemistry**, v. 75A, n. 1, p. 27, 1971.

DICKENS, B.; BROWN, W. E. The Crystal Structure of Calcium Carbonate Hexahydrate at ~ –120°. **Inorganic Chemistry**, v. 9, n. 3, p. 480–486, 1970.

DONNET, M.; BOWEN, P.; LEMAÎTRE, J. A thermodynamic solution model for calcium carbonate: Towards an understanding of multi-equilibria precipitation pathways. **Journal of Colloid and Interface Science**, v. 340, n. 2, p. 218–224, 2009.

DU, H. et al. Amorphous CaCO3: Influence of the Formation Time on Its Degree of Hydration and Stability. **Journal of the American Chemical Society**, 2018.

DU, H.; AMSTAD, E. Water: How Does It Influence the CaCO3 Formation? **Angewandte Chemie - International Edition**, 2019.

DUAN, Z. et al. An improved model for the calculation of CO2 solubility in aqueous solutions containing Na+, K+, Ca2+, Mg2+, Cl-, and SO42-. **Marine Chemistry**, v. 98, n. 2–4, p. 131–139, 2006.

DUAN, Z.; LI, D. Coupled phase and aqueous species equilibrium of the H2O-CO2-NaCl-CaCO3system from 0 to 250 °C, 1 to 1000 bar with NaCl concentrations up to saturation of halite. **Geochimica et Cosmochimica Acta**, v. 72, n. 20, p. 5128–5145, 2008.

DUAN, Z.; SUN, R. An improved model calculating CO2 solubility in pure water and aqueous NaCl solutions from 273 to 533 K and from 0 to 2000 bar Zhenhao. **Chemical Geology**, v. 193, p. 257–271, 2003.

EFFENBERGER, H. Crystal Structure and Infrared Absorption Spectrum of Synthetic Monohydrocalcite, CaCO3 H20. **Monatshefte fiir Chemic**, v. 112, n. 8–9, p. 899–909, 1981.

EFFENBERGER, H.; ZEMANN, J.; MEREITER, K. Crystal structure refinements of magnesite, calcite, rhodochrosite, siderite, smithonite, and dolomite, with discussion of some aspects of the stereochemistry of calcite type carbonates. **Zeitschrift fur Kristallographie - New Crystal Structures**, v. 156, n. 3–4, p. 233–243, 1981.

FARKAS, L. Keimbildungsgeschwindigkeit in übersättigten Dämpfen. **Zeitschrift für Physikalische Chemie**, v. 125U, n. 1, p. 236–242, 1927.

GARCÍA, A. V.; THOMSEN, K.; STENBY, E. H. Prediction of mineral scale formation in geothermal and oilfield operations using the Extended UNIQUAC model. Part II. Carbonate-scaling minerals. **Geothermics**, v. 35, n. 3, p. 239–284, 2006.

GARSIDE, J. The concept of effectiveness factors in crystal growth. **Chemical Engineering Science**, v. 26, n. 9, p. 1425–1431, 1971.

GARSIDE, J. Industrial crystallization from solution. **Chemical Engineering Science**, v. 40, n. 1, p. 3–26, 1985.

GEBAUER, D. et al. Pre-nucleation clusters as solute precursors in crystallisation. **Chemical Society Reviews**, v. 43, n. 7, p. 2348–2371, 2014.

GEBAUER, D. et al. On classical and non-classical views on nucleation. **American Journal of Science**, v. 318, n. 9, p. 969–988, 2018.

GEBAUER, D.; VÖLKEL, A.; CÖLFEN, H. Stable Prenucleation Calcium Carbonate Clusters. **Science**, v. 322, p. 1819–1823, 2008.

GOWER, L. B. Biomimetic model systems for investigating the amorphous precursor pathway and its role in biomineralization. **Chemical Reviews**, v. 108, n. 11, p. 4551–4627, 2008.

GRAHAM, G. M. et al. The Impact of Dissolved Iron on the Performance of Scale Inhibitors Under Carbonate Scaling Conditions. **Society of Petroleum Engineers International Symposium on Oielfiield Chemistry**, 80254,Texas, EUA: 2003.

GREENWOOD, G. . The growth of dispersed precipitates in solutions. **Acta Metallurgica**, v. 4, n. 3, p. 243–248, 1956.

HAARBERG, T.; SELM, I.; ET AL. SPE 19449 Scale Formation in Reservoir and Production Equipment During Oil Recovery : An Equilibrium Model. **Society of Petroleum Engineers**, n. February, p. 75–84, 1992.

HARDIE, L. A. Secular variation in seawater chemistry: An explanation for the coupled secular variation in the mineralogies of marine limestones and potash evaporites over the past 600 m.y. **Geology**, v. 24, n. 3, p. 279–283, 1996.

HARVIE, C. E.; MØLLER, N.; WEARE, J. H. The prediction of mineral solubilities in natural waters: The Na-K-Mg-Ca-H-Cl-SO4-OH-HCO3-CO3-CO2-H2O system to high ionic strengths at 25°C. **Geochimica et Cosmochimica Acta**, v. 48, n. 4, p. 723–751, 1984.

HEATH, A. R. et al. Estimating average particle size by focused beam reflectance measurement (FBRM). **Particle and Particle Systems Characterization**, v. 19, n. 2, p. 84–95, 2002.

HOUNSLOW, M. J. et al. A micro-mechanical model for the rate of aggregation during precipitation from solution. **Chemical Engineering Science**, v. 26, n. 3, p. 282–285, 2001.

HULL, H.; TURNBULL, A. G. A thermochemical study of monohydrocalcite. **Geochimica et Cosmochimica Acta**, v. 37, n. 6, p. 1593–1601, 1973.

HUME, J.; TOPLEY, B. The Density of Calcium Carbonate Hexahydrate. **Journal of the Chemical Society**, n. 129, p. 2932–2934, 1926.

IGGLAND, M.; MAZZOTTI, M. Population balance modeling with size-dependent solubility: Ostwald ripening. **Crystal Growth and Design**, v. 12, n. 3, p. 1489–1500, 2012.

IHLI, J. et al. Dehydration and crystallization of amorphous calcium carbonate in solution and in air. **Nature Communications**, v. 5, p. 1–10, 2014.

JIANG, L.; WORDEN, R. H.; YANG, C. Thermochemical sulphate reduction can improve carbonate petroleum reservoir quality. **Geochimica et Cosmochimica Acta**, v. 223, p. 127–140, 2018.

JIMOH, O. A. et al. Aragonite precipitated calcium carbonate from magnesium rich carbonate rock for polyethersulfone hollow fibre membrane application. **Journal of Cleaner Production**, v. 195, p. 79–92, set. 2018.

JR, J. F. Z. et al. **Handbook of Aqueous Electrolyte Thermodynamics: Theory & Application**. 1st. ed. New York, EUA: Wiley-AIChE, 1986.

KAMAL, M. S. et al. Oilfield scale formation and chemical removal: A review. **Journal of Petroleum Science and Engineering**, v. 171, n. July, p. 127–139, 2018.

KAMHI, S. R. On the structure of vaterite CaCO 3. **Acta Crystallographica**, v. 16, n. 8, p. 770–772, 1963.

KAN, A.; TOMSON, M. Scale Prediction for Oil and Gas Production. **SPE Journal**,

v. 17, n. 02, p. 362–378, 2012.

KARTHIKA, S.; RADHAKRISHNAN, T. K.; KALAICHELVI, P. A Review of Classical and Nonclassical Nucleation Theories. **Crystal Growth and Design**, v. 16, n. 11, p. 6663–6681, 2016.

KAWANO, J. et al. Precipitation diagram of calcium carbonate polymorphs: Its construction and significance. **Journal of Physics Condensed Matter**, v. 21, n. 42, 2009.

KELLERMEIER, M. et al. Entropy Drives Calcium Carbonate Ion Association. **ChemPhysChem**, v. 17, n. 21, p. 3535–3541, 2016.

KESZEI, E. **Chemical Thermodynamics**. 1st ed. Budapest, Hungary: Springer, 2012.

KITANO, Y. The Behavior of Various Inorganic Ions in the Separation of Calcium Carbonate from a Bicarbonate Solution. **Bulletin of the Chemical Society of Japan**, v. 35, n. 12, p. 1973–1980, 1962.

KITANO, Y.; KANAMORI, N.; OOMORI, T. Measurements of distribution coefficients of strontium and barium between carbonate precipitate and solution-Abnormally high values of distribution coefficients measured at early stages of carbonate formation. **Geochemical Journal**, v. 4, 1971.

KONRAD, F. et al. Transformation of Amorphous Calcium Carbonate in Air. **Crystal Growth and Design**, v. 16, n. 11, p. 6310–6317, 2 nov. 2016.

KONTOYANNIS, C. G.; VAGENAS, N. V. Calcium carbonate phase analysis using XRD and FT-Raman spectroscopy. **Analyst**, v. 125, n. 2, p. 251–255, 2000.

KOUTSOUKOS, P. G.; KONTOYANNIS, C. G. Precipitation of calcium carbonate in aqueous solutions. **Journal of the Chemical Society, Faraday Transactions 1: Physical Chemistry in Condensed Phases**, v. 80, n. 5, p. 1181–1192, 1984.

KRUPKA, K. M.; CANTRELL, K. J.; MCGRAIL, B. P. **Thermodynamic Data for Geochemical Modeling of Carbonate Reactions Associated with CO2 Sequestration – Literature Review**. Richland, Washington: Northwest, Pacific, 2010.

KUMAR, S.; NAIYA, T. K.; KUMAR, T. Developments in oilfield scale handling towards green technology-A review. **Journal of Petroleum Science and Engineering**, v. 169, p. 428–444, 2018.

LAGARIAS, J. C. et al. Convergence properties of the Nelder-Mead simplex method in low dimensions. **SIAM Journal on Optimization**, v. 9, n. 1, p. 112–147, 1998.

LAKSHMI, D. S. et al. Application of ionic liquid polymeric microsphere in oil field scale control process. **Journal of Petroleum Science and Engineering**, v. 112, p. 69–77, 2013.

LALLEMAN, S. et al. Determination of the Bromley contributions to estimate the activity coefficient of neodymium electrolytes. **Chemical Engineering Science**, v. 77, p. 189–195, 2012.

LASSIN, A. et al. Dynamics of calcium carbonate formation: Geochemical modeling of a two-step mechanism. **Geochimica et Cosmochimica Acta**, v. 240, p. 236–254, nov. 2018.

LASSIN, A.; ANDRÉ, L.; LACH, A. Considerations About the Building of a Thermodynamic Database for the Chemical Description of Highly Saline Systems. **Procedia Earth and Planetary Science**, v. 17, p. 304–307, 2017.

LI, J.; DUAN, Z. A thermodynamic model for the prediction of phase equilibria and speciation in the H2O-CO2-NaCl-CaCO3-CaSO4 system from 0 to 250°C, 1 to 1000 bar with NaCl concentrations up to halite saturation. **Geochimica et Cosmochimica Acta**, v. 75, n. 15, p. 4351–4376, 2011.

LI, Q. et al. Interfacial energies for heterogeneous nucleation of calcium carbonate on mica and quartz. **Environmental Science and Technology**, v. 48, n. 10, p. 5745–5753, 2014.

LIU, J. et al. The Summary of the Scale and the Treatment Measures in Oilfield. **Recent Innovations in Chemical Engineering (Formerly Recent Patents on Chemical Engineering)**, v. 7, n. 1, p. 25–33, 2015.

LIVK, I.; ILIEVSKI, D. A macroscopic agglomeration kernel model for gibbsite precipitation in turbulent and laminar flows. **Chemical Engineering Science**, v. 62, n. 14, p. 3787–3797, 2007.

LOWENSTEIN, T. K. et al. Secular variation in seawater chemistry and the origin and significance of calcium chloride basinal brines; Geological Society of America, 2003 annual meeting. **Geological Society of America, 2003 annual meeting, Seattle, WA, United States, Nov. 2-5, 2003**, v. 35, n. 6, p. 201, 2003.

M. SCHWAAB AND J.C. PINTO. **Análise de Dados Experimentais - Volume I Fundamentos de Estatística**. 1. ed. Rio de Janeiro, Brasil: COPPE/UFRJ, 2007.

MANN, S. Mineralization in biological systems. **Inorganic Elements in Biochemistry**, p. 125–174, 1983.

MARCHAL, P. et al. Crystallization and precipitation engineering-I. An efficient method for solving population balance in crystallization with agglomeration. **Chemical Engineering Science**, v. 43, n. 1, p. 59–67, 1988.

MARKGRAFR, S. .; REEDER, R. . High-temperature structure refinements of calcite and magnesite. **American Mineralogist**, v. 70, p. 590400, 1985.

MARSHALL, S. L.; MAY, P. M.; HEFTER, G. T. Least-Squares Analysis of Osmotic Coefficient Data at 25 °C According to Pitzer's Equation. 1. 1:1 Electrolytes. **Journal of Chemical and Engineering Data**, v. 40, n. 5, p. 1041–1052, 1995.

MATSOUKAS, T. **Fundamentals of chemical engineering thermodynamics : with applications to chemical processes**. 1st. ed. Boston, EUA: Prentice Hall, 2012.

MAYORGA, I. C.; ASTILLEROS, J. M.; FERNÁNDEZ-DÍAZ, L. Precipitation of caco 3 polymorphs from aqueous solutions: The role of ph and sulphate groups. **Minerals**, v. 9, n. 3, p. 1–16, 2019.

MAZZULLO, S. J.; CHILINGARIAN, G. V. **Depositional Models of Carbonate Reservoirs**. Amsterdã, Holanda: Elsevier, 1992. v. 30

MERSMANN, A. **Crystallization Technology Handbook**. Second Edi ed. Garching, Germany: Marcel Dekker, 1995.

MERSMANN, A. **Crystallization Technology Handbook**. 1st ed. Marcel Dekker, 2001.

MIRJALILI, S. **Particle Swarm Optimisation. In: Evolutionary Algorithms and Neural Networks. Theory and Applications**. 1st. ed. Brisbane, Australia: Springer, 2019.

MOGHADASI, J. et al. Formation Damage Due to Scale Formation in Porous Media Resulting From Water Injection. n. September, p. 1–11, 2007.

MORAIS, J. M. De. **Petróleo em Águas Profundas - Uma história tecnológica da PETROBRAS na exploração e produção offshore**. Brasilía, Brasil: Instituto de Pesquisa Econômica Aplicada - IPEA, 2013.

MORSE, J. W.; WANG, Q.; TSIO, M. Y. Influences of temperature and Mg:Ca ratio on CaCO3 precipitates from seawater. **Geology**, v. 25, n. 1, p. 85–87, 1997.

MUCCI, A.; MORSE, J. W. The incorporation of divalent Mg and divalent Sr into calcite overgrowths : influences of growth rate and solution composition. **Geochimica et Cosmochimica Acta**, v. 47, p. 217–233, 1983.

MULLIN, J. . **Crystallization**. 4. ed. Oxford: Reed Educacional and Professional Publishing Ltd, 2001.

MYASNIKOV, S. K.; CHIPRYAKOVA, A. P.; KULOV, N. N. Kinetics, energy characteristics, and intensification of crystallization processes in chemical precipitation of hardness ions. **Theoretical Foundations of Chemical Engineering**, v. 47, n. 5, p. 505–523, 2013.

NAGY, Z. K.; FUJIWARA, M.; BRAATZ, R. D. Modelling and control of combined

cooling and antisolvent crystallization processes. **Journal of Process Control**, v. 18, n. 9, p. 856–864, 2008.

NAKA, K.; CHUJO, Y. Control of crystal nucleation and growth of calcium carbonate by synthetic substrates. **Chemistry of Materials**, v. 13, n. 10, p. 3245–3259, 2001.

NANCOLLAS, G. H.; REDDY, M. M. The crystallization of calcium carbonate. II. Calcite growth mechanism. **Journal of Colloid And Interface Science**, v. 37, n. 4, p. 824–830, 1971.

NANCOLLAS, G. H.; REDDY, M. M. The Kinetics of Crystallization of Scale-Forming Minerals. **Society of Petroleum Engineers Journal**, v. 14, n. 02, p. 117–126, 1974.

NATSI, P. D.; ROKIDI, S.; KOUTSOUKOS, P. G. Calcium carbonate scale formation and prevention in aqueous solutions and mixed solvents. **NACE - International Corrosion Conference Series**, v. 3, 2016.

NAVROTSKY, A. Energetic clues to pathways to biomineralization: Precursors, clusters, and nanoparticles. **Proceedings of the National Academy of Sciences**, v. 101, n. 33, p. 12096–12101, 2004.

NIELSEN, M. H.; ALONI, S.; DE YOREO, J. J. In situ TEM imaging of CaCO3 nucleation reveals coexistence of direct and indirect pathways. **Science**, v. 345, n. 6201, p. 1158–1162, 2014.

NIELSEN, M. R. et al. Inhibition of Calcite Growth: Combined Effects of Mg2+ and SO42-. **Crystal Growth and Design**, v. 16, n. 11, p. 6199–6207, 2 nov. 2016.

OGINO, T.; SUZUKI, T.; SAWADA, K. The formation and transformation mechanism of calcium carbonate in water. **Geochimica et Cosmochimica Acta**, v. 51, n. 10, p. 2757–2767, 1987.

OGINO, T.; SUZUKI, T.; SAWADA, K. THE RATE AND MECHANISM OF POLYMORPHIC TRANSFORMATION OF CALCIUM CARBONATE IN WATER Takeshi OGINO, Toshio SUZUKI and Kiyoshi SAWADA. **Journal of Crystal Growth**, v. 100, p. 159–167, 1990.

OLAJIRE, A. A. A review of oilfield scale management technology for oil and gas production. **Journal of Petroleum Science and Engineering**, v. 135, p. 723–737, 2015.

ORAL, Ç. M.; ERCAN, B. Influence of pH on morphology, size and polymorph of room temperature synthesized calcium carbonate particles. **Powder Technology**, v. 332, p. 781–788, 2018.

OSTWALD, W. Studien über die Bildung und Umwandlung fester Körper. **Zeitschrift**

für Physikalische Chemie, v. 22U, n. 1, 1897.

PEIPER, J. C.; PITZER, K. S. Thermodynamics of aqueous carbonate solutions including mixtures of sodium carbonate, bicarbonate, and chloride. **The Journal of Chemical Thermodynamics**, v. 14, n. 7, p. 613–638, 1982.

PENG, C. et al. Kinetics of calcite dissolution in CO2-saturated water at temperatures between (323 and 373)K and pressures up to 13.8MPa. **Chemical Geology**, v. 403, p. 74–85, 2015.

PERRY et al. **Perry's Chemical Engineers' Handbook**. 9th. ed. McGraw-Hill, New York, EUA: 2007.

PIN, S. et al. Supersaturated calcium carbonate solutions are classical. **Science Advances**, v. 4, n. 1, p. 62-83, 2018.

PITZER, K. S. **Activity Coefficients in Electrolyte Solutions**. 2nd ed. London,UK: CRC press, 1991.

PITZER, K. S.; MAYORGA, G. Thermodynamics of Electrolytes. II. Activity and Osmotic Coefficients for Strong Electrolytes with One or Both Ions Univalent. **J. Phys. Chem.**, v. 77, n. 19, p. 2300–2308, 1973.

PLUMMER, L. N. et al. A computer program incorporating Pitzer's equations for calculation of geochemical reactions in brines. US Geological Survey. **Water-Resources Res.**, v. 9, p. 707–720, 1988.

PLUMMER, L. N.; BUSENBERG, E. Data on the Crystal Growth of Calcite From Calcium Bicarbonate Solutions At 34 ° C and Co2 Partial. **US Geological Survey**, v. 99–247, 1999.

PLUMMER, L. N.; WIGLEY, T. M. L.; PARKHURST, D. L. Kinetics of calcite dissolution in co2-water systems at 5 degree to 60 degree c and 0. 0 to 1. 0 atm co2. **Am J Sci**, v. 287, p. 179-216, 1978.

PLUMMER, N. L.; BUSENBERG, E. The solubilities of calcite, aragonite and vaterite in CO2-H2O solutions between 0 and 90°C, and an evaluation of the aqueous model for the system CaCO3-CO2-H2O. **Geochimica et Cosmochimica Acta**, v. 46, p. 1011–1040, 1982.

PRESS, W. . et al. **Numerical Recipes: The Art of Scientific Computing**. 3 rd ed. Cambridge University Press, 2007.

PRIETO, M. et al. Nucleation, growth, and zoning phenomena in crystallizing (Ba,Sr)CO3, Ba (SO 4,CRO4), (Ba,Sr) SO 4 , and (Cd,Ca) CO 3 solid solutions from aqueous solutions. **Geochimica et Cosmochimica Acta**, v. 61, n. 16, p. 3383–3397, 1997.

RAMISCH, F. et al. Calcite dissolution in two deep eutrophic lakes. **Geochimica et Cosmochimica Acta**, v. 63, n. 19–20, p. 3349–3356, 1999.

RAMKRISHNA, D.; SINGH, M. R. Population Balance Modeling: Current Status and Future Prospects. **Annual Review of Chemical and Biomolecular Engineering**, v. 5, n. 1, p. 123–146, 2014.

RAMSTAD, K. et al. Predicting Carbonate Scale in Oil Producers from High Temperature Reservoirs. **6th SPE International Symposium on Oilfield Scale, Aberdeen, 26–27 May**, n. June 2004, p. 26–27, 2005.

RASMUSSON, A. et al. **Mathematical Modeling in Chemical Engineering**. 1. ed. Cambridge: Cambridge University Press, 2014.

REIS, M. C. et al. Non-equilibrium thermodynamic model for calcium carbonate supersaturated solutions of high salinity. **Journal of Mathematical Chemistry**, v. 54, n. 1, p. 44–60, 2016.

REYNOLDS, C. W. Flocks, herds, and schools: A distributed behavioral model. **Proceedings of the 14th Annual Conference on Computer Graphics and Interactive Techniques, SIGGRAPH 1987**, v. 21, n. 4, p. 25–34, 1987.

RIGOPOULOS, S.; JONES, A. Modeling of Semibatch Agglomerative Gas-Liquid Precipitation of CaCO 3 in a Bubble Column Reactor. **Industrial and Engineering Chemistry Research**, v. 42, n. 25, p. 6567–6575, 2003.

RODRIGUEZ-BLANCO, J. D. et al. The role of pH and Mg on the stability and crystallization of amorphous calcium carbonate. **Journal of Alloys and Compounds**, v. 536, p. S477–S479, 2011.

RODRIGUEZ-BLANCO, J. D. et al. The role of Mg in the crystallization of monohydrocalcite. **Geochimica et Cosmochimica Acta**, v. 127, p. 204–220, 2014.

RODRIGUEZ-BLANCO, J. D.; SHAW, S.; BENNING, L. G. The kinetics and mechanisms of amorphous calcium carbonate (ACC) crystallization to calcite, via vaterite. **Nanoscale**, v. 3, n. 1, p. 265–271, 2011.

ROSA, A. J.; CARVALHO, R. S.; XAVIER, J. A. D. **Engenharia de reservatórios de petróleo**. 1ª ed. Rio de Janeiro, Brazil: Interciência, 2011.

ROSA, S.; LUNDAGER MADSEN, H. E. Kinetics of mass crystallization of calcium carbonate at 25, 30 and 37 °c. **Journal of Crystal Growth**, v. 318, n. 1, p. 99–102, 2011.

ROSSI, R. J. **Mathematical statistics**. 1st. ed. Hoboken, EUA: John Wiley & Sons, 2018. v. 104

SANJIV RAJ, K.; DEVI, N.; SUBRAMANIAN, V. K. Effect of barium and strontium ions on the morphology and polymorphism of CaCO3. **Chemical Physics Letters**, v. 750, n. January, 2020.

SANTEN, A. Van. The Ostwald Step Rule. **J. Phys.Chem.** n. 6, p. 5768–5769, 1984.

SANTOS, H. F. L. L. et al. A physical model for scale growth during the dynamic tube blocking test. **OTC Brasil 2017**, p. 161–180, 2017.

SAWADA, K.; OGINO, T.; SUZUKI, T. The distribution coefficients of Mg2+ ion between CaCO3 polymorphs and solution and the effects on the formation and transformation of CaCO3 in water. **Journal of Crystal Growth**, v. 106, n. 2–3, p. 393–399, 1990.

SCALA, F. **Fluidized bed technologies for near-zero emission combustion and gasification**. Philadelphia, EUA: Woodhead Publishing, 2013.

SCHEID, A. J. et al. Mechanism and Kinetic Modeling of Ethanol Conversion to 1 - Butanol over Mg and Al Oxide Derived from Hydrotalcites. **Industrial & Engineering Chemistry Research**, v. 58, p. 12981–12995, 2019.

SCHMIDT, B. et al. Application of process modelling tools in the scale-up of pharmaceutical crystallisation processes. **Organic Process Research and Development**, v. 8, n. 6, p. 998–1008, 2004.

SERPA, F. **Estudo Do Comportamento Termodinâmico E Cinético De Misturas Água + Meg Na Presença De Co 2 E Sais**. 2015. UNIT, 2015.

SHAMPINE, L. F.; REICHELT, M. W. ODE MATLAB SOLVERS. **Journal of Scientific Computing**, v. 18, p. 1–22, 1997.

SHI, W. et al. Dissolution of calcite at up to 250 °c and 1450 bar and the presence of mixed salts. **Industrial and Engineering Chemistry Research**, v. 52, n. 6, p. 2439–2448, 2013.

SHIRAKI, R.; BRANTLEY, S. L. Kinetics of near-equilibrium calcite precipitation at 100°C: An evaluation of elementary reaction-based and affinity-based rate laws. **Geochimica et Cosmochimica Acta**, v. 59, n. 8, p. 1457–1471, 1995.

SOLOMON, T. The definition and unit of ionic strength. **Journal of Chemical Education**, v. 78, n. 12, p. 1691, 2001.

SPANOS, N.; KOUTSOUKOS, P. G. Kinetics of Precipitation of Calcium Carbonate in Alkaline pH at Constant Supersaturation. Spontaneous and Seeded Growth. **The Journal of Physical Chemistry B**, v. 102, n. 34, p. 6679–6684, 1998.

SUN, Y. et al. Indirect CO2 mineral sequestration by steelmaking slag with NH4Cl as

leaching solution. **Chemical Engineering Journal**, v. 173, n. 2, p. 437–445, 2011.

SUNDERMANN, C. M. **Production of Calcium Carbonate from Steelmaking Slag and Captured CO2- Optimisation of the Carbonation Process and Product Quality**. 2016. Aalto University, Finland and Royal Institute of Technology, 2016.

TENG, H. H., DOVE, P. M., de YOREO, J. J. Kinetics of calcite growth: Surface processes and relationships to macroscopic rate laws. **Geochemical et Cosmochimica Acta**, v.64, p. 2255-2266, 2000.

THOMAS, J. . **Fundamentos da engenharia de petróleo**. 2ª ed. Rio de Janeiro, Brazil: Interciência, 2001.

TOBLER, D. J. et al. Effect of pH on Amorphous Calcium Carbonate Structure and Transformation. **Crystal Growth and Design**, v. 16, n. 8, 2016.

TRAMPUŽ, M.; TESLIĆ, D.; LIKOZAR, B. Crystallization of fesoterodine fumarate active pharmaceutical ingredient: Modelling of thermodynamic equilibrium, nucleation, growth, agglomeration and dissolution kinetics and temperature cycling. **Chemical Engineering Science**, v. 201, p. 97–111, 2019.

VENÂNCIO, F.; DO ROSÁRIO, F. F.; CAJAIBA, J. A low-cost system based on image analysis for monitoring the crystal growth process. **Sensors (Switzerland)**, v. 17, n. 6, 2017.

VETTER, T. et al. Modeling nucleation, growth, and ostwald ripening in crystallization processes: A comparison between population balance and kinetic rate equation. **Crystal Growth and Design**, v. 13, n. 11, p. 4890–4905, 2013a.

VILLIERS, J. P. . CRYSTAL STRUCTURES OF ARAGONITE , STRONTIANITE , AND WITHERITE. **The American Mineralogist**, v. 56, p. 758–767, 1971.

WAGNER, V. C. Theorie der Alterung von Niederschliigen durch Umlosen. **Z. Elektrochem**, v. 65, p. 581−591, 1961.

WALKER, J. M.; MARZEC, B.; NUDELMAN, F. Solid-State Transformation of Amorphous Calcium Carbonate to Aragonite Captured by CryoTEM. **Angewandte Chemie - International Edition**, v. 56, n. 39, p. 11740–11743, 2017.

WALY, T. K. . **Minimizing the use of chemicals to control scaling in SWRO _ improved prediction of the scaling potential of calcium carbonate**. 1st. ed. London: CRC press, 2011.

WANG, J.; BECKER, U. Structure and carbonate orientation of vaterite (caco3). **American Mineralogist**, v. 94, n. 2–3, p. 380–386, 2009.

WANG, P. C.; SHOUP, T. E. Parameter sensitivity study of the Nelder-Mead Simplex Method. **Advances in Engineering Software**, v. 42, n. 7, p. 529–533, 2011.

WEINER, S.; ADDADI, L. Design strategies in mineralized biological materials. **Journal of Materials Chemistry**, v. 7, n. 5, p. 689–702, 1997.

WINKLER, P. M. et al. Heterogeneous nucleation experiments bridging the scale from molecular ion clusters to nanoparticles. **Science**, v. 319, n. 5868, p. 1374–1377, 2008.

YAMANAKA, S. et al. AFM investigation for the initial growth processes of calcium carbonate on hydrophilic and hydrophobic substrate. **Crystal Growth and Design**, v. 9, n. 7, p. 3245–3250, 2009.

YANG, X. et al. The influence of O-carboxymethylchitosan on the crystallization of calcium carbonate. **Powder Technology**, v. 204, n. 2–3, p. 228–235, 20 dez. 2010.

ZEEBE, R. E. On the molecular diffusion coefficients of dissolved CO2, HCO3-, and CO32-and their dependence on isotopic mass. **Geochimica et Cosmochimica Acta**, v. 75, n. 9, p. 2483–2498, 2011.

ZHANG, Z. et al. Transformation of amorphous calcium carbonate into aragonite. **Journal of Crystal Growth**, v. 343, n. 1, p. 62–67, 2012.

ZHAO, J. et al. A review of heterogeneous nucleation of calcium carbonate and control strategies for scale formation in multi-stage flash (MSF) desalination plants. **Desalination**, v. 442, n. May, p. 75–88, set. 2018.

APPENDIX A

Table A1- Pitzer parameters values for the specific ion interaction pairs. Firstly, for the ionic pairs and then for ionic-neutral pairs. (Continues on next page)

Cation	Anion	β^0_{ca}	β^1_{ca}	β^2_{ca}	C^{Φ}_{ca}
Na^{+1}	Cl^{-1}	0.0765	0.2644	-	0.00127
Na^{+1}	SO_4^{-2}	0.01958	1.113	-	0.00497
Na^{+1}	HSO_4^{-1}	0.0454	0.398	-	-
Na^{+1}	OH^{-1}	0.0864	0.253	-	0.0044
Na^{+1}	HCO_3^{-1}	0.0277	0.0411	-	-
Na^{+1}	CO_3^{-2}	0.0399	1.389	-	0.0044
K^{+1}	Cl^{-1}	0.04835	0.2122	-	-0.00084
K^{+1}	SO_4^{-2}	0.04995	0.7793	-	-
K^{+1}	HSO_4^{-1}	-0.0003	0.1735	-	-
K^{+1}	OH^{-1}	0.1298	0.320	-	0.0041
K^{+1}	HCO_3^{-1}	0.0296	-0.013	-	-0.008
K^{+1}	CO_3^{-2}	0.1488	1.43	-	-0.0015
Ca^{+2}	Cl^{-1}	0.3159	1.614	-	-0.00034
Ca^{+2}	SO_4^{-2}	0.2	3.1973	-54.24	-
Ca^{+2}	HSO_4^{-1}	0.2145	2.53	-	-
Ca^{+2}	OH^{-1}	-0.1747	-0.2303	-5.72	-
Ca^{+2}	HCO_3^{-1}	0.4	2.977	-	-
Mg^{+2}	Cl^{-1}	0.35235	1.6815	-	0.00519
Mg^{+2}	SO_4^{-2}	0.2210	3.343	-37.23	0.025
Mg^{+2}	HSO_4^{-1}	0.4746	1.729	-	-
Mg^{+2}	HCO_3^{-1}	0.493	0.93	-	-
H^{+1}	Cl^{-1}	0.1775	0.2945	-	0.0008
H^{+1}	SO_4^{-2}	0.0298	-	-	0.0438
H^{+1}	HSO_4^{-1}	0.2065	0.5556	-	-
Ba^{+2}	SO_4^{-2}	0.2218	3.952	-64.02	0.025
Ba^{+2}	HSO_4^{-1}	0.2075	3.003	-	-
Ba^{+2}	HCO_3^{-1}	0.3577	0.67	-	-

Cation	Anion	β^0_{ca}	β^1_{ca}	β^2_{ca}	C^{Φ}_{ca}
Ba^{+2}	Cl^{-1}	0.3504	1.995	-	-0.03654
Ba^{+2}	OH^{-1}	0.2891	3.2646	-	-0.06525
Ba^{+2}	CO_3^{-2}	0.1827	2.6201	-	-0.12
Sr^{+2}	SO_4^{-2}	0.2220	2.88	-41.8	0.019
Sr^{+2}	HSO_4^{-1}	0.4767	1.4895	-	-
Sr^{+2}	HCO_3^{-1}	0.3271	0.7215	-	-
Sr^{+2}	Cl^{-1}	0.3810	2.223	-	-0.00246
Sr^{+2}	OH^{-1}	0.4768	1.1826	-	0.00311
Neutral-Ion	**Na^{+1}**	**K^{+1}**	**Ca^{+2}**	**SO_4^{-1}**	**HSO_4^{-2}**
$\lambda CO_{2,i}$	0.1	0.051	0.183	0.097	-0.003

Source: Pitzer (1991) for the Barium and Strontium pairs and for all others Harvie et al. (1984).

Table A2 – Interaction parameters in CO_2 liquid-vapour equilibrium.

T-P coefficient	$\frac{\mu^{l(0)}_{CO_2}}{RT}$	λ_{CO2-Na}	$\xi_{CO2-Na-Cl}$
c_1	28.9447706	-0.411370585	$3.36389723 \times 10^{-4}$
c_2	-0.0354581768	$6.07632013 \times 10^{-4}$	$-1.98298980 \times 10^{-5}$
c_3	-4770.67077	97.5347708	-
c_4	$1.02782768 \times 10^{-5}$	-	-
c_5	33.8126098	-	-
c_6	$9.04037140 \times 10^{-3}$	-	-
c_7	$-1.14934031 \times 10^{-3}$	-	-
c_8	-0.307405726	-0.0237622469	$2.12220830 \times 10^{-3}$
c_9	-0.0907301486	0.0170656236	$-5.24873303 \times 10^{-3}$
c_{10}	$9.32713393 \times 10^{-4}$	-	-
c_{11}	-	$1.41335834 \times 10^{-5}$	-

Source: Duan e Sun (2003).

Table A3 – Interaction parameters for the CO_2 fugacity calculation.

Coefficient	Temperature and Pressure range					
	1	2	3	4	5	6
c_1	1	-7.17×10^{-1}	-6.51×10^{-2}	5.03	-16.06	-1.56×10^{-1}
c_2	4.75×10^{-3}	1.59×10^{-4}	-2.14×10^{-4}	-4.42×10^{-3}	-2.71×10^{-3}	4.46×10^{-4}
c_3	-3.35×10^{-6}	-4.92×10^{-7}	-1.14×10^{-6}	0	0	-9.10×10^{-7}
c_4	0	0	0	1.96	1.41×10^{-1}	0
c_5	-1.32	0	0	0	0	0
c_6	-3.84×10^{-6}	-2.78×10^{-7}	1.15×10^{-7}	2.42×10^{-6}	8.11×10^{-7}	1.06×10^{-7}
c_7	0	1.18×10^{-9}	1.19×10^{-9}	0	0	2.42×10^{-10}
c_8	2.28×10^{-3}	0	0	-9.37×10^{-4}	-1.14×10^{-4}	0
c_9	0	0	0	-1.5	2.38	3.58×10^{-1}
c_{10}	0	0	0	3.02×10^{-3}	5.05×10^{-4}	6.33×10^{-5}
c_{11}	0	0	0	-31.37	-17.76	-249.89
c_{12}	-	-96.53	-221.34	-12.84	985.92	0
c_{13}	-	4.47×10^{-1}	0	0	0	0
c_{14}	-	101.81	71.82	0	0	888.76
c_{15}	-	5.37×10^{-6}	6.61×10^{-6}	-1.50×10^{-5}	-5.49×10^{-7}	6.63×10^{-7}

T-P range : 1 = 273 K< T< 573 K and P<P_1, P_1 being the saturation pressure of CO_2; 2 = 273 K<T<340 K and P_1<P<1000 bar; 3 = 273 K<T<340 K and P>1000 bar; 4 = 340 K<T<435 K and P_1<P<1000 bar; 5 = 340 K< T<435 K and P>1000 bar; 6 = T>435 K and P>P_1. Source: Duan and Li (2006).

Table A4- Values of physicochemical properties and crystallization $CaCO_3$ parameters.

Symbol	Value / Equation
a_{cat} [-]	$\exp\left(z_m^2 F + \sum_a m_a(2B_{ma} + Z\,C_{ma}) + \lvert z_m\rvert \sum_c \sum_a m_c m_a C_{ca}\right) m_c$ [a]
a_{anion} [-]	$\exp\left(z_x^2 F + \sum_a m_a(2B_{cx} + Z\,C_{cx}) + \lvert z_x\rvert \sum_c \sum_a m_c m_a C_{ca}\right) m_a$ [a]
D_{ff} [$m^2.s^{-1}$]	$7.92\ x\ 10^{-10}$ [b]
$D_{Mg,vat}$ [-]	$ranging\ from\ 0.042 - 0.071\ in\ relation\ with\ m_{Mg}\ and\ m_{Ca}$ [c]
$D_{Ba,calc}$ [-]	$ranging\ from\ 0.06 - 0.1\ in\ relation\ with\ m_{Ba}\ and\ m_{Ca}$ [d]
$D_{Sr,calc}$ [-]	$ranging\ from\ 0.15 - 0.4\ in\ relation\ with\ m_{Sr} and\ m_{Ca}$ [d]
$k_{a,calc}$ [-]	1(assuming cubic form)[e]
$k_{v,calc}$ [-]	1 (assuming cubic form) [e]
$k_{a,vat}$ [-]	1.0466 (assuming spherical form) [e]
$k_{v,vat}$ [-]	0.5236 (assuming spherical form) [e]
P [$W.kg^{-1}$]	$\frac{0.479}{m_r}$ [f]
$V_{m,calc}$ [$m^3.mol^{-1}$]	$3.69\ x\ 10^{-5}$ [g]
$V_{m,vat}$ [$m^3.mol^{-1}$]	$3.78\ x\ 10^{-5}$ [h]
$Re_{p,i}$ [-]	$\frac{\rho_r^3\ P\ L}{\mu_r^3}$ [j]
Sc [-]	$\frac{\mu_r}{\rho_r D_{ff}}$ [i]
γ_c [$N.m^{-1}$]	$1.42\ x\ 10^{-1}$ [l]
γ_v [$N.m^{-1}$]	$1.33\ x\ 10^{-1}$ [l]
μ_r [Pa.s]	$8.89\ x\ 10^{-4}$ [m]
ν_r[$m^2.s^{-1}$]	$8.917\ x\ 10^{-7}$ [m]
ρ_r [$kg.m^{-3}$]	997[m]
ρ_{cal} [$kg.m^{-3}$]	2711[n]
ρ_{vat} [$kg.m^{-3}$]	2645[n]

Source: [a]Harvie *et al.* (1984); Pitzer (1991);[b] Brečević and Kralj (2008); [c] Sawada (1990);[d] Kitano *et al.* (1971); [e] <http://rruff.geo.arizona.edu/AMS/amcsd.php> (Acessed in Mar. 2020);[f] Aldeia *et al.*, (2019);[g] Cosmo (2013);[h] Apps and Wilkin (2015);[i] Mersmann A., Crystallization Technology Handbook, 2001;[j] Welty J.R. *et. al.*, Fundamentals of Momentum, Heat and Mass Transfer, 2008;[l] (Donnet *et al*. (2009);[m] <https://wiki.anton-paar.com/br-pt/agua> (Acessed in Mar. 2020);[n] <https://www.mindat.org> (Acessed in Jan. 2020).